ASSESSING THE CARBON SEQUESTRATION POTENTIAL IN SOUTHWESTERN SWEDEN

A comparative study of igneous rock from Greenland, Iceland, and Sweden to evaluate the carbonatization potential of the Billdal area, SW Sweden

Alaël Temmar

UNIVERSITY OF GOTHENBURG

Faculty of Science

ASSESSING THE CARBON SEQUESTRATION POTENTIAL IN SOUTHWESTERN SWEDEN

A comparative study of igneous rock from Greenland, Iceland, and Sweden to evaluate the carbonatization potential of the Billdal area, SW Sweden

Alaël Temmar

ABSTRACT

The main purpose of this study is to investigate the potential of geological Carbon Capture and Storage (CCS) in SW Sweden using an innovative technique which mimics Earth's natural way of regulating the global carbon cycle by turning CO_2 gas into carbonate minerals. To achieve this, comparative experiments on CCS potential were conducted using six different igneous rock samples. These encompassed granite, gabbro, and dolerite of Proterozoic age from the Billdal area in Gothenburg, Sweden, 1.3 Ga nepheline syenite and carbonatite from the Grønnedal-Íka alkaline complex in SW Greenland, and a young basalt from the Holuhraun volcanic eruption in Iceland 2014 – 2015. Powdered rock samples of size 45 – 250 μm were subjected to carbonation reactions with carbonated deionized water in closed systems at ambient temperature, 50°C, and 100°C, respectively. The room temperature experiments lasted 63 days, while the 50°C ran for 32 days, and the 100°C were conducted in a manner of three hours. The three experimental sets were monitored daily by recording the pH of the solutions, showing gradual increases in pH with time until reaching stable levels within the basic range. Among the rock samples, gabbro exhibited the highest pH value (8.68) at room temperature, while syenite demonstrated the highest pH (9.01) at 50°C, and carbonatite displayed the highest pH (8.42) at 100°C. After reaching a stable pH ~8, a weak NaHCO3 – Na2CO3 solution of pH 9.2 was added to the solutions to enhance the potential of carbonate precipitation.

Pre- and post- treated powdered rock samples were analysed using X-Ray Diffraction (XRD), Scanning Electron Microscopy with Energy Dispersive X-Ray Spectroscopy (SEM – EDX), Circular Back Scatter detector (CBS), and Everhart-Thornley Detector (ETD). Results using XRD showed no carbonate precipitate while results of SEM-EDX found carbonate precipitates, most likely calcite, on basalt, carbonatite, and nepheline syenite, but no precipitation on the granite, gabbro, and dolerite. The low carbonatization rate of the latter three are ascribed to the lack of suitable divalent cations for carbonate mineral formation. One surprising result was the degree of mineral alteration in these Swedish rocks, which had turned pyroxenes into amphiboles. Pyroxenes would otherwise have been ideal candidates for CCS. With these results at hand, the highly altered rocks of SW Sweden are deemed unsuitable for CO_2 sequestration through carbonate precipitation.

Keywords:

Climate change, carbon sequestration, rock – water geochemistry, petrology, carbonatization reaction, XRD, SEM.

七転び八起き

"Stumbling Seven Times, But Standing Up Eight"

Of the art of perseverance and consistency, despite repeated hardships.

Table of Contents

1. INTRODUCTION

During the 58th Session of the Intergovernmental Panel on Climate Change (IPCC) in March 2023, the Synthesis Report for the Sixth Assessment Report (AR6) was released, providing crucial insights into the state of our planet. The report highlights the observed increase in global surface temperature from $1850 - 1900$ to $2011 - 2022$, averaging 1.1°C, with a more pronounced rise over land (1.59°C) compared to the ocean (0.88°C). The IPCC affirms with a high level of certainty that human activities, primarily the emission of anthropogenic greenhouse gases (GHGs) such as carbon dioxide (CO_2) and methane (CH_4), are the predominant drivers of observed climate change. Additionally, various other human-induced factors, including warming aerosols, land-use changes, tropospheric ozone, and halogenated gases, contribute to the complex web of climate change dynamics (IPCC, 2021).

Examining the concentration of these GHGs provides further evidence of the profound impact of human activities on our atmosphere. As of 2019, atmospheric CO_2 concentrations reached 410 parts per million (ppm), while CH_4 and nitrous oxide (N_2O) concentrations stood at 1866 parts per billion (ppb) and 332 ppb, respectively. Remarkably, these CH_4 and N_2O levels are unparalleled in at least 800,000 years, and CO_2 concentrations exceed those observed over at least the past two million years, primarily due to human-driven activities (IPCC, 2021). To illustrate the ongoing changes, recent measurements from the Mauna Loa Observatory in Hawaii recorded CO_2 concentrations of 424.72 ppm as of May 6th, 2023, compared to 419.61 ppm on the same day in 2022, indicating an annual increase of 5.11 ppm (1.22%) (CO2.Earth, n.d.).

Turning our attention to the geological realm, the weathering or low-grade metamorphism of mafic and ultramafic rocks yields fascinating interactions between carbon-bearing fluids and silicate minerals, leading to the formation of carbonate minerals (Jamtveit and Hammer, 2012). Previous research by Hartmann et al. (2009) estimated that silicate weathering accounts for approximately 150 million tonnes of carbon consumption per year, while Alt and Teagle (1999) found that carbonation of basaltic lavas on the seafloor contributes around 10 million tonnes of carbon consumption annually. In stark contrast, current anthropogenic carbon emissions amount to approximately 10 billion tonnes per year (Jamtveit and Hammer, 2012).

Given its ability to mimic natural processes that regulate the global carbon cycle, geologic carbon sequestration has gathered significant attention as a promising method to mitigate carbon dioxide emissions. Carbonation reactions play a crucial role by effectively removing CO_2 from the atmosphere while inducing rock weathering. Intriguingly, if not for the continuous restoration of CO_2 to the atmosphere through various global processes, the normal rates of rock weathering would remove all atmospheric CO_2 in just over 3000 years (Klein and Philpotts, 2017). It is important to note that the effectiveness of this process depends on the type of rock involved. For instance, limestone weathering leads to the release of CO_2, as observed in the formation of the Tibetan Plateau. However, geochemical reactions involving igneous minerals offer tremendous potential to sequester substantial amounts of CO_2 from the atmosphere (Klein and Philpotts, 2017).

Natural mineral carbonation is a vital component of the global carbon cycle, and researchers have explored the possibility of artificially enhancing this process to counteract the escalating CO_2 levels resulting from anthropogenic emissions. The rate of interaction between carbon-bearing fluids and common rock types is a critical factor in this endeavour (Jamtveit and Hammer, 2012). Among the minerals, olivine exhibits the highest reactivity with CO_2-bearing fluids. Peridotite, a rock predominantly composed of olivine, has the potential to consume approximately 1 million tonnes of

carbon per year through carbonate formation. Peridotites are found in slow-spreading ocean ridges and tectonically exposed on-land mantle regions in the form of ophiolites, both containing at least 70-85% olivine (Kelemen et al., 2011).

Carbon Capture and Storage (CCS) represents a key approach to addressing CO_2 emissions by capturing and storing CO_2 before its release into the atmosphere. This process involves extracting CO_2 from industrial power plants and combustion facilities, purifying it from other gases like N_2 and H_2, compressing it, transporting it via pipelines, and finally injecting it into geological formations for long-term storage as carbonate precipitates (Benson, 2005). Geological formations with significant storage capacities, including deep saline aquifers, depleted oil and gas reservoirs, and basaltic to ultramafic rock units, are considered the most promising candidates (Stockmann, 2012).

Notably, ongoing CCS projects involve the establishment of permanent CO_2 injection fields worldwide. Examples include the Sleipner project in Norway (Utsira formation), the Weyburn Enhanced Oil Recovery project in Canada (Williston Basin Oilfield), the Snøvit fields in the Barents Sea, Norway, and the Carbfix project in Iceland (Stockmann, 2012).

Launched in 2007, the Carbfix project is a collaborative effort between the University of Iceland, Reykjavik Energy, the Earth Institute at Columbia University in New York (U.S.A), and Université Paul Sabatier in France. Its objective is to develop a secure, long-lasting, and cost-effective carbon storage technology through in-situ mineralization in Icelandic basalts (Stockmann, 2012). The CO_2 storage site is located near the Hellisheidi geothermal power plant, around 30 km east of Reykjavik. The power plant utilizes water and steam extracted from pipes to generate geothermal heat, with a magma chamber situated a few kilometres beneath the facility (Stockmann, 2012). As a result, the power plant emits over 40 kT of CO_2 annually. The CarbFix project aims to store this CO_2 into basaltic bedrock at the Hellisheidi site (Stockmann, 2012). Unlike other storage sites, CO_2 at the CarbFix project is first fully dissolved into water before injection, forming a carbonated solution with a pH of 3-4. The carbonated water is currently injected at a depth of around 800m where it triggers basalt dissolution and carbonate precipitation within 6 – 12 months after injection (Gíslason et al., 2019). The resulting carbonate minerals mainly include calcite, magnesite, siderite, ankerite, dolomite, or Ca-Mg-Fe carbonate solid solution, depending on divalent cation ratios, pH, and temperature (Stockmann, 2012). While basalts tend to undergo alteration to clay minerals and zeolites during weathering, highly altered specimens exhibit low porosity due to secondary mineral precipitates, limiting their storage capacity (Stockmann, 2012 and references therein). However, the relatively young age of the basalts at the Hellisheidi site, coupled with their reactivity and slight alteration, results in a porosity of approximately 8.5% (Aradóttir et al., 2012, as cited by Stockmann, 2012).

The main method employed at Carbfix is to inject water-dissolved CO_2 into the bedrock with drastically reduces its leakage to the surface, but this process requires very large quantities of freshwater, which can be a limiting factors in producing the same results in other parts of the globe. It is the very reason why Carbfix has also started exploring the potential of seawater as a solute, since carbonate minerals have been observed to form due to the interaction of basaltic oceanic crust with seawater through the process of percolation in hydrothermal systems (Voigt et al., 2021 and references therein).

1.1 Purpose of this study

The main objective of this study is to assess the feasibility of carbon capture and storage (CCS) in Sweden by examining the potential of different rock types as storage reservoirs. The focus is primarily on gabbro, granite, and dolerite sourced from the Billdal region in southwest Sweden, with a comparative analysis of syenite and carbonatite from Greenland, along with a basaltic rock from Iceland. The selection of these rock types is based on their recognized reactivity and successful implementation in prior CCS projects, respectively.

To investigate the dissolution and reaction of the rock samples with carbonated water under varying temperatures, laboratory experiments has been conducted. Regular monitoring of pH and temperature allowed for observation of pH changes, as higher pH levels are conducive to the precipitation of carbonate minerals, particularly calcite. Subsequently, a weak $NaHCO_3$ - Na_2CO_3 solution (referred to as treatment) was introduced to the systems after a specified period to enhance carbonate precipitation.

Chemical analysis of the rock samples, both before and after Na-treatment, were performed using techniques such as X-ray diffraction (XRD), Scanning Electron Microscopy (SEM), and Energy-Dispersive X-ray spectroscopy (EDX). Comparison of the obtained results with existing literature provided insights into the geochemical characteristics and composition of each rock sample, as well as their potential for undergoing carbonatization reactions.

The objective of this research is to contribute to a deeper understanding of the geochemical behaviour exhibited by these rock types and their suitability for carbon sequestration. The findings will offer valuable insights for evaluating the feasibility of CCS in Sweden and potentially identifying more effective rock candidates for long-term carbon storage.

2. Theoretical background

2.1 Chemical concepts

Water reacting with CO_2 (gas) leads to the formation of carbonic acid which in turn dissociates into H^+ and HCO_3^- ions, as shown in reactions (1), (2), and (3):

$$CO_{2\ (gas)} + H_2O_{\ (liquid)} \rightleftharpoons H_2CO_{3\ (aqueous)} \tag{1}$$

$$H_2CO_{3\ (aqueous)} \rightleftharpoons HCO_{3\ (aqueous)}^- + H^+_{\ (aqueous)} \tag{2}$$
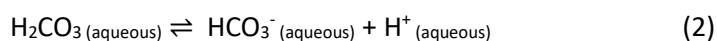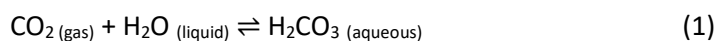
HCO_3^- can in turn dissociate further into CO_3^{2-} and H^+, as shown in reaction (3):

$$HCO_{3\ (aqueous)}^- \rightleftharpoons CO_{3\ (aqueous)}^{2-} + H^+_{\ (aqueous)} \tag{3}$$
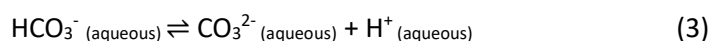
These reactions are dependent on pH, where CO_2 conversion to H_2CO_3 and CO_3^{2-} ions is favoured at higher pH levels. The protons (H^+) in solution increase acidity and consequently lower the pH of water (Doney et al., 2021). The pH is highly dependent on temperature and pressure as well as the salinity of the solution, such that the pH value decreases as temperature increases due to increased kinetics of the molecules in solution as well as increased dissociation of water (H_2O) molecules leading to increased concentrations of protons. Salinity affects pH such that the consequent presence of higher amounts of salts in solution have the potential to release more protons. The pH can also depend on other factors such as the chemical composition of the solution, which in turn dictates the types of ions which are available to interact with protons (Dickson et.al, 2007).

2.2 Carbonate precipitation

The existence of particular geological settings, providing rocks which can successfully undergo chemical reactions with CO_2-rich waters to form carbonate minerals, is the basis of promoting long-term storage of CO_2 in the form of carbonate precipitation. Current research and technological means aim to mimic this natural process as a means to mitigate anthropogenic CO_2 emissions. One of these technological means is known as Carbon Capture and Storage (CCS) and focuses on mineral trapping.

Basic silicate minerals, which have a relatively lower silica content and a higher Fe, Mg, and Ca content are the most reactive to CO_2-enriched water and therefore have the greatest potential for carbonate precipitation. The Fe, Mg, and Ca are dissolved in solution in the form of divalent cations which then react with divalent carbonate ions to form metal-carbonate complexes. Of the most reactive minerals are basalt (especially basaltic glass), plagioclase, pyroxenes, serpentine, and olivine (Matter and Kelemen, 2009). The process of carbonate precipitation is achieved through a series of reactions, beginning with the dissolution of CO_2 in water as shown in equations (1), (2), and (3). The degree of solubility of CO_2 is driven by factors such as temperature and pressure as well as the ionic strength of the solution, such that higher ionic strength, higher temperature, and lower pressure lead to poorer CO_2 dissolution and vice versa (Matter and Kelemen, 2009) . The CO_2 dissolution is, as mentioned in section 2.1, also dependent on pH, such that higher pH favours the dissociation of CO_2 into bicarbonate and further dissociation into carbonate ions (Doney et al., 2021).

The CO_2 dissolution leads to higher concentrations of protons (H^+) in the solution, as seen in reaction (2) and (3), which in turn acts to leach out divalent metal cations and drive them into solution. The cations are then prone to react with dissolved CO_2 to form carbonate complexes, as seen in the reaction (4):

$$(Ca, Mg, Fe)^{2+} + H_2CO_3 \rightleftharpoons (Ca, Mg, Fe)CO_3 + 2\,H^+ \qquad (4)$$
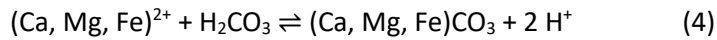
The equation (4) shows that every mole of precipitated metal-carbonate complex is associated with two moles of produced protons (H^+). These released protons need to further undergo a chemical reaction for the process to advance, a process known as couple reaction (Adam et al., 2019). Proton pairs are assimilated into minerals as they replace divalent cations which are further leached out, which increases their concentration in solution (Matter and Kelemen, 2009).

Reaction (5) shows a coupled reaction for the Mg-rich endmember of the olivine solid solution series, fosterite which further release divalent metal cations into solution:

$$Mg_2SiO_4 + 4H^+ \rightleftharpoons 2Mg^{2+} + H_2O + SiO_{2\,(aq)} \qquad (5)$$
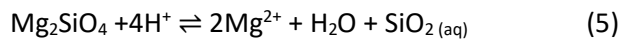
Another example can be shown in the coupled reaction (6) of protons with anorthite, the Ca-rich end member of the plagioclase solid solution series:

$$CaAl_2Si_2O_8 + 8H^+ \rightleftharpoons Ca^{2+} + 2Al^{3+} + 4H_2O + 2SiO_{2\,(aq)} \qquad (6)$$
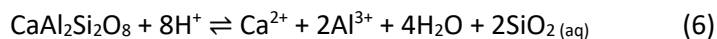
Finally, the reaction same reaction can be illustrated through reaction (7) involving the dissolution of clinopyroxene:

$$CaMgSi_2O_6 + 4H^+ \rightleftharpoons Ca^{2+} + Mg^{2+} + 2SiO_{2(aq)} + 2H_2O \qquad (7)$$
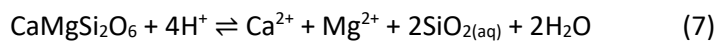
As reactions in equations (5), (6), and (7) illustrate, silicon dioxide and water are a result of this reaction. The newly released cations will further react with dissolved CO_2, leading to further carbonate precipitation. These reactions will ideally progress in a cycle as long as there are available cations in solution and as long as there are protons which can be consumed. As a result of this reactive cycle, the solution pH will witness a steady increase in value until reaching equilibrium conditions (Adam et al., 2019).

Figure 1 compares conventional CO_2-water injection reactions when reacting with a sedimentary basin compared to the types of reactions occurring when CO_2-water is instead injected into basaltic rocks, as is done at Carbfix.

Figure 1. . Left: Conventional CO₂ injection as supercritical fluid into sedimentary basin with impermeable cap rock. Right: Injection of CO₂-charged water into basaltic rocks at the Carbfix pilot injecting site at Hellisheidi, Iceland. Both show potential dissolution and precipitation reactions occurring after CO2 injection, assuming 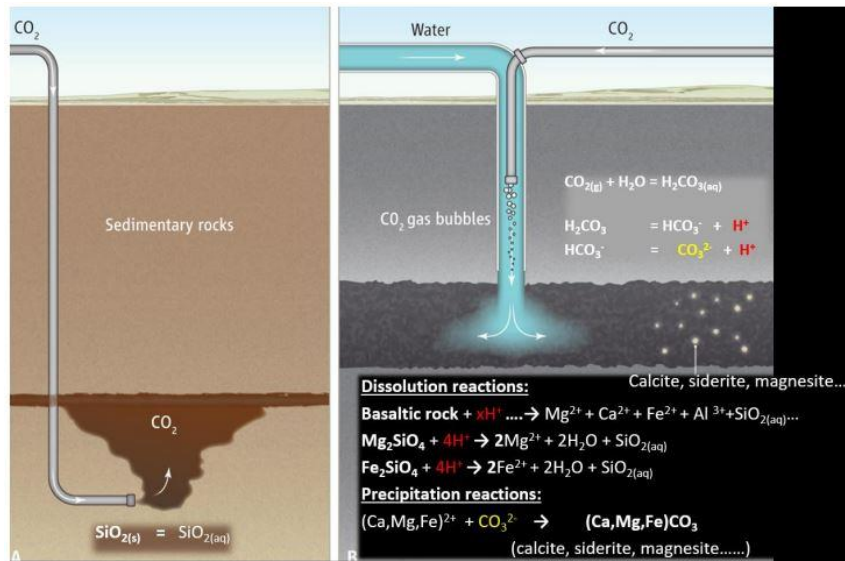that the porous sedimentary basins are predominantly composed of quartz sandstone. Modified from Gislason et al. (2019) .

2.3 Carbonates of interest

The main carbonate precipitates following carbonation reaction with igneous rocks are calcite, aragonite, dolomite – ankerite, magnesite, and siderite. However, dolomite is known to be virtually impossible to precipitate in laboratory conditions at room-temperature. Experiments show that magnesium ions in aqueous solutions develop strong solvation shells as well as a complex crystallisation barrier which impedes the precipitation of long-range ordered crystallographic structures at ambient surface conditions (Montes-Hernandez, Findling, and Renard, 2016).

Calcite is always nearly entirely composed of pure $CaCO_3$, especially when formed in sedimentary environments. However, when calcite crystallises at higher temperatures, its crystal structure allows for other cations such as Fe, Mg, Mn, or Zn to substitute for Ca, where Mg is the most common. In some cases, larger cations such as Ba or Sr can substitute for Ca (Nesse, 2020). Aragonite is a polymorph of calcite and may in certain alteration processes be replaced by dolomite or inverted to calcite, while dolomite and ankerite are part of a solid solution series whose endmembers are dolomite, $CaMg(CO_3)_2$, and ferrodolomite, $CaFe(CO_3)_2$ (Nesse, 2020). There is also a complete solid solution between siderite, $FeCO_3$, and magnesite, $MgCO_3$, as well between magnesite and rhodochrosite, $MnCO_3$, although it is incomplete due to the size difference of the cations, making substitution limited.

Carbonatites are known to host REE ore deposits, mainly in in the form of bastnäsite, $REE(CO_3)F$, burbankite, = $Na_2CaLa_2(CO_3)_5$, and lukechangite, $Na_3La_2(CO_3)_4F$. These REE-carbonates precipitate from carbonatite melts at temperatures of 600 – 800°C and at pressures of 100 MPa (Veksler, Stepanov, and Nikolenko, 2022) . These relatively rare carbonates are likely to be found in the carbonatite samples and are therefore briefly included in this subsection.

3. Geologic background

3.1 Syenite and carbonatite

The syenite (18ER04) and carbonatite (GS1804) used in the context of this study are both extracted from the Grønnedal-Íka igneous complex in the South-western part of Greenland. The coordinates of the area from which syenite was extracted are 61.20982° N -48.00751° W, and those of carbonatite are 61.22271° N -48.03943° W, as shown in Figure 2. The Grønnedal-Íka complex extends from the former naval base Grønnedal to Ikka Fjord and surrounds the inner part of the 13 km long glacier-carved Ikka Fjord (Adalsteinsdottir, 2020). The fjord hosts a suite of relatively rare alkaline bedrocks and is also the only region where the hydrated carbonate mineral ikaite ($CaCO_3.6H_2O$) is known to form submarine column formations at shallow water of the inner part of Ikka Fjord. These columns only grow within the area following the outcrops of the Grønnedal-Íka complex. Ikaite is precipitated where carbonate-rich submarine springs meet calcium-rich seawater and rise vertically because of the density contrast, creating perpendicular formations in low-temperature (less than 6°C) conditions (Ranta, 2015).

The alkaline complex formed around 1.3 Ga ago during the first stages of the continental rifting episode known as Gardar. Furthermore, the absence of tectonic activity in the last 1.1 Ga combined with glacier coverage during the Quaternary, has led to a relatively excellent preservation of both the carbonatite and the nepheline-syenites in the region (Upton et al. (2013). The complex hosts two units of layered nepheline syenites which intruded the host bedrock consisting of both metasediment (Emeleus, 1964) and gneiss (Bedford, 1989). Emeleus (1964) further noted that the syenites were in turn intruded at a later stage by a distinct syenite unit of porphyritic nature which bore xenoliths of the layered syenites as well as by a carbonatite unit. The complex consisting of both syenite and carbonatite was later subjected to deformation, leading to the formation of faulting systems and subsequent dyke intrusions (Emeleus, 1964). According to Ranta (2015), Coulson et al. (2003) demonstrated that the first dykes are comprised of lamprophyres, which are probably formed from the cool melt of metasomatized mantle material and contain phenocrysts of biotite, amphibole, and pyroxene or olivine, but not of feldspar (Farndon, 2019). The lamprophyres have then been cut by trachytes and phonolites (Coulson et al., 2003). Later intrusions occurred in the form of olivine dolerite dykes which intruded the complex in at least four different episodes (Emeleus, 1964). The dykes are thought to be related to the Gardar rifting episode (Upton et al., 2013).

Syenite is a silica-undersaturated as well as an alkali- and alumina-rich rock which represents the plutonic counterpart of trachyte. Nepheline syenites are simply syenites in which the feldspathoid nepheline $(Na,K)AlSiO_4$ represents a major component, and are additionally rich in alkaline mafic minerals (Adalsteinsdottir, 2020). The general mineral composition of a nepheline syenite, in addition to the nepheline, is the presence of an alkali-feldspar of the composition $(K,Na)AlSi_3O_8$) known as cryptoperthite, where the main feldspar orthoclase ($KAlSi_3O_8$) displays exsolution lamellae of the sodic alkali feldspar albite ($NaAlSi_3O_8$) in alternating patterns which can only be observed under microscope (Adalsteinsdottir, 2020). Other minerals which comprise nepheline syenites are of ferromagnesian composition, such as biotite $K(Mg,Fe)_3AlSi_3O_{10}(F,OH)_2$, the amphibole hornblende $(Ca,Na)_{2-3}(Mg,Fe^{2+},Fe^{3+},Al)_5(Al,Si)_8O_{22}(OH,F)_2$, or a pyroxene with the general chemical formula $(Fe,Mg)Si_2O_6$ such as the clinopyroxene aegirine-augite $(NaCaFe^{2+}Mg)(Fe^{3+}AlFe^{2+}Mg)Si_2O_6$ (Emeleus, 1964). Nepheline syenites are often enriched in Light Rare Earth Elements (LREE), which can be

explained by the high degree of differentiation which the parental magma underwent (Adalsteinsdottir, 2020).

Carbonatite is considered a relatively rare type of igneous rock which is predominantly found in association with alkaline silicate magmas, either in the context of distinct complexes or as a regional occurrence in magmatic provinces (Adalsteinsdottir, 2020). The carbonatite examined in this study belongs to the main carbonatite body in the Grønnedal-Íka complex, which is predominantly composed of calciocarbonatites and Fe-rich carbonatites with an age of 1.3 Ga (Ranta et al., 2018).
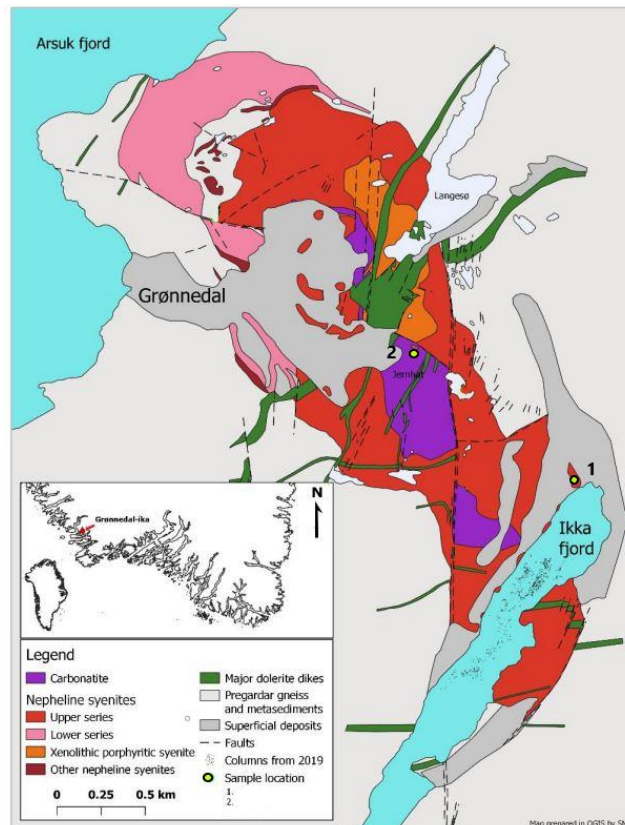

Figure 2. Geological map of the Grønnedal-Íka igneous complex, modified after Emeleus (1964) and prepared by Adalsteinsdottir (2020) in QGIS. The locations of the syenite and carbonatite used in this study have been incorporated into the map where 1 represents syenite and 2 carbonatite.

3.2 Gabbro, Granite, and Dolerite

The granite (BILL01), gabbro (12BILL8), and dolerite (12FF80) samples were all obtained from South-west Sweden in a region known as Billdal, located around 17 km southwest of Gothenburg. Coordinates from where the gabbro was extracted are 57.56816°N 11.9684° W, those of granite are 57.5687° N 11.96778° W, and those of dolerite are 57.5758° N 11.9624° W, as illustrated in Figure 3b.

The Sveconorwegian Province, also known as the Southwest Scandinavian Domain (SSD), encompasses the southwestern part of Sweden and the southern part of Norway. This region has a complex geological history resulting from a continent-continent collision between Baltica and another debated large continent referred to as Amazonia (Hegardt, 2010).

The Sveconorwegian Province is analogous to the Grenville orogeny, representing the Scandinavian counterpart (Hegardt, 2010). Integration of the Sveconorwegian Province into the Fennoscandian shield occurred during the later stages of the earlier Gothian orogeny, approximately 1.52 billion years ago (Åhäll and Connelly, 2008, as cited in Hegardt, 2010). Rocks formed during the Sveconorwegian orogeny are believed to be a combination of depleted mantle sources and existing continental crust, as interpreted by various authors (Petersson et al., 2015). The Sveconorwegian Province is divided into several lithotectonic units, dating from 1.68 to 1.59 billion years ago, separated by zones of ductile deformation that stretch from north to south. The Telemarkia, Kongsberg, and Bamble units are located west of the Palaeozoic Oslo rift, while the Western, Median, and Eastern Segments are found east of the rift zone (Bingen et al., 2008, as cited in Hegardt, 2010). The Mylonite Zone separates the Eastern and Median Segments, while the Göta Älv Shear Zone divides the Western and Median Segments. The Western and Median Segments together form the Idefjorden Terrane (Berthelsen, 1980, as cited in Hegardt, 2010).

The region of Billdal belongs to the southern Idefjorden Terrane and specifically the Hisingen Suite of the Western Segment (Petersson et al., 2015). This suite is dominated by 1.58-1.52 billion years old granitoids that intruded both the Åmål Belt and the Stora Le-Marstrand formation (Åhäll and Connelly, 2008, as cited in Petersson et al., 2015). Within the Hisingen Suite, heterogeneous deformation is observed, with some sections showing migmatization while others exhibit no signs of deformation. Xenoliths of the host rock, notably the Stora-Le Marstrand formation, are also present in some regions of the Hisingen Suite, displaying varying degrees of deformation and migmatization, indicative of conditions preceding the Sveconorwegian orogeny and pointing to Gothian metamorphism and deformation (Petersson et al., 2015).

The late stages of the Sveconorwegian orogeny included several mafic intrusion events, some of which are the 1.46 Ga Tuna Dolerites, the 1.27 – 1.25 Ga Central Scandinavian Dolerite Group, and the 0.98 – 0.95 Ga Blekinge-Dalarna Dolerites (Petersson et al. (2015) and references therein). The largest dyke is attributed to the monzogabbroic dykes of the extended Gothenburg area and is known as the 14 km long Tuve dyke, dated to around 0.93 Ga by Hellström et al. (2004). The Western part of the Idéfjorden Terrane is composed of Gothenburg Dolerites which were emplaced into a brittle upper crust along pre-existing fractures with a WNW to W trend. According to Hellström (2009) , the dolerites are of mafic composition and can be classified as leucocratic olivine dolerites with a plagioclase-rich composition as well as high Ti, K, Fe, and P contents compared to low Ca content, with an average SiO_2 content of 50.1%. All dykes have a low pyroxene content (5% or less) of diopside, $CaMgSi_2O_6$, while TiO_2 is predominantly found in ilmenite, $Fe^{2+}TiO_3$. Some of the Mg content in dykes can also be attributed to the olivine magnesium endmember forsterite, Mg_2SiO_4 (Hellström et al., 2004).

The granite belonging to the Hisingen suite contain lenses of varying sizes of metasedimentary xenoliths, as stated by Connelly and Åhäll (1996) and Åhäll (1990) in Petersson et al. (2015). The granite, coined Rönnäng granite, has been dated to around 1.58 Ga by Connelly and Åhäll (1996) as it intruded the Stora Le-Marstrand formation and is found to be predominantly composed of quartz, SiO_2 and feldspar (e.g. plagioclase, $(Na,Ca)[(Si,Al)AlSi_2]O_8$), with lesser amounts of the micas biotite, with the simplified chemical formula $K(Mg,Fe)_3AlSi_3O_{10}(OH)_2$, and muscovite, $KAl_2(AlSi_3O_{10})(OH)_2$ (Petersson et al., 2015). The Bohus granite is the youngest granite inclusion in the pre-Cambrian Swedish rock basement, with an age of 0.92 Ga determined by Eliasson (1992) as cited in Hellström et al. (2004).
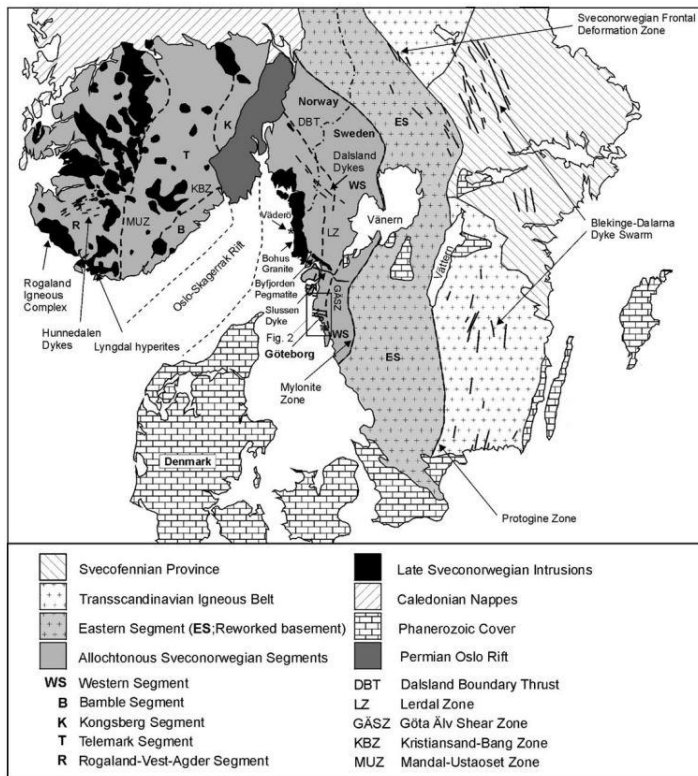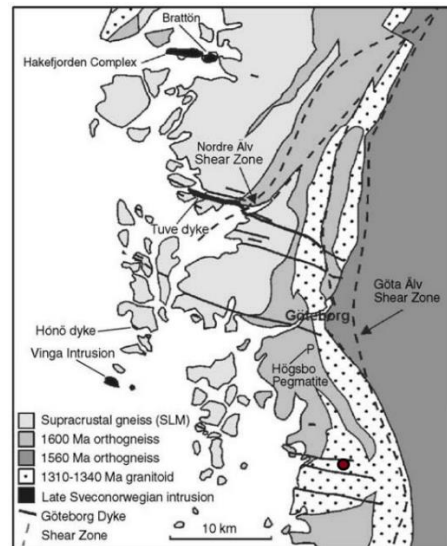
Figure 3b. Simplified geology of the Gothenburg area. Modified after Lundergårdh, 1953, 1958 ; Lundqvist, 2000 , by Hellström et al., 2004. Modified to include the locations of the gabbro, granite, and dolerite samples, represented by a red dot.

Figure 3a. Geological outline of southern Scandinavia. The Sveconorwegian province is marked in light grey. Modified from Hellström et al. (2004).

3.3 Basalt

The basalt rock sample (22FF163) used in the context of this study belongs to the Holuhraun fissure eruption which took place in 2014 – 2015 and is, according to Halldórsson et al., (2018) , probably the best monitored and studied moderate- to – large-scale basaltic fissure eruption ever recorded, providing generous amounts of data, notably in the fields of geomorphology, petrology, mineralogy, and geochemistry. Coordinates of the location from where the basalt sample was extracted are 64,91906° N and -16,73781° W, as shown in Figure 4.

The eruption was located within the Askja dyke swarm north of Dyngjujökull in central Iceland but was coeval to the subsidence of a caldera located 45 km to the southwest, in the Bárðarbunga central volcano (Geiger et al., 2016) . The lava flow was predominantly erupting through the largest spatter rampart above the main fissure (Dewangan et al., 2021) , lasted for a period of 6 months until February 27th, 2015, and resulted in a bulk lava volume of 1.44 ± 0.07 km^3 to 1.8 ± 0.2 km^3, according to Gudmunsson et al. (2016) as cited by Dewangan et al. (2021). Furthermore, the extruded lava was of exceptionally homogeneous olivine tholeiitic composition (Halldórsson et al., 2018), with a mean flow velocity of around 80 m^3/s, according to Bonny et al. (2018) as cited by Dewangan et al. (2021). Tholeiitic basalts are known to contain high amounts of Ca-poor pyroxenes such as pigeonite and hypersthene (Farndon, 2019).

All whole-rock samples belonging to the 2014 – 2015 Holuhraun eruption have similar compositions and contain MgO and TiO_2 in concentrations of 6.5 – 7.0 wt% and 1.8 – 2.1 wt%, respectively (Halldórsson et al., 2018). Furthermore, several authors agree that the rocks have a distinct chemical signature and composition compared to those of the adjacent Askja and Grímsvötn volcanoes (Halldórsson et al., (2018) and references therein). As cited by Halldórsson et al., (2018), Hartley and Thordarson (2013) confirmed that the 2014 – 2015 eruption lava has a composition similar so older Holuhraun lava units, although classified as a moderately more evolved olivine tholeiitic basalt compared to older eruptions. The groundmass of the 2014 – 2015 whole-rocks samples consists of microlite plagioclase, pyroxene, olivine, skeletal titanomagnetite, as well as gabbro fragments (Geiger et al., 2016). Plagioclase is seen both as macrocrysts with the composition An_{70-91} and as microphenocrysts of An_{65-75} while clinopyroxene is augitic in composition (Halldórsson et al., 2018). The clinopyroxene are in the form of macrocrysts with various amounts of Cr_2O_3 and Al_2O_3, up to 1.2 wt% and 1.5 – 4.7 wt%, respectively. The olivine macrocrysts display a homogeneous chemical composition Fo_{86-78} (Halldórsson et al., 2018). Furthermore, the forsterite consists of varying amounts of Ni in the range of 850 – 1500 ppm as Ni decreases with decreasing forsterite content, as well as varying amounts of Ca which also show a decreasing trend with decreasing Fo content (Halldórsson et al., 2018). Olivine microphenocrysts have a core composition of Fo_{76-80} with the same compositional trends as the macrocryst Fo, with Ca content in the range of 2100 – 2800 ppm (Halldórsson et al., 2018).
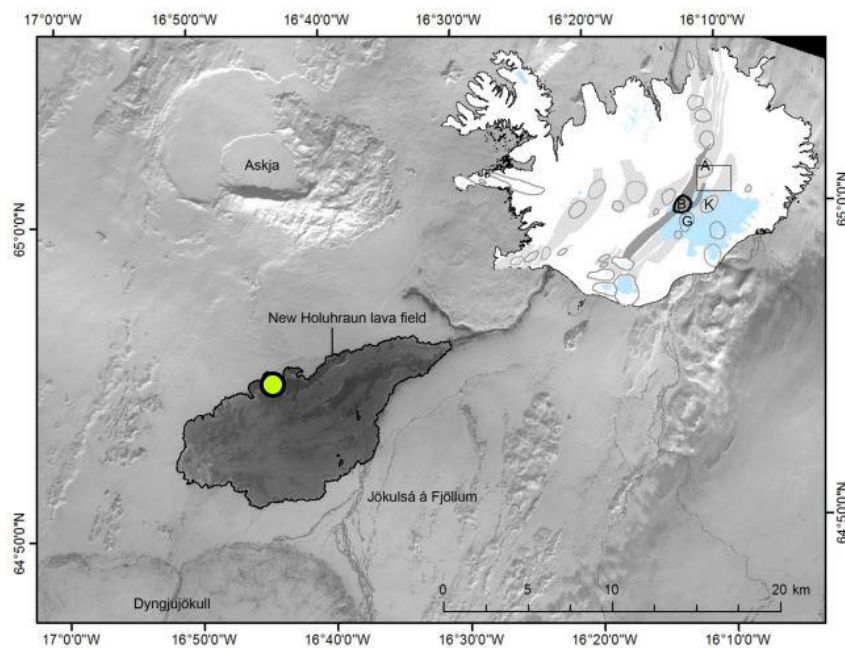

Figure 4. The 2014–2015 Holuhraun lava field as imaged by a LANDSAT on April 2nd, 2015; 33 days after the eruption stopped. The upper right corner shows the outline of the Bárðarbunga (B) fissure swarm (dark grey) and location of nearby central volcanoes (A: Askja, G: Grímsvötn and K: Kverkfjöll). Modified from Pedersen et al. (2017) by Halldórsson et al. (2018). The location of the basalt sample used in this study is represented by a green dot.

4. Rock Sampling

The six different rock samples used in this study are part of a collection which has previously served in the context of research and were kindly provided by my supervisors. Additionally, the samples were presented with a complete chemical analysis using X-Ray Fluorescence (XRF), with the exception of the basalt sample which underwent a chemical analysis using Inductively Coupled Plasma Atomic Emission Spectroscopy (ICP-OES). The main chemical elements of each rock sample are displayed in percentages (Table 1), where all data has also been provided by my supervisors. Syenite holds the sample I.D. 18ER04, carbonatite GS1804, gabbro 12BILL01, granite BILL01, dolerite 12FF80, and basalt 22FF163. It is worth noting that carbonatite has a relatively high Loss of Ignition (LOI) of 32.07%, indicating the loss of volatile elements upon heating (namely CO_2 and H_2O). The chemical data for the basalt sample did not include its LOI value, which is why it is not represented in Table 1.

Table 1. Main chemical elements of the six rock samples used in this study, as well as their LOI, in percentages.

%	SiO_2	Al_2O_3	Fe_2O_3	CaO	MgO	Na_2O	K_2O	Cr_2O_3	TiO_2	MnO	P_2O_5	SrO	BaO	C	S	LOI
18ER-04	54.67	19.71	4.66	0.71	-------	10.57	4.25	-------	0.08	0.29	0.07	-------	-------	-------	-------	4.79
GS18-04	1.37	0.32	21.78	39.63	0.26	-------	0.24	-------	0.01	2.56	0.78	-------	-------	-------	-------	32.07
12BI-LL8	52.80	16.30	10.45	8.94	4.97	3.49	0.90	0.01	1.17	0.13	0.26	0.05	0.02	0.02	0.14	1.20
BILL-01	72.90	14.00	2.73	2.10	0.68	3.31	4.24	0.01	0.35	0.04	0.10	0.03	0.10	0.03	0.01	0.84
12FF-80	50.90	15.4	13.15	6.30	3.97	3.88	1.73	0.01	3.47	0.16	0.78	0.07	0.08	0.06	0.13	0.79
22FF-163	50.00	13.80	12.34	12.01	6.83	2.44	0.20	-------	1.87	0.21	0.17	-------	-------	-------	-------	-------

The syenite sample consists of 54.67% SiO_2, 19.71% Al_2O_3, 10.57% Na_2O, and 4.25% K_2O and the carbonates that may precipitate in the syenite are siderite, calcite, and rhodochrosite.

The carbonatite sample is mainly composed of calcium oxide (39.63% CaO). Calcite, siderite, and rhodochrosite are the most likely carbonate precipitates.

The gabbro sample contains high concentrations of SiO_2 (52.8%), Al_2O_3 (16.3%), and Fe_2O_3 (10.45%). It also includes CaO, MgO, Na_2O, TiO_2, K_2O, and P_2O_5. Carbonates such as siderite, calcite, and rhodochrosite may precipitate in the gabbro.

The granite sample is rich in SiO_2 (72.9%) and Al2O3 (14%). It also contains K_2O, Na_2O, Fe_2O_3, CaO, and minor amounts of MgO and TiO_2. The most probable carbonate precipitation phases in the granite are siderite and calcite.

In addition to ICP-OS, the basalt sample also underwent chemical analysis using EPMA which revealed a composition including basaltic glass, plagioclase, olivine, sulfides, clinopyroxenes, and spinel. Carbonates such as siderite and calcite may form in the basalt.

5. METHODS

5.1 Sample Preparation

All six rock samples were subjected to a mechanical laboratory crusher in order to reduce them to the same grain size as sand (Figure 5). The crushed product was then wet sieved, first with a 250 μm and then with a 45 μm sieve. Consequently, the retained range of grain size for all samples is in the order of   45 - 250 μm. The crushed and sieved rocks were then placed in a laboratory oven at around 90°C for a period of 12 hours.

Figure 5. From left to right: 3 of the whole-rock samples used; the laboratory crusher; the metal container with the gyrating plate where the samples are put before being subjected to crushing.

Each rock sample was weighted to exactly 10,0 g and placed in its respective glass container which was propped with a plastic O-ring to avoid gas escaping from the systems throughout the experiments. A magnet was also placed in each container in order for the rock-fluid mixture to be constantly stirred using to a magnetic stirring plate (Figure 6).

Figure 6. 10 g of the crushed rock samples are put in individual glass containers in preparation for experimentations.

A liquid mixture using deionized (D.I.) water and CO_2 was prepared using a commercial soda stream. Individual doses of carbonated D.I. water mixtures were prepared for each sample by letting the D.I water react with CO2 for 4 seconds and repeating this process 3 times. D.I water's pH before carbonation was measured to 5.62 at 20.6°C while carbonated D.I. water's pH was on average 3.81 at room temperature, averaging 20.5°C.

Before each pH measurement, the Hanna instrument pH metre - equipped with temperature sensor – was to be calibrated using two buffers: HI7007 with pH = 7 and HI7004 with pH = 4. The pH measurements have an accuracy of ± 0.1 pH units. Solution were constantly stirred on a magnetic stirring plate while measuring pH for homogeneity and accurate results (Figure 7). Each dose of carbonated D.I. water was poured into its corresponding sample container until reaching the upper white mark in each container, before the sealed containers were placed on a 6-plated stirring station, with the stirring velocity set at 290 rotations per minute (rpm) (Figure 8).

Figure 7. pH meter with both a pH and a temperature sensor.

Figure 8. The containers including the rock samples and CO2 D.I. water were placed on a magnetic stirring station for constant stirring during the room temperature experiments.

5.2 Room temperature experiments

The rock samples underwent a 31-day reaction with carbonated D.I. water under constant stirring at room-temperature before commencing the next step in the process. First, 20 ml of liquid was extracted from each sample container and sealed in separate sample bottles for further analysis (Figure 9). The remaining liquid in each experiment bottle was then diminished down to the 100 ml mark. Samples of the rock powder were then extracted and placed in small plastic containers to dry at room temperature (Figure 10).

The $NaHCO_3$-Na_2CO_3 mixture served as an application of Le Chatelier's rule, where the equilibrium between eventual $CaCO_3$ precipitates and their saturated solution is disturbed by the addition of CO_3^{2-}. The equilibrium responds by consuming the addition of CO_3^{2-} by increased precipitation of $CaCO_3$ (Krauskopf and Bird, 2008). The rock samples were subjected to the $NaHCO_3$-Na_2CO_3 solution for an additional 32 days, completing a total period of 63 days for the room temperature experiment. Post-treated samples in powder form were extracted from the experiment bottles and dried in small containers at room temperature. Table 2 shows the pH the $NaHCO_3$-Na_2CO_3 solution prior to its introduction to the rock samples.

Figure 9. 20 ml liquid samples were extracted before further treatment with Na-rich solution.
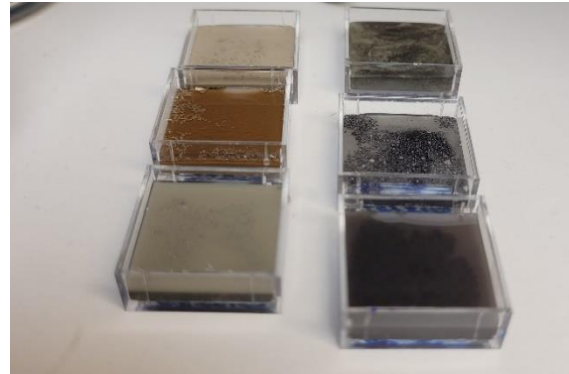
Figure 10. Solid samples were carefully extracted and placed in square containers to dry.

Table 2. Weight of NaHCO₃ and Na₂CO₃ powders relative to D.I water solute and the pH of the NaHCO₃-Na₂CO₃ solution.

NaHCO$_3$ (g)	Na$_2$CO$_3$ (g)	D.I. water (g)	pH	Temp. (°C)
0.72	0.9	1000	9.20	21.0

5.3 Experiments at 50°C

The rock samples underwent a 14-day reaction with carbonated D.I. water at a temperature of 50°C while being continuously stirred (Figure 11). Following the 14-day period, a similar procedure as in the room experiments was conducted. A 20 ml liquid sample was extracted from each container, and the remaining liquid was emptied until reaching the 100 ml mark. It was then replaced with a fresh batch of NaHCO₃-Na₂CO₃ solution with pH 9.20 (similar to Table 2), filling it up to the 200 ml mark. Subsequently, solid samples were carefully collected and placed in separate small containers which were then placed in an oven to dry at 50°C. The Na-rich mixture was allowed to react with the rock samples for an additional 17 days, concluding the 50°C experiments and resulting in a total duration of 31 days.

Figure 11. Set-up of the 50°C experiments. Rock samples mixed with carbonated D.I water were placed in sealed glass bottles and placed in a 50°C water bath which was then covered with aluminium foil to prevent water evaporation.

5.4 Experiments at 100°C

Within a 24-hour period, the 100°C experiments exhibited pH levels comparable to those observed in the room temperature and 50°C experiments. Consequently, no further administration of $NaHCO_3$-Na_2CO_3 solution was required for these experiments. The 100°C experiments were concluded by extracting a 20 ml liquid sample and a solid sample from each container. The solid samples were carefully placed in glass containers and subjected to a drying process in an oven set at approximately 100°C for a duration of three hours. Subsequently, the dried samples were transferred to sealed containers for further analysis.

Finally, the dried solid samples for all three sets of experiments as well as untreated rock samples were then transferred to sealed containers until further preparation for analysis (Figure 12).

Figure 12. A total of 36 solid samples, including one untreated sample per rock type, were sealed in containers for further analysis.

5.5 Instruments

5.5.1   X-Ray diffraction (XRD)

X-Ray Diffraction (XRD) is an analytical instrument that utilizes the interference patterns of monochromatic X-rays to determine the atomic or molecular structure of a crystalline sample in powder form. This technique provides valuable chemical information about the composition and phases present in the sample. Geologists frequently employ XRD to identify minerals and assess their concentrations using signal intensity measured in counts per minute (cpm) (Alderton, 2021).

Preparations for XRD analysis involved a pressed pellet technique (Figure 13). All the material needed was thoroughly washed using first D.I. water then acetone (CH_3COCH_3). Each sample was prepared individually by placing a fraction of it in a stone mortar composed of agate, with a hardness of 7 on Mohs scale. The rock sample was then mixed with a small quantity of acetone to liquify it. The mixture was then manually ground to fine powder using a stone pestle also made of agate. The powder was then carefully transferred to an air-tight aluminium pellet equipped with a zero diffraction plate made of a silica (Si) single crystal and the sample was then pressed unto the plate to

form a homogeneous circular shape. Each individual pellet was placed in the XRD machine for analysis under a period of 20 minutes.

Figure 13a. The XRD instrument used in this study is at Naturhistoriska Museet in Stockholm, Sweden.

Figure 13b. Acetone was used to clean material and create a liquid solution using rock samples in an agate mortar.

Figure 13c. : The rock samples mixed with acetone are manually ground to a fine powder and mounted on a pellet equipped with a zero diffraction plate.

5.5.2   Scanning Electron Microscope (SEM)

Scanning electron microscopy (SEM) is a powerful technique for high-magnification analysis of samples, ranging from micrometres (μm) to nanometres (nm). The SEM technology utilizes high-energy electron beams in a vacuum chamber to generate precise grayscale images. The resulting secondary electrons (SE) and backscattered electrons (BSE) are processed by a computer and displayed on a viewer screen (Mohammed and Abdullah, 2018). A SEM instrument employs detectors such as the Everhart-Thornley Detector (ETD) for detecting secondary electrons (Zhang et al., 2016), Circular Back Scatter Detector (CBS) for surface topography (Wan et al., 2018), and Energy Dispersive X-ray Spectroscopy (EDX) for chemical composition analysis (Mohammed & Abdullah, 2018). Sample preparation for SEM analysis involved putting a small fraction of the samples on a metal stub equipped with a non-reflective adhesive carbon disk to increase conductivity. The samples were then subjected to sputter coating with gold which further increases conductivity. The gold coating was thick enough to prevent charging and thin enough to not obscure surface details on the samples. The metal stubs with the samples were then placed inside the SEM for analysis using CBS, EDT, and EDX (Figure 14).

Figure 14. The SEM used for ETD and CBS in this study.
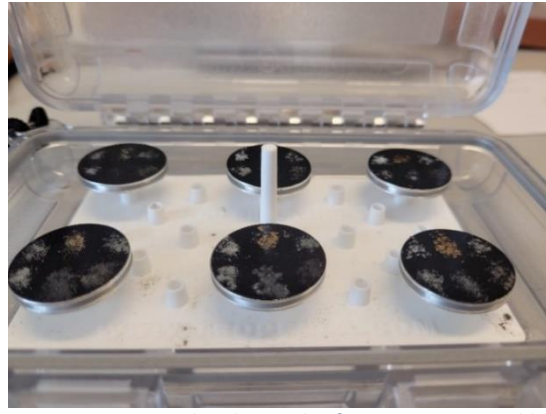
Figure 15. Mounted rock samples for SEM prior to gold-coating.

6. RESULTS

6.1 Temperature and pH

6.1.1 Room-temperature experiments

Daily measurements of temperature and pH were recorded for solutions containing the six rock samples, of which diagrams are shown in Figure 16. Data which was used to create the diagrams can be found in the form of tables in Appendix A. The diagrams include both pre- and post-treatment using a weak $NaHCO_3$-Na_2CO_3 solution, where the red line in each diagram represents the moment the solution was introduced to each system. The pre-treatment experiment lasted 32 days and the post-treatment 31, totalling a period of 63 days. Syenite showed an initial average temperature of 20.5°C and a pH increase from 3.88 at T_0 to 7.23 over 32 days, followed by a pH increase from 8.62 at T_0 to 8.67 with an average temperature of 20.9°C upon treatment, reflecting a net pH increase of 4.79 units over 63 days. Similarly, carbonatite exhibited a pH increase from 3.77 to 7.36 in 31 days, followed by a further increase from 7.89 to 8.67 after treatment, resulting in a net pH increase of 4.90 units. The gabbro sample displayed an average temperature of 20.7°C, with the pH values first increasing from 3.77 to 8.20 and then decreasing from 8.92 to 8.68 upon $NaHCO_3$-Na_2CO_3 treatment, indicating a net pH increase of 4.91 units. Results for granite showed a pH increase from 3.80 to 7.88 before, followed by a decrease from 8.94 to 8.6 after treatment, resulting in a net pH increase of 4.8. Similarly to gabbro and granite, dolerite measurements indicated a pH increase from 3.78 to 7.65 before Na treatment, followed by a decrease from 8.76 to 8.51 after treatment, resulting in a net pH increase of 4.73 units. Finally, the basalt experiments exhibited a pre-treatment pH increase from 3.88 to 7.94, followed by a decrease from 8.91 to 8.81 after treatment, resulting in a net pH increase of 4.93 units over the room-temperature experiment's duration.
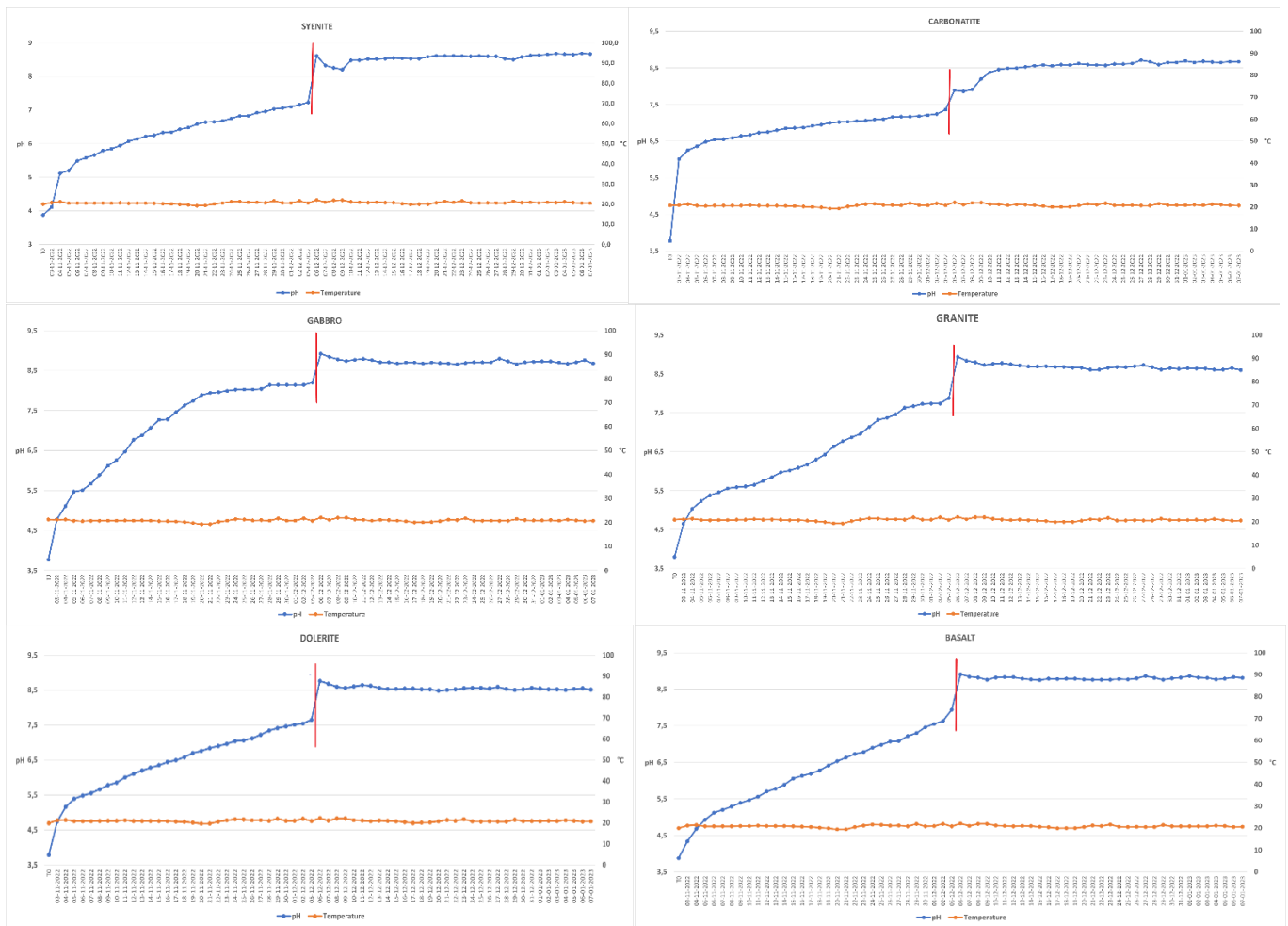
Figure 16. Combined results of pre- and post-Na-treated rocks samples at room-temperature in regard to pH and temperature measurements.

6.1.2   Experiments at 50°C

Figure 17 illustrates the pH and temperature measurements for the pre- and post-treated rock samples in the 50°C experiments, of which the data can be viewed in Appendix A. The pre-treatment phase lasted 14 days while the post-treatment phase ran for 17 days. Temperatures laying outside the range of 45-55°C were not included in the data display. Outlying temperatures correspond to T0 on 06/12/2022 (beginning of the 50°C experiment) and T0 on 21/12/2022 (when the $NaHCO_3$-Na_2CO_3 solution was introduced to the systems), where the solution's pH was measured at room temperature, as well as the dates where the heating plates were observed to produce temperatures lower than 45°C.

The pH of syenite at 50°C increased first from 3.79 at T_0 to 8.30 in a period of 14 days and then from 8.43 to 9.01 in 17 days after adding the $NaHCO_3$-Na_2CO_3 to the system, resulting in pH net increase of 5.09 units at an average temperature of 45.9°C. As for carbonatite, the initial phase showed a pH increase from 3.64 to 8.00, while the post-treatment phase reflected a pH increase from 8.33 to 8.80, reflecting a net pH increase of 5.16 units at 47.6°C in a total period of 31 days. The gabbro experiment showed an initial pH increase from 3.65 to 8.28 and a further increase from 8.38 to 8.88 in the post-treatment stage, leading to a net increase of 5.23 units at an averaging temperature of

45.5°C. As for granite, the pH values first reflected a pH increase from 3.68 to 8.25 and then an increase from 8.08 to 9.98, resulting in a net pH increase of 5.30 units at 47.3°C. The pH for dolerite initially increased from 3.73 to 8.14 and then from 7.84 to 8.85 at an average temperature of 47.2°C, resulting in a net pH increase of 5.12 units. Finally, the basalt sample showed a pH increase from 3.63 to 8.03 at 46.8°C as well as a post-treatment increase from 8.28 to 8.95, displaying an overall increase of 5.32 units in the 50°C experiments.
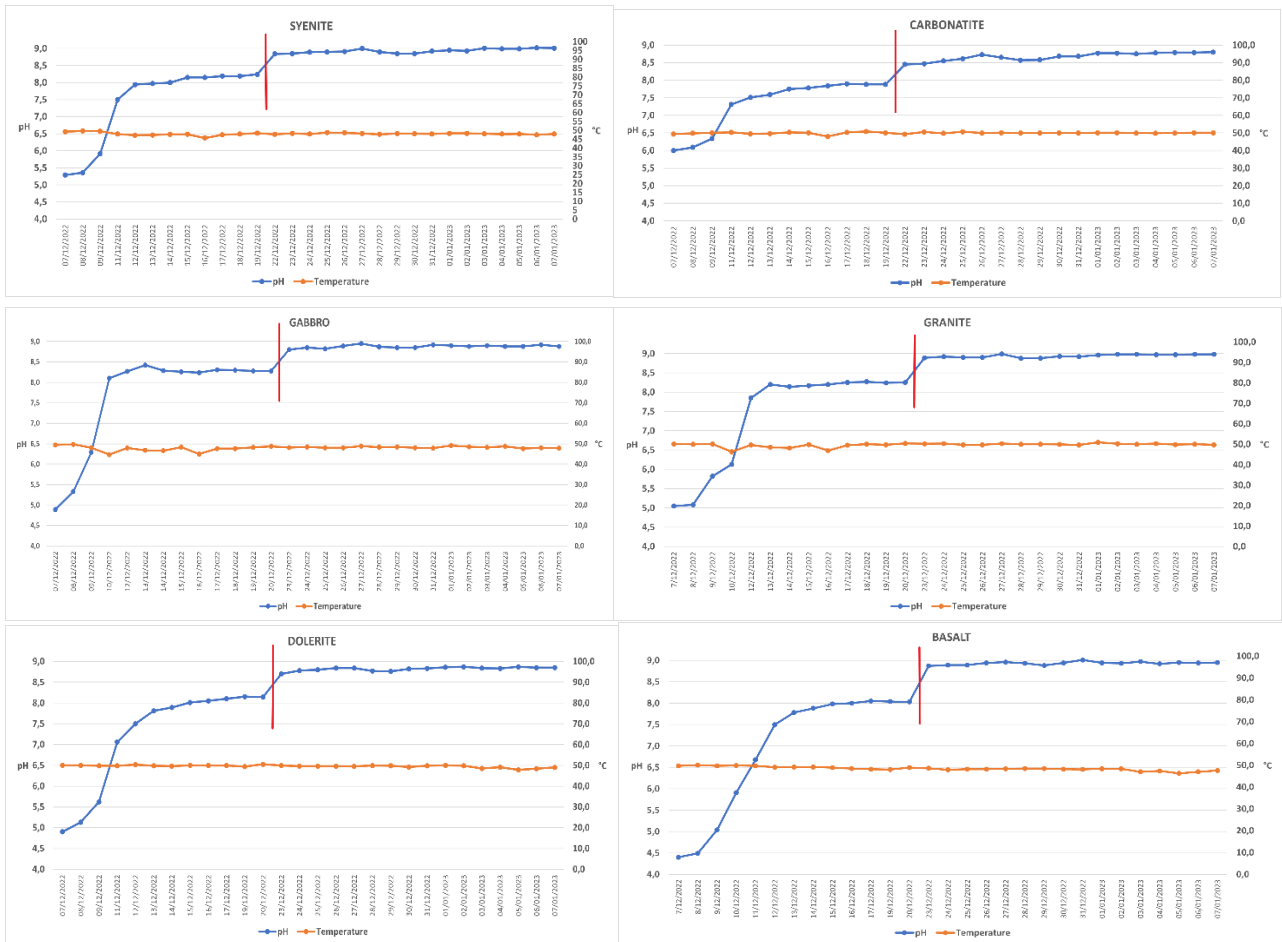
Figure 17. Combined results of pre- and post-Na-treated rocks samples at 50°C in regard to pH and temperature measurements, excluding values of which temperatures lay outside the 45 – 55°C. The red line represents NaHCO$_3$-Na$_2$CO$_3$ introduction to the systems.

6.1.3   Experiments at 100°C

All rock samples at 100°C experienced a pH increase comparable to those at room-temperature and 50°C in a manner of three hours, as illustrated in the graphs shown in Figure 18. The highest pH was observed in carbonatite (8.42), followed by gabbro (8.35) and granite (8.34). Dolerite and basalt reflected a pH of 8.21 and 8.11, respectively, while syenite scored the lowest pH (7.96).
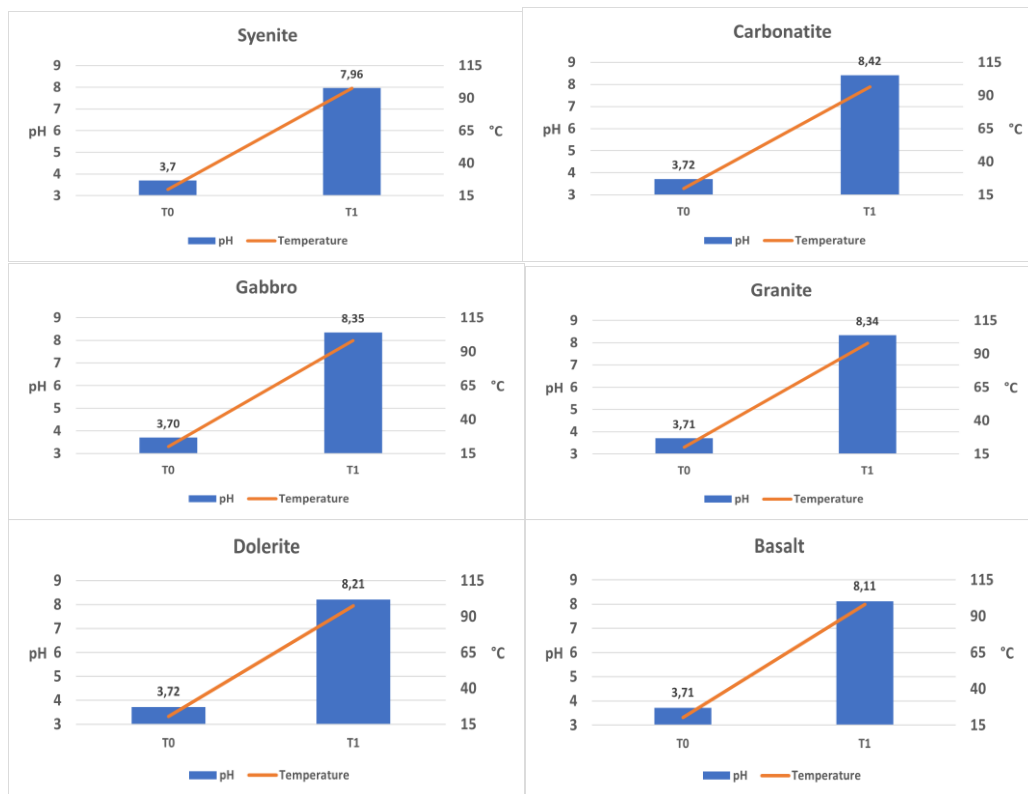
Figure 18. Diagrams showing pH and temperature measurements of the rock samples at 100°C.

6.2 XRD analysis

The tables including identified mineral phases in each rock sample and in each set of experiments as well as the graphs showing the relative peak intensities can be found in Appendix B.

6.2.1   Room-temperature experiments

The XRD analysis of syenite sample at room temperature revealed a composition comprising 40.4% analcime ($Na(AlSi_2O_6)\,H_2O$), 44.4% microcline ($K(AlSi_3O_8)$), and 15.2% aegirine ($NaFe^{3+}\,(Si_2O_6)$). The addition of the $NaHCO_3$-Na_2CO_3 solution did not alter the chemical composition of syenite, maintaining consistent concentrations of analcime, microcline, and aegirine.

The carbonatite sample at room temperature exhibited a diverse mineralogy, with calcite ($CaCO_3$) being the dominant mineral (83%), followed by apatite ($Ca_5(P_6O_4)_3F$) (10%), goethite ($Fe^{3+}O(OH)$) (4%), and lepidocrocite ($Fe^{3+}O(OH)$) (3%). The post-treated carbonatite samples showed comparable concentrations of lepidocrocite and goethite, a slight increase in apatite (11.1%), and a slight decrease in calcite (81.8%).

The XRD analysis of the gabbro sample at room temperature indicated a composition consisting of 28% magnesio-hornblende ($Ca_2\,(Mg_4Al)\,(Si_7Al)\,O_{22}\,(OH)_2$), 53% calcian albite (($Ca_{0.25},Na_{0.75})\,(AlSi_3O_8)_2$), 12% quartz ($SiO_2$), and 7% Ti-enriched biotite ($K\,(Mg,Fe,Ti)_3\,AlSi_3O_{10}\,(OH)_2$). Post-treated gabbro samples at room temperature showed similar amounts of biotite, a slight decrease in albite (53%), and increases in magnesio-hornblende (28%) and quartz (12%).

21

The granite sample revealed nearly equal concentrations of quartz (35%) and albite ($Na(AlSi_3O_8)$) (34%), along with 24% microcline and 7% siderophyllite ($K\,Fe^{2+}_2Al(Al_2Si_2O_{10})(OH)_2$). Post-treated granite samples at room temperature displayed similar amounts of quartz (36%), lower concentrations of albite (26%), higher amounts of microcline (34%), and slightly lower amounts of siderophyllite (4%).

The XRD results for the dolerite sample demonstrated a dominant composition of calcian albite (82.8%), accompanied by 5.1% magnetite ($Fe^{2+}Fe^{3+}_2O_4$), and equal concentrations (3%) of ilmenite ($Fe^{2+}TiO_3$), siderophyllite, and clinochlore ($Mg_5\,Al(AlSi_3O_{10})(OH)_8$). Na-treated dolerite samples at room temperature exhibited slightly lower concentrations of albite (81%) and ilmenite (2%), double the concentration of quartz (6%), and virtually equal concentrations of magnetite, siderophyllite, and clinochlore compared to pre-treated dolerite samples at room temperature.

Lastly, the basalt sample displayed a relatively simple chemical composition, with 62% sodian anorthite (($Ca_{0,65}\,Na_{0,35}$) ($Al_2\,Si_2O_8$)) and 38% aluminian diopside (($Ca_{0.85}\,Al_{0.15}$) ($Mg\,Si_2O_6$)). The post-treated basalt samples exhibited the same chemical composition and phase fractions as the pre-treated basalt samples at room temperature.

6.2.2 Experiments at 50°C

Syenite at 50°C treatment showed slightly different concentrations of analcime (49%), microcline (39%), and aegirine (12%) compared to the room-temperature experiments. Addition of the $NaHCO_3$-Na_2CO_3 solution showed the exact same concentrations for aegirine (12%), with slight differences in regard to analcime (48%) and microcline (40%) compared to pre-treated syenite.

The XRD results for carbonatite displayed approximately the same concentrations as in room-temperature conditions, with 82% calcite, 13% apatite, 2% lepidocrocite, and 3% goethite. However, post-treated carbonatite showed a slight decrease in calcite content (79.8%) contrasted by a slight increase in apatite (13%), lepidocrocite (3%), and goethite (4%).

In gabbro, albite is still the dominant phase (50%) with 26% magnesio-hornblende, 10% quartz, and twice as much biotite (14%) as the room-temperature experiments showed. The XRD analysis of the post-treated gabbro at 50°C showed slightly higher concentrations for albite (54.5%) and quartz (13.1%) compared to lower concentrations of magnesio-hornblende (25.3%) and biotite (7.1%).

The XRD results of the granite sample at 50°C showed a similar composition than the post-treated granite at room-temperature, with 35% quartz, 34% microcline, 26% albite, and 5% siderophyllite, while post-treated granite at 50°C displayed different phase concentrations than in the pre-treatment phase. Albite concentrations were almost twice as high (54.5%) and microcline concentrations were thrice as low (11.9%), while siderophyllite concentrations were similar to pre-treated granite at 50°C.

As for dolerite sample XRD data shows slightly lower concentrations of calcian albite (73.5%) and quartz (4.1%) as well similar concentrations of ilmenite (3.1%), clinochlore (3.1%) and siderophyllite (2%). The largest difference lays in the magnetite content with almost thrice the amount (14.1%) as the post-treated dolerite and five times the amount as the pre-treated dolerite at room-temperature. Post-treated dolerite at 50°C showed similar phase fractions as the post-treated dolerite at room-temperature, which represents a slight increase in calcian albite (81%) and quartz (6%) compared to pre-treated dolerite at 50°C, as well as a slight decrease in ilmenite (2%), an increase in siderophyllite (5%) and clinochlore (3%), and a considerable decrease in magnetite (3%).

Finally, XRD results for basalt at 50°C showed a slight decrease in anorthite (58%) coupled with a slight increase in diopside (42%) compared to room-temperature experiments. Post-treated basalt at 50°C showed similar fractions compared to room-temperature experiments, with 61% anorthite and 39% diopside.

6.2.3 Experiments at 100°C

The 100°C experiments involving syenite showed a slight increase in analcime and microcline concentrations (53%) in contrast to a slight decrease in both microcline and aegirine (39% and 8%, respectively).

The XRD results for carbonatite showed similar proportions in regard to calcite, apatite, and lepidocrocite concentrations. However, the calcite at 100°C contained magnesium in the order of 6%. Instead of goethite, which was found in all other results, the 100°C experiments showed a clear peak of quartz at concentrations of 2%.

As for the gabbro sample at 100°C, it contained lower concentrations of calcian albite (45%) and magnesio-hornblende (21%) compared to higher contents of quartz (21%) and biotite (9%). Epidote was also found in concentrations of 9% in the 100°C experiments but not in the room-temperature or 50°C experiments.

The XRD results of granite showed 35% albite which comparable to pre-treated room-temperature experiments, 34.7% quartz which is similar to both room-temperature and pre-treated 50°C results, 13.9% microcline comparable to post-treated granite at 50°C, and 15.8% biotite instead of siderophyllite, with more than twice as much biotite as siderophyllite compared to the remaining experiments.

Dolerite at 100°C shows a significantly reduced calcian albite content (69%) as well as similar concentrations of quartz (5%), ilmenite (3%), and magnetite (5%) as post-treated dolerite at room-temperature and at 50°C. The major difference with all other experiments is the presence of annite, $KFe^{2+}_3(AlSi_3O_{10})(OH)_2$ (1%) instead of siderophyllite, as well as ferroan diopside (6%), with almost a quadruple increase in clinochlore concentrations (11%).

The XRD results of basalt at 100°C showed similar concentrations of anorthite as all other experiments, with the unique addition of magnetite (10%) and a non-specified clinopyroxene, $((Ca,Mg,Fe,Na)(Mg,Fe,Al)(Si,Al)_2O_6)$ (27%) instead of diopside.

6.3 SEM analysis

Results from the EDX analysis of all rock samples during all three sets of experiments are presented in the following subsections. Additionally, untreated samples of all rocks have been analysed for comparison, which serves as a useful way to explore the types of minerals originally present in each rock sample, and as a means for comparison against the results obtained for the samples reacting at different temperatures. These can be found in Appendix C together with full-scale chemical analysis of all spectra relevant to the EDX analysis shown in this section as well as complementary photomicrographs.

6.3.1   Room-temperature experiments

In the analysed syenite sample at room-temperature, most spectra reflect a composition including Si, O, Al, Na, and K, while other spectra show the presence of Ca, Fe, and Mn together with relatively high peaks of Si and or Al. Only a single spectrum out of nine directed at the crystal grain shown in Appendix C.2 demonstrates a composition consistent with that of a carbonate, containing the elements Ca, C, O, and Fe, suggesting a combination of calcite and/or siderite in the sample. The EDX analysis of the post-treated syenite displayed a composition dominated by Si, Al, Na, Ca, and O, with minor amounts of Na and K as well as negligible amounts of K and occasional F peaks. A few chemical spectra showed relatively negligible Si peaks compared to overwhelming peaks for Fe and Mn, followed by O, C, and Ca.

It is apparent that the grain size for of some of the crystals in carbonatite dissolved at room-temperature has been considerably reduced compared to the untreated carbonatite sample. Four individual clusters of grains have been chemically analysed, of which one cluster is shown in Appendix C.2. Most spectra reflect clear peaks of C, Ca, and O, while others also include Mn and/or Fe or occasional W or Sc peaks, reflecting a composition dominated by calcium carbonates. Growth patterns could be evidence for secondary carbonate precipitation in the carbonatite sample at room-temperature. Looking at the post-treated carbonatite sample at room-temperature, the spectral profile unambiguously reflects carbonate composition, with no Si signature as well as clear Ca, C, and C peaks, with occasional Mn and Fe peaks as well as uncommon signatures of W, Tc, Nb, and P. Similarly to the pre-treated carbonatite sample, the presence of growth patterns on the surface of the crystal grain representing the post-carbonatite sample (Appendix C.2) could indicate the presence of secondary carbonate precipitates.

The cluster of grains (Appendix C.2) belongs to the pre-treated gabbro sample and reflects a relatively homogenous composition which is found in other investigated clusters within the sample. These include Al, Fe, Mg, Ti, Ca, C, O, and K as well as clear Si peaks which prevents the determination of carbonate precipitates. The post-treated gabbro showed similar EDX results with the same chemical elements previously listed as well as relatively high Si peaks, displaying no carbonate signature.

The pre-treated granite sample at room-temperature displayed a composition dominated by Si, O, followed by Ti, Fe, Al, Mg, Na, C, and K, with occasional Ba peaks. The post-treated granite is essentially identical in chemical composition, except for an occasional addition of P and F peaks. Of

the six grain clusters investigated in the post-treated granite, only one spectral profile displayed a relatively lower Si peak with the presence of prominent Ca, Fe, and P peaks as well as clear C, Ca, F, and Al signatures. However, due to the presence of elements such as P and F, the profile is deemed devoid of any carbonate signature.

The EDX results of the pre-treated dolerite sample show a composition of Si, Ti, Fe, and O, followed by Fe and Ti, as well as lesser Al and Mg signatures and minor Na, Ca, and K. The dolerite grain shown in Appendix C.2 is part of one of the 6 cluster grains investigated in the sample, of which none showed a carbonate signature. The post-treated dolerite displays a similar composition, where clear Ca, Fe, and/or Mn peaks are coupled with non-negligible Si and Al signatures, providing no chemical proof of a carbonate precipitate.

Finally, the pre-treated basalt at room temperature mainly showed clear peaks of Si, Fe, Ca, Mg, C, and O, as well as Ti and Al and lesser Na, with a single spectrum in the grain shown in Appendix C.2 reflecting a negligible Si peak compared to prominent Ca, C, and O as well as a moderately high Mg peak. Post-treated basalt showed a chemical composition comprising Si, Fe, O, and Al, with lesser K, Ca, and Na, and minor Ti. Of the seven different grain clusters which have been analysed in the basalt sample dissolved at room temperature, only the grain shown in Appendix C have suggested carbonate composition, with a single spectrum displaying negligible Si as well as clear Ca, C, and O signatures.

6.3.2 Experiments at 50°C

Syenite at 50°C is predominantly composed of Si, Al, and O, with minor amounts of Na and Ca as well as negligible K and occasional F peaks. Investigating seven other sites than the one comprising the grain shown in Appendix C.3 leads to the conclusion of no clear carbonate signature in the pre-treated syenite sample. Seven other clusters of grains were investigated in the post-treated syenite sample, of which a single spectrum showed prominent Fe, C, and O peaks, although these are coupled with an Si-poor signal and minor Al and Na peaks, which impeded the classification of this chemical signature as that of a carbonate mineral.

The carbonatite grain (Appendix C.3) was chosen to represent the pre-treated carbonatite sample, since it is dominated by Fe and Ca as well as C, O, and Mn, with minor Mg and Mn. All the spectra provided by analysing the carbonatite grain display unmistakable carbonate signatures. The post-treated carbonatite grain also displays clear carbonate signatures, with occasional Nb, La, Ce, F, P, and W peaks. The relatively rough surface shows signs of secondary carbonate precipitation.

EDX analysis of the gabbro at 50°C displays a chemical composition including Si, Al, O, Ca, and Na, with lesser peaks for Ti, K, and Mg. The grain shown in Figure 35 contains the only spectral signature which could be classified as a carbonate, although the presence of minor Mg and Si peaks makes it less convincing. The post-treated gabbro grain shown in Appendix C is dominated by Si, Fe, Ti, and O, followed by Al and Mg as well as minor K, Ca, Na, and Ti, with no observed carbonate signature due to prominent Si peaks.

The granite sample is dominated by Si, Al, Fe, Mn, Ti, and O as well as minor K, Ca, and Mg, where all the sites of grains investigated showed no clear carbonate signature. This trend is also found in the post-treated granite sample.

As for the dolerite sample at 50°C, EDX analysis displayed a composition of Si, Fe, and O as well as moderate Mg, Al, Ca, lesser Ti and negligible C peaks. The only spectrum which shows prominent Fe, Ca, Mg, O and C peaks also displays a lesser Si peak, which makes carbonate identification uncertain. Post-treated dolerite essentially shows the same chemical composition, and the spectra containing prominent Fe and/or Mn peaks also show Si and Al peaks, although at relatively much lower intensity, as well as significant Ti peaks.

Lastly, EDX analysis of the pre-treated basalt sample at 50°C showed prominent Fe, O, Al, and Mn, and moderately low peaks for Ti, Ca, C, and Mg. The only five spectra in a total of 7 investigated grain cluster sites which showed high Fe and O compared to negligible Si peaks also displayed relatively low C signatures, so it is unclear whether the signal belongs to a carbonate precipitate or to an Fe-rich phase. Two of these five spectra belong to the basalt grain shown in Appendix C.3. The post-treated basalt sample is dominated by Si, Fe, O and Al, with moderately high Mg and Ca, as well as minor Na, Mn, and Ti. The presence of Ti as well as Si peaks prevented classifying Ca-, Fe-, C-, and O-rich spectra into carbonate signatures.

6.3.3   Experiments at 100°C

The syenite sample at 100°C is predominantly composed of Si, Al, Fe, Mn, and O, followed by lesser Ca and C as well as minor K. The grain shown which has been chosen to represent the sample gave distinguished carbonate signatures, seen as a light-coloured, textured veil covering the otherwise dark-coloured surface area, which classifies these signatures as secondary carbonate precipitates.

The carbonatite also shows the same growth pattern on the investigated grain's surface, giving signs of secondary carbonate precipitation. The EDX analysis showed clear peaks of Ca, O, Mn, and Fe, as well as Ca and C.

The gabbro sample reflects prominent Fe and O peaks, as well as moderately high Si, Al, and Ca, followed by minor Na, Mg, and K. Of the four grain clusters which were investigated, including the grain chosen to represent the gabbro sample (Appendix C.4), no spectra displayed a carbonate signature due to prominent Si peaks.

As for the granite sample dissolved at 100°C, spectral data returned a composition of Si, Fe, and O, followed by Al and Na, as well as minor Mg, Ca, and K. Some spectra showed prominent Ca, C, and O peaks, although the simultaneous presence of clear Si, Al and/or Ti signatures cannot allow for carbonate classification.

The dolerite sample mainly showed more prominent Fe and O signals compared to Si, followed by moderately high Al, Mg, and Ti, as well as minor Ca and Na. A single spectrum in the representative dolerite grain showed relatively high Ca, C, and O peaks, coupled with a low Si peak as well as minor Ti, Al, Mg, and Na, of which the overall signature cannot be matched with that of a carbonate.

EDX analysis of the basalt sample at 100°C reflects a chemical composition comprising Fe, O, Mn, and Si, with moderate Al, Ti, and K, as well as minor Na, Ca, and Mn. All resulting spectra from the analysis did not yield any clear carbonate signature.

7. DISCUSSION

7.1 Temperature and pH

Measurements of pH and temperature across the three experimental sets revealed a gradual increase in pH until reaching stable levels within the basic range. Among the rock samples, gabbro exhibited the highest pH value (8.68) at room temperature, while syenite demonstrated the highest pH (9.01) at 50°C, and carbonatite displayed the highest pH (8.42) at 100°C. The addition of the $NaHCO_3$ - Na_2CO_3 solution had limited impact on pH increase, with the most significant increases observed in carbonatite at room temperature by 0.78 units and dolerite at 50°C by 1.01 units. Contrastingly, the $NaHCO_3$ - Na_2CO_3 solution slightly lowered the pH levels of gabbro, granite, and dolerite at room temperature by an average 0.27 units.

The efficacy of the $NaHCO_3$ - Na_2CO_3 solution in contributing CO_3^{2-} anions and promoting carbonate precipitation in aqueous solution may have been enhanced if the solution had been more concentrated, although further testing needs to be conducted to confirm this concept. It is crucial to consider that the availability of cations in solution depends on the composition of the dissolved rock sample. For instance, rocks rich in silicon (Si) but poor in alkali metals may have limited contributions of essential cations such as Ca^{2+}, Fe^{2+}, or Mn^{2+} necessary for carbonate precipitation. Granite, dominated by SiO_2 with minor amounts of Fe and Ca (1.5 – 1.9%) and even less Mn (0.03%), exemplifies this limitation. Additionally, a Mg-rich rock sample forms solvation shells around Mg ions, impeding further reaction with anions and subsequent crystallization under ambient conditions. Consequently, even olivine, which is typically reactive in carbonatization reactions, may contribute minimally to carbonate precipitation. Therefore, an increase in pH can indicate dissolution reactions as H^+ is consumed to leach various cations, but it does not necessarily confirm the occurrence of carbonatization reactions leading to carbonate precipitation. The increase in pH could be attributed to other factors such as the increased presence of sodium (Na) in solution, known to elevate pH levels, as well as to poorer CO_2 dissolution at higher temperatures.

To ensure accurate pH measurements, the pH meter was calibrated with two different buffers before each daily measurement. Ideally, the calibration process should be conducted at the same temperature setting as the experiments. However, the buffers were consistently calibrated at room temperature, which is considered optimal for the room-temperature experiments but introduces uncertainty regarding pH values in the 50°C and 100°C experiments. Rounding all pH values to one decimal place can provide a more reliable estimation.

The experiments were conducted in closed systems, although more advanced research has employed mixed-flow reactor systems with both inlet and outlet for the reaction water. This configuration allows for a continuous CO_2-water input, facilitating the renewal of H^+ and CO_3^{2-} contributions for leaching and binding with cations, respectively, thus favouring carbonation reactions. Consequently, it is possible that neither the cations nor the anion complexes reached a state of saturation in the experiments conducted within this study.

During the room-temperature and 50°C experiments, fluctuations in temperature were observed throughout the testing period. In the room-temperature experiments, the temperature varied within a few degrees, influenced by factors such as the presence of individuals in the laboratory, operation of ovens, and the heating system itself. For the 50°C experiments, temperature fluctuations were attributed to the heating plates intermittently failing to reach the desired temperature and the

gradual malfunction of three out of the six plates, which necessitated changes in the experimental setup. Implementing a heating and stirring station for both the room-temperature and 50°C experiments would be a valuable improvement for future studies.

7.2 XRD

The X-ray diffraction (XRD) analysis was conducted to examine the mineral phases present in each rock sample. The analysis successfully identified phases that occurred in significant concentrations. However, it is important to note that phases present as accessory minerals, which are typically found in less than 1% abundance, may not be detectable using this method and are therefore more challenging to assess.

No carbonate precipitation was observed through XRD analysis, except for the carbonatite sample, which was expected since it consists of more than 80% calcite. Furthermore, the addition of a $NaHCO_3 - Na_2CO_3$ solution did not alter the detectable composition of the rock samples. It can be inferred that carbonate precipitates exceeding 1% abundance may be identifiable using XRD analysis, and this possibility could be explored in future research endeavours.

The mineral phases reported in the XRD results and Appendix B represent those that exhibited the clearest signatures during the investigation. Due to time limitations in examining the XRD data and utilizing the instrument's software, other potential mineral phases that could be present in the samples were not included to avoid potential errors in the results. Consequently, the mineral composition information provided is incomplete and does not fully reflect the actual chemical composition of the rock samples. Devoting more time to thoroughly study the XRD data would be an area of improvement for achieving a more accurate chemical profile.

Nevertheless, the XRD analysis provided valuable insights into the geochemical composition of the samples investigated in this study.

7.3 SEM

The SEM analysis, particularly in conjunction with EDX, proved to be more effective in identifying carbonate phases compared to other techniques. However, the question remains as to whether this technique provides a representative assessment of the entire rock sample and the geological area from which the samples were obtained. A challenge arises in quantifying the amounts of carbonate precipitates in each sample since only a few grains out of the 10 g used in the experiments were chemically analysed with EDX.

Another concern regarding EDX analysis is that, although carbonate precipitates were potentially detected in certain samples, their volume was often insufficient to fully occupy the circumference of electron beam directed at them. Given that the electron beam has a radius of 1 μm, it was frequently too large for the observed carbonate precipitates. This situation could generate a mixed chemical signal, encompassing both the carbonate precipitate and the host crystal, and therefore impeding any carbonate classification. Additionally, gold-coating prior to analysis resulted in the presence of gold (Au) signatures in all samples. While these signatures did not introduce ambiguity in interpreting the chemical data, the carbon (C) peaks presented a degree of uncertainty when

evaluating the prominence of C signatures, particularly in the context of assessing carbonate precipitation. The underlying plate in each sample holder, composed of pure carbon, exhibited a distinct C peak during chemical analysis. Consequently, any candidate grains smaller than 1 μm located at crystal edges invariably displayed a stronger C signature.

During the experimental process, all rock samples were constantly stirred using a magnet and a magnetic stirring station. This stirring action contributed to mechanical erosion, leading to a noticeable decrease in grain size to the order of clay particles. It is important to clarify that this reduction in size refers to the rock samples being reduced to the dimensions of clay particles, not to the presence of clay minerals, although the possibility of their occurrence cannot be ruled out.

Icelandic basalt was selected as an ideal candidate for this study due to its demonstrated propensity to readily react with carbonated water, resulting in relatively higher rates of carbonate precipitation. However, even basalt did not exhibit a significant quantity of carbonate precipitates. The carbonate signatures in the basalt sample were clearest in both the pre- and post-treated basalt samples at room temperature, yet they were ambiguous in the samples dissolved at 50°C and non-existent in the 100°C sample. This suggests that further improvements are required in the experimental setup to maximize carbonatization potential under laboratory conditions. Possible avenues for enhancement include calibrating the rock/CO_2-fluid ratio to achieve more promising results or allowing the experiments to run for extended periods to promote carbonate precipitation.

7.4 Implications and perspectives

The gabbro sample analysed in this study exhibited a significant presence of amphibole in the form of hornblende, which is an alteration product of augite. Normally, a pristine gabbro specimen consists of pyroxene (augite) and plagioclase. However, the altered nature of the rock renders it non-reactive in terms of carbon capture and storage (CCS). Furthermore, the Mg-rich composition of hornblende in the gabbro hampers its reactivity in low to moderate temperature fluid-rock interactions. In ambient laboratory conditions, Mg tends to form a hydrous layer around the mineral, inhibiting the formation of complexes between Mg^{2+} and CO_3^{2-}.

The syenite sample primarily consists of the feldspathoid nepheline, along with orthoclase, albite, and hornblende. The main cations present in the sample are K^+, Al^{3+}, Na^{2+}, and Ca^{2+}. However, in terms of carbonatization potential, the only mineral within the syenite that can contribute to this process is aegirine-augite, which contains the cations Fe^{2+} and minor amounts of Ca^{2+}. Consequently, the syenite sample exhibits limited capability for carbonate precipitation, which was reflected in the EDX results, although clear carbonate signatures were found in the room-temperature samples as well as the 100°C sample. Furthermore, anomalously high concentrations of analcime were observed in the syenite sample, whereas typically it occurs as a secondary mineral. In contrast to other zeolites, analcime can form at different temperatures. This suggests that syenite has previously undergone a certain degree of alteration and therefore holds limited capacity for carbonation reactions.

Additionally, in basalt, plagioclase usually undergoes zeolite alteration due to changes in temperatures, leading to poorer carbonatization potential. It could be argued that the basalt sample dissolved at 100°C underwent zeolite alteration. This, combined with the relatively short time of the 100°C experiments, could be a reason why no carbonate precipitation was observed in the basalt dissolved at this temperature.

In contrast, the carbonatite sample exhibited unambiguous evidence of secondary carbonate precipitation, as observed in the EDX results. The presence of secondary carbonate growth in carbonatite suggests its potential suitability for effective carbon sequestration processes.

However, the dolerite sample also displayed extensive alteration, evident from the presence of minerals such as siderophyllite and clinochlore in the XRD results. The age of the rocks used in this study emerged as a limiting factor, as they were found to be non-porous, chemically altered, and exhibited poor reactivity towards carbonation, as indicated by the low amount of carbonate precipitates observed in the EDX results and the lack of chemical carbonate signature with EDX in regard to gabbro, granite, and dolerite.

Furthermore, the granite sample predominantly consisted of quartz, albite, and microcline, along with the presence of siderophyllite, indicating a lower potential for carbonatization and reduced reactivity due to extensive alteration. The composition of granite, characterized by these minerals, suggests that it may not be an optimal candidate for efficient carbon sequestration processes.

Considering the relatively old age and non-porous nature of the rock samples from Billdal, Sweden, in contrast to the reactive and young basalt from Iceland, carbon capture and storage in Sweden would necessitate crushing the rocks to initiate the carbonation reaction, assuming that the rocks in question provide the necessary cations for successful carbonation reactions. Smaller grain sizes offer larger surface areas for interaction with carbonated water, but this approach incurs additional costs for crushing and material transport. Furthermore, if direct injection of carbonated water into the bedrock were considered, as practiced in Iceland, it would require highly fractured or faulted areas where secondary porosity could potentially develop. However, due to the absence of significant seismic activity in Sweden and the pre-existing hydrothermal alteration of fractures and faults within the relatively old bedrocks, primary and secondary porosity are lacking, posing a considerable challenge.

7.5 Further Research

Further research is warranted to identify suitable rocks for carbon sequestration in Sweden, necessitating a comprehensive examination of regional petrology and geochemistry. Among potential candidate rocks, peridotite, olivine, and pyroxenes have demonstrated high reactivity and susceptibility to carbonatization. These rocks should undergo extensive laboratory experiments to assess their behaviour and carbonatization potential before aiming for large-scale applications.

To achieve optimal outcomes in laboratory conditions, various factors such as temperature, pH, saturation levels, and fluid-to-rock ratios require further investigation. Additionally, introducing pressure as a variable in these experiments would enable more accurate simulation of CO_2-water injections into deep crystalline bedrock.

Another avenue for research could involve exploring low-temperature rock-fluid interactions with a focus on carbonate mineralization. This investigation could involve the utilization of seawater in combination with alkali-rich rock types such as syenite and carbonatite. Such studies would contribute to a deeper understanding of the processes occurring at the Grønnedal-Íka igneous complex in Greenland and shed light on making an industrial potential out of the natural carbon sequestration taking place through ikaite in this geological setting.

Conclusions

The investigation of fluid-rock interactions involving six different types of rocks and carbonated deionized (D.I.) water has revealed a relatively low rate of carbonatization. This can be attributed, in part, to the relatively old age of the Swedish rocks under investigation, which exhibit signs of alteration and limited reactivity. The case of Icelandic basalt presents an intriguing contrast, as its comparatively younger age and high porosity would suggest a greater potential for significant carbonate precipitation. However, it remains unclear whether syenite and carbonatite, which are known to contribute to the precipitation of ikaite in Greenland under cold temperature conditions (<5°C) and in the presence of seawater, possess similar potential for carbonatization at higher temperatures and with fresh water. Further research is required to address these uncertainties and provide insights into the carbonatization potential of these rock types under different conditions.

References

Adalsteinsdottir, S.M. (2020). The Low-Temperature Weathering of the Grønnedal-Íka Carbonatite-Alkaline Silicate Igneous Complex in Southwest Greenland. Dissertation, University of Iceland.

Adam, L., van Wijk, K., Otheim, T., & Batzle, M. (2019). Changes in elastic wave velocity and rock microstructure due to basalt-CO2-water reactions. International Journal of Greenhouse Gas Control, 88, 256-271. doi: 10.1016/j.ijggc.2019.06.014.

Alderton, D. (2021). X-Ray Diffraction (XRD). In Encyclopaedia of Geology (Second Edition), 520-531. Elsevier. (https://doi.org/10.1016/B978-0-08-102908-4.00178-8; https://www.sciencedirect.com/science/article/abs/pii/B9780081029084001788?via%3Dihub. Accessed 20/04/2023.

Aradóttir, E.S.P., Sigurdardóttir, H., Sigfússon, B., Gunnlaugsson, E. (2011). CarbFix, a CCS pilor project imitating and accelerating natural CO_2 sequestration. Greenhouse Gases: Science and Technology 1, 105-118.

Bedford, C. M. (1989). The mineralogy, geochemistry, and petrogenesis of the Grønnedal-Íka alkaline igneous complex, south-west Greenland: Unpublished PhD thesis, University of Durham.

Benson, S. M. (2005). Carbon capture and storage in underground geologic formations. Journal of Petroleum Science and Engineering, 47(3-4), 167-174. https://doi.org/10.1016/j.petrol.2005.06.009

Bingen, B., Nordgulen, Ø., Viola, G. (2008). A four-phase model for the Sveconorwegian orogeny, SW Scandinavia. Norwegian Journal of Geology 88, 43- 72.

CO2.Earth. (n.d.). Daily CO2. https://www.co2.earth/daily-co2. Accessed 08/06/2023.

Coulson, I.M., Goodenough, K.M, Pearce, N.J.G., Leng, M.J. (2003). Carbonatites and lamprophyres of the Gardar province - a 'window' to the sub-Gardar mantle? Mineralogical Magazine, Vol. 67(5), pp.855-872.

Dewangan, P., Rust, A., & Walter, T. R. (2021). Geomorphological characterization of the 2014–2015 Holuhraun lava flow-field in Iceland. Journal of Volcanology and Geothermal Research, 417, 107386. doi: 10.1016/j.jvolgeores.2021.107386

Dickson, A. G., Sabine, C. L., & Christian, J. R. (2007). Guide to best practices for ocean CO_2 measurements. PICES Special Publication, 3(186), 1-191

Doney, S. C., Busch, D. S., Cooley, S. R., & Kroeker, K. J. (2021). The impacts of ocean acidification on marine ecosystems and reliant human communities. Annual Review of Environment and Resources, 46, 213-236. https://doi.org/10.1146/annurev-environ-012320-083019

Farndon, J. (2019). Illustrated guide to rocks and minerals. Anness Publishing Ltd.

Geiger H, Mattson T, Deegan FM, Troll VR, Burchardt S, Gudmundsson Ó, Tryggvason A, Krumbholz M, Harris C (2016) Magma plumbing of the 2014–2015 Holuhraun eruption, Iceland. Geochem Geophys Geosyst. https://doi. org/10.1002/2016GC006317

Gíslason, S. R., Sigurdardóttir, H., Aradóttir, E. S., & Oelkers, E. H. (2019). A brief history of CarbFix: Challenges and victories of the project's pilot phase. Energy Procedia, 158, 4366-4371. doi: 10.1016/j.egypro.2019.01.797

Gudmundsson, M.T., Jónsdóttir, K., Hooper, A., Holohan, E.P., Halldórsson, S.A., Ófeigsson, B.G., Cesca, S., Vogfjörd, K.S., Sigmundsson, F., Högnadóttir, T., Einarsson, P., Sigmarsson, O., Jarosch, A.H., Jónasson, K., Magnússon, E., Hreinsdóttir, S., Bagnardi, M., Parks, M.M., Hjörleifsdóttir, V., Pálsson, F., Walter, T.R., Schöpfer, M.P.J., Heimann, S., Reynolds, H.I., Dumont, S., Bali, E., Gudfinnsson, G.H., Dahm, T., Roberts, M.J., Hensch, M., Belart, J.M.C., Spaans, K., Jakobsson, S., Gudmundsson, G.B., Fridriksdóttir, H.M., Drouin, V., Dürig, T., Aðalgeirsdóttir, G., Riishuus, M.S., Pedersen, G.B.M., van Boeckel, T., Oddsson, B., Pfeffer, M.A., Barsotti, S., Bergsson, B., Donovan, A., Burton, M.R. and Aiuppa, A. (2016). Gradual caldera collapse at Bárdarbunga volcano, Iceland, regulated by lateral magma outflow. Science, 353(6296).

Halldórsson, S. A., Bali, E., Hartley, M. E., Neave, D. A., Peate, D. W., Guðfinnsson, G. H., Bindeman, I., Whitehouse, M. J., Riishuus, M. S., Pedersen, G. B. M., Jakobsson, S., Askew, R., Gallagher, C. R., Guðmundsdóttir, E. R., Gudnason, J., Moreland, W. M., Óskarsson, B. V., Nikkola, P., Reynolds, H. I., Schmith, J., & Thordarson, T. (2018). Petrology and geochemistry of the 2014-2015 Holuhraun eruption, central Iceland: compositional and mineralogical characteristics, temporal variability and magma storage. Contributions to Mineralogy and Petrology, 173, 64. https://doi.org/10.1007/s00410-018-1487-9.

Hegardt, E.A. (2010) Pressure, temperature and time constraints on tectonic models for southwestern Sweden. [Doctoral dissertation, University of Gothenburg].

Hellström, F. (2009). Geochronology and petrology of mafic dykes in the Idefjorden Terrane of the Sveconorwegian Orogen, South-west Sweden. Thesis for Ph. Licentiate Degree. Earth Sciences Centre, University of Gothenburg, A121, 21 pp.

Hellström, F.A., Johansson, Å., & Larson, S.Å. (2004). Age and emplacement of late Sveconorwegian monzogabbroic dykes, SW Sweden, Precambrian Research, 128, 39–55.

Intergovernmental Panel on Climate Change. (2021). Climate Change 2021: The Physical Science Basis. Contribution of Working Group I to the Sixth Assessment Report of the Intergovernmental Panel on Climate Change. Cambridge University Press. Accessed 12/04/2023.

Jamtveit, B., & Hammer, Ø. (2012). Sculpting of rocks by reactive fluids. Geochemical Perspectives, 1(3), 195-275.

Kelemen, P.B., Matter, J., Streit, E.E., Rudge, J.F., Curry, W.B., Blusztjan, j. (2011) Rates and mechanisms of mineral carbonation in peridotite: Natural processes and receipts for enhanced, in situ CO2 capture and storage. Annual Reviews of Earth and Planetary Sciences 39, 545-576.

Klein, C., & Philpotts, A. (2017). Earth Materials: An Introduction to Mineralogy and Petrology (2nd ed.). Cambridge University Press.

Krauskopf, K.B., & Bird, D.K. (2006). Introduction to Geochemistry (3rd ed.). McGraw-Hill. ISBN: 0-390-74045-4.

Matter, J. M., & Kelemen, P. B. (2009). Permanent storage of carbon dioxide in geological reservoirs by mineral carbonation. Nature Geoscience, 2(12), 837-841. https://doi.org/10.1038/ngeo683.

Mohammed, A., & Abdullah, A. (2018). Scanning electron microscopy (SEM): A review. In Proceedings of 2018 International Conference on Hydraulics and Pneumatics - HERVEX.

Montes-Hernandez, G., Findling, N., & Renard, F. (2016). Dissolution-precipitation reactions controlling fast formation of dolomite under hydrothermal conditions. Applied Geochemistry, 73, 42-54. https://doi.org/10.1016/j.apgeochem.2016.08.011.

Nesse, W. D. (2020). Introduction to Mineralogy (2nd ed.). Oxford University Press.

Petersson, A., Scherstén, A., Bingen, B., Gerdes, A., & Whitehouse, M. J. (2015). Mesoproterozoic continental growth: U–Pb–Hf–O zircon record in the Idefjorden Terrane, Sveconorwegian Orogen. Precambrian Research, 261, 75-95. https://doi.org/10.1016/j.precamres.2015.01.008

Ranta, E. (2015). Study of opaque phases in carbonatites of the Grønnedal-Íka alkaline complex, Southwest Greenland. Dissertation, University of Stockholm.

Ranta, E., Stockmann, G., Wagner, T., Fusswinkel, T., Sturkell, E., Tollefsen, E., Skelton, A. (2018). Fluid-rock reactions in the 1.3 Ga siderite carbonatite of the Grønnedal–Íka alkaline complex, Southwest Greenland. Contributions to Mineralogy and Petrology, 173(78). https://doi.org/10.1007/s00410-018-1505-y.

Stockmann, G. J. (2012). Experimental study of basalt carbonatization [Doctoral dissertation, University of Iceland]. Skemman.

Upton, B.G.J. (2013). Tectono-magmatic evolution of the younger Gardar southern rift, South Greenland. Geology Survey of Denmark and Greenland Bulletin 29, pp. 1-128.

Veksler, I. V., Nikolenko, A., & Stepanov, K. (2022). Experimental study of phase equilibria between bastnäsite, burbankite and La phosphates in the system $La(CO_3)F$ -$CaCO_3$ - Na_2CO_3 - $Ca_3(PO_4)_2$ at 100 MPa. EGU General Assembly Conference Abstracts, 24, 6360. https://doi.org/10.5194/egusphere-egu22-6360

Wan, Q., Masters, R. C., Lidzey, D., Abrams, K. J., Dapor, M., Plenderleith, R. A., Rimmer, S., Claeyssens, F., & Rodenburg, C. (2018). Angle selective backscattered electron contrast in the low-voltage electron scanning microscope. Ultramicroscopy, 184, 235-241. doi: 10.1016/j.ultramic.2017.09.019

Zhang, X., Cen, X., Ravichandran, R., Hughes, L. A., & van Benthem, K. (2016). Simultaneous Scanning Electron Microscope Imaging of Topographical and Chemical Contrast Using In-Lens, In-Column and Everhart Thornley Detector Systems. Microscopy and Microanalysis, 22(6), 1256-1265. doi: 10.1017/S1431927616000751.

APPENDIX A: Temperature and pH

A1. Room temperature experiments

Syenite

Table A1. Daily pH and temperature measurements of pre-Na-treated syenite at room-temperature.

Date	pH	°C
03-11-2022 T_0 = 09:25	3.88	20.0
03-11-2022 (12:12)	4.11	20.8
04-11-2022	5.12	21.2
05-11-2022	5.20	20.5
06-11-2022	5.49	20.5
07-11-2002	5.58	20.5
8-11-2022	5.66	20.5
9-11-2022	5.79	20.5
10-11-2022	5.85	20.5
11-11-2022	5.94	20.7
12-11-2022	6.07	20.4
13-11-2022	6.14	20.5
14-11-2022	6.22	20.5
15-11-2022	6.25	20.4
16-11-2022	6.33	20.3
17-11-2022	6.34	20.1
18-11-2022	6.43	19.9
19-11-2022	6.48	19.6
20-11-2022	6.58	19.2
21-11-2022	6.64	19.3
22-11-2022	6.65	20.1
23-11-2022	6.68	20.6
24-11-2022	6.75	21.3
25-11-2022	6.83	21.3
26-11-2022	6.83	20.9
27-11-2022	6.92	20.9
28-11-2022	6.96	20.7
29-11-2022	7.03	21.7
30-11-2022	7.06	20.7
01-12-2022	7.10	21.2
02-12-2022	7.16	20.8
03-12-2022	7.23	20.5
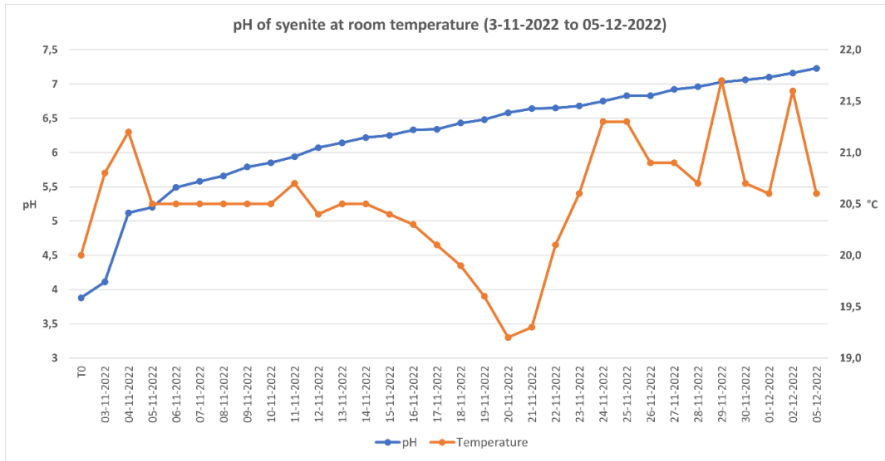
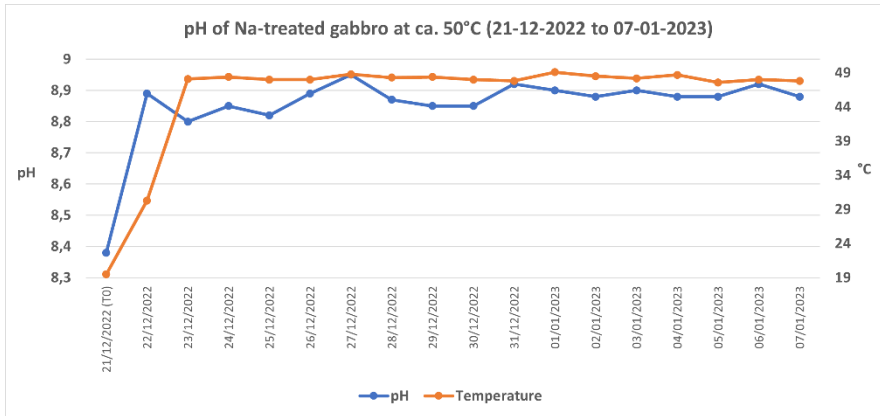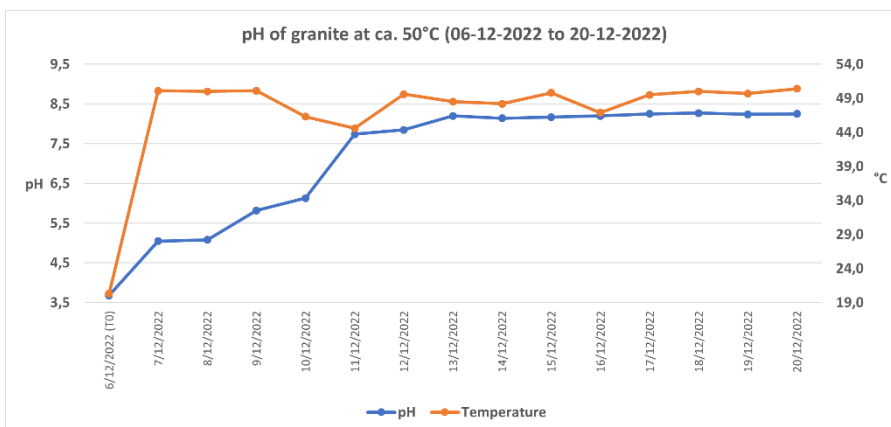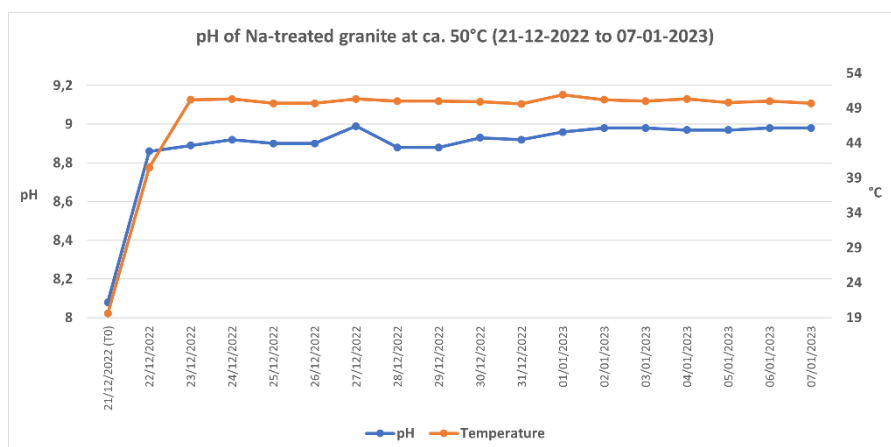*Figure A1. Diagram showing pH and temperature measurements of syenite at room-temperature.*

Table A2. Daily pH and temperature measurements of Na-treated syenite at room-temperature.

Date	pH	°C
06-12-2022	8.62	22.1
07-12-2022	8.33	21.0
08-12-2022	8.26	21.9
09-12-2022	8.21	22.0
10-12-2022	8.48	21.2
11-12-2022	8.48	20.9
12-12-2022	8.52	20.8
13-12-2022	8.52	21.0
14-12-2022	8.53	20.8
15-12-2022	8.55	20.8
16-12-2022	8.54	20.3
17-12-2022	8.53	19.8
18-12-2022	8.53	20.0
19-12-2022	8.59	20.0
20-12-2022	8.62	20.7
21-12-2022	8.62	21.4
22-12-2022	8.62	20.9
23-12-2022	8.61	21.6
24-12-2022	8.60	20.7
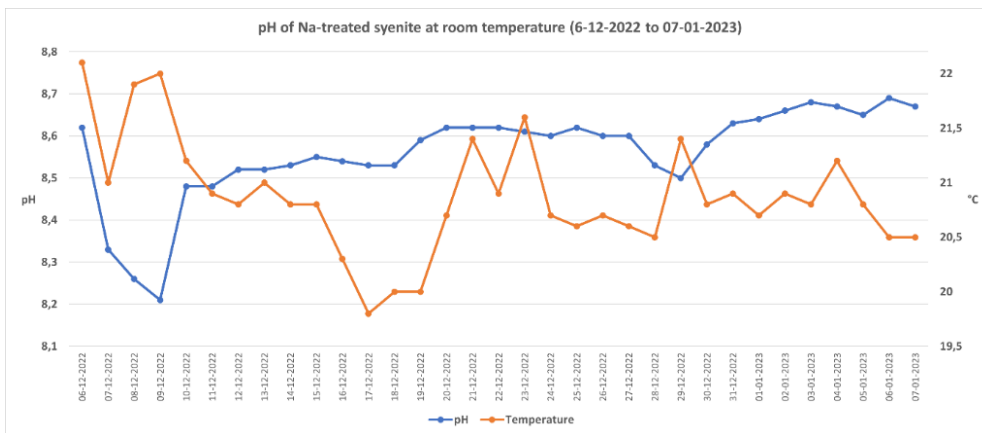
Figure A2. Diagram showing pH and temperature measurements of Na-treated syenite at room-temperature.

Carbonatite

Table A3. Daily pH and temperature measurements of carbonatite at room-temperature.

Date	pH	°C
03-11-2022 T_0 = 09:38	3.77	20.7
03-11-2022 (12:12)	6.01	20.8
04-11-2022	6.25	21.3
05-11-2022	6.36	20.6
06-11-2022	6.48	20.5
07-11-2002	6.54	20.6
08-11-2022	6.55	20.6
09-11-2022	6.59	20.6
10-11-2022	6.64	20.6
11-11-2022	6.67	20.8
12-11-2022	6.73	20.6
13-11-2022	6.75	20.6
14-11-2022	6.80	20.6
15-11-2022	6.85	20.5
16-11-2022	6.86	20.4
17-11-2022	6.87	20.2
18-11-2022	6.92	20
19-11-2022	6.95	19.8
20-11-2022	7.00	19.3
21-11-2022	7.02	19.3
22-11-2022	7.03	20.2
23-11-2022	7.05	20.7
24-11-2022	7.06	21.3
25-11-2022	7.09	21.4
26-11-2022	7.10	20.9
27-11-2022	7.16	20.9
28-11-2022	7.17	20.7
29-11-2022	7.17	21.7
30-11-2022	7.18	20.8
01-12-2022	7.21	20.7
02-12-2022	7.24	21.6
03-12-2022	7.36	20.7
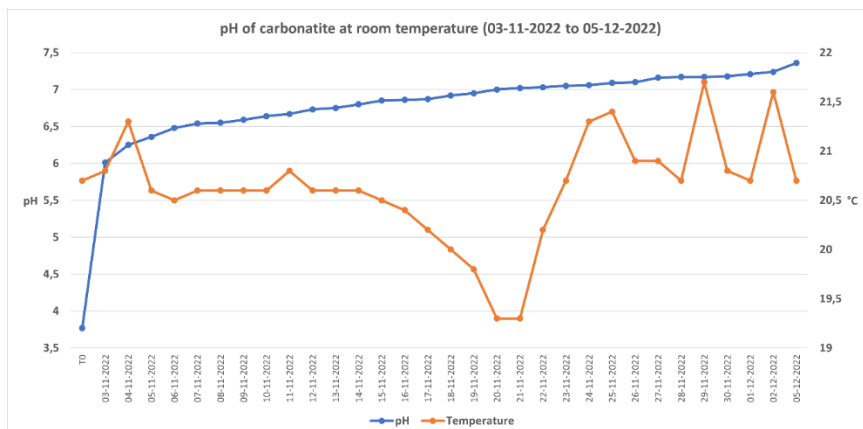
Figure A3. Diagram showing pH and temperature measurements of carbonatite at room-temperature.

Table A4. Daily pH and temperature measurements of Na-treated carbonatite at room-temperature.

Date	pH	°C
06-12-2022	7.89	22.1
07-12-2022	7.86	21.0
08-12-2022	7.91	21.9
09-12-2022	8.20	22.0
10-12-2022	8.38	21.3
11-12-2022	8.46	21.2
12-12-2022	8.49	20.8
13-12-2022	8.50	21.1
14-12-2022	8.53	21.0
15-12-2022	8.56	20.8
16-12-2022	8.58	20.4
17-12-2022	8.56	20.0
18-12-2022	8.59	20.0
19-12-2022	8.58	20.1
20-12-2022	8.62	20.7
21-12-2022	8.59	21.4
22-12-2022	8.58	21.0
23-12-2022	8.57	21.7
24-12-2022	8.61	20.7
25-12-2022	8.61	20.7
26-12-2022	8.62	20.8
27-12-2022	8.71	20.6
28-12-2022	8.67	20.6
29-12-2022	8.59	21.5
30-12-2022	8.65	20.9
31-12-2022	8.65	20.8
01-01-2023	8.69	20.8
02-01-2023	8.65	21.0
03-01-2023	8.68	20.8
04-01-2023	8.66	21.2
05-01-2023	8.65	21.0
06-01-2023	8.67	20.7
07-01-2023	8.67	20.6
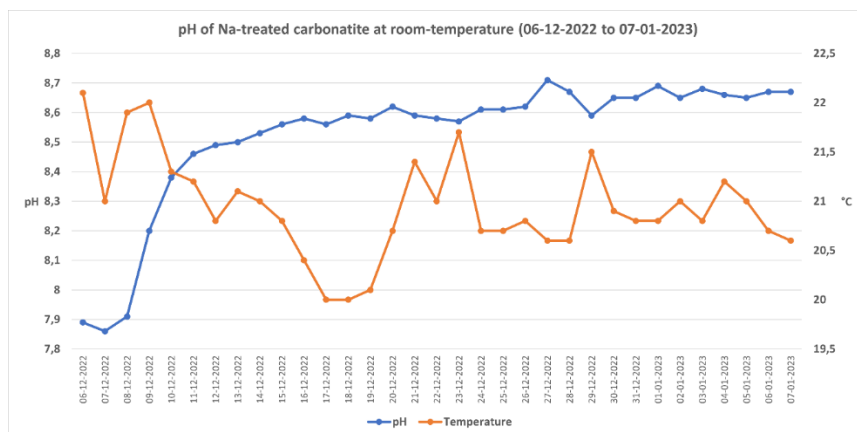
Figure A4. Diagram showing pH and temperature measurements of Na-treated carbonatite at room-temperature.

Gabbro

Table A5. Daily pH and temperature measurements of gabbro at room-temperature.

Date	pH	°C
03-11-2022 T_0 = 09:47	3.77	21.3
03-11-2022 (12:12)	4.78	21.2
04-11-2022	5.11	21.3
05-11-2022	5.47	20.7
06-11-2022	5.51	20.6
07-11-2002	5.67	20.7
08-11-2022	5.89	20.7
09-11-2022	6.12	20.8
10-11-2022	6.26	20.8
11-11-2022	6.47	20.9
12-11-2022	6.77	20.8
13-11-2022	6.88	20.9
14-11-2022	7.07	20.8
15-11-2022	7.27	20.6
16-11-2022	7.28	20.6
17-11-2022	7.46	20.4
18-11-2022	7.63	20.2
19-11-2022	7.74	19.8
20-11-2022	7.89	19.3
21-11-2022	7.94	19.3
22-11-2022	7.96	20.3
23-11-2022	7.99	20.8
24-11-2022	8.02	21.4
25-11-2022	8.03	21.3
26-11-2022	8.03	20.9
27-11-2022	8.04	21.0
28-11-2022	8.14	20.8
29-11-2022	8.14	21.7
30-11-2022	8.14	20.8
01-12-2022	8.14	20.8
02-12-2022	8.14	21.7
05-12-2022	8.20	20.7
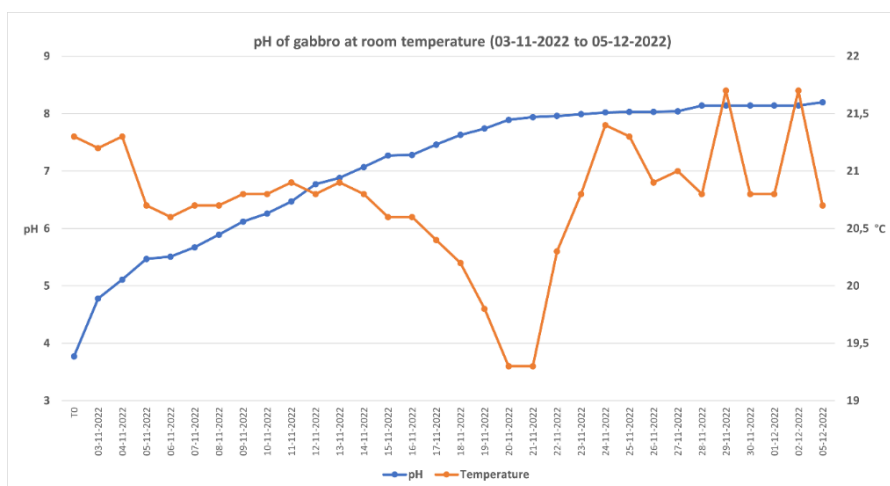
Figure A5. Diagram showing pH and temperature measurements of gabbro at room-temperature.

Table A6. Daily pH and temperature measurements of Na-treated gabbro at room-temperature.

Date	pH	°C
06-12-2022	8.92	22.1
07-12-2022	8.84	21.1
08-12-2022	8.78	22.0
09-12-2022	8.74	22.0
10-12-2022	8.77	21.3
11-12-2022	8.79	21.1
12-12-2022	8.76	20.8
13-12-2022	8.71	21.1
14-12-2022	8.71	21.0
15-12-2022	8.68	20.8
16-12-2022	8.70	20.5
17-12-2022	8.70	20.0
18-12-2022	8.68	20.1
19-12-2022	8.70	20.2
20-12-2022	8.69	20.6
21-12-2022	8.68	21.2
22-12-2022	8.66	21.0
23-12-2022	8.69	21.8
24-12-2022	8.71	20.7
25-12-2022	8.71	20.7
26-12-2022	8.71	20.8
27-12-2022	8.80	20.7
28-12-2022	8.73	20.7
29-12-2022	8.66	21.5
30-12-2022	8.71	21.0
31-12-2022	8.72	20.9
01-01-2023	8.73	20.9
02-01-2023	8.73	21.0
03-01-2023	8.70	20.8
04-01-2023	8.67	21.2
05-01-2023	8.71	20.9
06-01-2023	8.76	20.6
07-01-2023	8.68	20.7
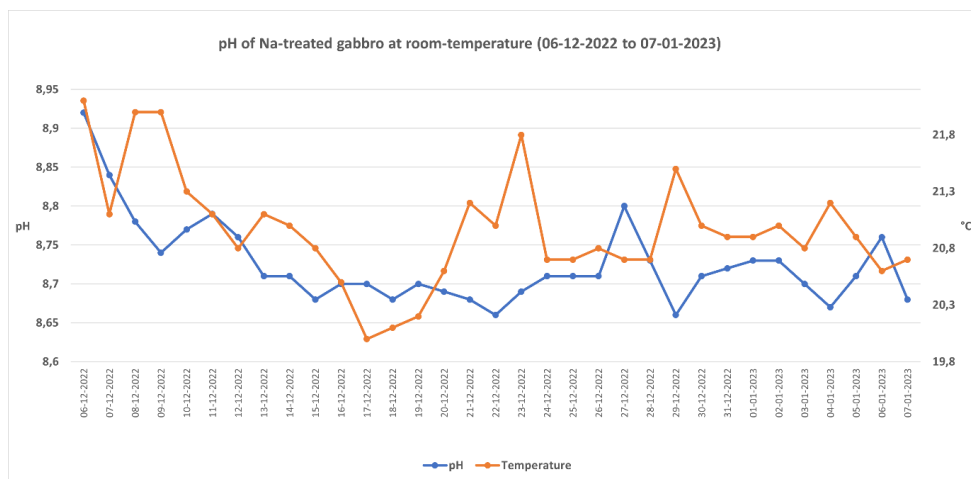
Figure A6. Diagram showing pH and temperature measurements of Na-treated gabbro at room-temperature.

Granite

Table A7. Daily pH and temperature measurements of granite at room-temperature.

Date	pH	°C
03-11-2022 T_0 = 09:42	3.8	20.9
03-11-2022 (12:12)	4.65	21.1
04-11-2022	5.04	21.4
05-11-2022	5.23	20.8
06-11-2022	5.38	20.7
07-11-2002	5.46	20.8
08-11-2022	5.56	20.8
09-11-2022	5.59	20.9
10-11-2022	5.61	20.9
11-11-2022	5.65	21.2
12-11-2022	5.75	20.9
13-11-2022	5.85	21.0
14-11-2022	5.97	20.9
15-11-2022	6.02	20.7
16-11-2022	6.09	20.7
17-11-2022	6.17	20.5
18-11-2022	6.30	20.3
19-11-2022	6.43	19.9
20-11-2022	6.64	19.4
21-11-2022	6.77	19.3
22-11-2022	6.87	20.4
23-11-2022	6.96	21.0
24-11-2022	7.14	21.5
25-11-2022	7.32	21.4
26-11-2022	7.37	21.1
27-11-2022	7.46	21.1
28-11-2022	7.63	20.9
29-11-2022	7.67	21.9
30-11-2022	7.73	20.9
01-12-2022	7.74	20.9
02-12-2022	7.74	21.9
03-12-2022	7.88	20.8
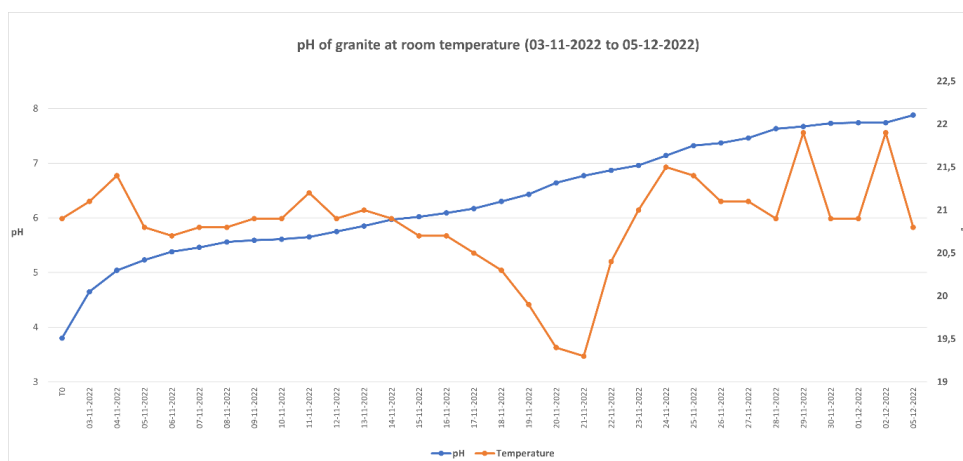
Figure A7. Diagram showing pH and temperature measurements of granite at room-temperature.

Table A8. Daily pH and temperature measurements of Na-treated granite at room-temperature.

Date	pH	°C
06-12-2022	8.94	22.1
07-12-2022	8.84	21.1
08-12-2022	8.80	22.0
09-12-2022	8.73	22.0
10-12-2022	8.76	21.3
11-12-2022	8.78	21.0
12-12-2022	8.75	20.8
13-12-2022	8.72	21.0
14-12-2022	8.69	20.7
15-12-2022	8.69	20.6
16-12-2022	8.70	20.4
17-12-2022	8.68	19.9
18-12-2022	8.68	20.0
19-12-2022	8.66	20.0
20-12-2022	8.66	20.5
21-12-2022	8.61	21.1
22-12-2022	8.61	20.9
23-12-2022	8.66	21.7
24-12-2022	8.68	20.6
25-12-2022	8.67	20.6
26-12-2022	8.70	20.7
27-12-2022	8.73	20.6
28-12-2022	8.67	20.6
29-12-2022	8.61	21.4
30-12-2022	8.65	20.8
31-12-2022	8.63	20.8
01-01-2023	8.65	20.8
02-01-2023	8.64	20.9
03-01-2023	8.64	20.7
04-01-2023	8.61	21.2
05-01-2023	8.61	20.8
06-01-2023	8.65	20.5
07-01-2023	8.60	20.6

Figure A8. Diagram showing pH and temperature measurements of Na-treated granite at room-temperature.

Dolerite

Table A9. Daily pH and temperature measurements of dolerite at room-temperature.

Date	pH	°C
03-11-2022 T_0 = 09:21	3.78	19.8
03-11-2022 (12:12)	4.74	21.2
04-11-2022	5.16	21.4
05-11-2022	5.39	20.8
06-11-2022	5.48	20.8
07-11-2002	5.55	20.8
08-11-2022	5.66	20.9
09-11-2022	5.78	21.0
10-11-2022	5.85	21.0
11-11-2022	6.00	21.2
12-11-2022	6.10	20.9
13-11-2022	6.20	20.9
14-11-2022	6.28	20.9
15-11-2022	6.35	20.9
16-11-2022	6.44	20.8
17-11-2022	6.49	20.6
18-11-2022	6.58	20.5
19-11-2022	6.70	20.1
20-11-2022	6.76	19.6
21-11-2022	6.84	19.6
22-11-2022	6.90	20.6
23-11-2022	6.96	21.2
24-11-2022	7.04	21.7
25-11-2022	7.06	21.6
26-11-2022	7.12	21.2
27-11-2022	7.22	21.3
28-11-2022	7.34	21.0
29-11-2022	7.41	22.0
30-11-2022	7.46	21.0
01-12-2022	7.51	21.0
02-12-2022	7.54	22.0
05-12-2022	7.65	20.9
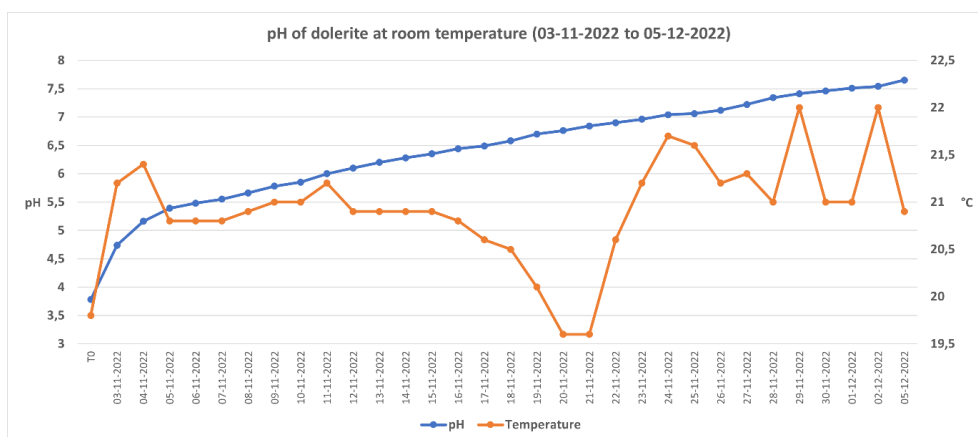
Figure A9. Diagram showing pH and temperature measurements of dolerite at room-temperature.

Table A9. Daily pH and temperature measurements of Na-treated dolerite at room-temperature.

Date	pH	°C
06-12-2022	8.94	22.1
07-12-2022	8.84	21.1
08-12-2022	8.80	22.0
09-12-2022	8.73	22.0
10-12-2022	8.76	21.3
11-12-2022	8.78	21.0
12-12-2022	8.75	20.8
13-12-2022	8.72	21.0
14-12-2022	8.69	20.7
15-12-2022	8.69	20.6
16-12-2022	8.70	20.4
17-12-2022	8.68	19.9
18-12-2022	8.68	20.0
19-12-2022	8.66	20.0
20-12-2022	8.66	20.5
21-12-2022	8.61	21.1
22-12-2022	8.61	20.9
23-12-2022	8.66	21.7
24-12-2022	8.68	20.6
25-12-2022	8.67	20.6
26-12-2022	8.70	20.7
27-12-2022	8.73	20.6
28-12-2022	8.67	20.6
29-12-2022	8.61	21.4
30-12-2022	8.65	20.8
31-12-2022	8.63	20.8
01-01-2023	8.65	20.8
02-01-2023	8.64	20.9
03-01-2023	8.64	20.7
04-01-2023	8.61	21.2
05-01-2023	8.61	20.8
06-01-2023	8.65	20.5
07-01-2023	8.60	20.6

Figure A9. Diagram showing pH and temperature measurements of Na-treated dolerite at room-temperature.

Basalt

Table A10. Daily pH and temperature measurements of basalt at room-temperature.

Date	pH	°C
03-11-2022 T_0 = 09:33	3.88	20.0
03-11-2022 (12:12)	4.34	21.1
04-11-2022	4.68	21.4
05-11-2022	4.93	20.8
06-11-2022	5.12	20.8
07-11-2002	5.20	20.8
08-11-2022	5.29	20.8
09-11-2022	5.39	20.9
10-11-2022	5.47	20.9
11-11-2022	5.56	21.1
12-11-2022	5.70	20.9
13-11-2022	5.78	20.9
14-11-2022	5.89	20.9
15-11-2022	6.06	20.8
16-11-2022	6.13	20.7
17-11-2022	6.19	20.5
18-11-2022	6.28	20.2
19-11-2022	6.41	19.9
20-11-2022	6.53	19.4
21-11-2022	6.63	19.4
22-11-2022	6.73	20.5
23-11-2022	6.78	21.1
24-11-2022	6.90	21.6
25-11-2022	6.98	21.5
26-11-2022	7.07	21.1
27-11-2022	7.08	21.2
28-11-2022	7.22	20.8
29-11-2022	7.30	21.9
30-11-2022	7.46	20.8
01-12-2022	7.55	20.9
02-12-2022	7.63	21.9
05-12-2022	7.94	20.8
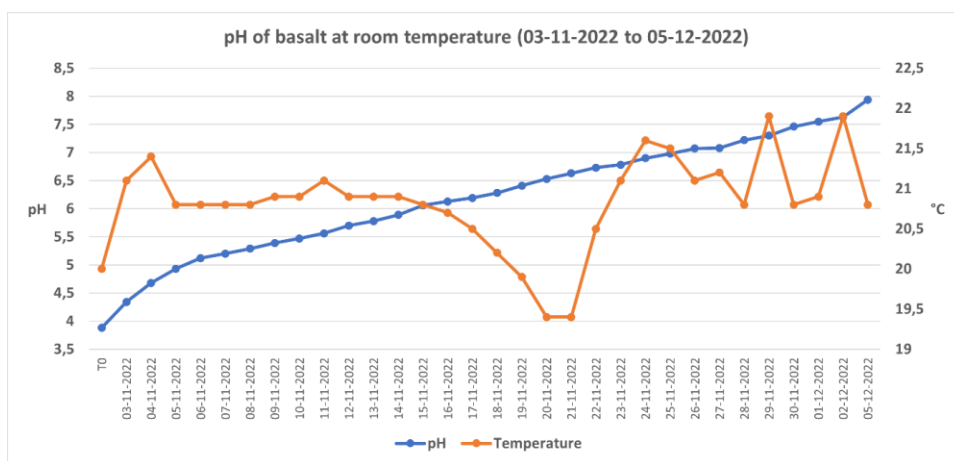
Figure A10.Diagram showing pH and temperature measurements of basalt at room-temperature.

Table A11. Daily pH and temperature measurements of Na-treated basalt at room-temperature.

Date	pH	°C
06-12-2022	8.91	22.1
07-12-2022	8.84	21.0
08-12-2022	8.82	21.9
09-12-2022	8.76	21.9
10-12-2022	8.82	21.2
11-12-2022	8.83	21.0
12-12-2022	8.83	20.8
13-12-2022	8.79	21.0
14-12-2022	8.77	20.9
15-12-2022	8.75	20.6
16-12-2022	8.79	20.4
17-12-2022	8.78	19.9
18-12-2022	8.79	20.0
19-12-2022	8.79	20.0
20-12-2022	8.77	20.5
21-12-2022	8.76	21.2
22-12-2022	8.76	20.9
23-12-2022	8.76	21.6
24-12-2022	8.78	20.6
25-12-2022	8.77	20.5
26-12-2022	8.80	20.6
27-12-2022	8.86	20.5
28-12-2022	8.81	20.5
29-12-2022	8.76	21.4
30-12-2022	8.80	20.8
31-12-2022	8.82	20.8
01-01-2023	8.86	20.8
02-01-2023	8.82	20.8
03-01-2023	8.81	20.8
04-01-2023	8.77	21.1
05-01-2023	8.79	20.9
06-01-2023	8.83	20.5
07-01-2023	8.81	20.6
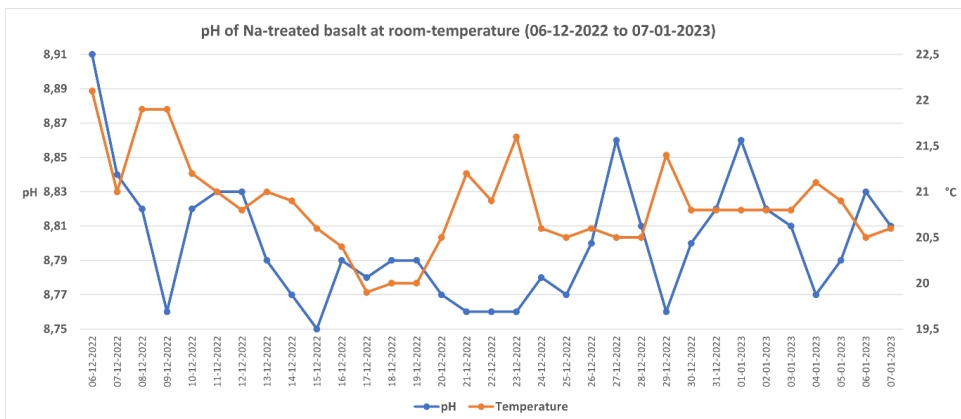
Figure A11. Diagram showing pH and temperature measurements of Na-treated basalt at room-temperature.

A2. Experiments at 50°C

Syenite

Table A12. Daily pH and temperature measurements of syenite at 50°C.

Date	pH	°C
06/12/2022 (T0)	3,79	20,4
07/12/2022	5,29	49,3
08/12/2022	5,36	49,7
09/12/2022	5,91	49,5
10/12/2022	6,12	39,8
11/12/2022	7,50	47,9
12/12/2022	7,94	47,3
13/12/2022	7,97	47,4
14/12/2022	8,00	47,7
15/12/2022	8,15	47,8
16/12/2022	8,15	45,7
17/12/2022	8,19	47,5
18/12/2022	8,19	47,9
19/12/2022	8,24	48,4
20/12/2022	8,30	41,8
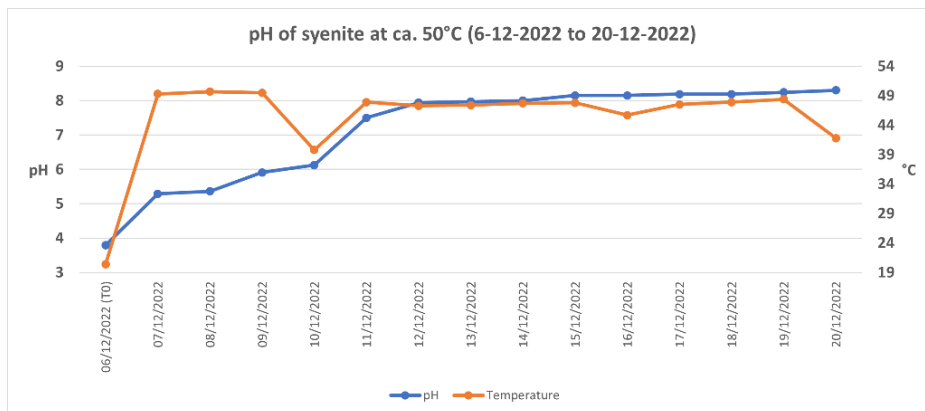
Figure A12. Diagram showing pH and temperature measurements of syenite at 50°C.

Table A13. Daily pH and temperature measurements of Na-treated syenite at 50°C.

Date	pH	°C
21/12/2022 (T0)	8,43	19,5
22/12/2022	8,84	47,8
23/12/2022	8,85	48,3
24/12/2022	8,89	47,9
25/12/2022	8,90	48,8
26/12/2022	8,91	48,6
27/12/2022	9,00	48,2
28/12/2022	8,90	47,8
29/12/2022	8,85	48,2
30/12/2022	8,85	48,1
31/12/2022	8,92	48,0
01/01/2023	8,95	48,3
02/01/2023	8,93	48,3
03/01/2023	9,01	48,1
04/01/2023	8,99	47,9
05/01/2023	8,99	48,0
06/01/2023	9,02	47,5

| 07/01/2023 | 9,01 | 48,0 |
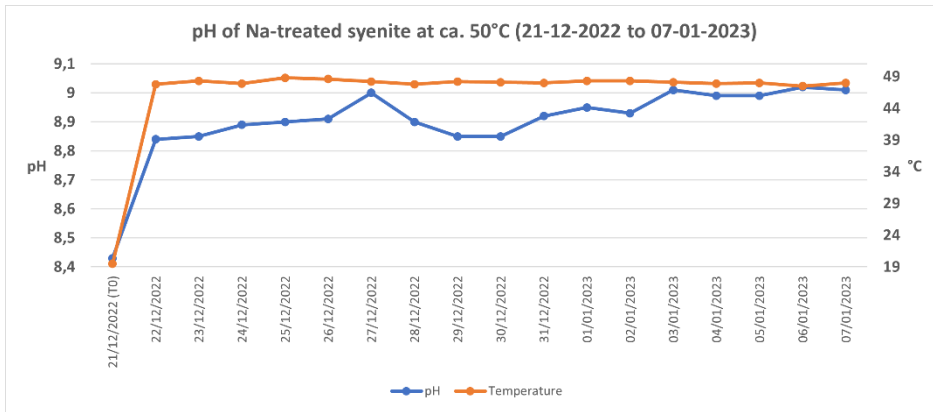
Figure A13. Diagram showing pH and temperature measurements of Na-treated syenite at 50°C.

Carbonatite

Table A14. pH and temperature measurements of carbonatite at 50°C.

Date	pH	°C
06/12/2022 (T0)	3,64	20,2
07/12/2022	6,00	49,4
08/12/2022	6,09	49,8
09/12/2022	6,34	50,1
10/12/2022	6,60	41,2
11/12/2022	7,31	50,3
12/12/2022	7,51	49,5
13/12/2022	7,59	49,6
14/12/2022	7,75	50,4
15/12/2022	7,78	50,1
16/12/2022	7,84	48,0
17/12/2022	7,90	50,3
18/12/2022	7,88	50,8
19/12/2022	7,88	50,1
20/12/2022	8,00	43,4
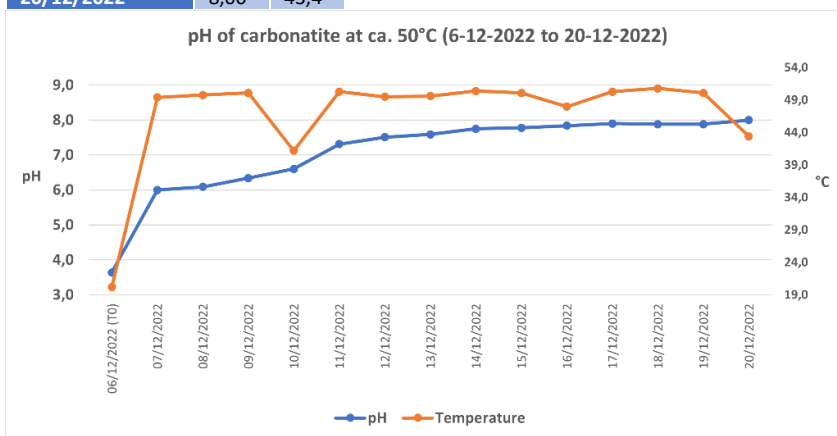
Figure A14. Diagram showing pH and temperature measurements of Na-treated carbonatite at room-temperature.

Table A15. pH and temperature measurements of Na-treated carbonatite at 50°C.

Date	pH	°C
21/12/2022 (T0)	8,33	19,7
22/12/2022	8,45	49,3
23/12/2022	8,47	50,6
24/12/2022	8,55	49,8
25/12/2022	8,61	50,7
26/12/2022	8,73	50,0
27/12/2022	8,65	50,1
28/12/2022	8,57	50,0
29/12/2022	8,58	50,0
30/12/2022	8,68	50,0
31/12/2022	8,68	50,0
01/01/2023	8,77	50,1
02/01/2023	8,77	50,1
03/01/2023	8,75	50,0
04/01/2023	8,78	49,9
05/01/2023	8,79	50,0
06/01/2023	8,79	50,1
07/01/2023	8,80	50,1
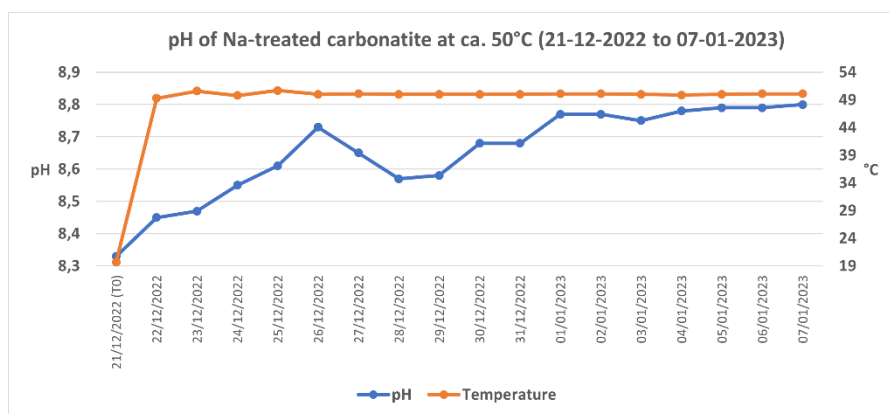
Figure A15. Diagram showing pH and temperature measurements of Na-treated carbonatite at 50°C.

Gabbro

Table A16. Daily pH and temperature measurements of gabbro at 50°C.

Date	pH	°C
06/12/2022 (T0)	3,65	20,2
07/12/2022	4,89	49,4
08/12/2022	5,33	49,7
09/12/2022	6,29	48,0
10/12/2022	8,10	44,7
11/12/2022	8,23	43,2
12/12/2022	8,27	47,9
13/12/2022	8,42	46,8
14/12/2022	8,29	46,6
15/12/2022	8,26	48,3
16/12/2022	8,24	45,0
17/12/2022	8,31	47,6
18/12/2022	8,30	47,6
19/12/2022	8,28	48,2
20/12/2022	8,28	48,7
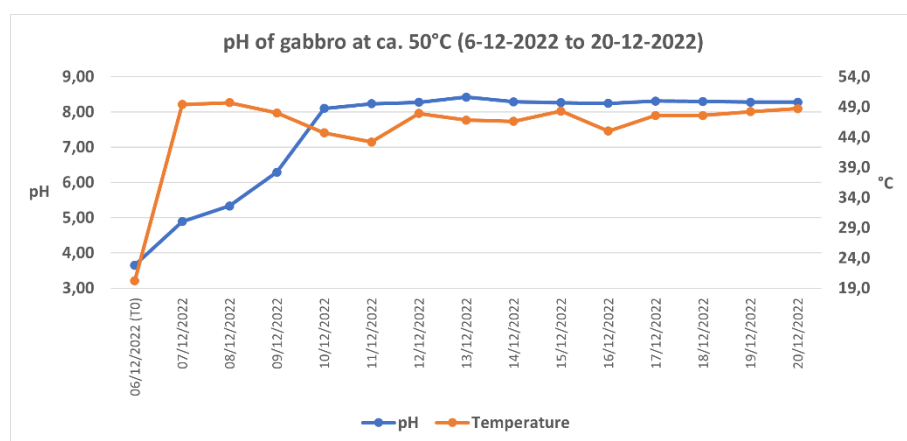
Figure A16. Diagram showing pH and temperature measurements of gabbro at 50°C.

Table A17. Daily pH and temperature measurements of Na-treated gabbro at 50°C.

Date	pH	°C
21/12/2022 (T0)	8,38	19,5
22/12/2022	8,89	30,3
23/12/2022	8,8	48,1
24/12/2022	8,85	48,4
25/12/2022	8,82	48,0
26/12/2022	8,89	48,0
27/12/2022	8,95	48,8
28/12/2022	8,87	48,3
29/12/2022	8,85	48,4
30/12/2022	8,85	48,0
31/12/2022	8,92	47,8
01/01/2023	8,9	49,1
02/01/2023	8,88	48,5
03/01/2023	8,9	48,2
04/01/2023	8,88	48,7
05/01/2023	8,88	47,6
06/01/2023	8,92	48,0
07/01/2023	8,88	47,8

Figure A17. Diagram showing pH and temperature measurements of Na-treated gabbro at 50°C.

Granite

Table A18. Daily pH and temperature measurements of granite at 50°C.

Date	pH	°C
06/12/2022 (T0)	3,68	20,3
07/12/2022	5,05	50,1
08/12/2022	5,08	50,0
09/12/2022	5,82	50,1
10/12/2022	6,13	46,3
11/12/2022	7,74	44,6
12/12/2022	7,85	49,6
13/12/2022	8,20	48,5
14/12/2022	8,14	48,2
15/12/2022	8,17	49,8
16/12/2022	8,20	46,9
17/12/2022	8,25	49,5
18/12/2022	8,27	50,0
19/12/2022	8,24	49,7
20/12/2022	8,25	50,4

Figure A18. Diagram showing pH and temperature measurements of granite at 50°C.

Table A18. Daily pH and temperature measurements of Na-treated gabbro at 50°C.

Date	pH	°C
21/12/2022 (T0)	8,08	19,6
22/12/2022	8,86	40,5
23/12/2022	8,89	50,2
24/12/2022	8,92	50,3
25/12/2022	8,90	49,7
26/12/2022	8,90	49,7
27/12/2022	8,99	50,3
28/12/2022	8,88	50,0
29/12/2022	8,88	50,0
30/12/2022	8,93	49,9
31/12/2022	8,92	49,6
01/01/2023	8,96	50,9
02/01/2023	8,98	50,2
03/01/2023	8,98	50,0
04/01/2023	8,97	50,3
05/01/2023	8,97	49,8
06/01/2023	8,98	50,0
07/01/2023	8,98	49,7

Figure A18. Diagram showing pH and temperature measurements of Na-treated gabbro at 50°C.

Dolerite

Table A19. Daily pH and temperature measurements of dolerite at 50°C.

Date	pH	°C
06/12/2022 (T0)	3,73	20,6
07/12/2022	4,90	50,0
08/12/2022	5,13	50,0
09/12/2022	5,62	49,8
10/12/2022	6,12	43,9
11/12/2022	7,06	49,8
12/12/2022	7,50	50,3
13/12/2022	7,81	49,8
14/12/2022	7,89	49,6
15/12/2022	8,01	50,0
16/12/2022	8,05	49,9
17/12/2022	8,10	49,9
18/12/2022	8,09	44,2
19/12/2022	8,15	49,4
20/12/2022	8,14	50,5
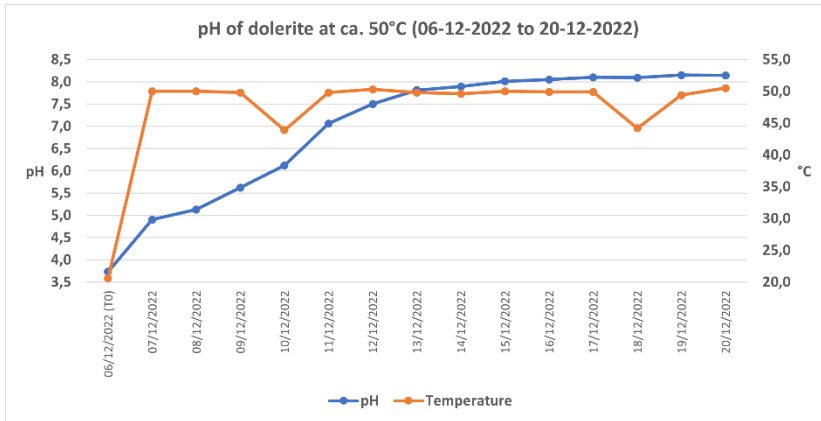
Figure A19. Diagram showing pH and temperature measurements of dolerite at 50°C.

Table A20. Daily pH and temperature measurements of Na-treated dolerite at 50°C.

Date	pH	°C
21/12/2022 (T0)	7,84	19,8
22/12/2022	8,81	41,6
23/12/2022	8,7	49,9
24/12/2022	8,78	49,6
25/12/2022	8,8	49,6
26/12/2022	8,84	49,6
27/12/2022	8,84	49,5
28/12/2022	8,77	49,9
29/12/2022	8,76	49,8
30/12/2022	8,82	49,2
31/12/2022	8,83	49,8
01/01/2023	8,86	50,0
02/01/2023	8,87	49,8
03/01/2023	8,84	48,5
04/01/2023	8,83	49,1
05/01/2023	8,87	47,8
06/01/2023	8,85	48,4
07/01/2023	8,85	49,0
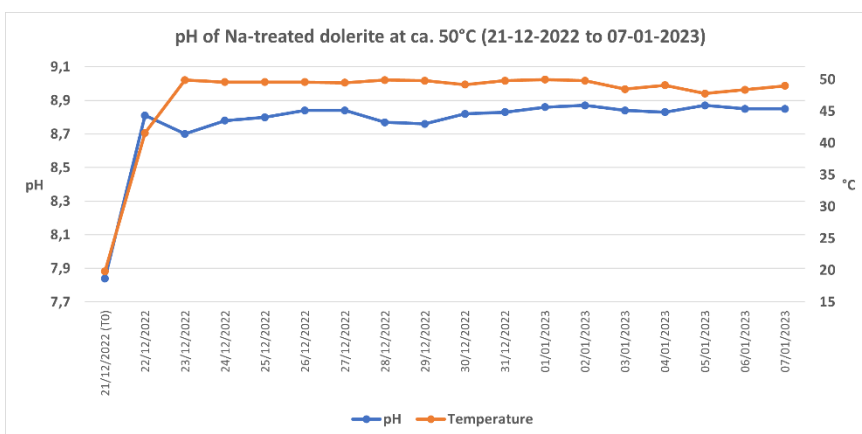
Figure A20. Diagram showing pH and temperature measurements of Na-treated dolerite at 50°C.

Basalt

Table A21. Daily pH and temperature measurements of basalt at 50°C.

Date	pH	°C
06/12/2022 (T0)	3,63	20,1
07/12/2022	4,40	49,7
08/12/2022	4,49	50,1
09/12/2022	5,04	49,7
10/12/2022	5,91	49,9
11/12/2022	6,68	49,7
12/12/2022	7,50	49,1
13/12/2022	7,78	49,2
14/12/2022	7,88	49,2
15/12/2022	7,98	48,9
16/12/2022	8,00	48,5
17/12/2022	8,05	48,2
18/12/2022	8,09	42,3
19/12/2022	8,04	48,0
20/12/2022	8,03	48,9
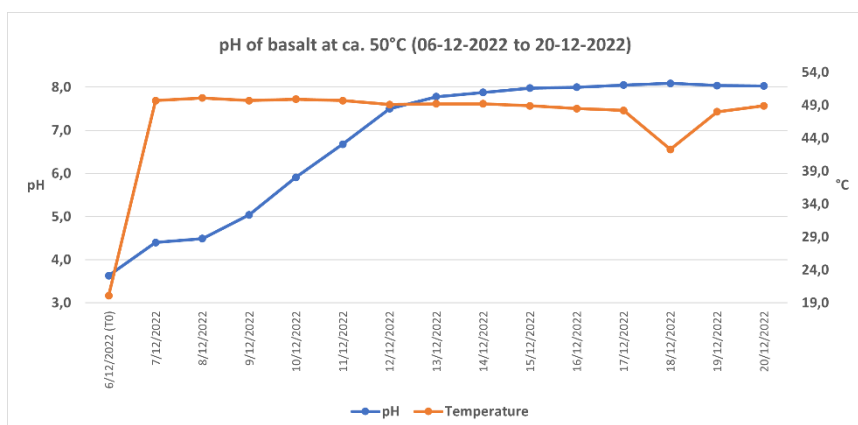
Figure A21. Diagram showing pH and temperature measurements of basalt at 50°C.

Table A22. Daily pH and temperature measurements of Na-treated basalt at 50°C.

Date	pH	°C
21/12/2022 (T0)	8,28	19,7
22/12/2022	8,91	40,2
23/12/2022	8,87	48,6
24/12/2022	8,89	47,9
25/12/2022	8,89	48,2
26/12/2022	8,94	48,2
27/12/2022	8,96	48,4
28/12/2022	8,93	48,5
29/12/2022	8,88	48,5
30/12/2022	8,94	48,2
31/12/2022	9,01	48,1
01/01/2023	8,94	48,4
02/01/2023	8,93	48,4
03/01/2023	8,97	47,0
04/01/2023	8,92	47,4
05/01/2023	8,95	46,3
06/01/2023	8,94	47,0
07/01/2023	8,95	47,6
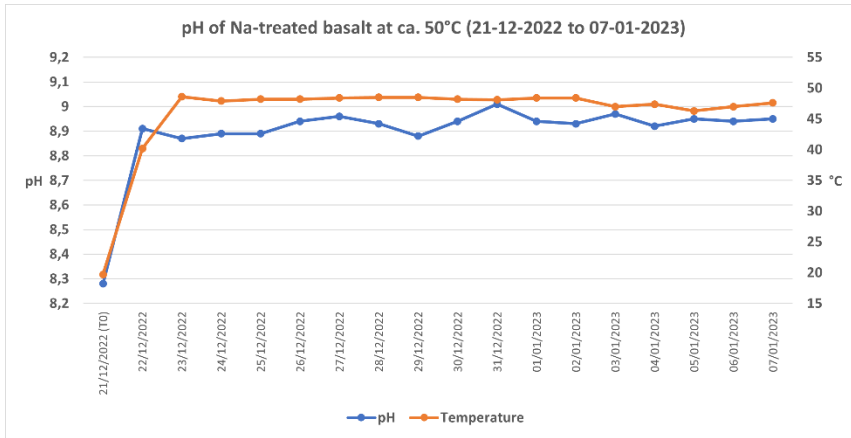
Figure A22. Diagram showing pH and temperature measurements of Na-treated basalt at 50°C.

APPENDIX B: XRD

B1. Room temperature

Syenite

Table B1. Identified mineral phases within syenite in room temperature experiments.

Ref. code	Chemical formula	Score	Compound name	[°2Th]	Scale Factor	%
98-000-2930	$Na(AlSi_2O_6) H_2O$	64	Analcime	0.008	0.836	40.4
98-020-1600	$K(AlSi_3O_8)$	46	Microcline	0.007	0.278	44.4
98-016-1975	$NaFe^{3+} (Si_2O_6)$	46	Aegirine	0.016	0.266	15.2
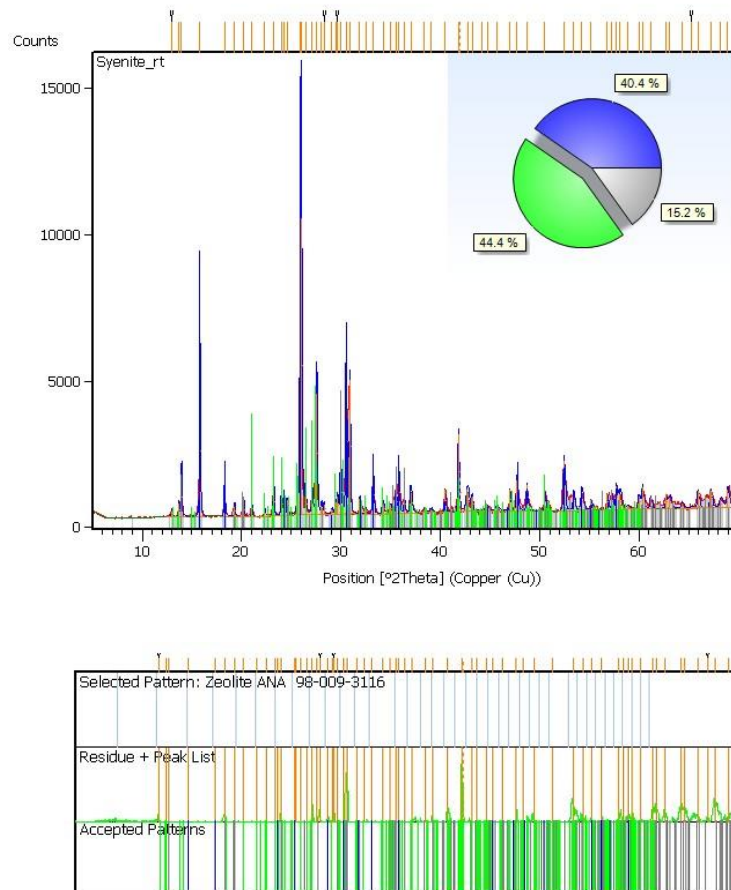
Figure B1. XRD peaks and percentages of defined mineral phases within syenite at room-temperature.

Table B2. Identified mineral phases within Na-treated syenite in room temperature experiments.

Ref. code	Chemical formula	Score	Compound name	[°2Th]	Scale Factor	%
98-000-2930	$Na(AlSi_2O_6) H_2O$	65	Analcime	0.044	0.863	40.4
98-020-1600	$K(AlSi_3O_8)$	48	Microcline	0.030	0.321	44.4
98-016-1975	$NaFe^{3+} (Si_2O_6)$	45	Aegirine	0.092	0.205	15.2
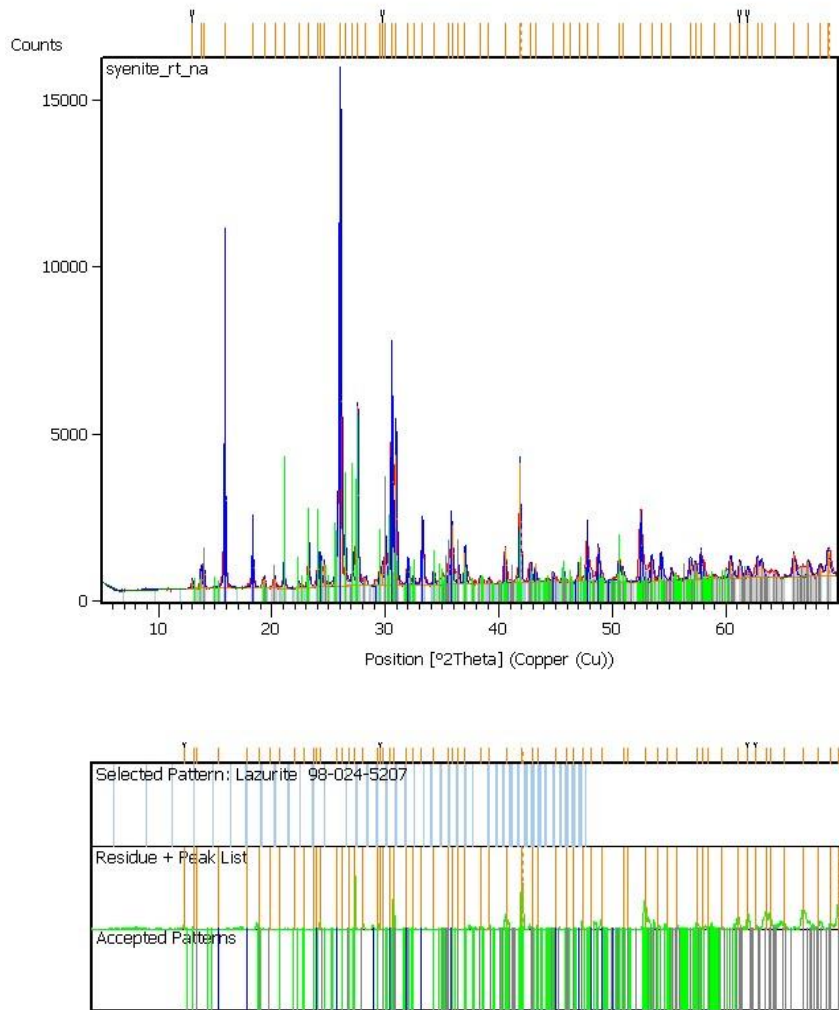
Figure B2. XRD peaks and percentages of defined mineral phases within Na-treated syenite at room-temperature.

Carbonatite

Table B3. Identified mineral phases within carbonatite in room-temperature experiments.

Ref. code	Chemical formula	Score	Compound name	[°2Th]	Scale Factor	%
98-003-7241	$Ca\ CO_3$	80	Calcite	0.010	0.643	83
98-024-0658	$Ca_5\ (P_6O_4)_3\ F$	33	Apatite	0.084	0.025	10
98-009-3948	$Fe^{3+}\ O\ (OH)$	31	Lepidocrocite	0.025	0.023	3
98-024-5057	$Fe^{3+}\ O\ (OH)$	29	Goethite	0.018	0.025	4
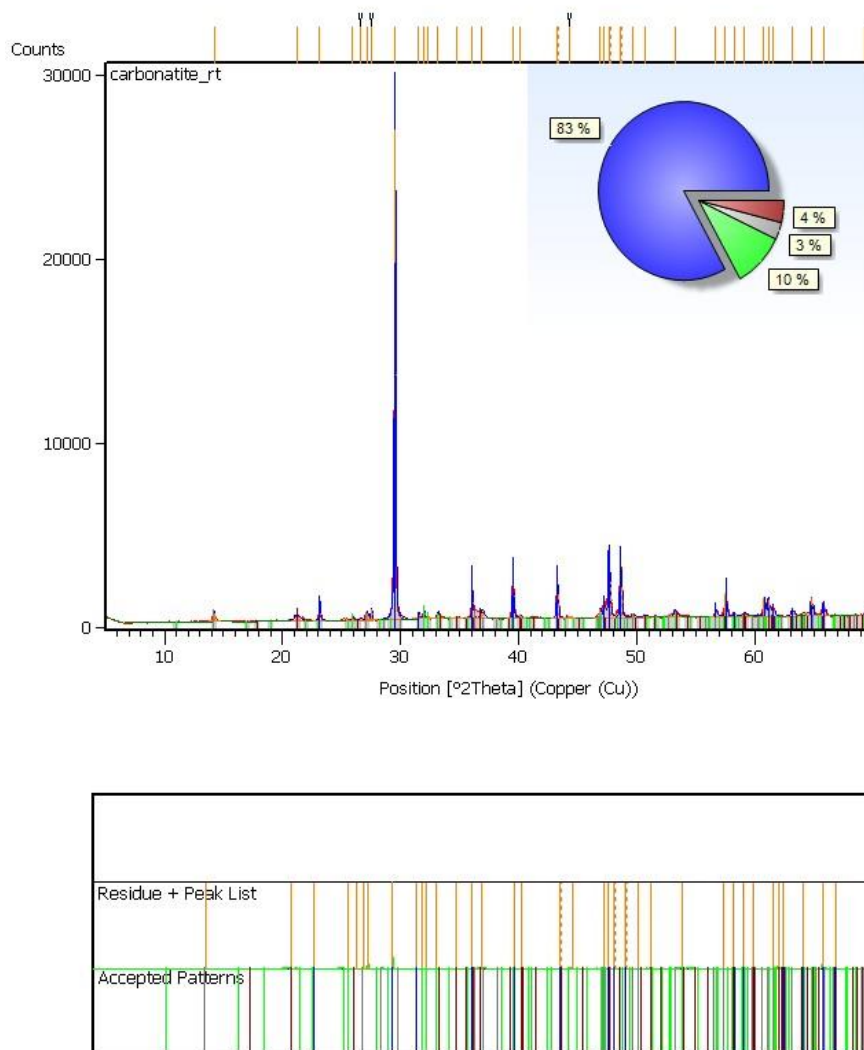
Figure B3. XRD peaks and percentages of defined mineral phases within carbonatite at room-temperature.

Table B4. Identified mineral phases within Na-treated carbonatite in room-temperature experiments.

Ref. code	Chem. formula	Score	Compound name	[°2Th]	Scale Factor	%
98-003-7241	$Ca\ CO_3$	80	Calcite	-0.014	0.731	81.8
98-024-0657	$Ca_5 (P_6O_4)_3\ F$	33	Apatite	0.024	0.033	11.1
98-009-3948	$Fe^{3+}\ O\ (OH)$	31	Lepidocrocite	-0.008	0.028	3
98-016-3341	$Fe^{3+}\ O\ (OH)$	29	Goethite	-0.019	0.029	4
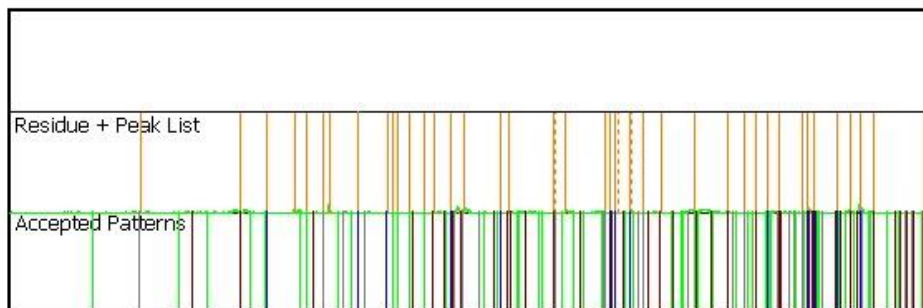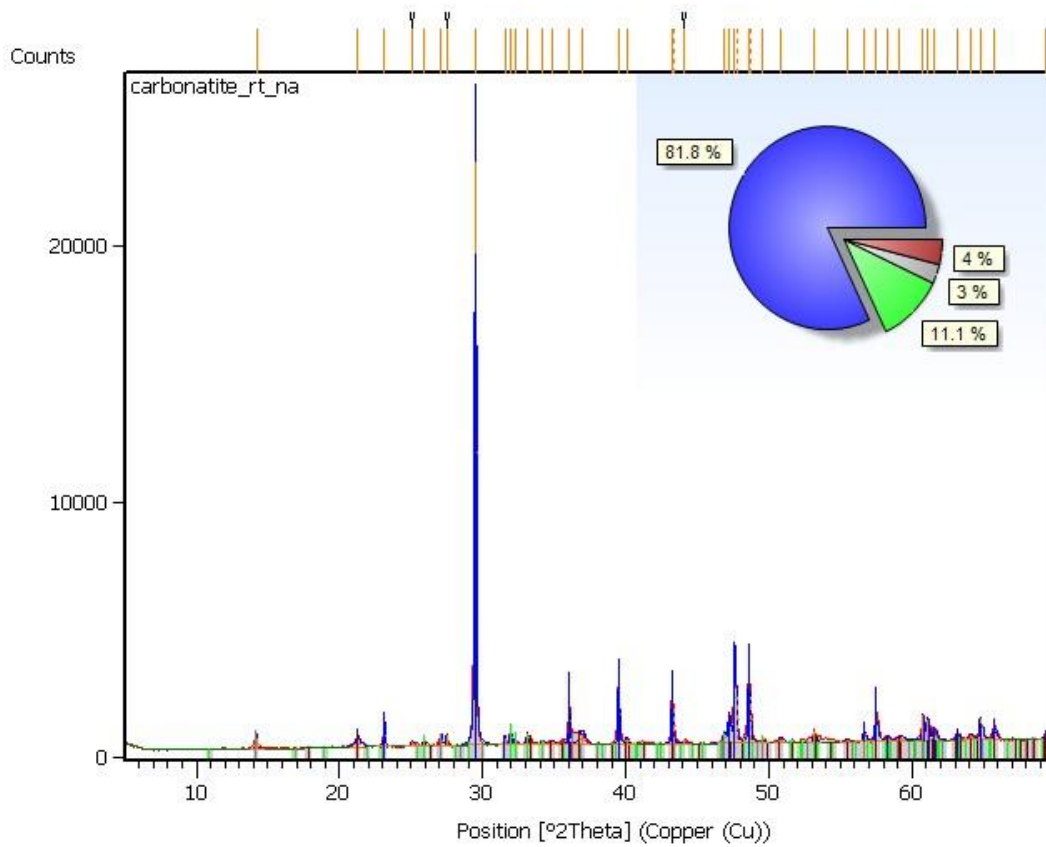
Figure B4. XRD peaks and percentages of defined mineral phases within Na-treated carbonatite at room-temperature.

Gabbro

Table B5. Identified mineral phases within gabbro in room-temperature experiments.

Ref. code	Chemical formula	Score	Compound name	[°2Th]	Scale Factor	%
98-007-9835	$Ca_2 (Mg_4Al) (Si_7Al) O_{22} (OH)_2$	56	Magnesio-hornblende	0.051	0.278	25.3
98-003-4916	$(Ca_{0,25},Na_{0,75}) (AlSi_3O_8)_2$	53	Albite low, calcian	0.051	0.516	57.6
98-007-9634	SiO_2	47	Quartz low	0.082	0.482	10.1
98-004-0641	$K (Mg,Fe,Ti)_3 AlSi_3O_{10} (OH)_2$	30	Biotite (Ti-rich)	-0.008	0.199	7.1
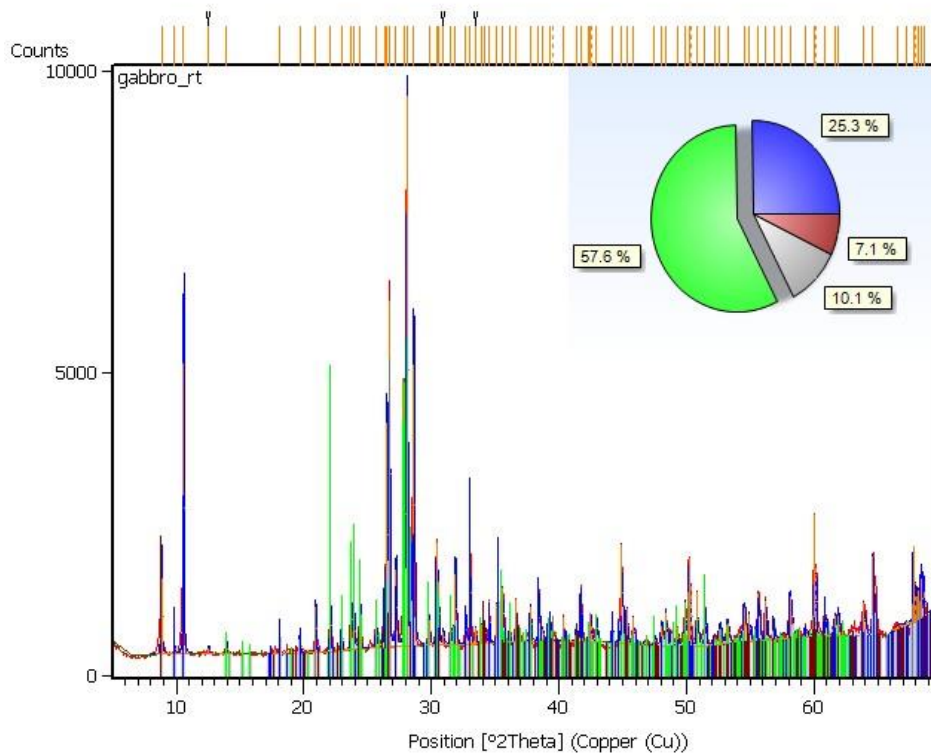
Figure B5. XRD peaks and percentages of defined mineral phases within gabbro at room-temperature.

Table B6. Identified mineral phases within Na-treated gabbro in room-temperature experiments.

Ref. code	Chemical formula	Score	Compound name	[°2Th]	Scale Factor	%
98-007-9835	$Ca_2 (Mg_4Al) (Si_7Al) O_{22} (OH)_2$	55	Magnesio-hornblende	0.050	0.365	28
98-003-4916	$(Ca_{0,25}, Na_{0,75}) (AlSi_3O_8)_2$	52	Albite low, calcian	0.049	0.565	53
98-020-0722	SiO_2	46	Quartz low	-0.076	0.672	12
98-004-0637	$K (Mg,Fe,Ti)_3 AlSi_3O_{10} (OH)_2$	19	Biotite (Ti-rich)	0.018	0.171	7
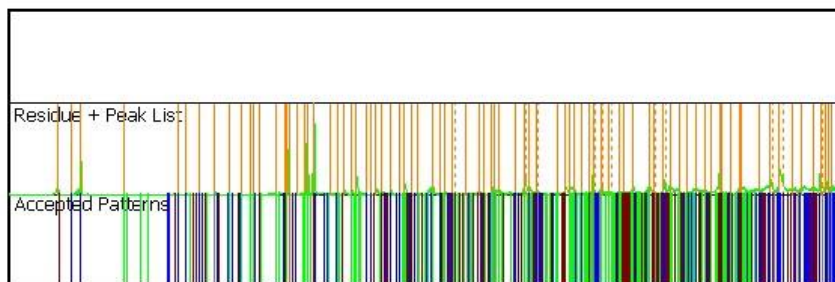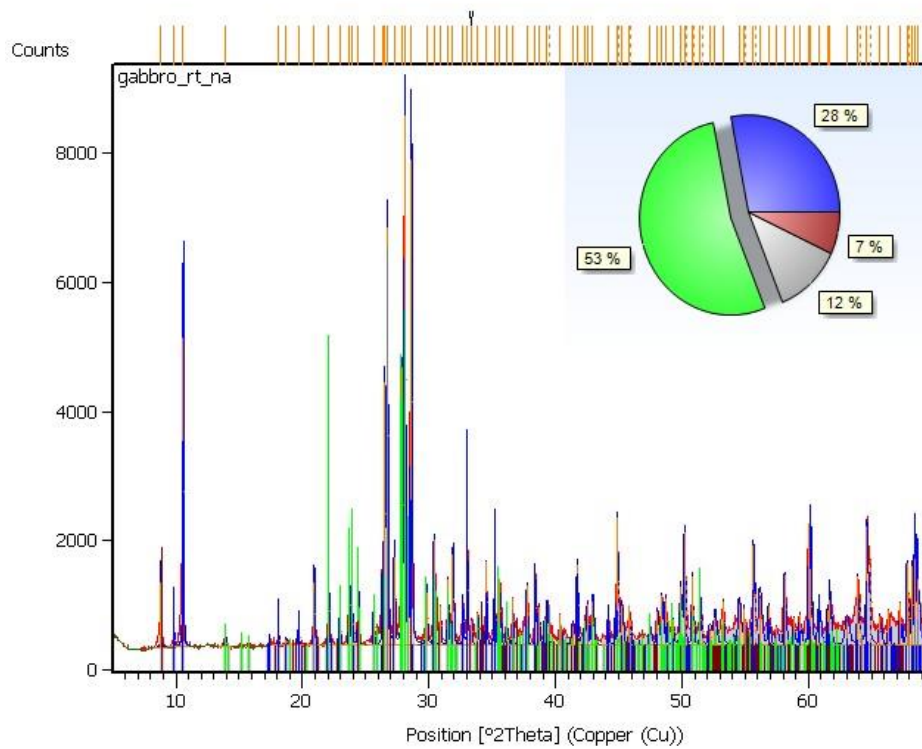
Figure B6. XRD peaks and percentages of defined mineral phases within Na-treated gabbro at room-temperature.

Granite

Table B7. Identified mineral phases within granite in room-temperature experiments.

Ref. code	Chemical formula	Score	Compound name	[°2Th]	Scale Factor	%
98-020-1353	SiO_2	61	Quartz	-0.032	0.898	35
98-003-4916	$Na\,(AlSi_3O_8)$	48	Albite	0.024	0.167	34
98-008-9811	$K\,Fe^{2+}_2\,Al\,(Al_2Si_2O_{10})(OH)_2$	41	Siderophyllite	0.094	0.216	7
98-003-4790	$K\,(AlSi_3O_8)$	30	Microcline	0.049	0.119	24
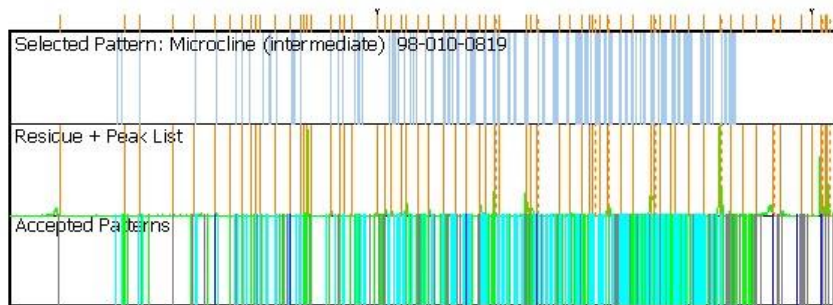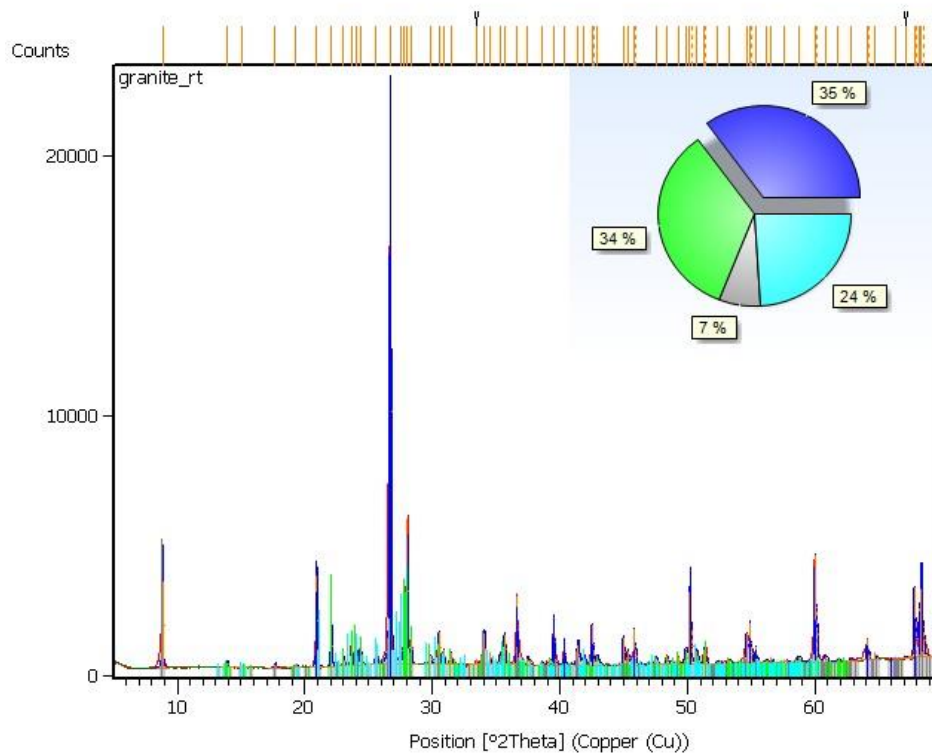
Figure B7. XRD peaks and percentages of defined mineral phases within granite at room-temperature.

Table B8. Identified mineral phases within Na-treated granite in room-temperature experiments.

Ref. code	Chemical formula	Score	Compound name	[°2Th]	Scale Factor	%
98-007-9634	SiO_2	61	Quartz	0.113	0.877	36
98-003-4916	$Na\,(AlSi_3O_8)$	48	Albite	0.052	0.124	26
98-008-9813	$K\,Fe^{2+}_2\,Al\,(Al_2Si_2O_{10})(OH)_2$	41	Siderophyllite	0.08	0.103	4
98-003-8135	$K\,(AlSi_3O_8)$	30	Microcline	-0.034	0.141	34
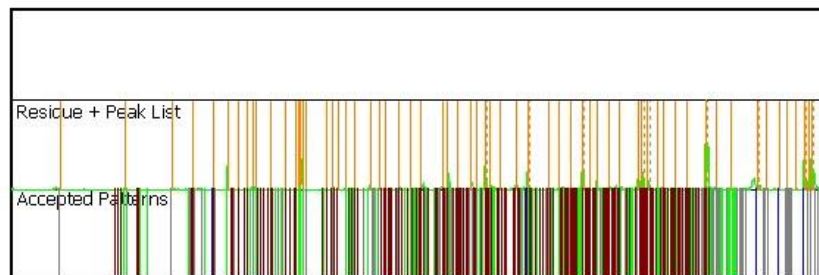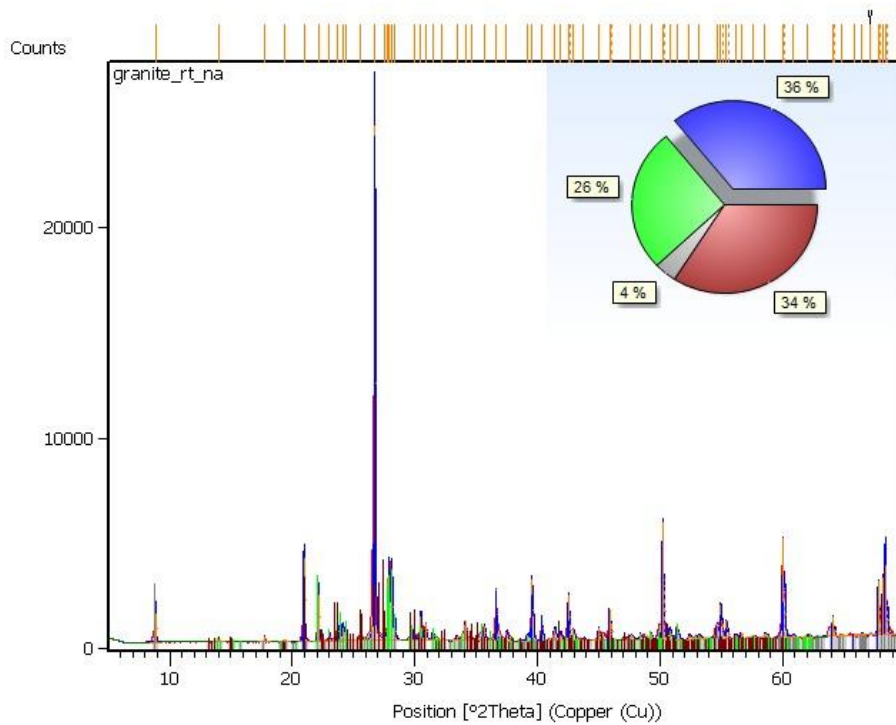
Figure B8. XRD peaks and percentages of defined mineral phases within Na-treated granite at room-temperature.

Dolerite

Table B9. Identified mineral phases within dolerite in room-temperature experiments.

Ref. code	Chemical formula	Score	Compound name	[°2Th]	Scale Factor	%
98-003-4916	$(Ca_{0.25},Na_{0.75})(AlSi_3O_8)_2$	59	Albite, low, calcian	0.029	0.360	82,8
98-016-2609	$Si\ O_2$	35	Quartz, low	-0.055	0.076	3
98-002-9209	$Fe^{2+}\ TiO_3$	39	Ilmenite	-0.013	0.078	3
98-006-6678	$K\ Fe^{2+}_2\ Al\ (Al_2Si_2O_{10})(OH)_2$	21	Siderophyllite	0.037	0.060	3
98-016-4813	$Fe^{2+}\ Fe^{3+}_2\ O_4$	22	Magnetite	-0.024	0.030	5,1
98-001-6732	$Mg_5\ Al\ (AlSi_3O_{10})\ (OH)_8$	3	Clinochlore	0.079	0.028	3
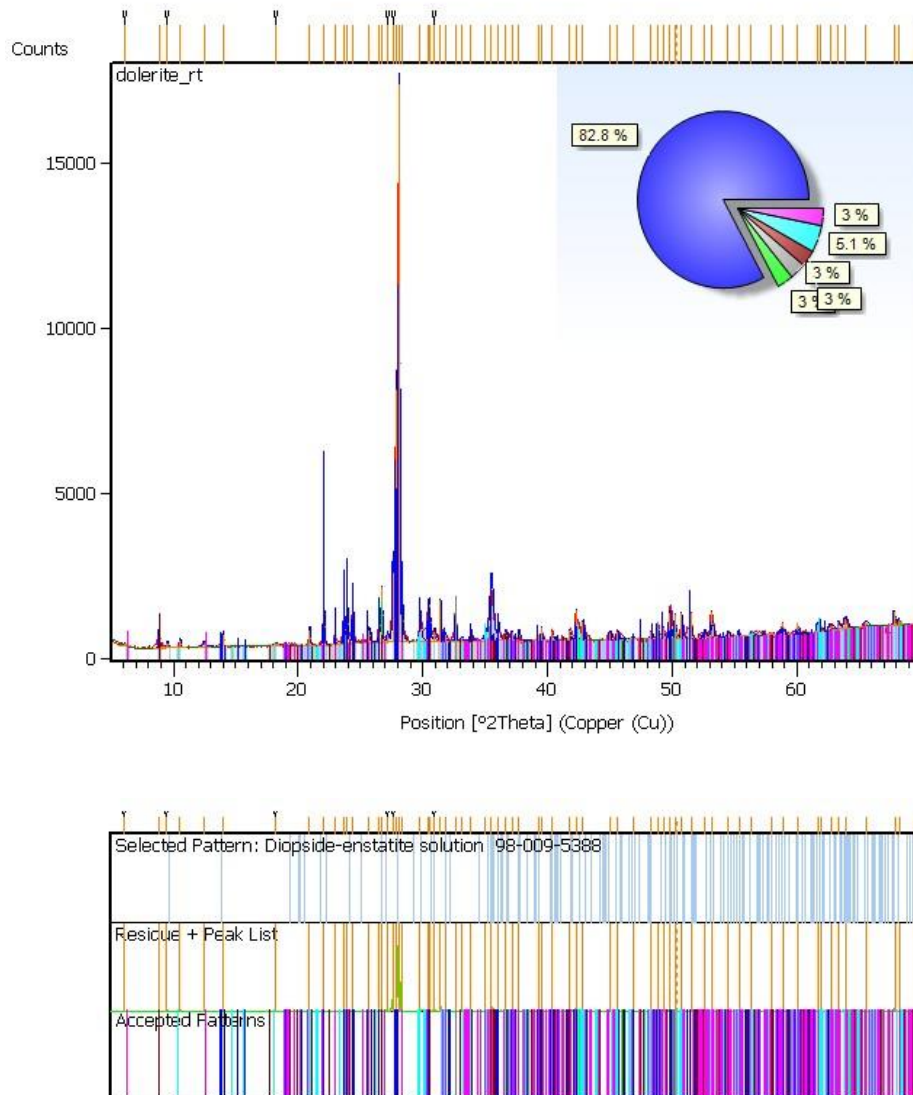
Figure B9. XRD peaks and percentages of defined mineral phases within dolerite at room temperature.

Table B10. Identified mineral phases within Na-treated dolerite in room-temperature experiments.

Ref. code	Chemical formula	Score	Compound name	[°2Th]	Scale Factor	%
98-003-4916	$(Ca_{0.25},Na_{0.75})\,(AlSi_3O_8)_2$	60	Albite, low, calcian	0.028	0.360	81.0
98-020-1353	$Si\,O_2$	43	Quartz, low	0.036	0.076	6
98-002-3730	$Fe^{2+}\,TiO_3$	38	Ilmenite	-0.013	0.049	2
98-006-6678	$K\,Fe^{2+}_2\,Al\,(Al_2Si_2O_{10})(OH)_2$	22	Siderophyllite	0.037	-0.004	3
98-016-4813	$Fe^{2+}\,Fe^{3+}_2\,O_4$	25	Magnetite	-0.024	0.039	5
98-001-6732	$Mg_5\,Al\,(AlSi_3O_{10})\,(OH)_8$	3	Clinochlore	0.079	0.076	3
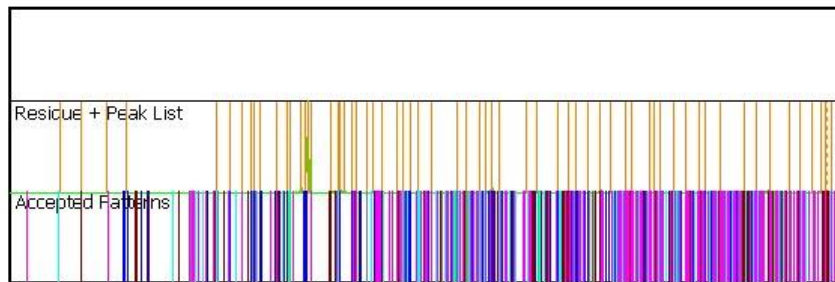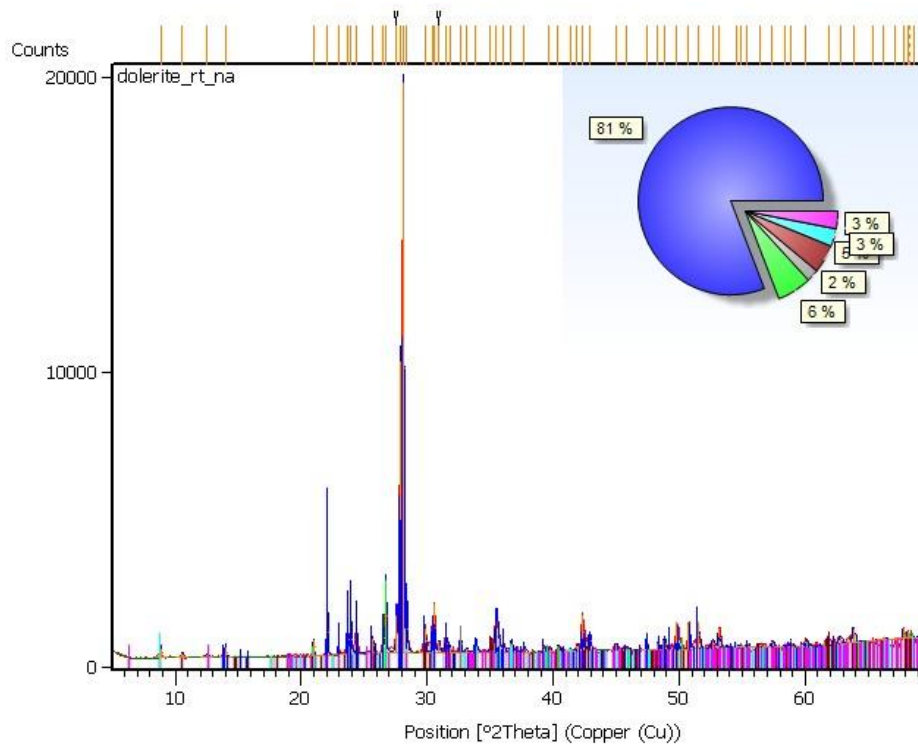
Figure B10. XRD peaks and percentages of defined mineral phases within Na-treated dolerite at room-temperature.

Basalt

Table B11. Identified mineral phases within basalt in room-temperature experiments.

Ref. code	Chemical formula	Score	Compound name	[°2Th]	Scale Factor	%
98-008-0685	$(Ca_{0.85} Al_{0.15}) (Mg\ Si_2O_6)$	65	Diopside, aluminian	-0.022	1.018	38
98-010-0235	$(Ca_{0.65} Na_{0.35}) (Al_2\ Si_2O_8)$	64	Anorthite, sodian	0.035	0.869	62
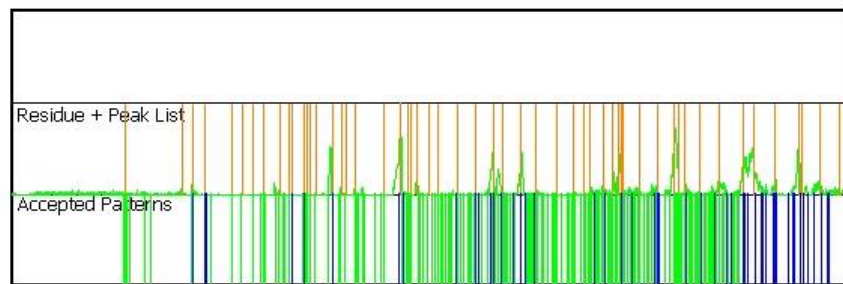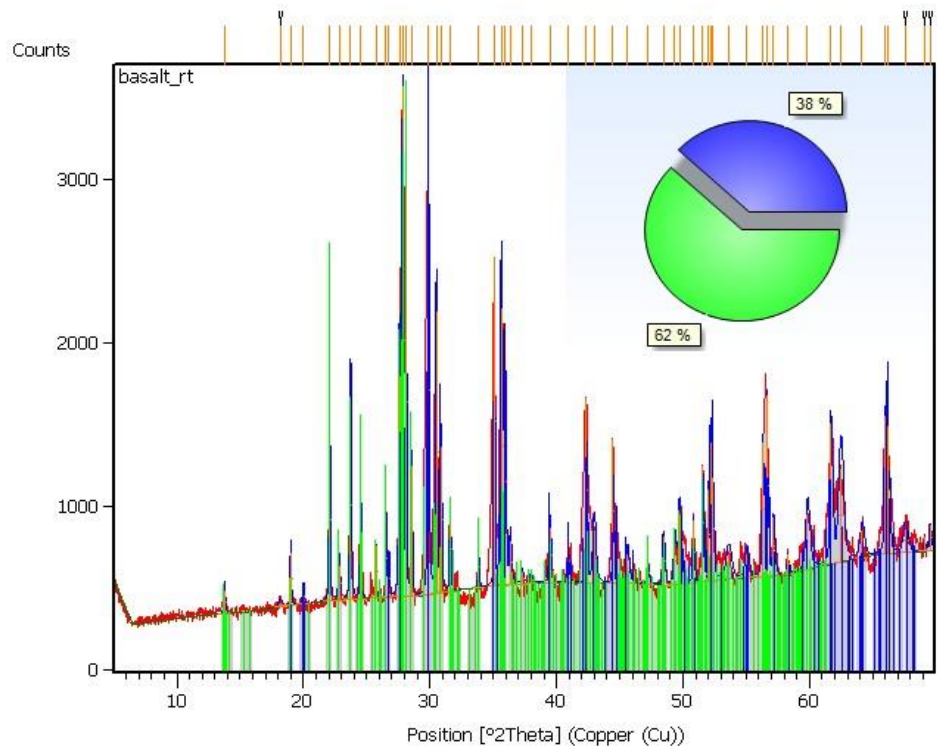
Figure B11. XRD peaks and percentages of defined mineral phases within basalt at room-temperature.

Table B12. Identified mineral phases within Na-treated basalt in room-temperature experiments.

Ref. code	Chemical formula	Score	Compound name	[°2Th]	Scale Factor	%
98-008-0685	$(Ca_{0.85} Al_{0.15}) (Mg\ Si_2O_6)$	66	Diopside, aluminian	-0.027	1.203	38
98-010-0232	$(Ca_{0.65} Na_{0.35}) (Al_2\ Si_2O_8)$	67	Anorthite, sodian	0.035	0.981	62
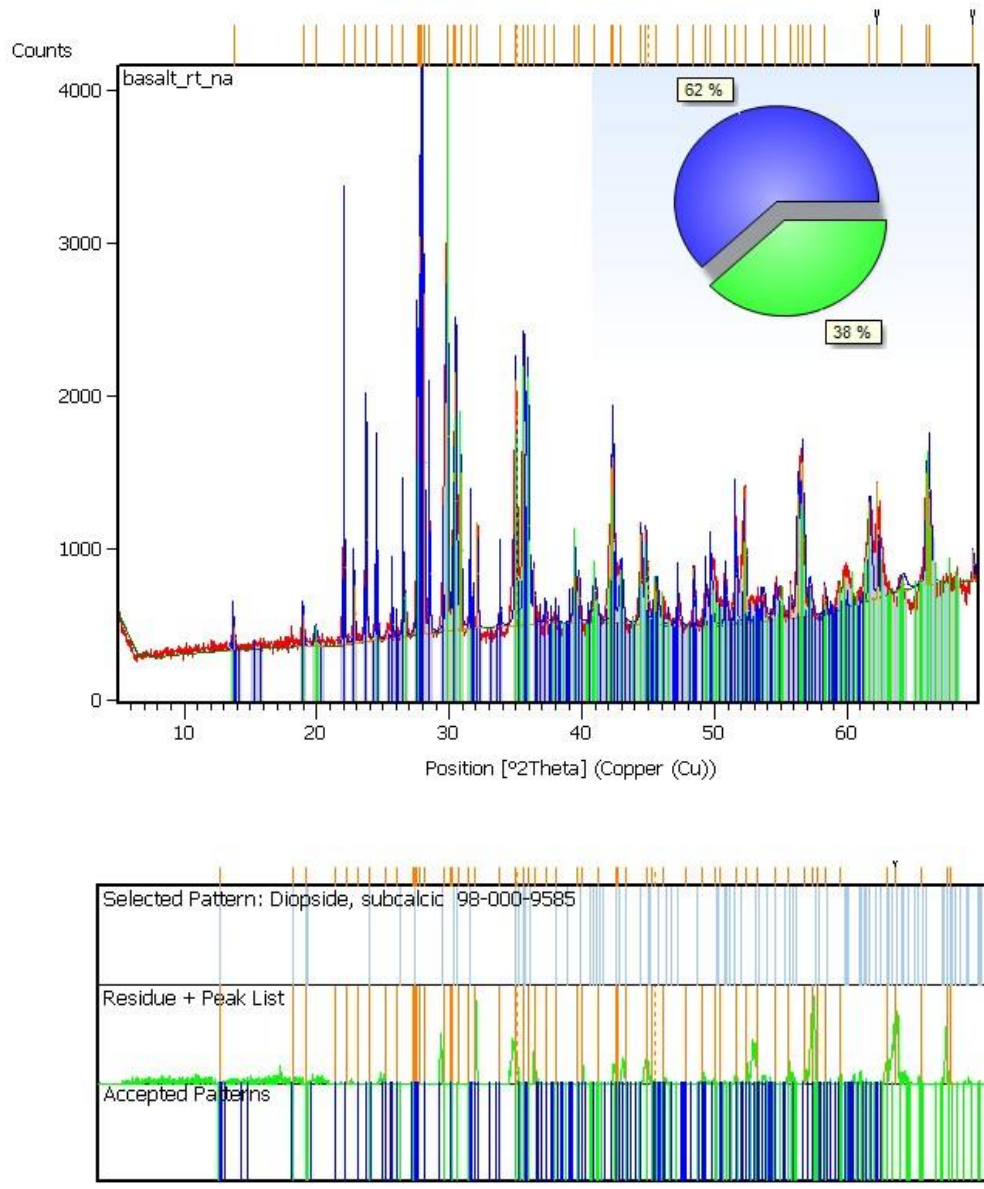
Figure B12. XRD peaks and percentages of defined mineral phases within Na-treated basalt at room-temperature.

B2. Experiments at 50°C

Syenite

Table B13. Identified mineral phases within syenite in 50°C experiments.

Ref. code	Chemical formula	Score	Compound name	[°2Th]	Scale Factor	%
98-003-4876	$Na(AlSi_2O_6) H_2O$	61	Analcime	0.027	0.770	49
98-015-8082	$K(AlSi_3O_8)$	48	Microcline	0.055	0.212	39
98-003-4896	$NaFe^{3+} (Si_2O_6)$	45	Aegirine	0.041	0.274	12
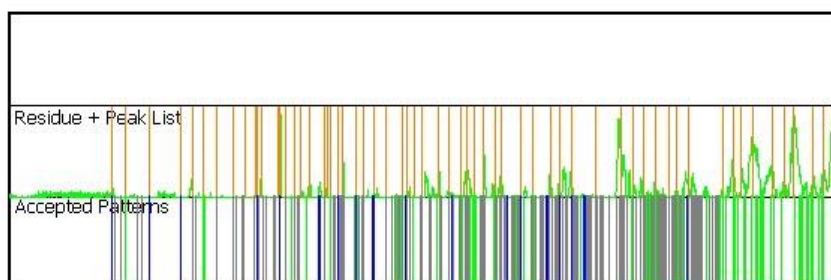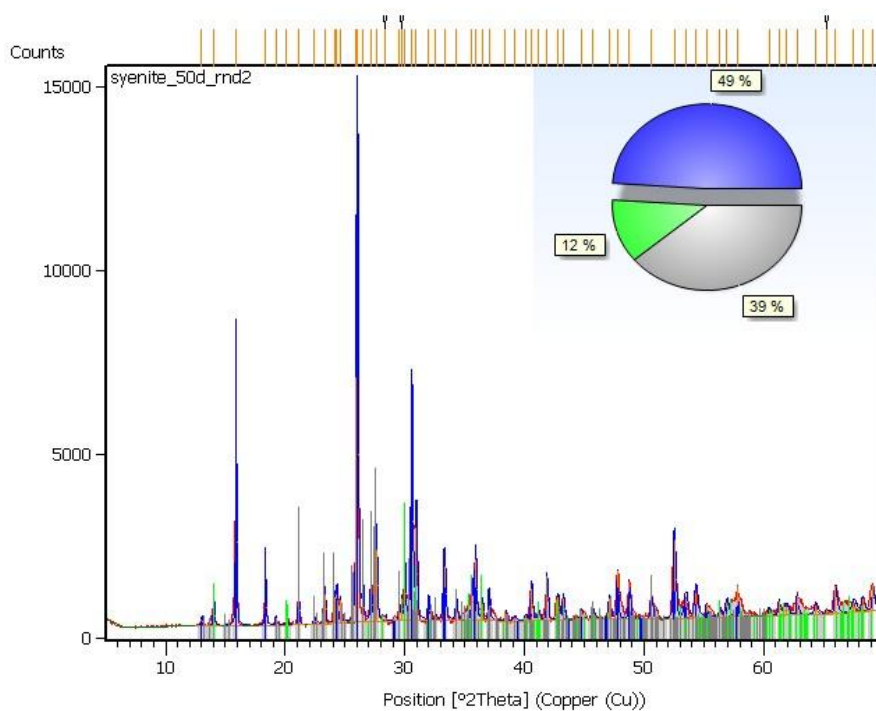
Figure B13. XRD peaks and percentages of defined mineral phases within syenite at 50 °C.

Table B14. Identified mineral phases within Na-treated syenite in 50°C experiments

Ref. code	Chemical formula	Score	Compound name	[°2Th]	Scale Factor	%
98-000-9357	$Na(AlSi_2O_6)\ H_2O$	65	Analcime	0.034	0.754	48
98-003-4896	$K(AlSi_3O_8)$	45	Microcline	-0.006	0.189	40
98-015-7733	$NaFe^{3+}\ (Si_2O_6)$	44	Aegirine	0.088	0.153	12
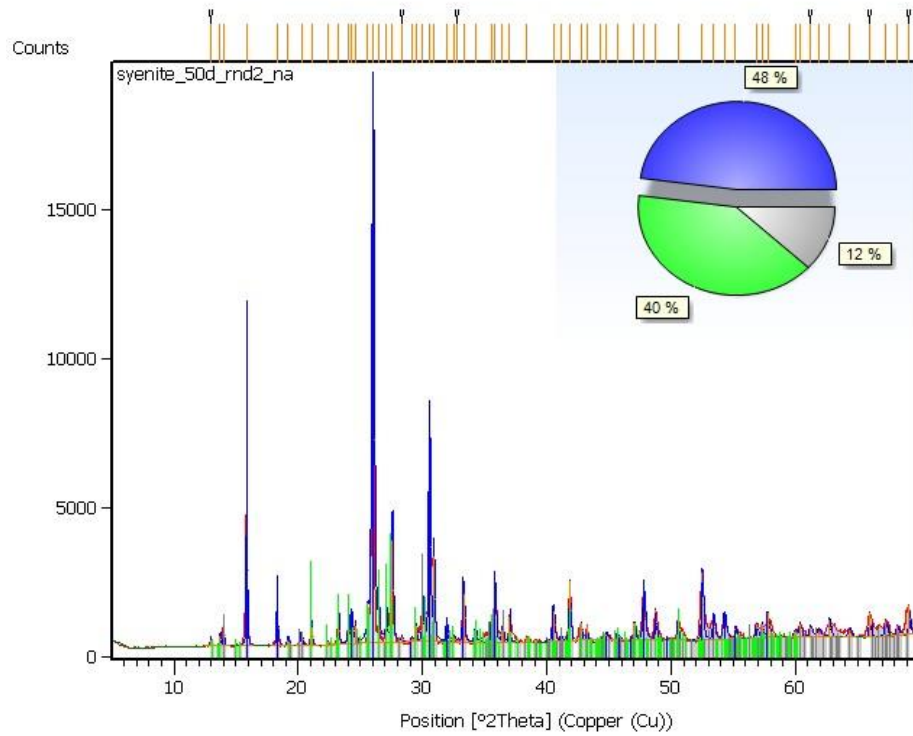
Figure B14. XRD peaks and percentages of defined mineral phases within Na-treated syenite at 50 °C.

Carbonatite

Table B15. Identified mineral phases within carbonatite in 50°C experiments.

Ref. code	Chem. formula	Score	Compound name	[°2Th]	Scale Factor	%
98-002-8827	$Ca\ CO_3$	68	Calcite	-0.012	0.575	82
98-024-0658	$Ca_5\ (P_6O_4)_3\ F$	49	Apatite	0.042	0.031	13
98-009-3948	$Fe^{3+}\ O\ (OH)$	26	Lepidocrocite	0.011	0.013	2
98-010-9041	$Fe^{3+}\ O\ (OH)$	33	Goethite	-0.028	0.019	3
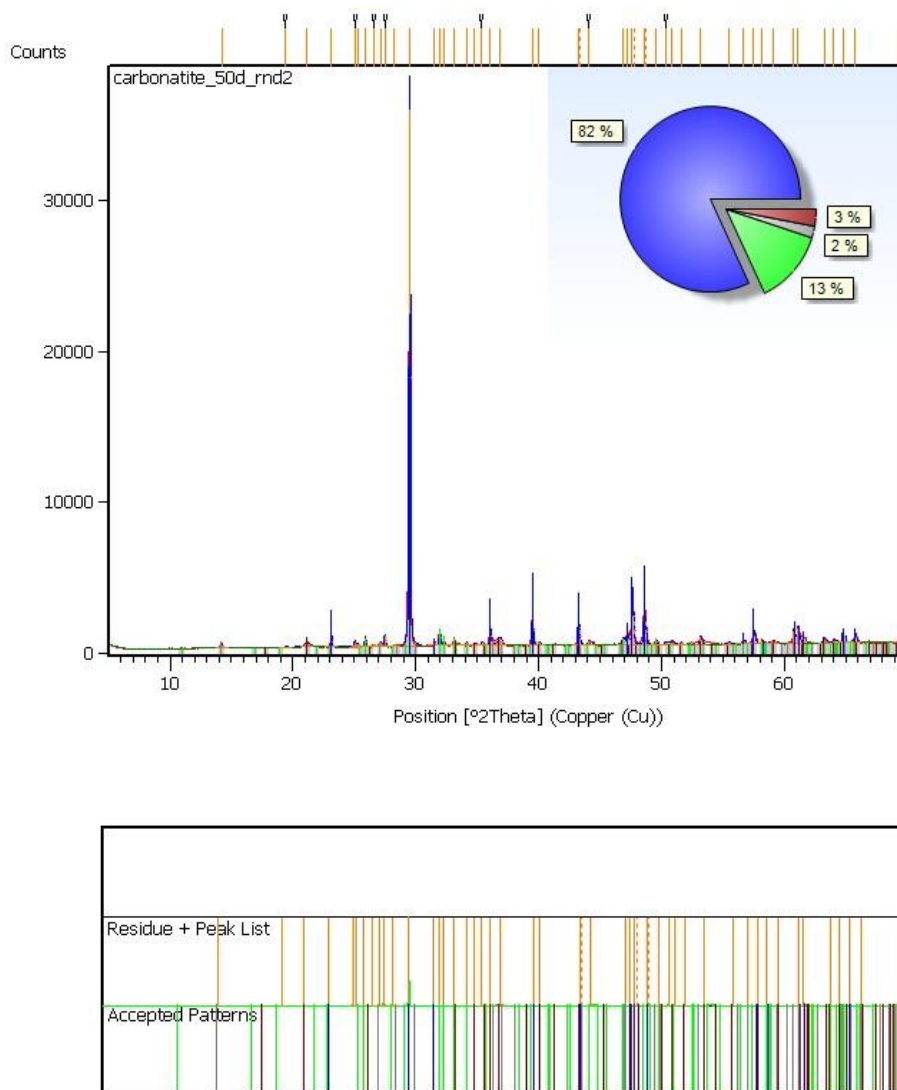
Figure B15. XRD peaks and percentages of defined mineral phases within carbonatite at 50 °C.

Table B16. Identified mineral phases within Na-treated carbonatite in 50°C experiments.

Ref. code	Chem. formula	Score	Compound name	[°2Th]	Scale Factor	%
98-002-8827	$Ca\ CO_3$	80	Calcite	-0.011	0.734	79.8
98-002-4236	$Ca_5\ (P_6O_4)_3\ F$	45	Apatite	0.003	0.043	13.1
98-009-3948	$Fe^{3+}\ O\ (OH)$	34	Lepidocrocite	0	0.036	3
98-007-1810	$Fe^{3+}\ O\ (OH)$	31	Goethite	0.038	0.036	4
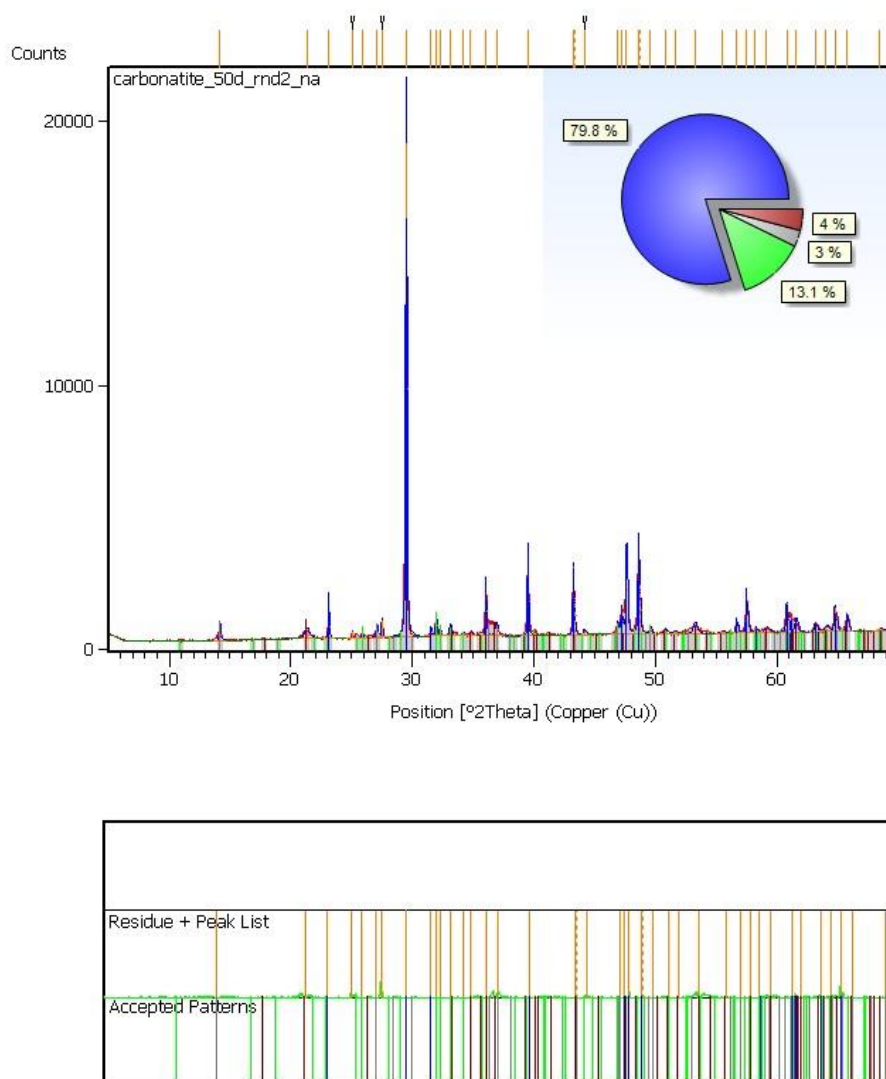
Figure B16. XRD peaks and percentages of defined mineral phases within Na-treated carbonatite at 50 °C.

Gabbro

Table B17. Identified mineral phases within gabbro in 50°C experiments.

Ref. code	Chemical formula	Score	Compound name	[°2Th]	Scale Factor	%
98-007-9835	$Ca_2 (Mg_4Al) (Si_7Al) O_{22} (OH)_2$	54	Magnesio-hornblende	0.057	0.349	26
98-003-4916	$(Ca_{0.25},Na_{0.75}) (AlSi_3O_8)_2$	54	Albite low, calcian	0.052	0.549	50
98-008-3849	SiO_2	42	Quartz low	0.045	0.77	10
98-004-0638	$K (Mg,Fe,Ti)_3 AlSi_3O_{10} (OH)_2$	22	Biotite (Ti-rich)	-0.011	0.228	14
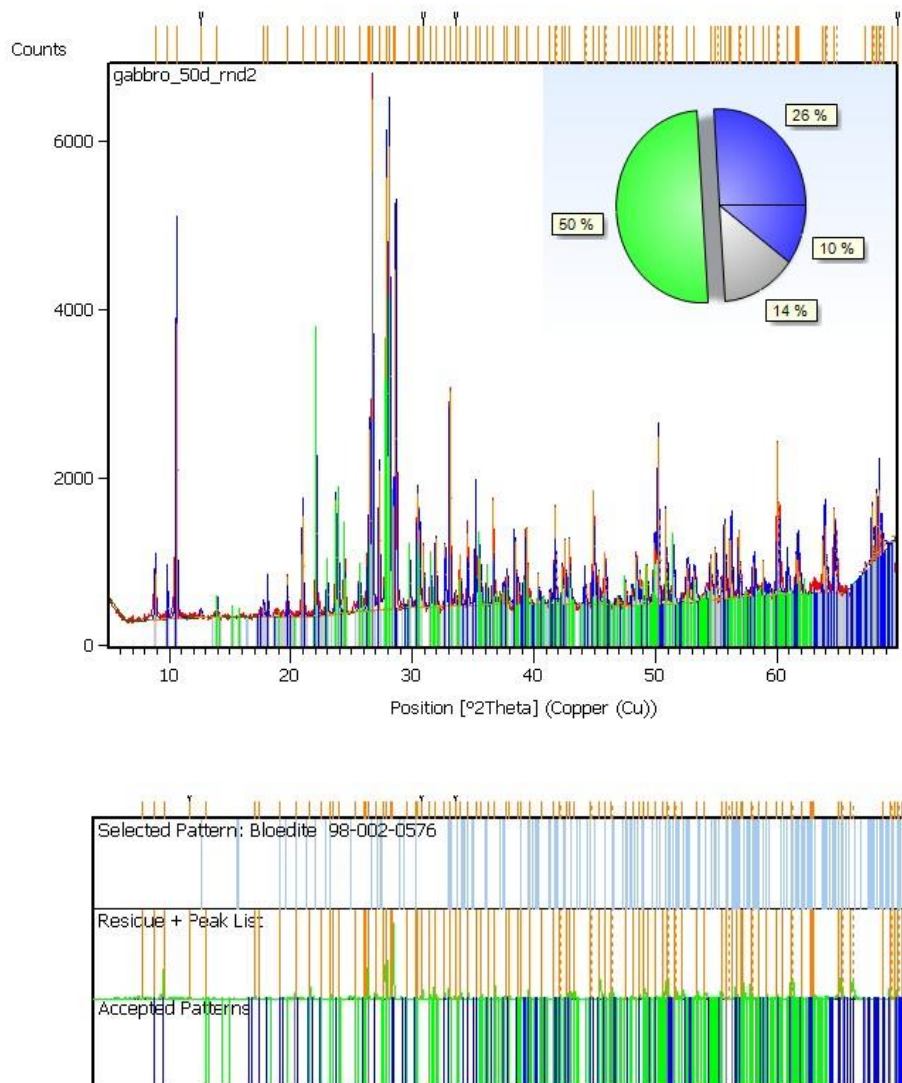
Figure B17. XRD peaks and percentages of defined mineral phases within gabbro at 50 °C.

Table B18. Identified mineral phases within Na-treated gabbro in 50°C experiments.

Ref. code	Chemical formula	Score	Compound name	[°2Th]	Scale Factor	%
98-007-9835	$Ca_2 (Mg_4Al) (Si_7Al) O_{22} (OH)_2$	58	Magnesio-hornblende	0.057	0.289	25.3
98-003-4916	$(Ca_{0.25}, Na_{0.75}) (AlSi_3O_8)_2$	53	Albite low, calcian	0.049	0.509	54.5
98-002-9210	SiO_2	51	Quartz low	-0.023	0.683	13.1
98-015-9335	$K (Mg,Fe,Ti)_3 AlSi_3O_{10} (OH)_2$	34	Biotite	0.016	0.211	7.10
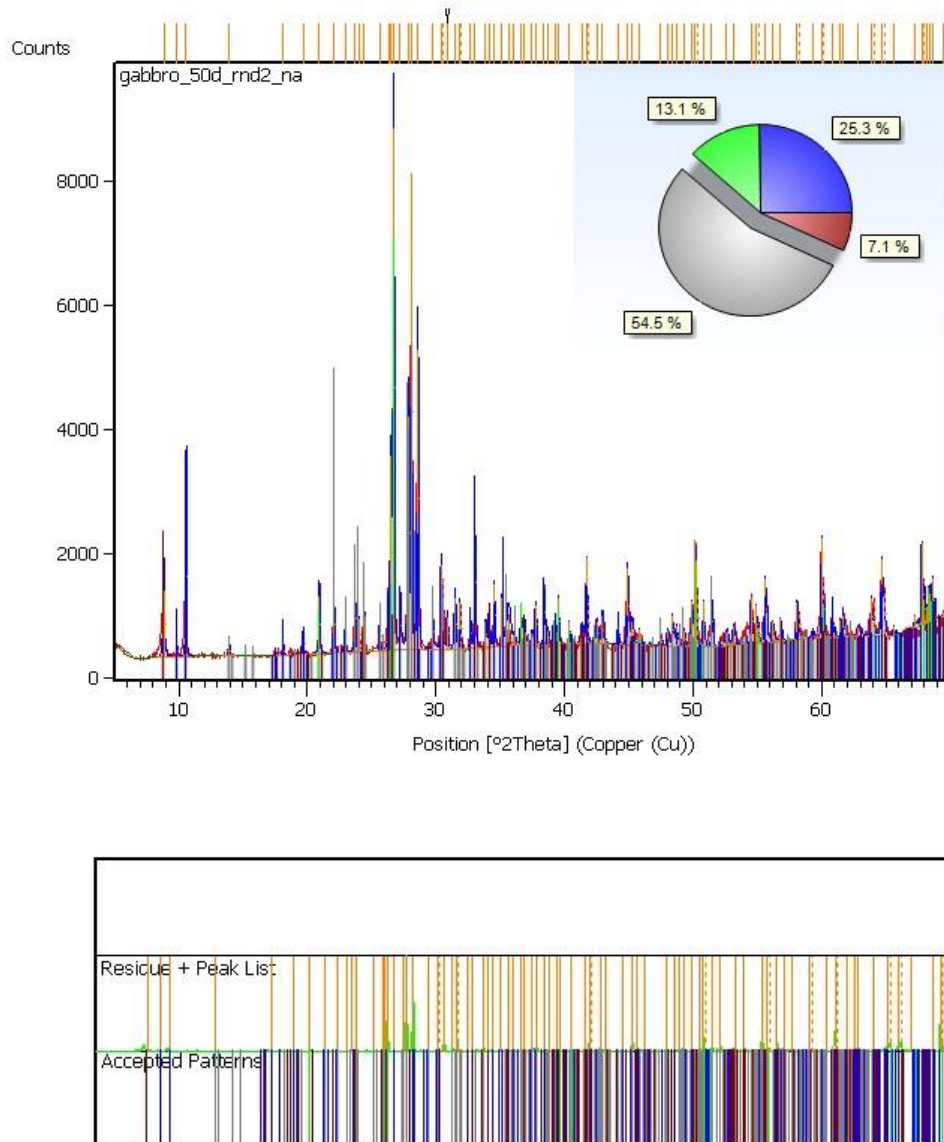
Figure B18. XRD peaks and percentages of defined mineral phases within Na-treated gabbro at 50 °C.

73

Granite

Table B19. Identified mineral phases within granite in 50°C experiments.

Ref. code	Chemical formula	Score	Compound name	[°2Th]	Scale Factor	%
98-010-0341	SiO_2	60	Quartz	0.052	0.919	35
98-003-4917	$Na(AlSi_3O_8)$	51	Albite	0.033	0.134	26
98-008-9813	$K Fe^{2+}_2 Al (Al_2Si_2O_{10})(OH)_2$	35	Siderophyllite	0.091	0.162	5
98-003-8135	$K(AlSi_3O_8)$	32	Microcline	0.024	0.149	34
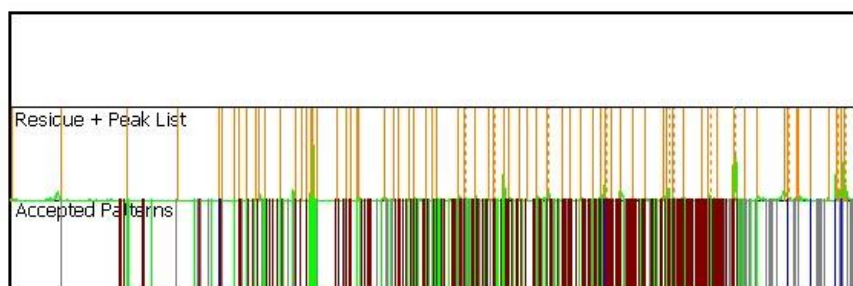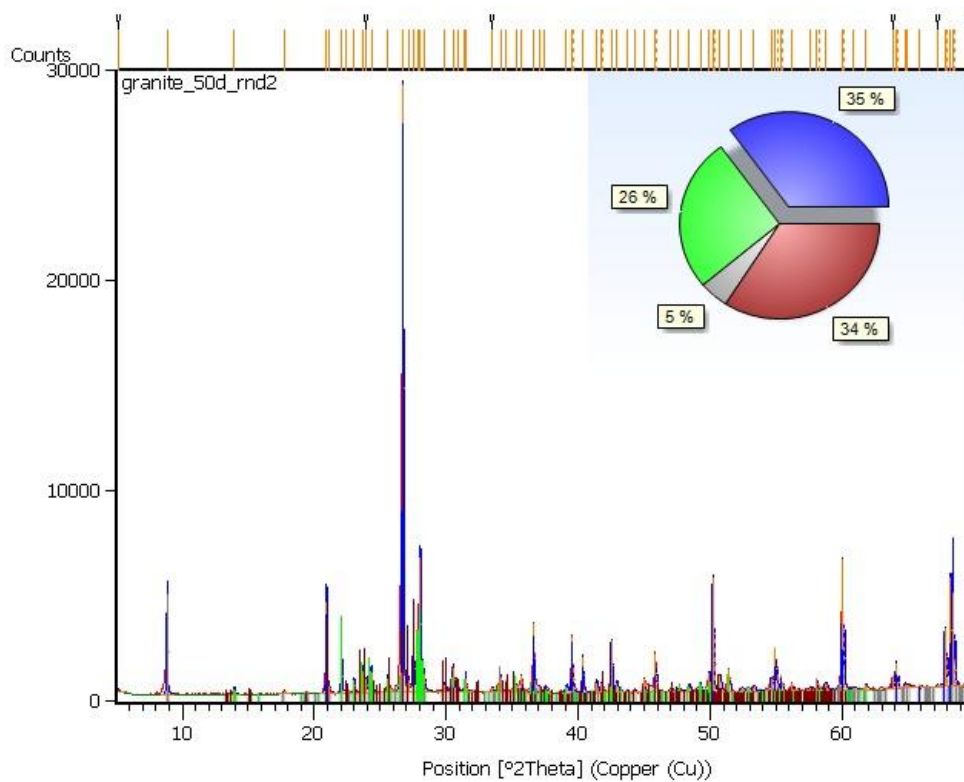
Figure B19. XRD peaks and percentages of defined mineral phases within granite at 50°C.

Table B20. Identified mineral phases within Na-treated granite in 50°C experiments.

Ref. code	Chemical formula	Score	Compound name	[°2Th]	Scale Factor	%
98-010-0341	SiO_2	60	Quartz	0.002	0.909	28.7
98-003-4917	$Na(AlSi_3O_8)$	54	Albite	0.043	0.35	54.5
98-008-9813	$K Fe^{2+}_2 Al (Al_2Si_2O_{10})(OH)_2$	39	Siderophyllite	0.078	0.173	5
98-003-4786	$K(AlSi_3O_8)$	30	Microcline	-0.033	0.071	11.9
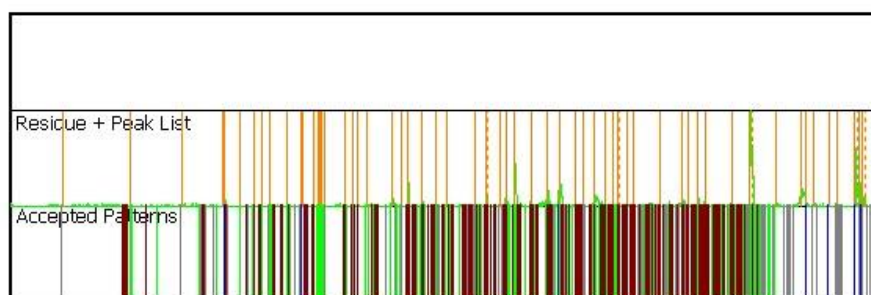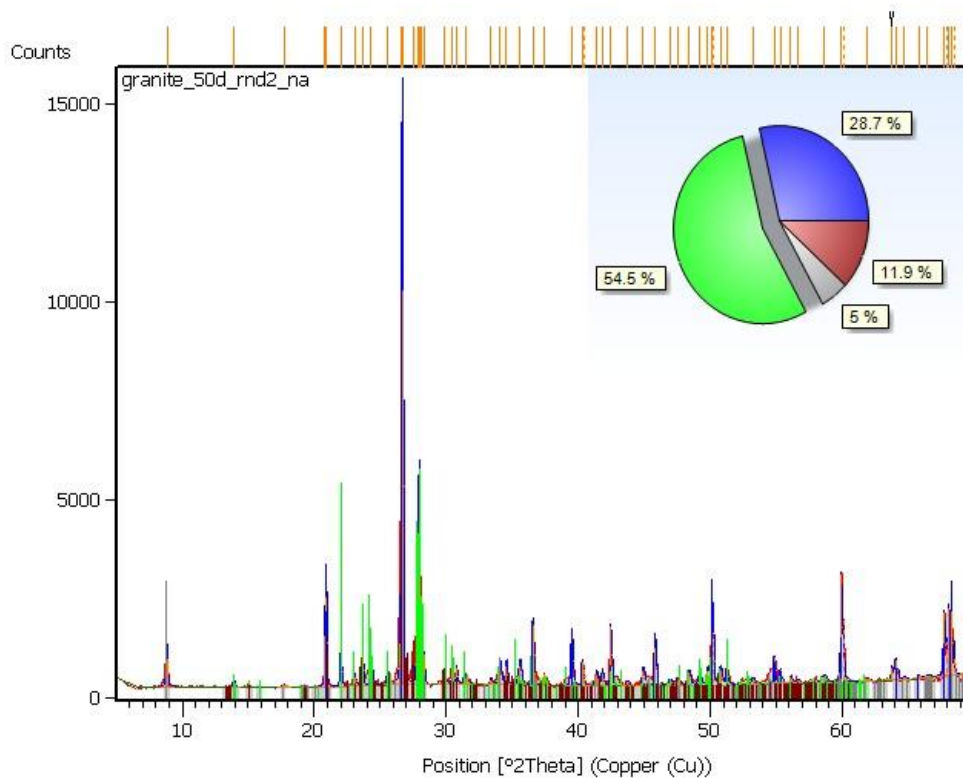
Figure B20. XRD peaks and percentages of defined mineral phases within Na-treated granite at 50°C.

Dolerite

Table B21. Identified mineral phases within dolerite in 50°C experiments.

Ref. code	Chemical formula	Score	Compound name	[°2Th]	Scale Factor	%
98-003-4916	$(Ca_{0.25},Na_{0.75})(AlSi_3O_8)_2$	56	Albite, low, calcian	0.019	0.315	73.5
98-006-7117	$Si\,O_2$	47	Quartz, low	0.033	0.1	4.1
98-004-3466	$Fe^{2+}TiO_3$	42	Ilmenite	0.073	0.073	3.1
98-006-6678	$K\,Fe^{2+}_2\,Al\,(Al_2Si_2O_{10})(OH)_2$	21	Siderophyllite	-0.007	0.045	2
98-009-8088	$Fe^{2+}Fe^{3+}_2\,O_4$	31	Magnetite	0.022	0.092	14.3
98-001-6732	$Mg_5\,Al\,(AlSi_3O_{10})\,(OH)_8$	3	Clinochlore	0.088	0.029	3.1
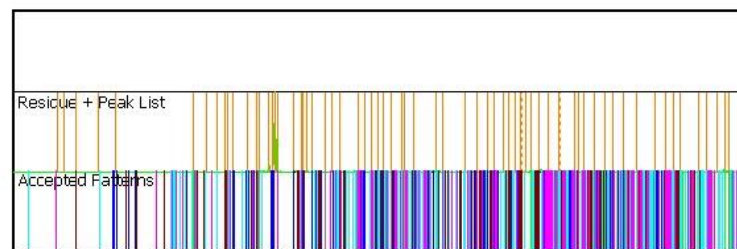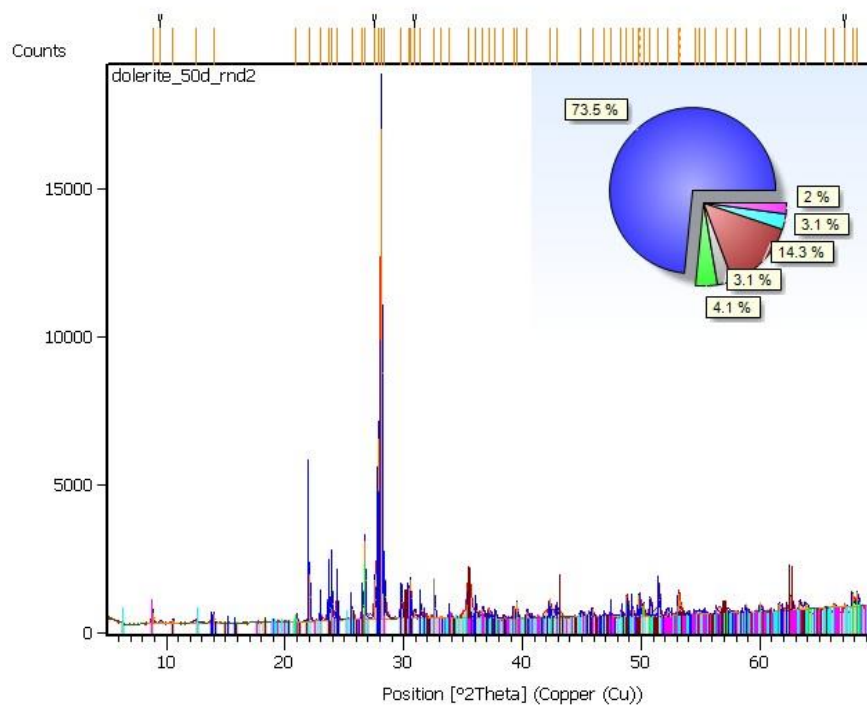
Figure B21. XRD peaks and percentages of defined mineral phases within dolerite at 50°C.

Table B22. Identified mineral phases within Na-treated dolerite in 50°C experiments.

Ref. code	Chemical formula	Score	Compound name	[°2Th]	Scale Factor	%
98-003-4916	$(Ca_{0.25},Na_{0.75}) (AlSi_3O_8)_2$	60	Albite, low, calcian	0.004	0.362	81
98-008-9278	$Si O_2$	50	Quartz, low	0.115	0.144	6
98-002-3729	$Fe^{2+} TiO_3$	36	Ilmenite	0.065	0.048	2
98-006-6678	$K Fe^{2+}_2 Al (Al_2Si_2O_{10})(OH)_2$	26	Siderophyllite	0.000	0.052	5
98-016-4813	$Fe^{2+} Fe^{3+}_2 O_4$	18	Magnetite	0.051	0.035	3
98-001-6732	$Mg_5 Al (AlSi_3O_{10}) (OH)_8$	3	Clinochlore	0.048	0.025	3
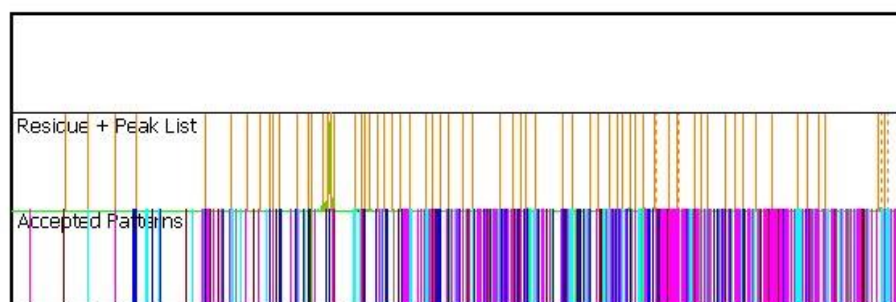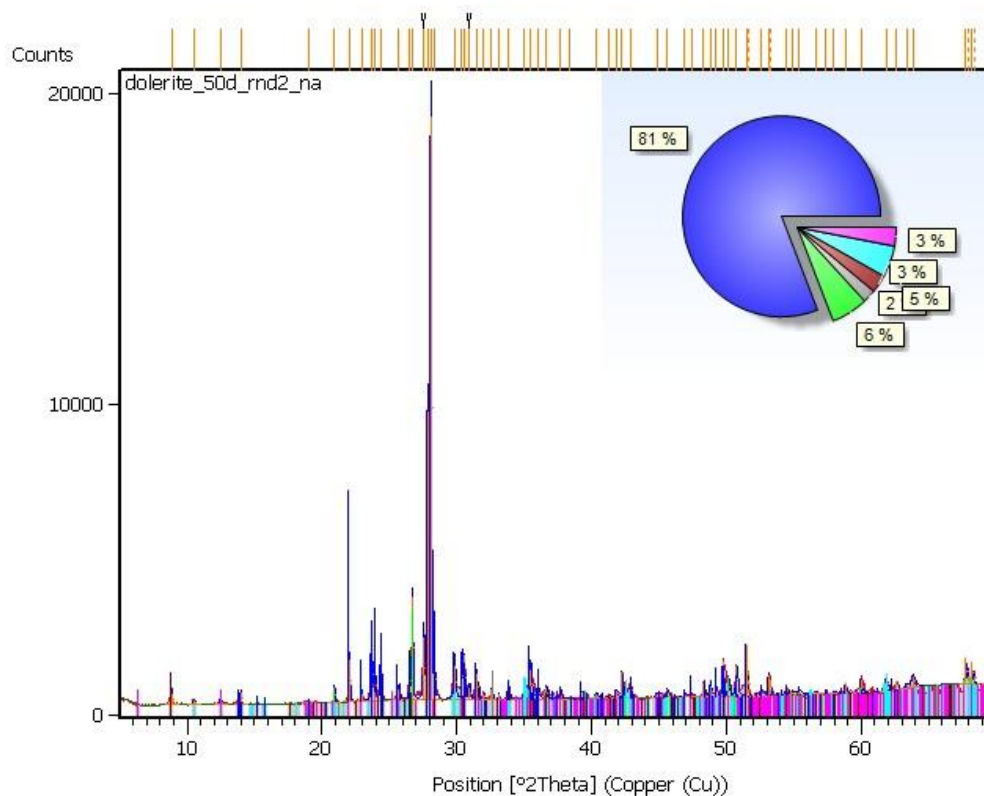
Figure B22. XRD peaks and percentages of defined mineral phases within Na-treated dolerite at 50°C.

Basalt

Table B23. Identified mineral phases within basalt in 50°C experiments.

Ref. code	Chemical formula	Score	Compound name	[°2Th]	Scale Factor	%
98-008-0684	$(Ca_{0.85} Al_{0.15}) (Mg\ Si_2O_6)$	65	Diopside, aluminian	0.005	0.832	42
98-010-0232	$(Ca_{0.65} Na_{0.35}) (Al_2\ Si_2O_8)$	66	Anorthite, sodian	0.055	0.601	58
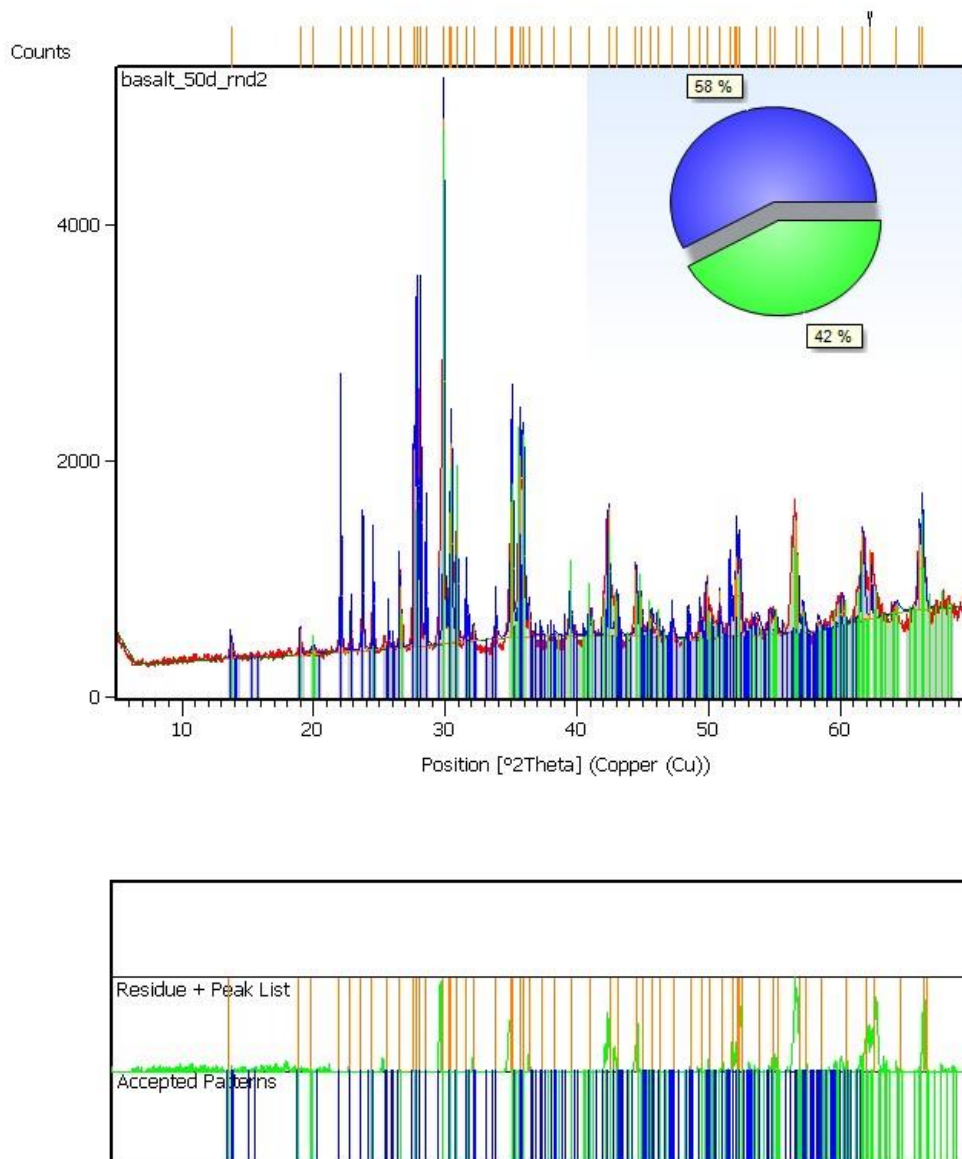
Figure B23. XRD peaks and percentages of defined mineral phases within basalt at 50°C.

Table 24. Identified mineral phases within Na-treated basalt in 50°C experiments.

Ref. code	Chemical formula	Score	Compound name	[°2Th]	Scale Factor	%
98-008-0683	$(Ca_{0.85} Al_{0.15}) (Mg\ Si_2O_6)$	59	Diopside, aluminian	-0.05	1.100	39
98-010-0233	$(Ca_{0.65} Al_{0.35}) (Al_2\ Si_2O_8)$	65	Anorthite, sodian	0.03	0.878	61
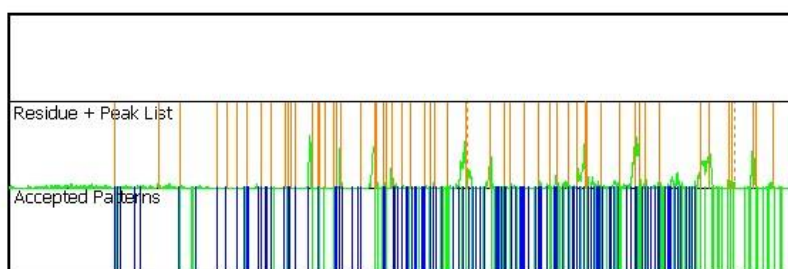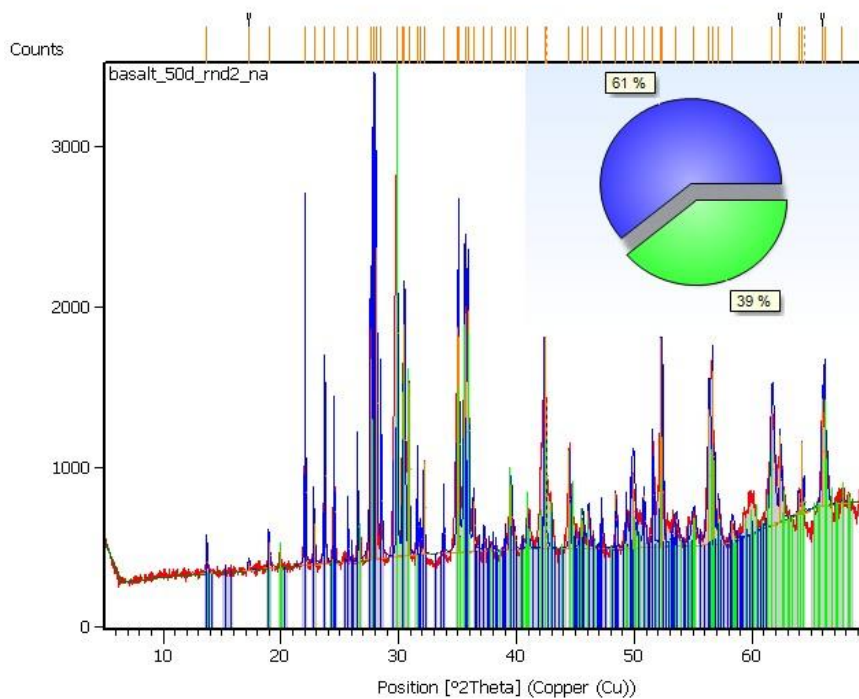
Figure B24. XRD peaks and percentages of defined mineral phases within Na-treated basalt at 50°C.

B3. Experiments at 100°C

Syenite

Table B25. Identified mineral phases within syenite in 100°C experiments

Ref. code	Chemical formula	Score	Compound name	[°2Th]	Scale Factor	%
98-003-4876	$Na(AlSi_2O_6)\ H_2O$	65	Analcime	0.046	0.655	53
98-003-4896	$K(AlSi_3O_8)$	45	Microcline	0.069	0.212	39
98-015-6559	$NaFe^{3+}\ (Si_2O_6)$	44	Aegirine	0.051	0.125	8
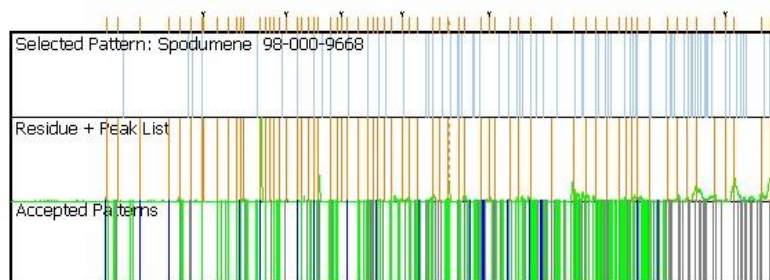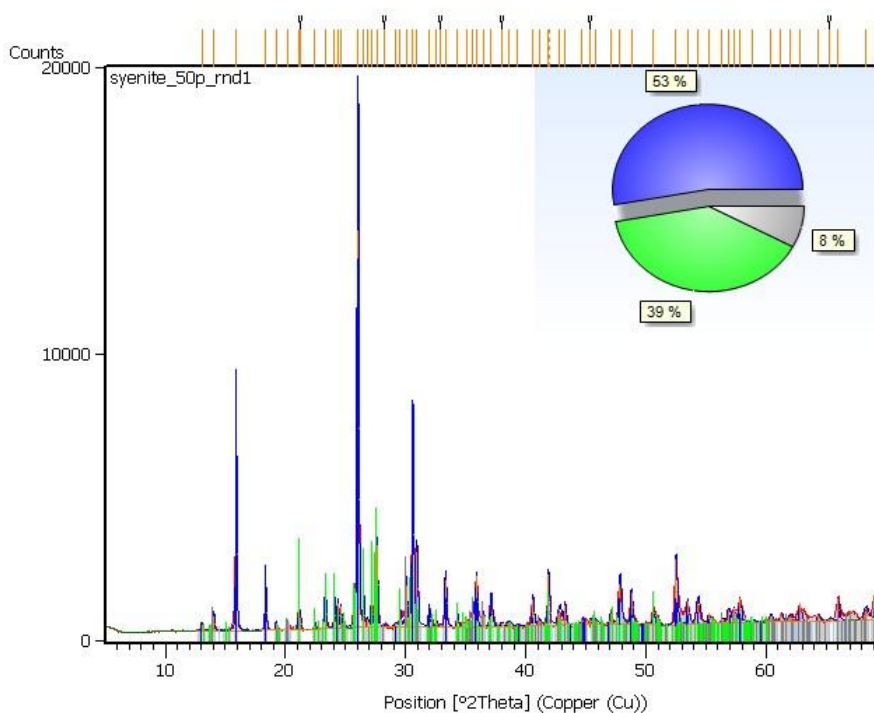
Figure B25. XRD peaks and percentages of defined mineral phases within Na-treated syenite at 100 °C.

Carbonatite

Table B3. Identified mineral phases within Na-treated carbonatite in 100°C experiments.

Ref. code	Chem. formula	Score	Compound name	[°2Th]	Scale Factor	%
98-008-6162	$Ca_{0.94} Mg_{0.06} CO_3$	80	Mg-Calcite	-0.126	0.373	82
98-009-4081	$Ca_5 (P_6O_4)_3 F$	45	Apatite	0.063	0.014	13
98-010-8876	$Fe^{3+} O (OH)$	34	Lepidocrocite	0.073	0.007	3
98-006-2408	$Si O_2$	31	Quartz	0.026	0.008	2
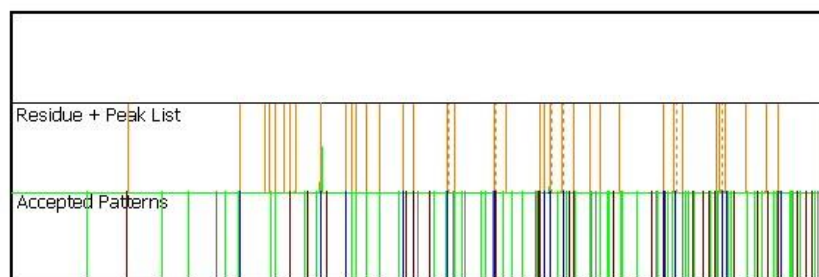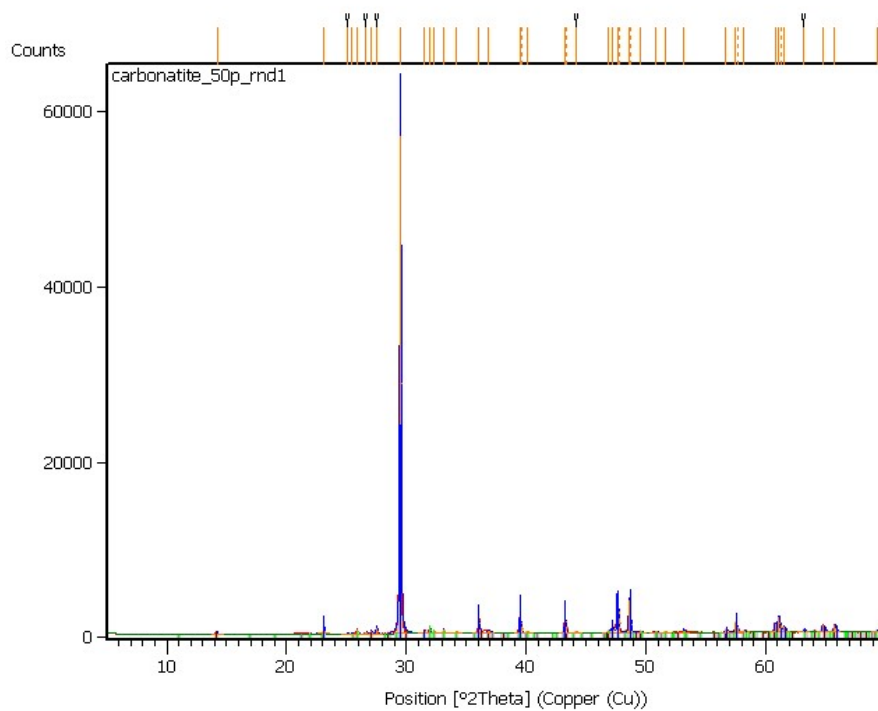
Figure B26. XRD peaks and percentages of defined mineral phases within Na-treated carbonatite at 100 °C.

Gabbro

Table B27. Identified mineral phases within gabbro in 100°C experiments.

Ref. code	Chemical formula	Score	Compound name	[°2Th]	Scale Factor	%
98-007-9835	$Ca_2 (Mg_4Al) (Si_7Al) O_{22} (OH)_2$	58	Magnesio-hornblende	0.073	0.165	21
98-003-4916	$(Ca_{0.25},Na_{0.75}) (AlSi_3O_8)_2$	53	Albite low, calcian	0.074	0.284	45
98-008-3849	SiO_2	51	Quartz low	0.07	0.502	16
98-002-4167	$K (Mg,Fe,Ti)_3 AlSi_3O_{10} (OH)_2$	34	Biotite	0.093	0.147	9
98-006-3661	$Ca_2 (Al_2 Fe3^+) O [Si_2O_7] [SiO_4] (OH)$	19	Epidote	0.035	0.075	9
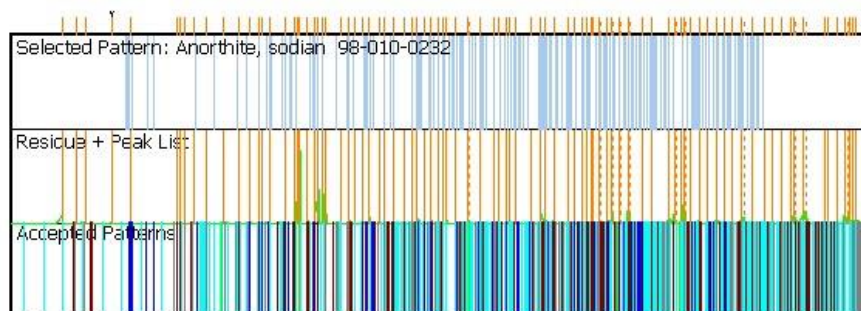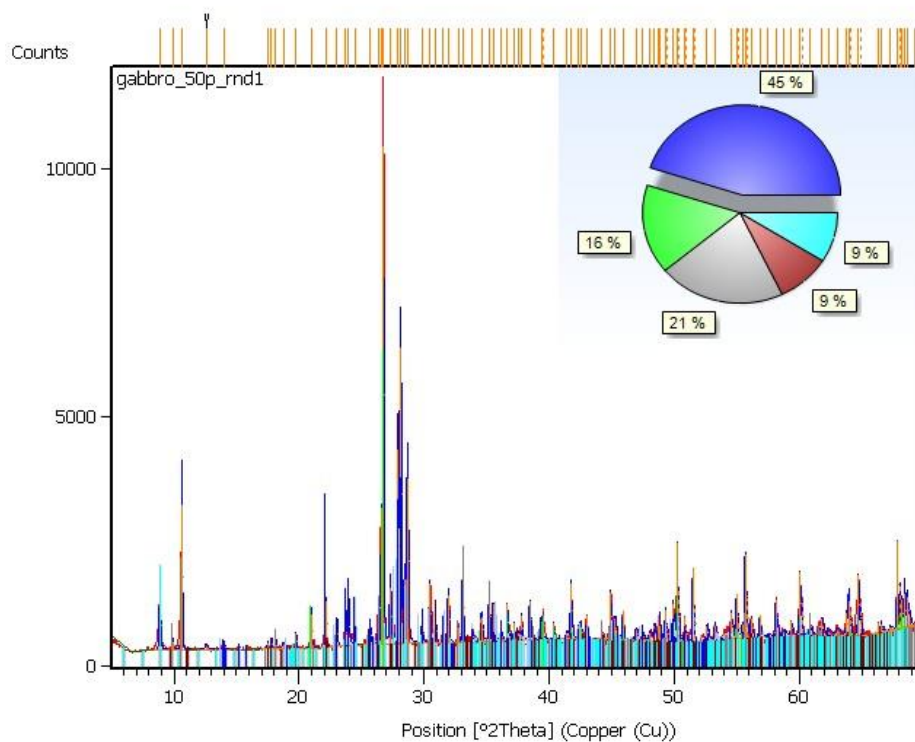
Figure B27. XRD peaks and percentages of defined mineral phases within gabbro at 100 °C.

Granite

Table B28. Identified mineral phases within granite in 100°C experiments.

Ref. code	Chemical formula	Score	Compound name	[°2Th]	Scale Factor	%
98-008-9277	SiO_2	57	Quartz	0.100	0.798	34.7
98-007-7423	$Na\,(AlSi_3O_8)$	42	Albite	-0.054	0.177	35.6
98-015-9336	$K\,(Mg,Fe)_2\,AlSi_3O_{10}\,(OH)_2$	26	Biotite	0.034	0.221	15.8
98-003-4785	$K\,(AlSi_3O_8)$	27	Microcline	-0.036	0.061	13.9
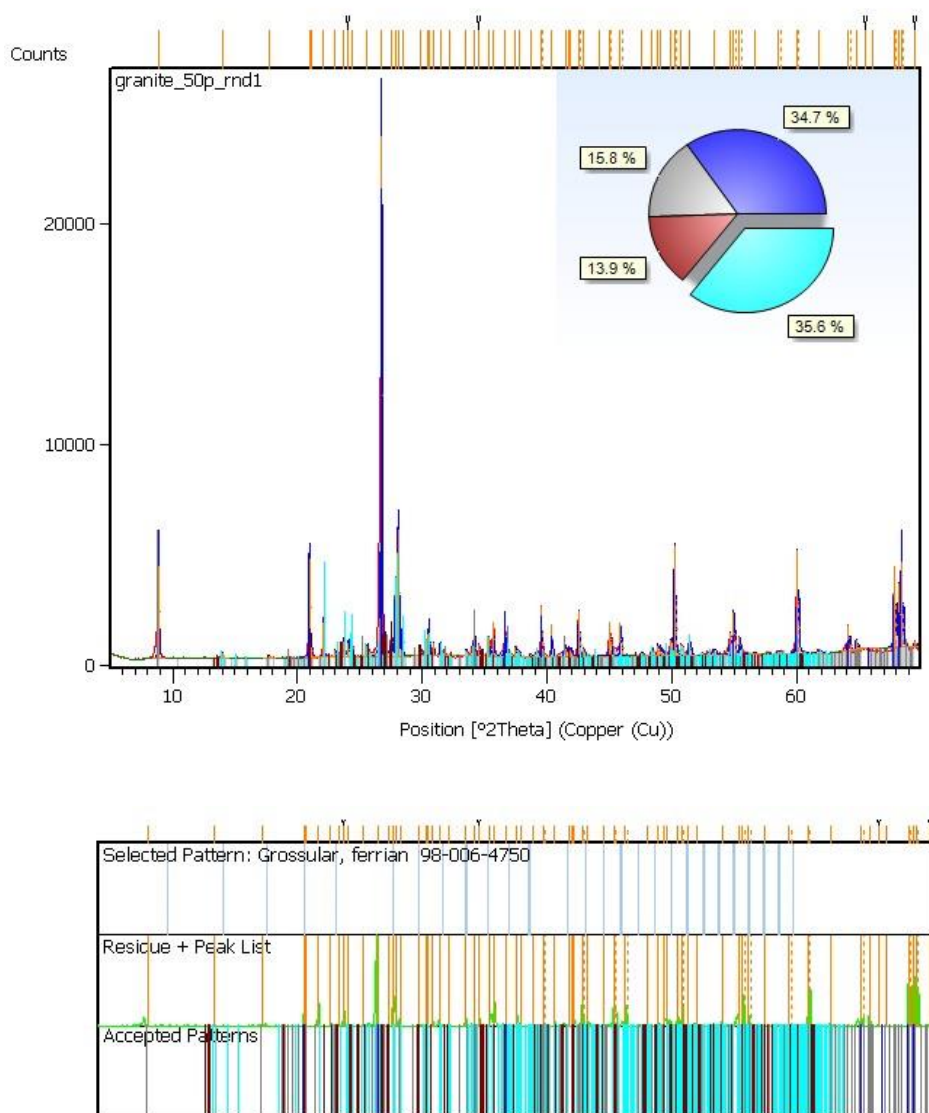
Figure B28. XRD peaks and percentages of defined mineral phases within granite at 100°C.

Dolerite

Table B29. Identified mineral phases within dolerite in 100°C experiments.

Ref. code	Chemical formula	Score	Compound name	[°2Th]	Scale Factor	%
98-003-4916	$(Ca_{0.25}, Na_{0.75})(AlSi_3O_8)_2$	60	Albite, low, calcian	0.021	0.475	69
98-004-0009	SiO_2	50	Quartz, low	0.044	0.17	5
98-015-3491	$Fe^{2+}TiO_3$	36	Ilmenite	0.08	0.096	3
98-002-2008	$K Fe^{2+}_3 (AlSi_3O_{10})(OH)_2$	26	Annite	-0.015	0.053	1
98-016-4813	$Fe^{2+}Fe^{3+}_2O_4$	18	Magnetite	0.018	0.049	5
98-001-6732	$Mg_5 Al (AlSi_3O_{10})(OH)_8$	3	Clinochlore	0.069	0.156	11
98-006-4976	$Ca_2 (Mg_{0.82} Fe_{0.18})_2 (Si_2O_6)_2$	29	Diopside, ferroan	0.012	0.099	6
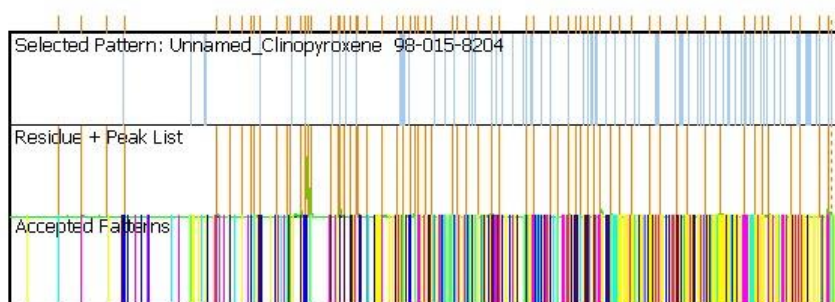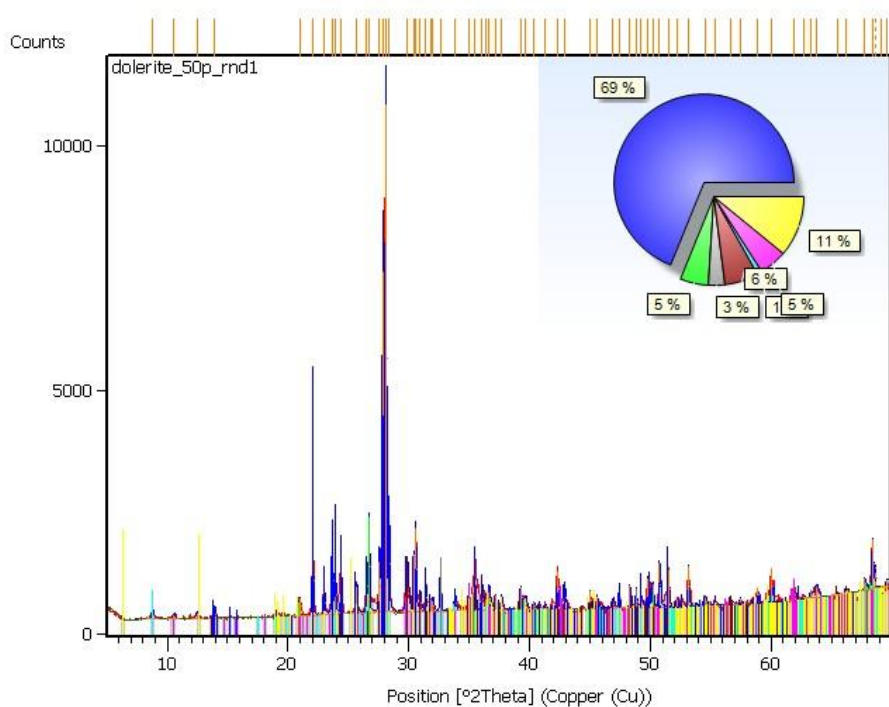
Figure B29. XRD peaks and percentages of defined mineral phases within dolerite at 100°C.

Basalt

Table B30. Identified mineral phases within basalt in 100°C experiments.

Ref. code	Chemical formula	Score	Compound name	[°2Th]	Scale Factor	%
98-010-0233	$(Ca_{0.65}\,Al_{0.35})\,(Al_2\,Si_2\,O_8)$	66	Anorthite, sodian	0.023	0.807	63
98-015-2225	$(Ca,Mg,Fe,Na)(Mg,Fe,Al)\,(Si,Al)_2\,O_6$	58	Clinopyroxene	-0.009	0.693	27
98-008-5807	$Fe^{2+}\,Fe^{3+}{}_2\,O_4$	32	Magnetite	-0.02	0.532	10
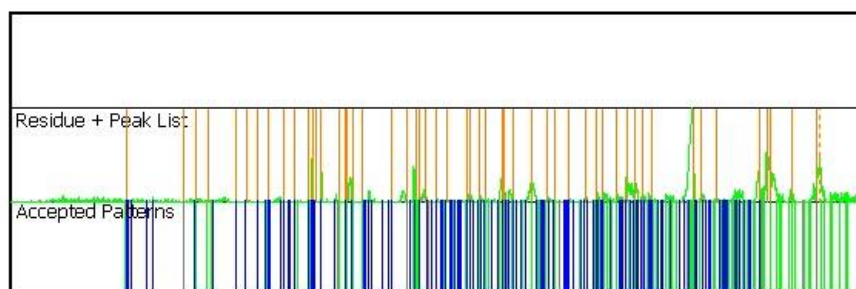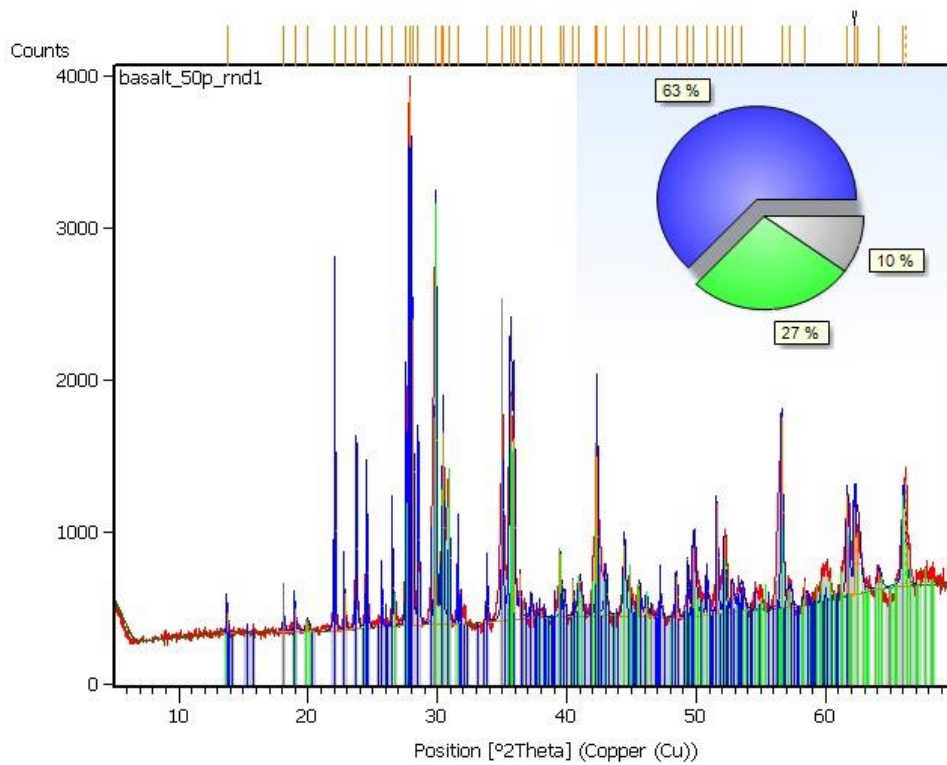
Figure B30. XRD peaks and percentages of defined mineral phases within basalt at 100°C.

APPENDIX C: SEM – EDX

C1. Untreated samples

Syenite
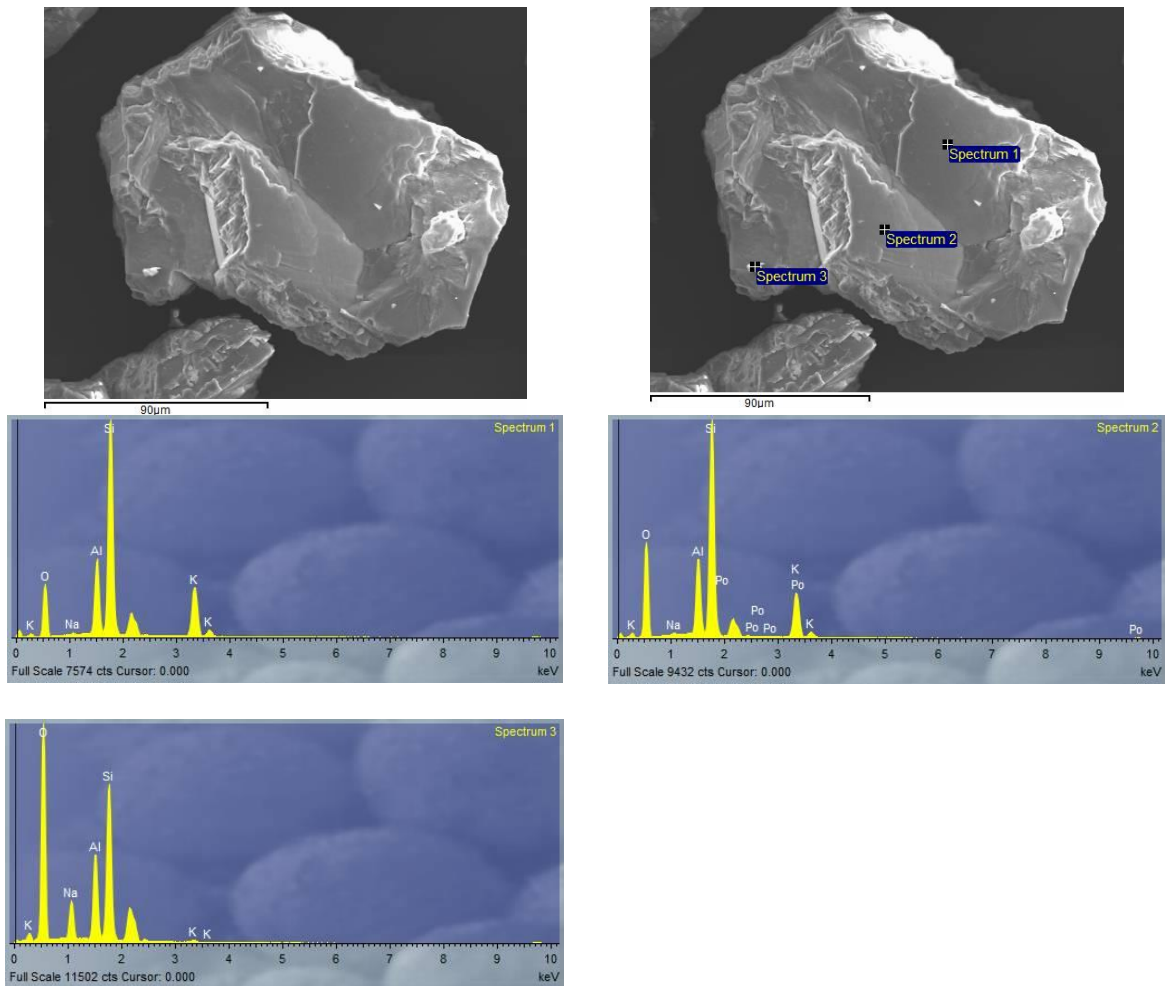
Figure C1. Photomicrograph and spectral analysis of a grain in untreated syenite sample.

Carbonatite
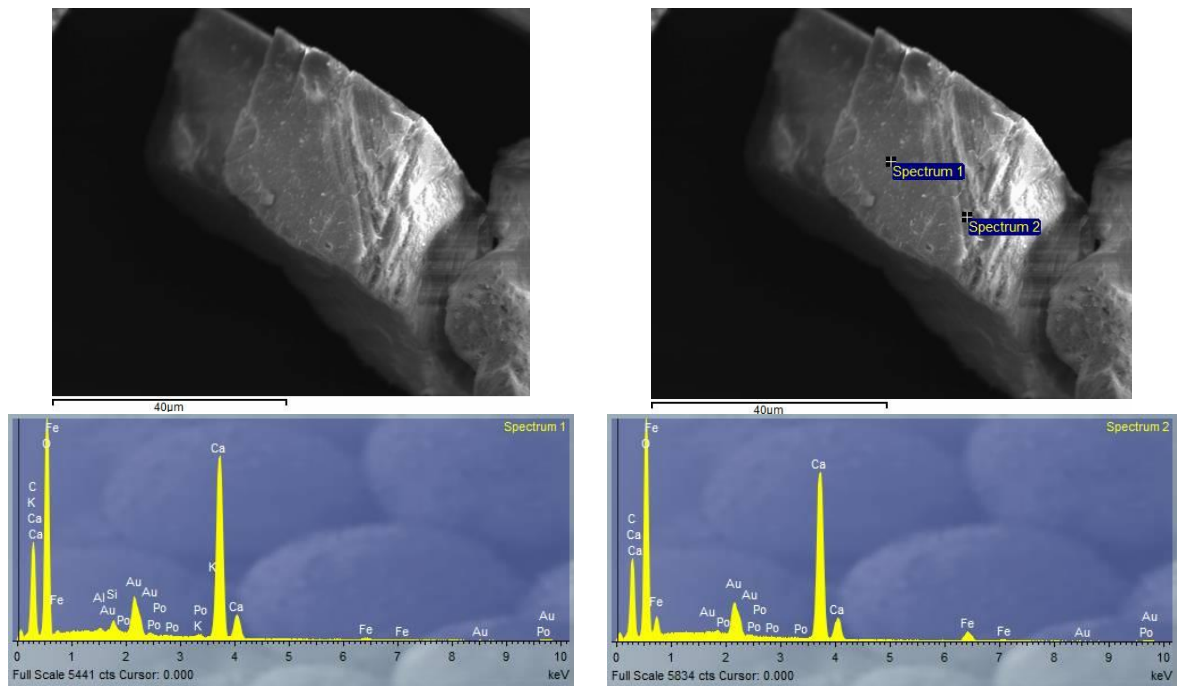
Figure C2. Photomicrograph and spectral analysis of a grain in untreated carbonatite sample.

Gabbro
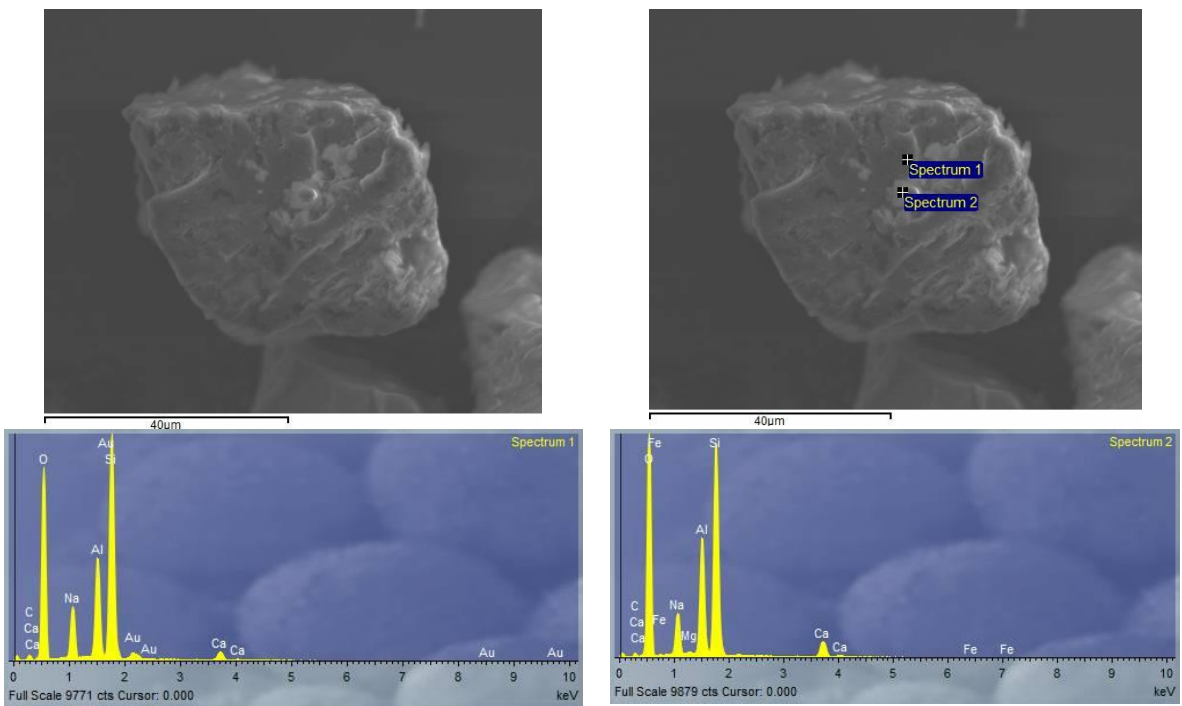
Figure C3. Photomicrograph and spectral analysis of a grain in untreated gabbro sample.

Granite
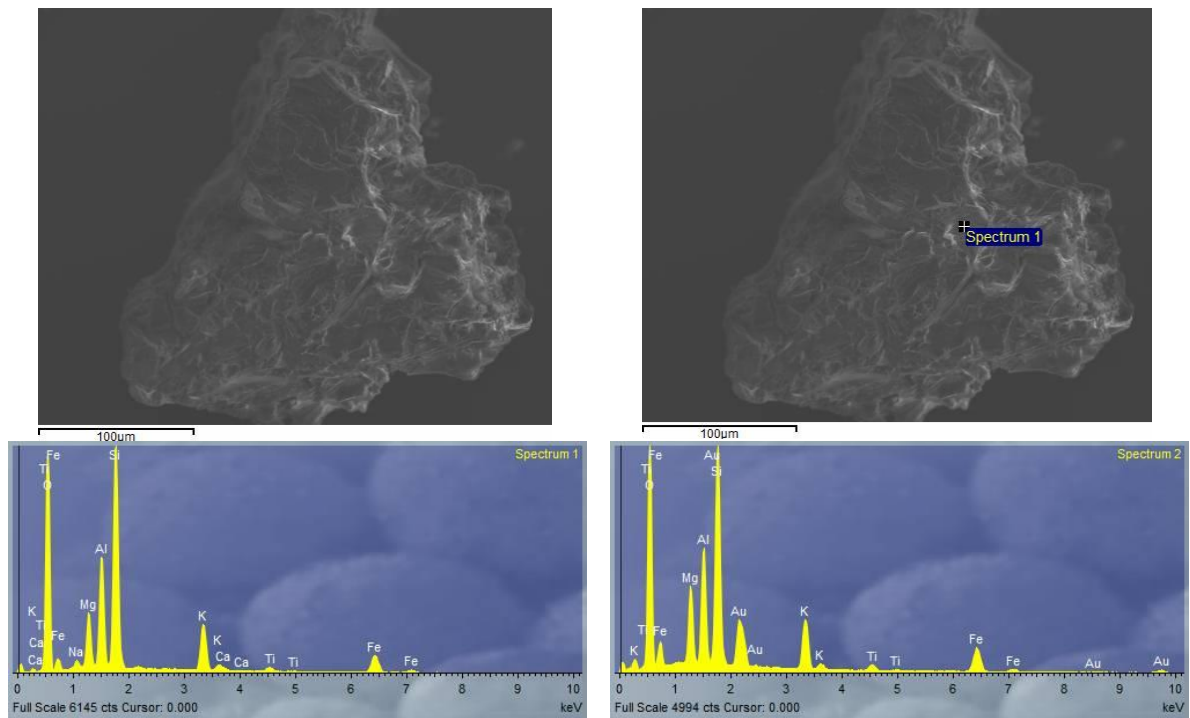
Figure C4. Photomicrograph and spectral analysis of a grain in untreated granite sample. Point for spectrum 2 does not appear on the upper right image due to a technical issue.

Dolerite
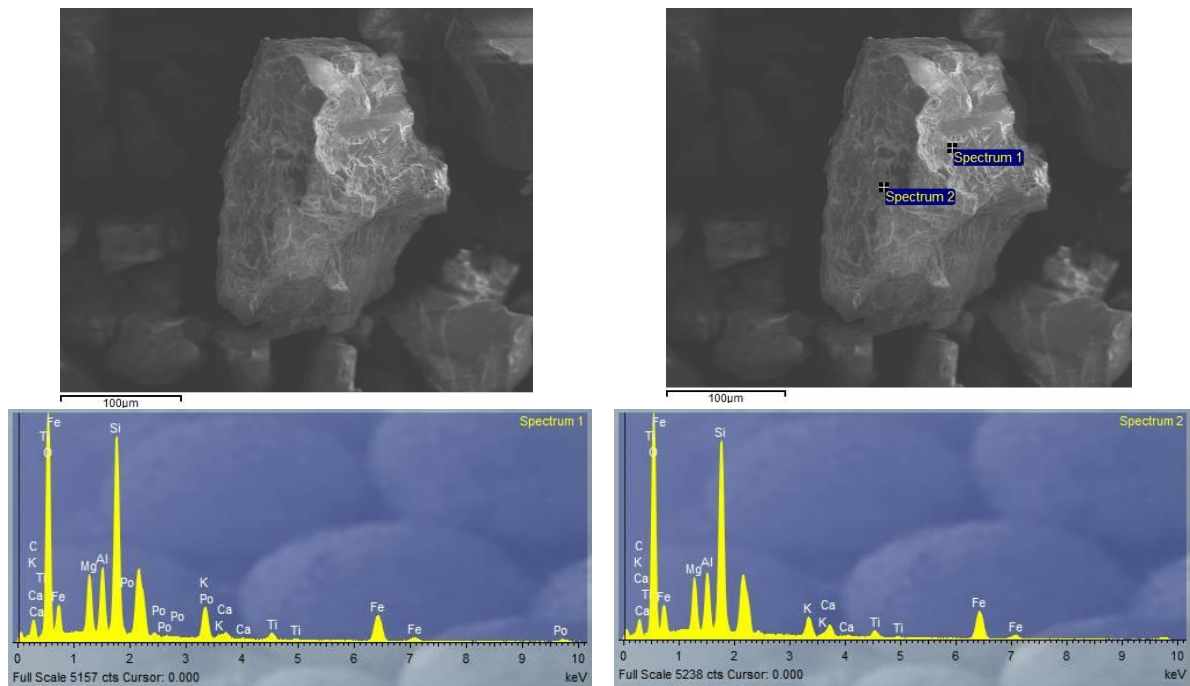
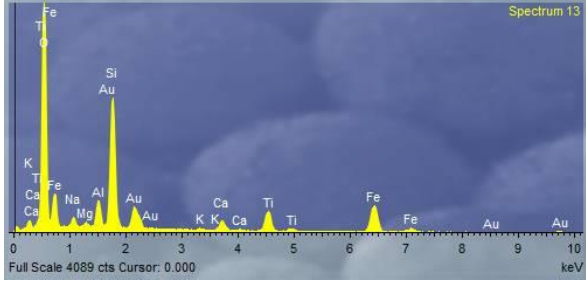*Figure C5. Photomicrograph and spectral analysis of a grain in untreated dolerite sample.*

Basalt
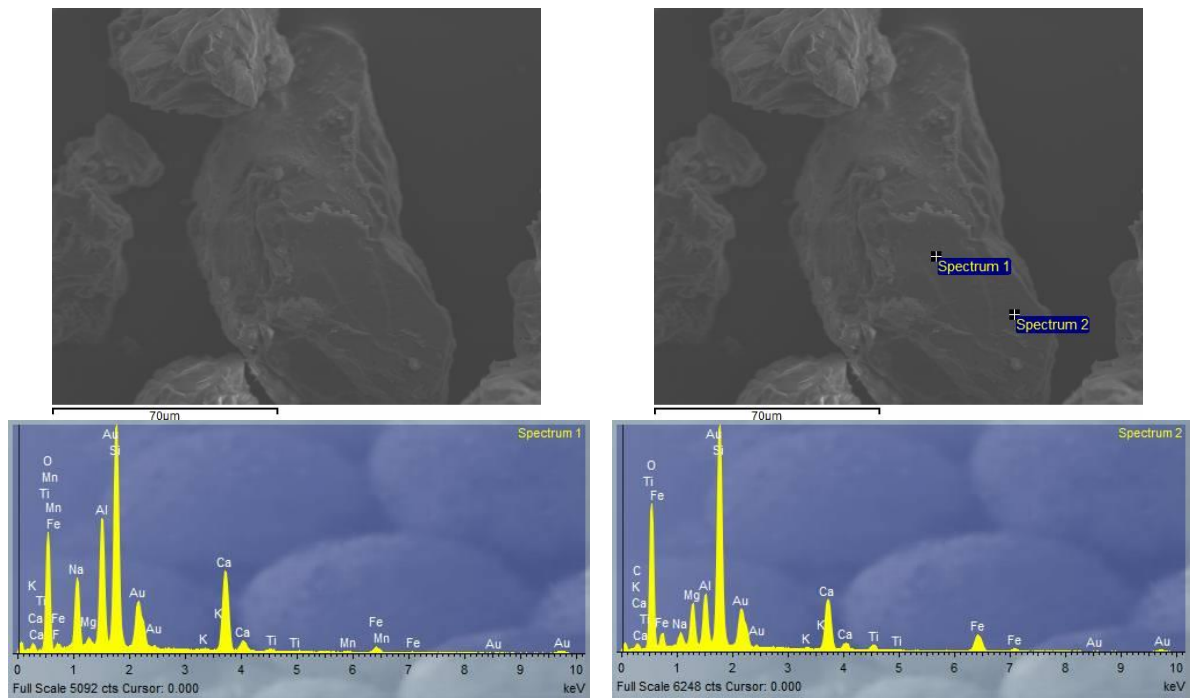
Figure C6. Photomicrograph and spectral analysis of a grain in untreated basalt sample.

C2. Room temperature experiments
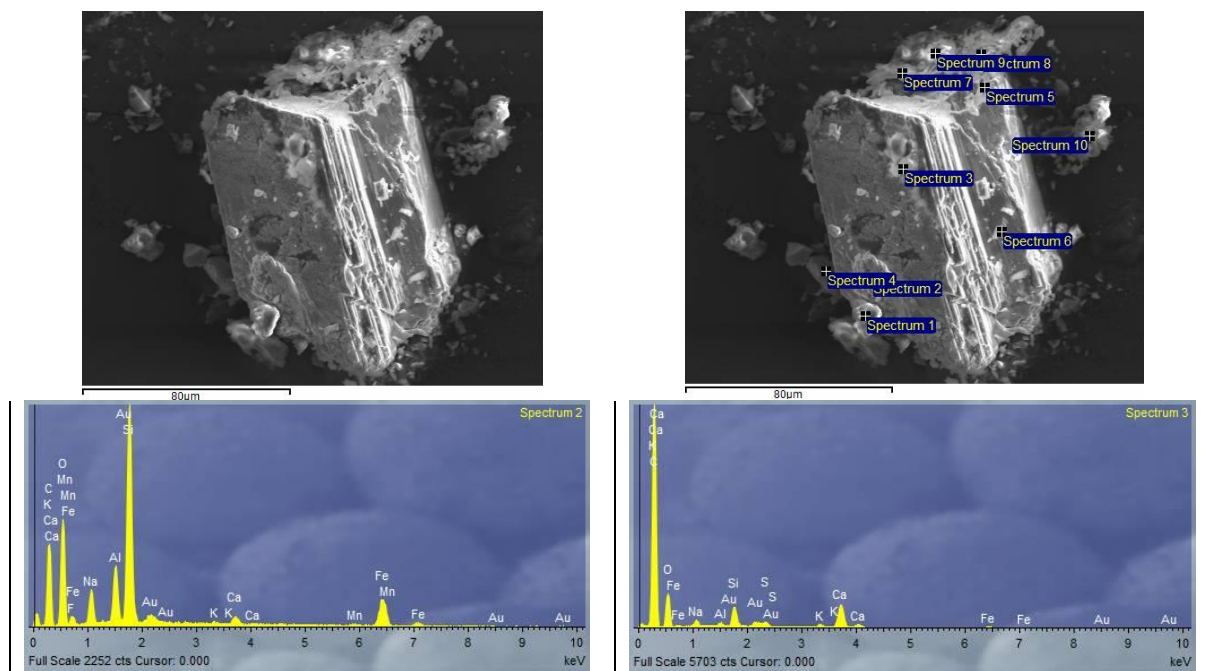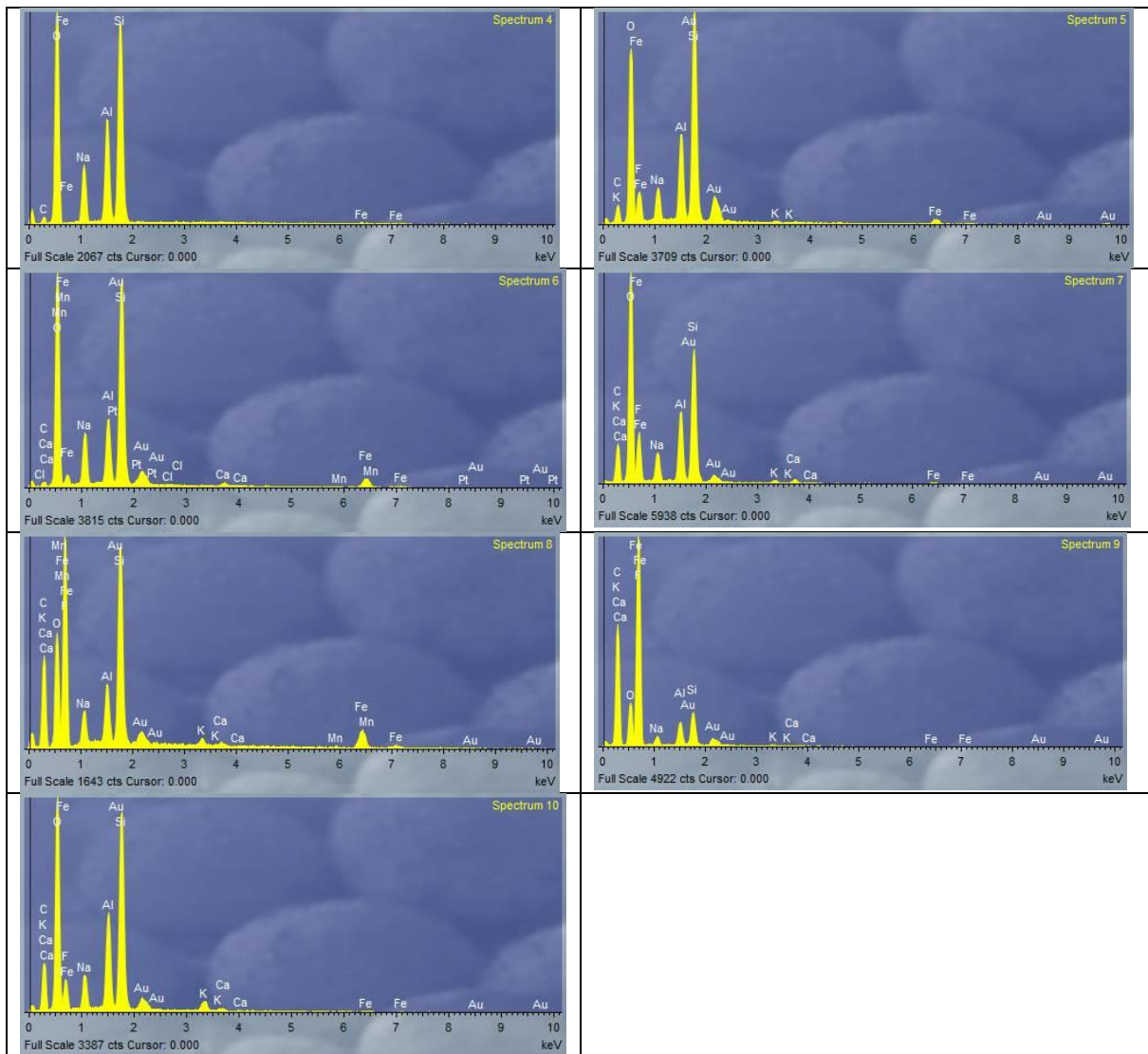
Syenite

Figure C7. Photomicrograph and spectral analysis of a grain in syenite at room temperature.
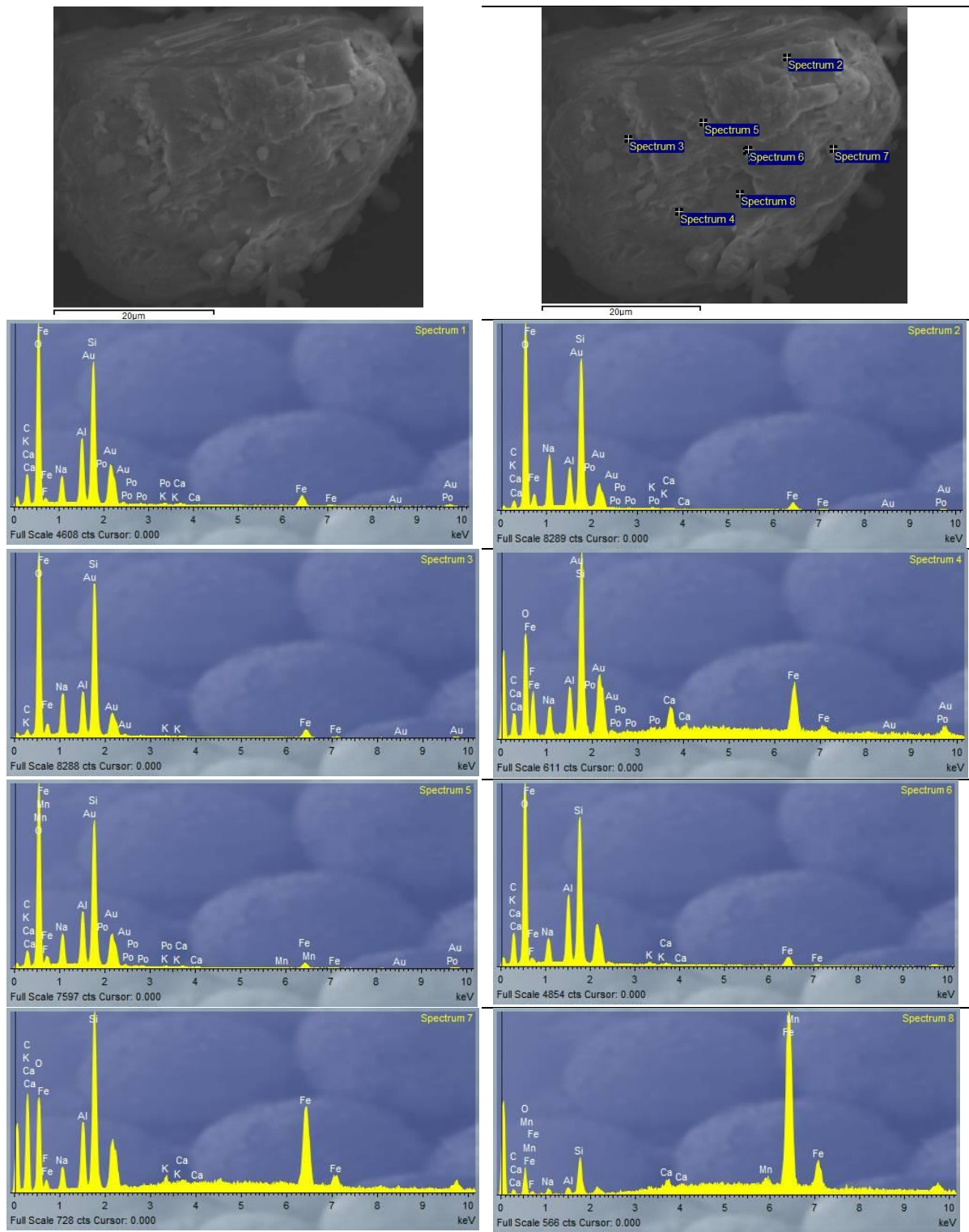
Figure C8. Photomicrograph and spectral analysis of a grain in Na-treated syenite at room temperature.
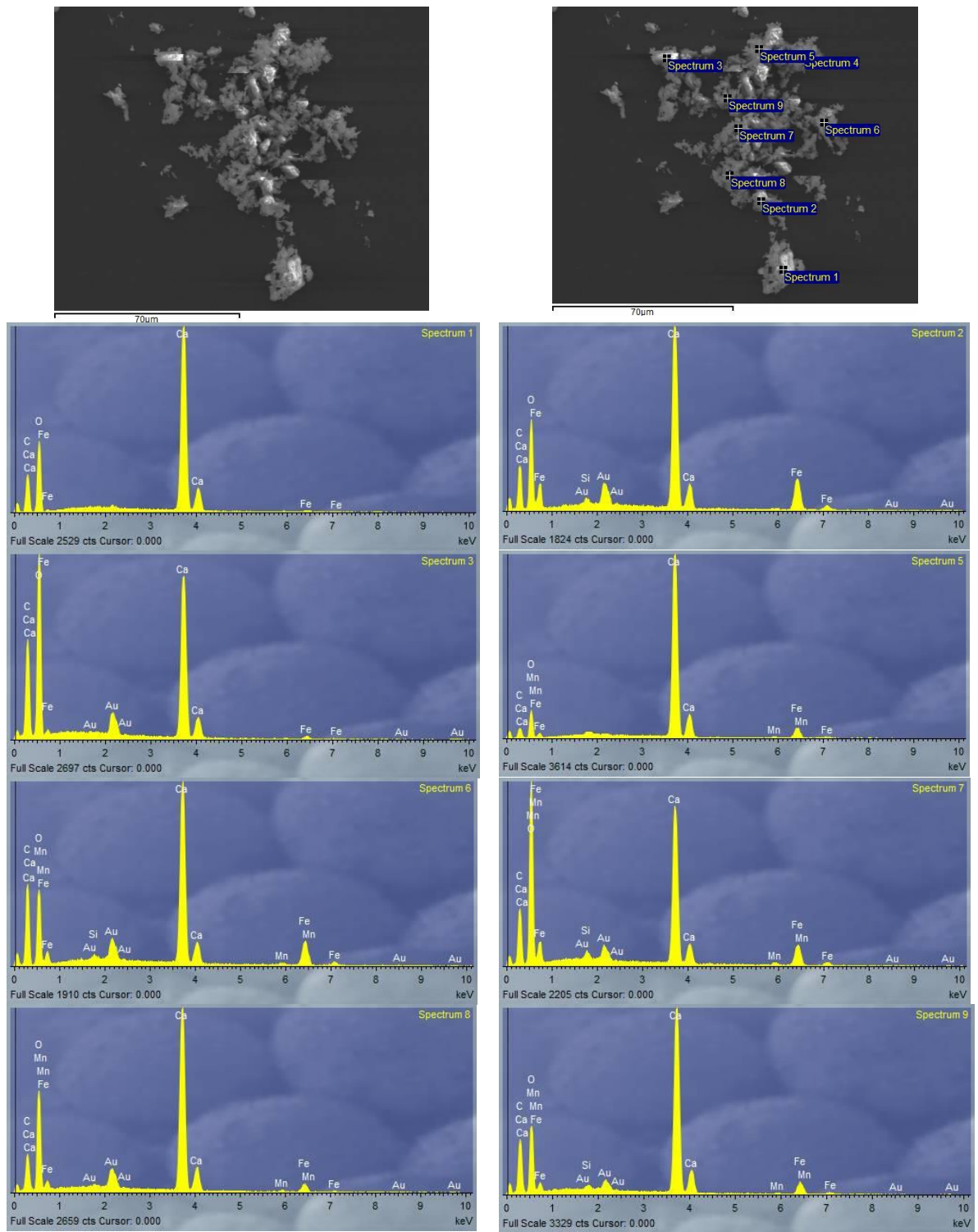
Carbonatite

Figure C9. Photomicrograph and spectral analysis of a grain in carbonatite at room temperature.
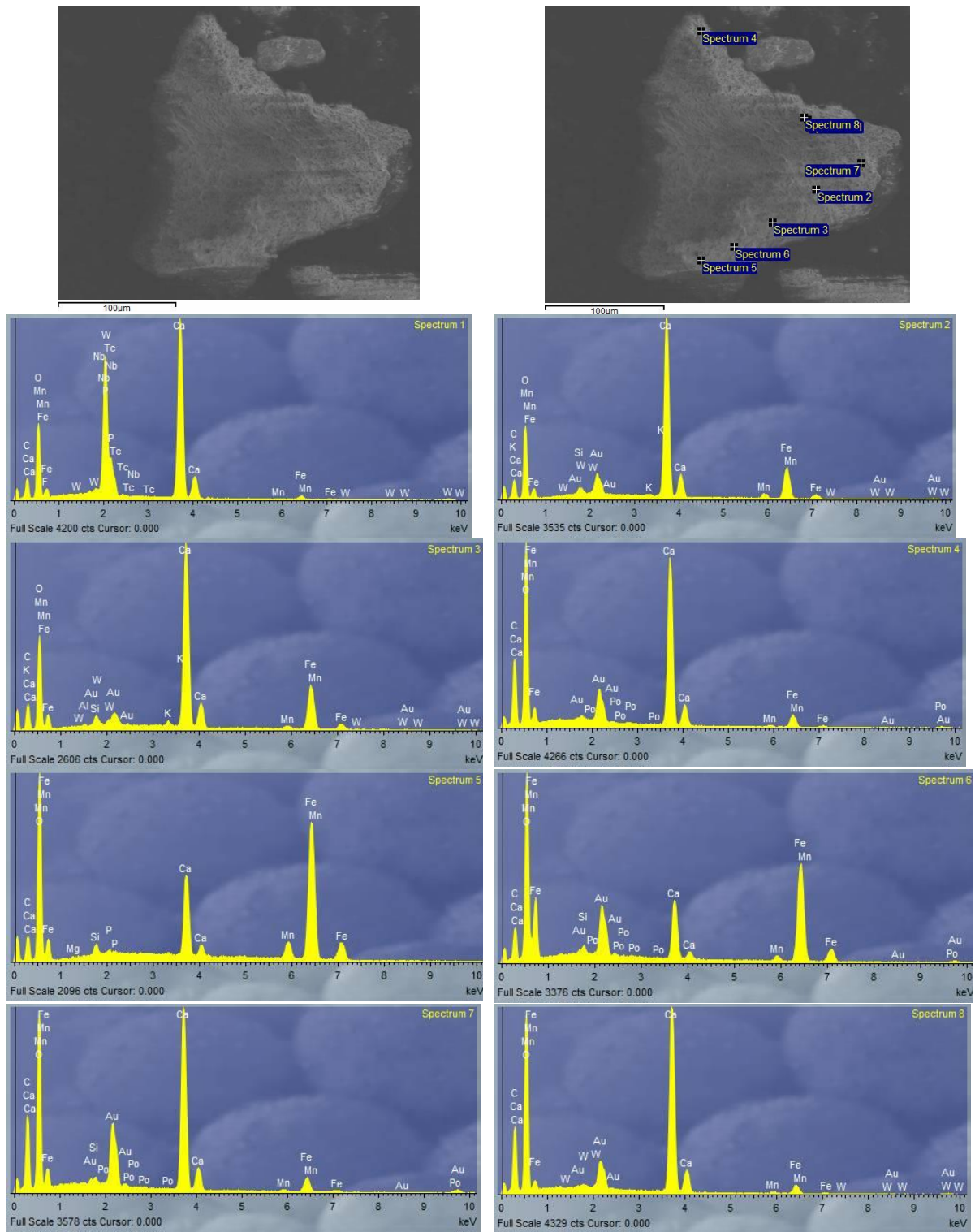
Figure C10. Photomicrograph and spectral analysis of a grain in Na-treated carbonatite at room temperature.
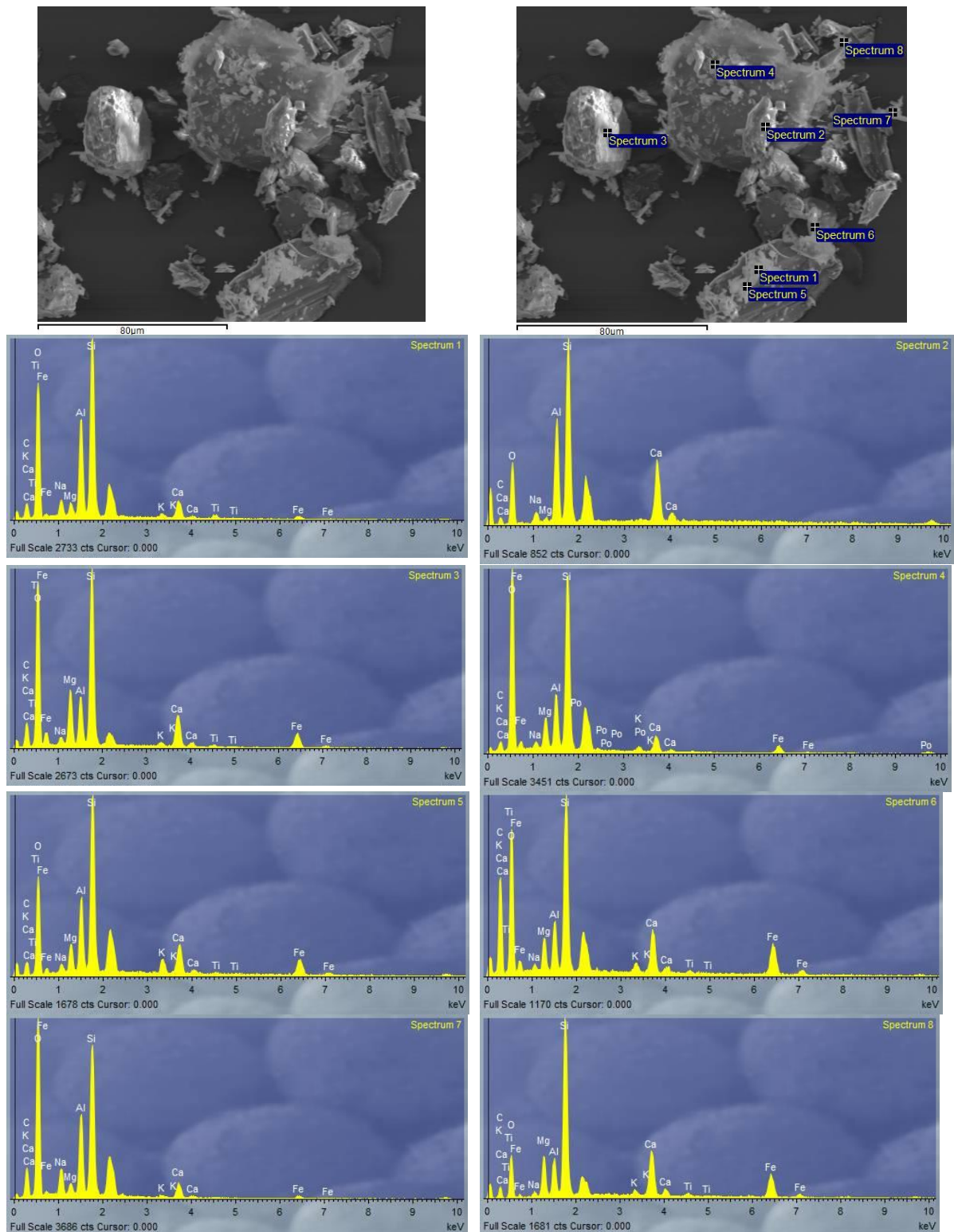
Gabbro

Figure C11. Photomicrograph and spectral analysis of a grain in gabbro at room temperature.
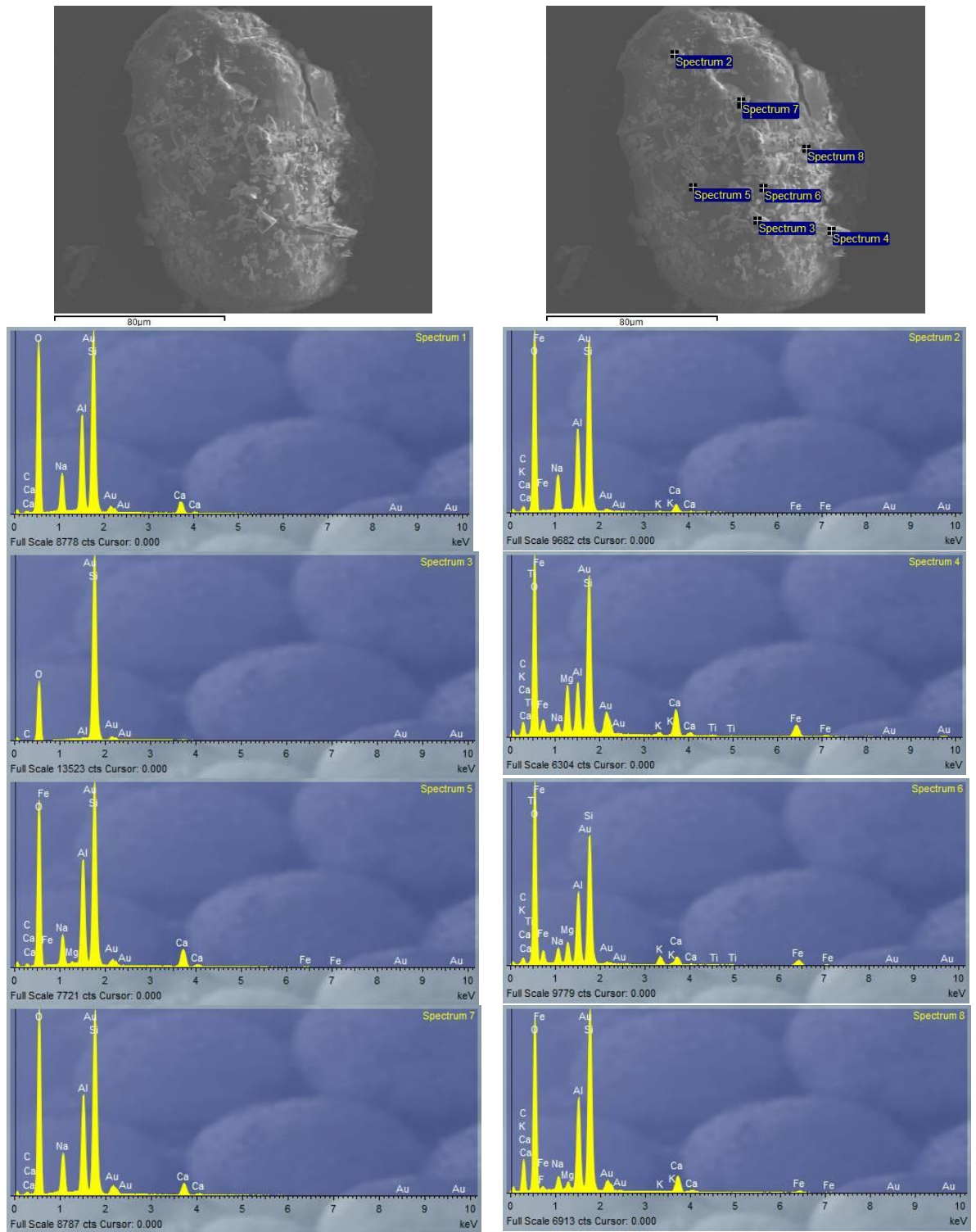
Figure C12. Photomicrograph and spectral analysis of a grain in Na-treated gabbro at room temperature.
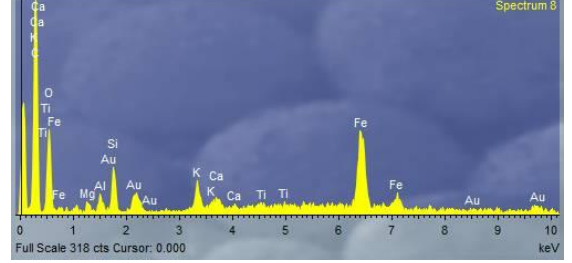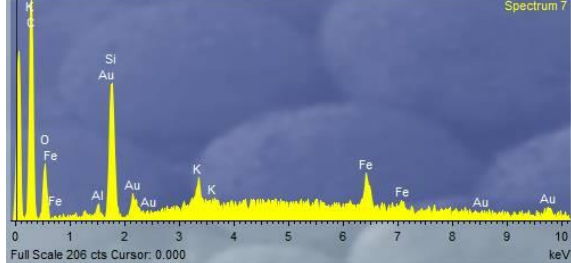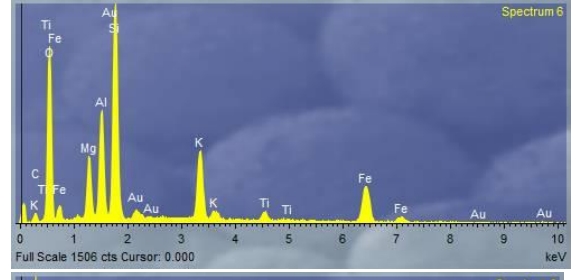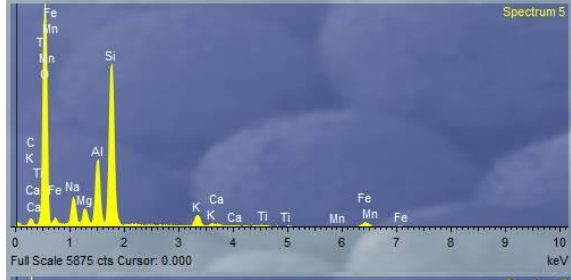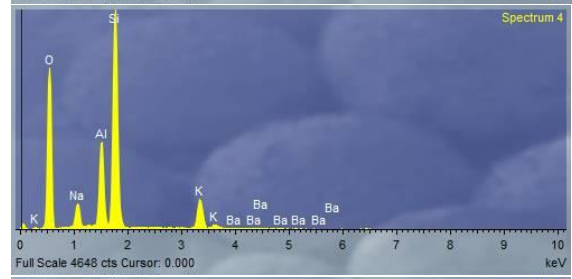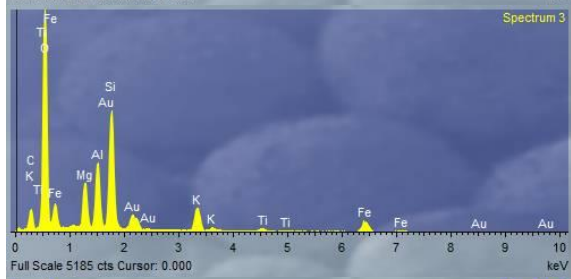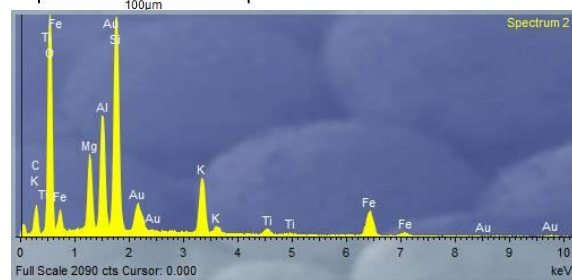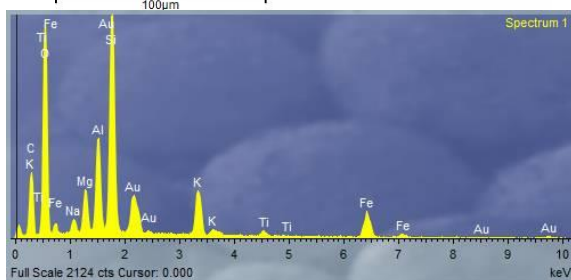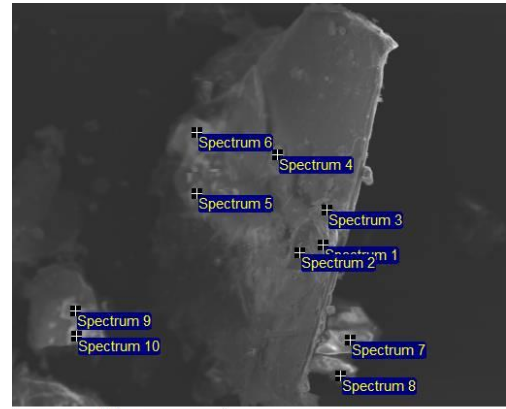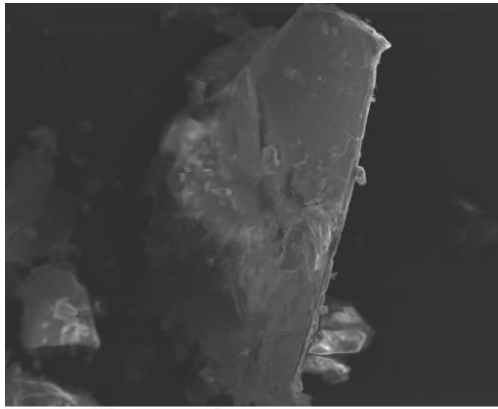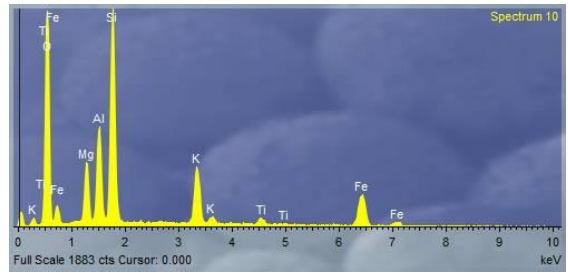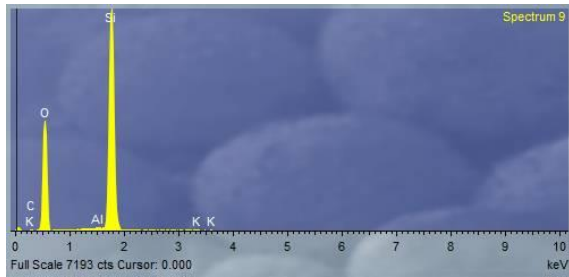
Granite

Figure C13. Photomicrograph and spectral analysis of a grain in granite at room temperature.
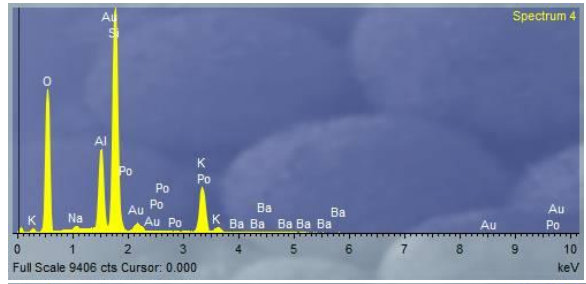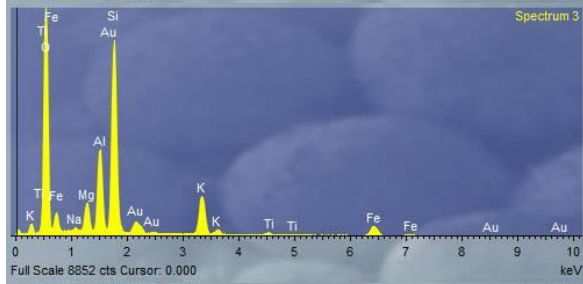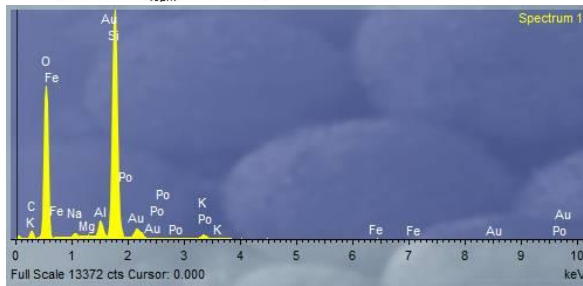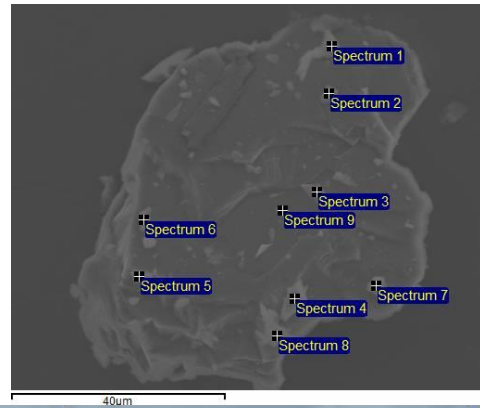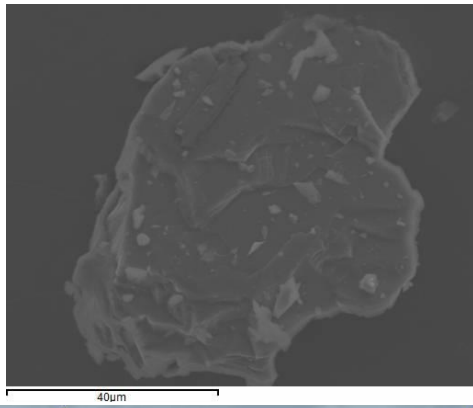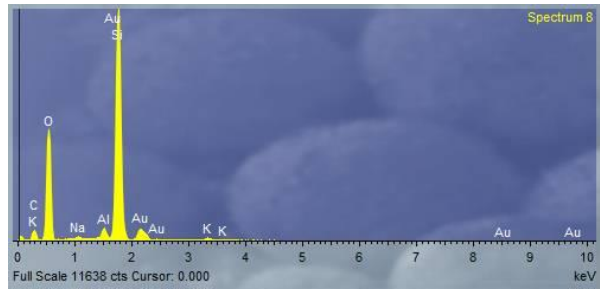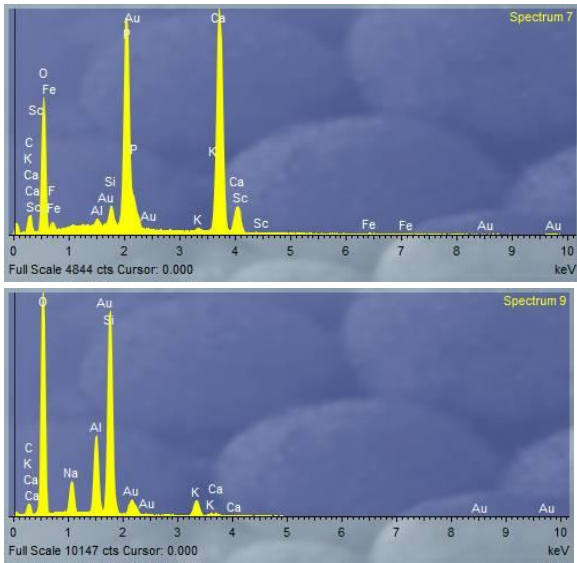
Figure C14. Photomicrograph and spectral analysis of a grain in Na-treated granite at room temperature.
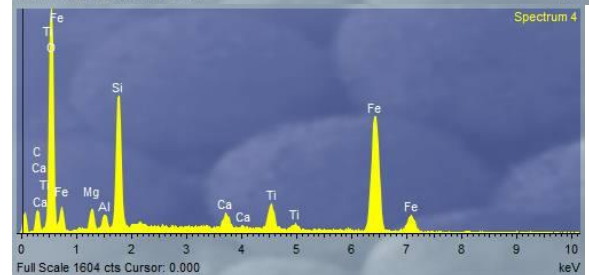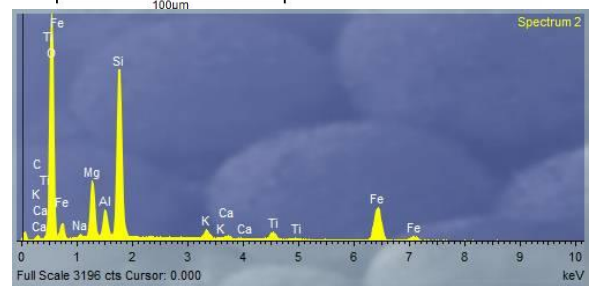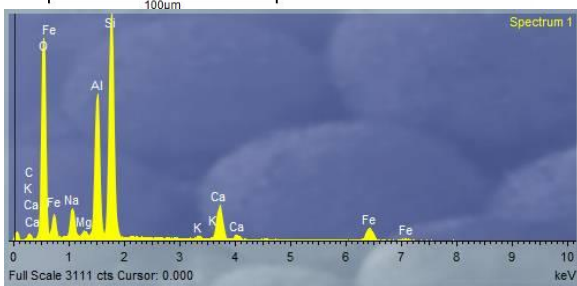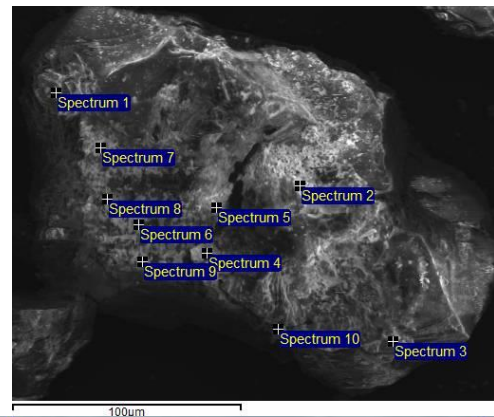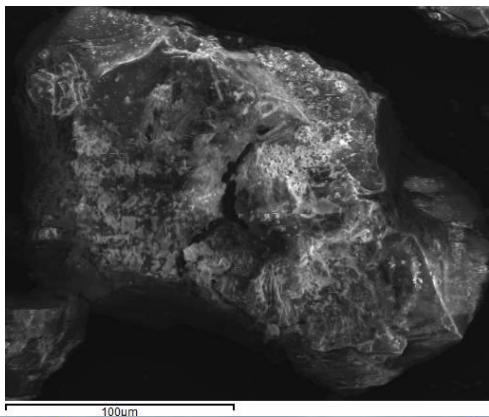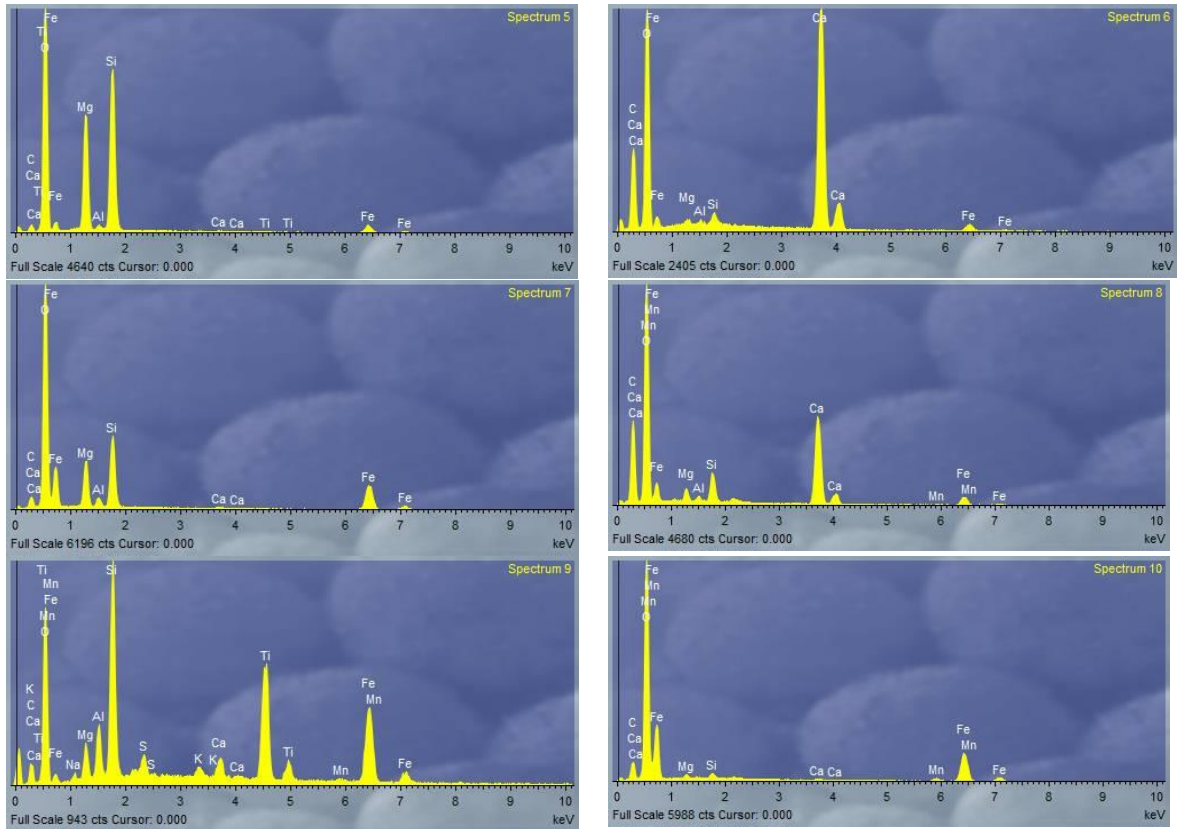
Dolerite

Figure C15. Photomicrograph and spectral analysis of a grain in dolerite at room temperature.
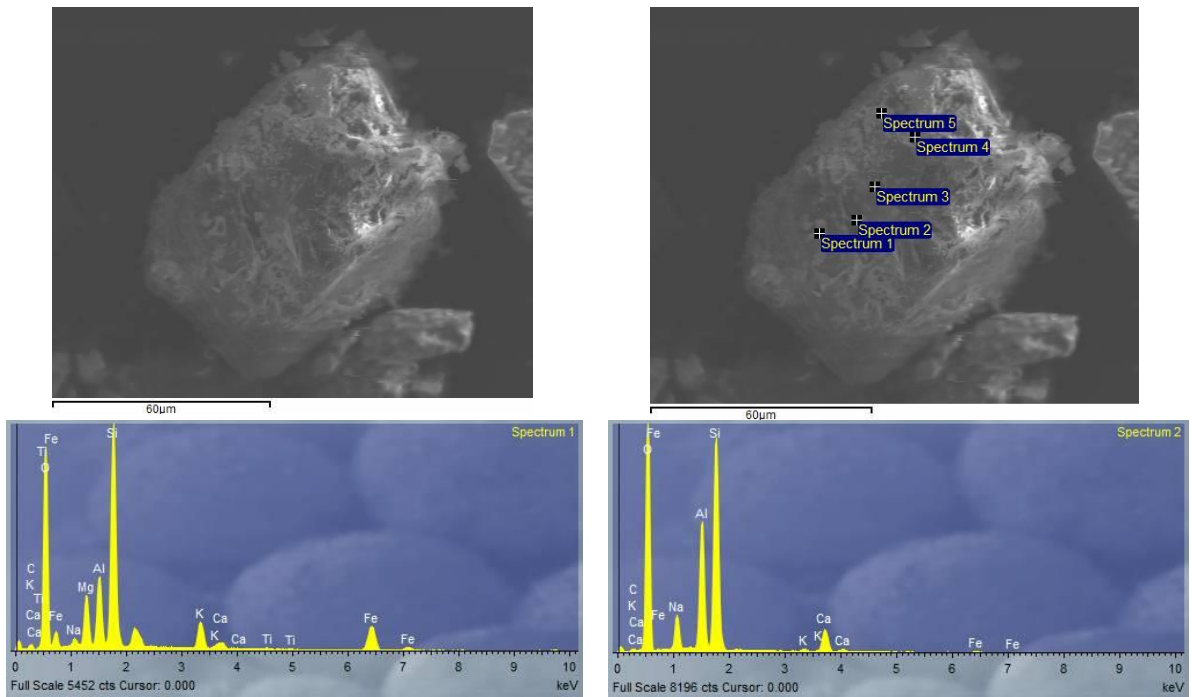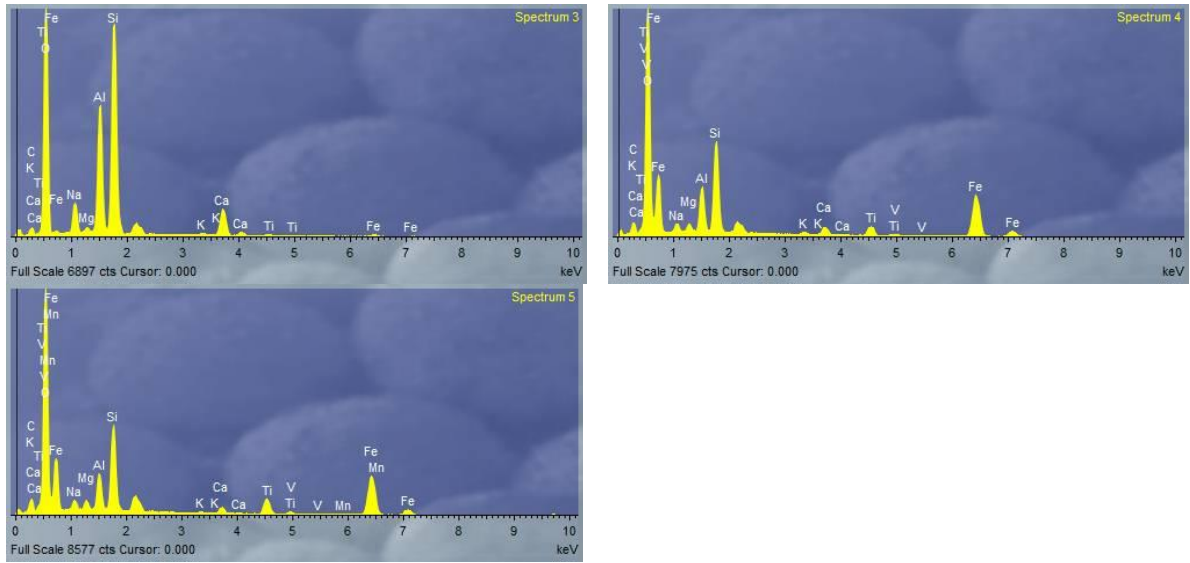
Figure C16. Photomicrograph and spectral analysis of a grain in Na-treated dolerite at room temperature.
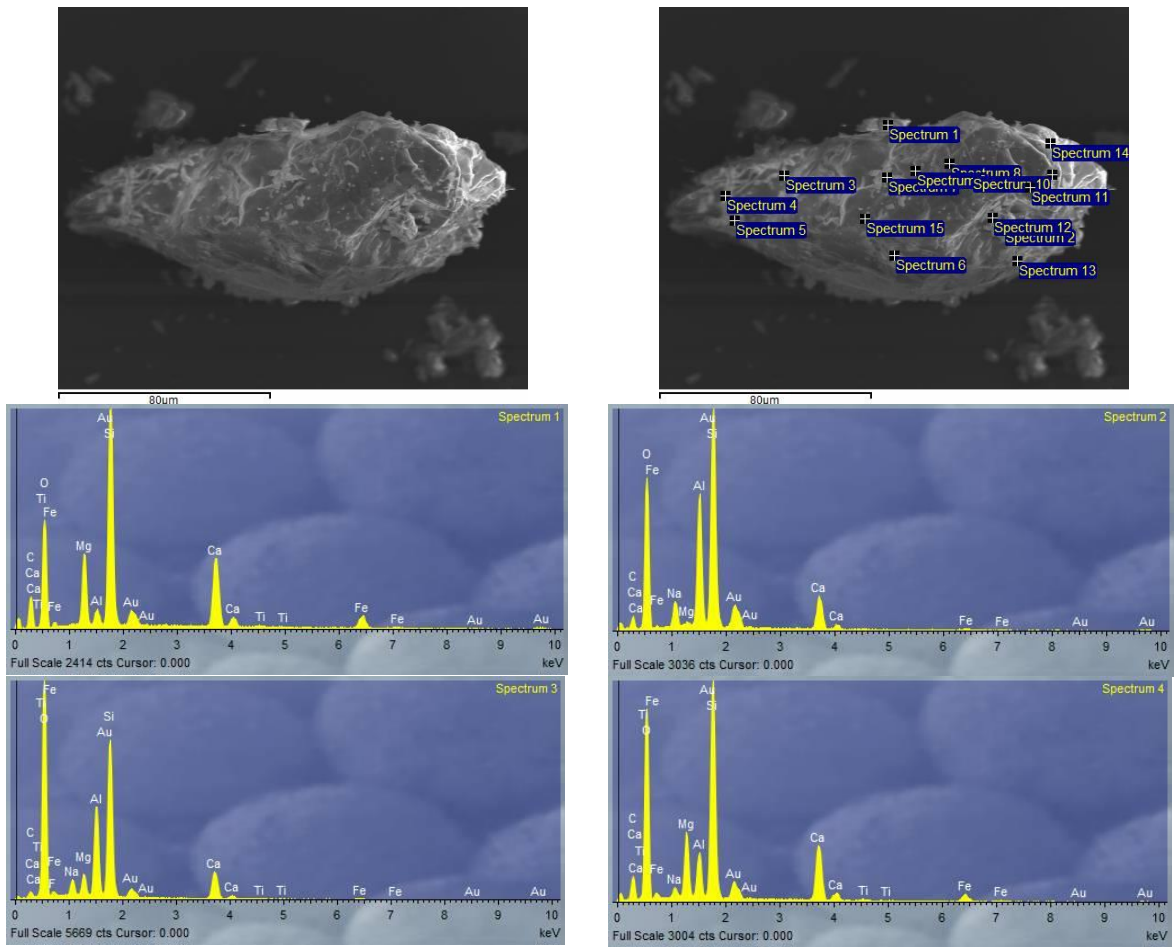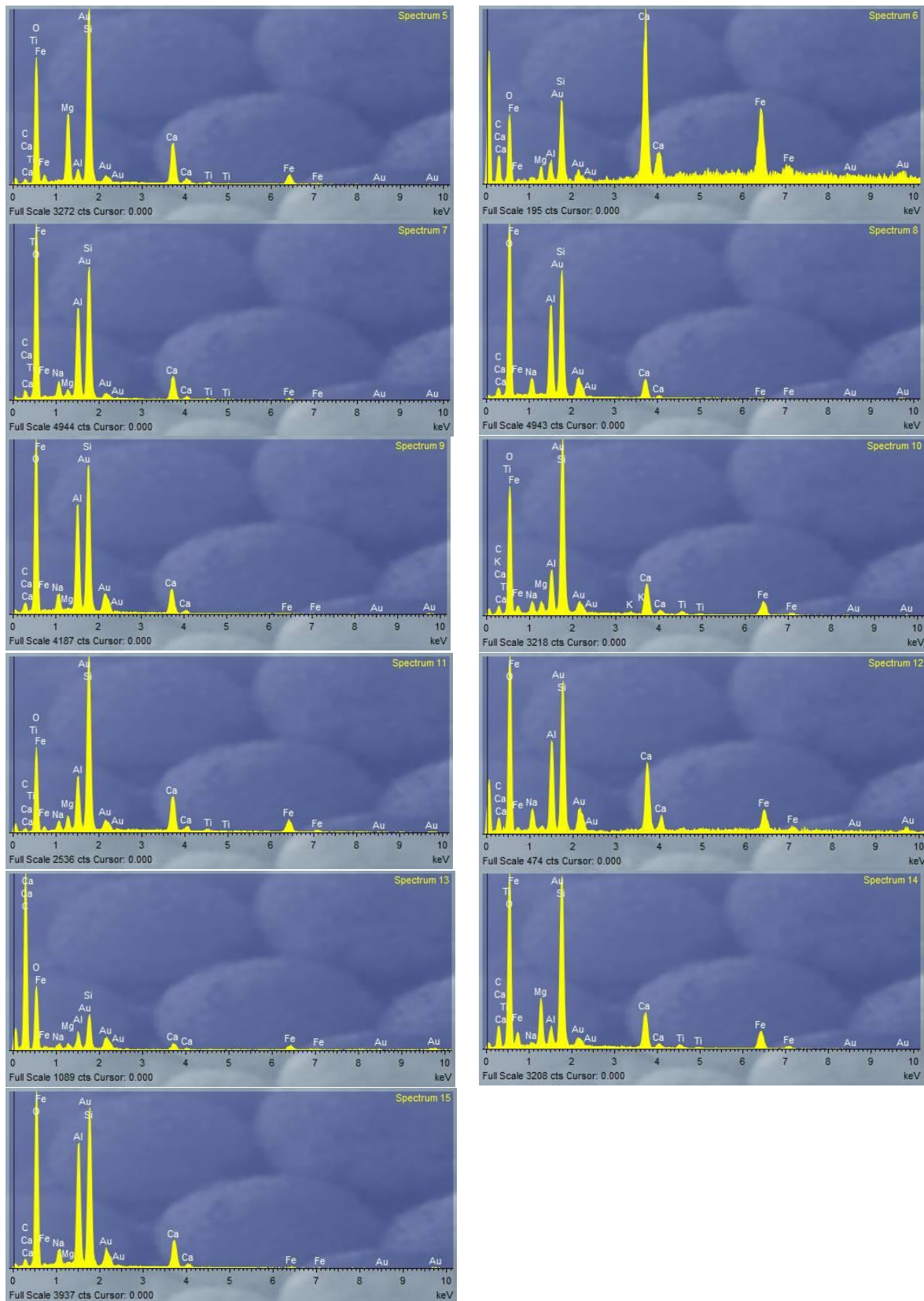
Basalt

Figure C17. Photomicrograph and spectral analysis of a grain in basalt at room temperature.
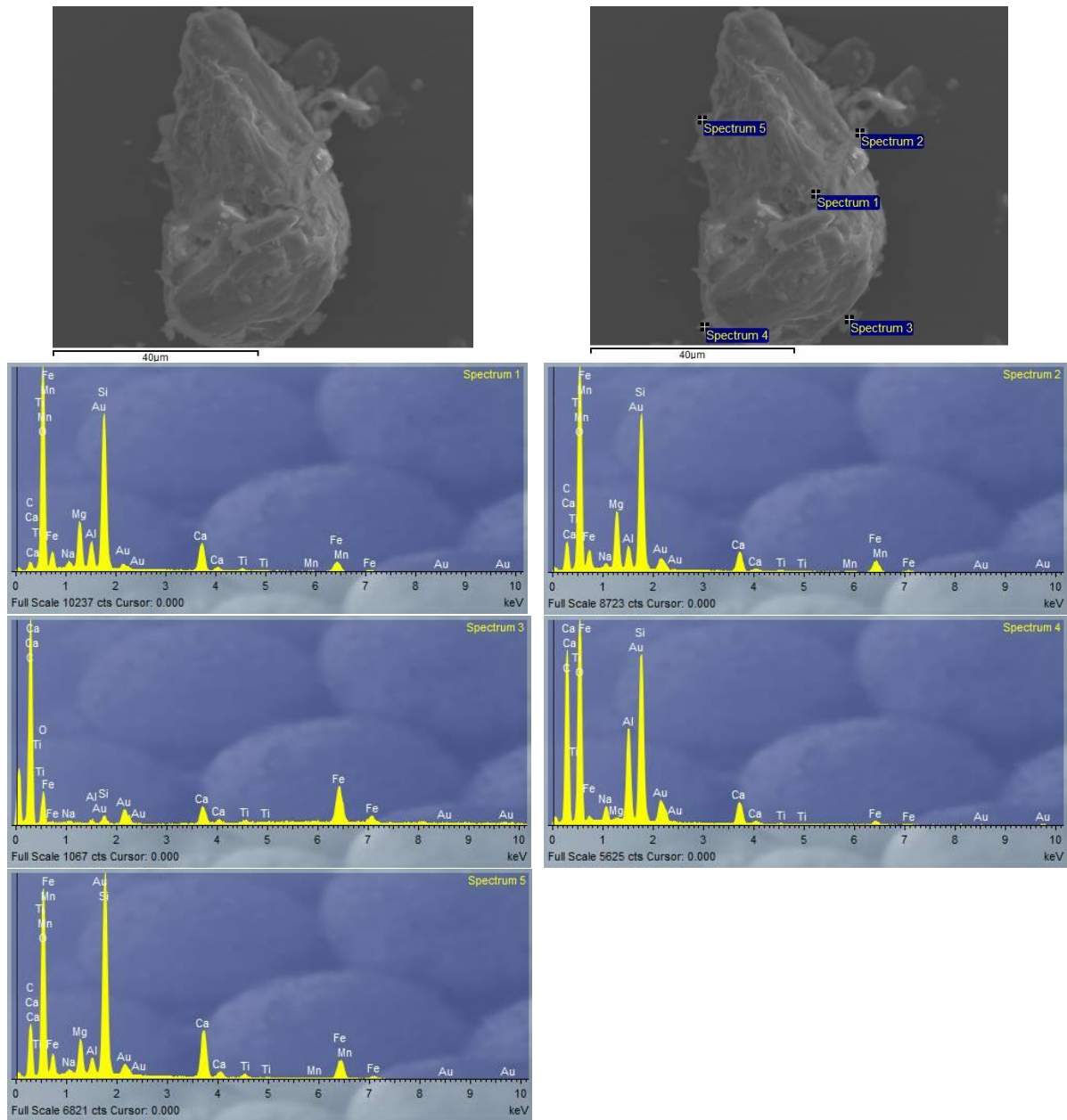
Figure C18. Photomicrograph and spectral analysis of a grain in Na-treated basalt at room temperature.

C3. Experiments at 50°C
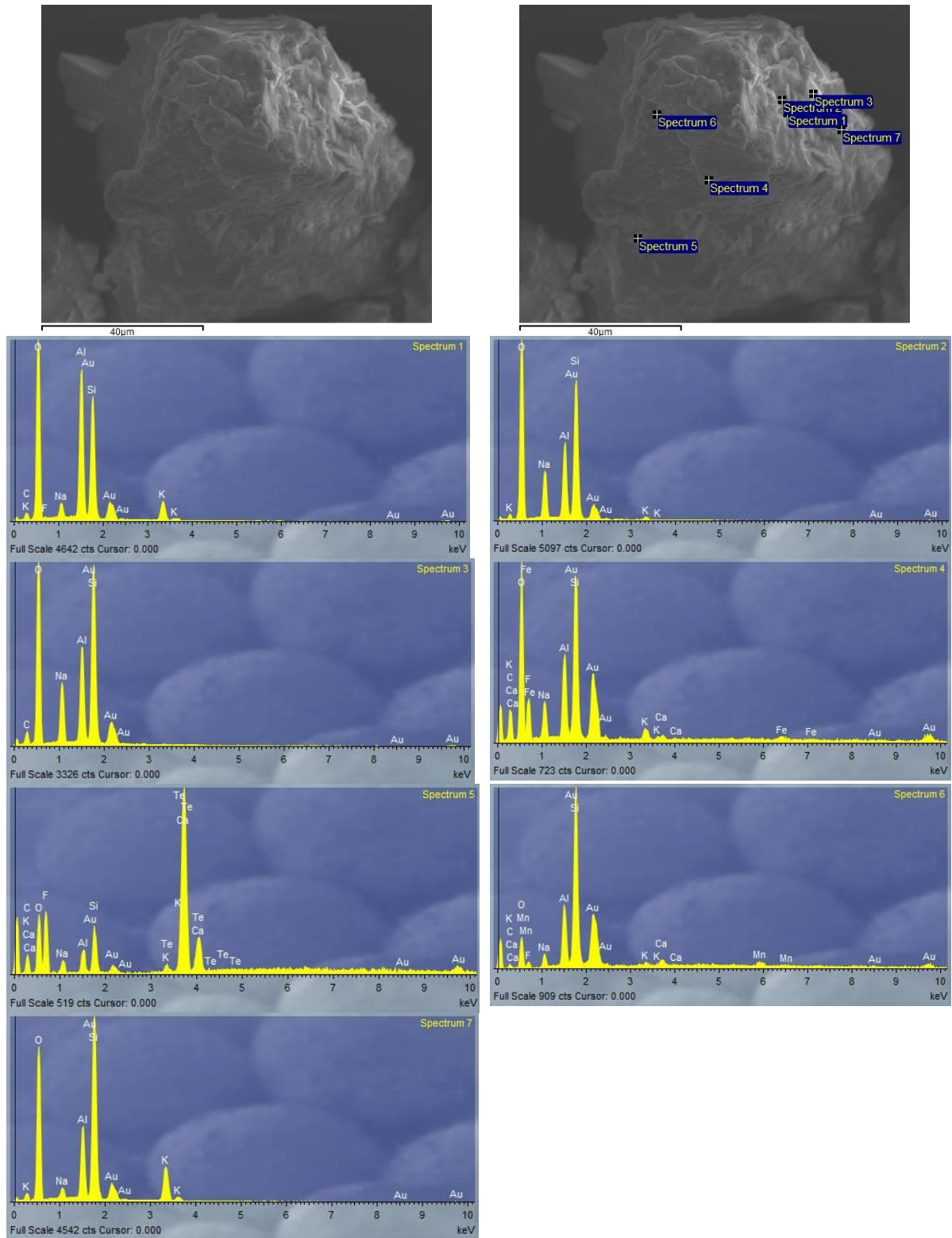
Syenite

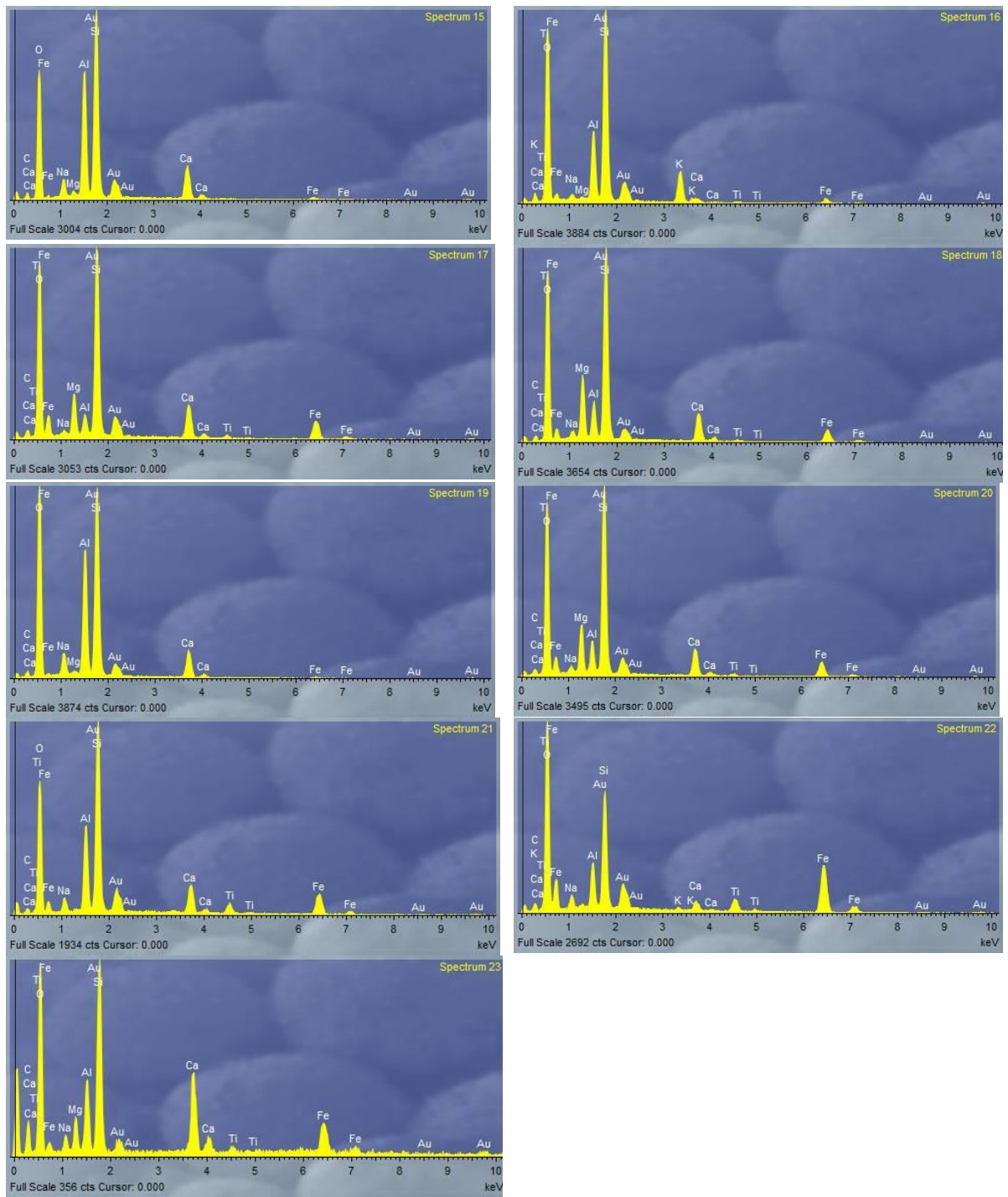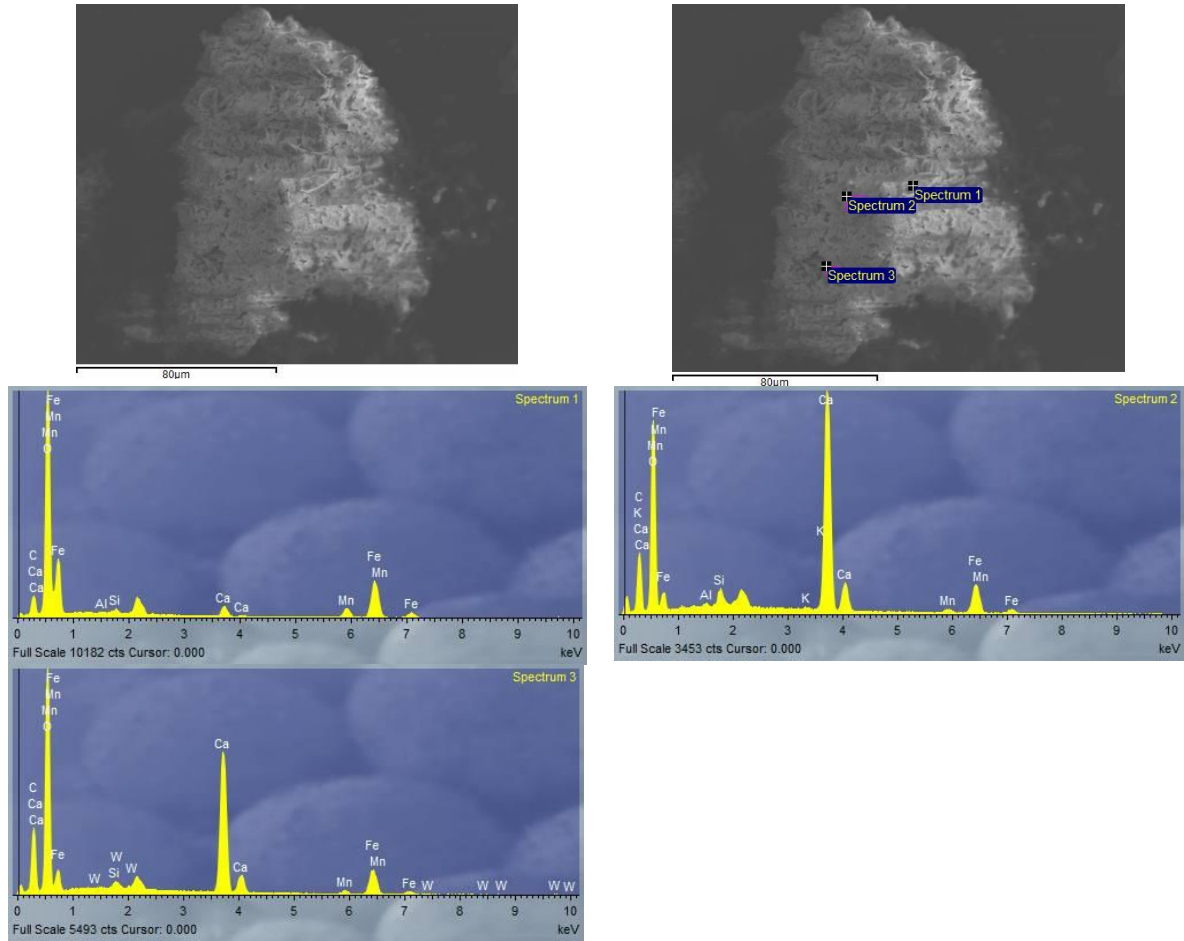*Figure C19. Photomicrograph and spectral analysis of a grain in syenite dissolved at 50°C.*
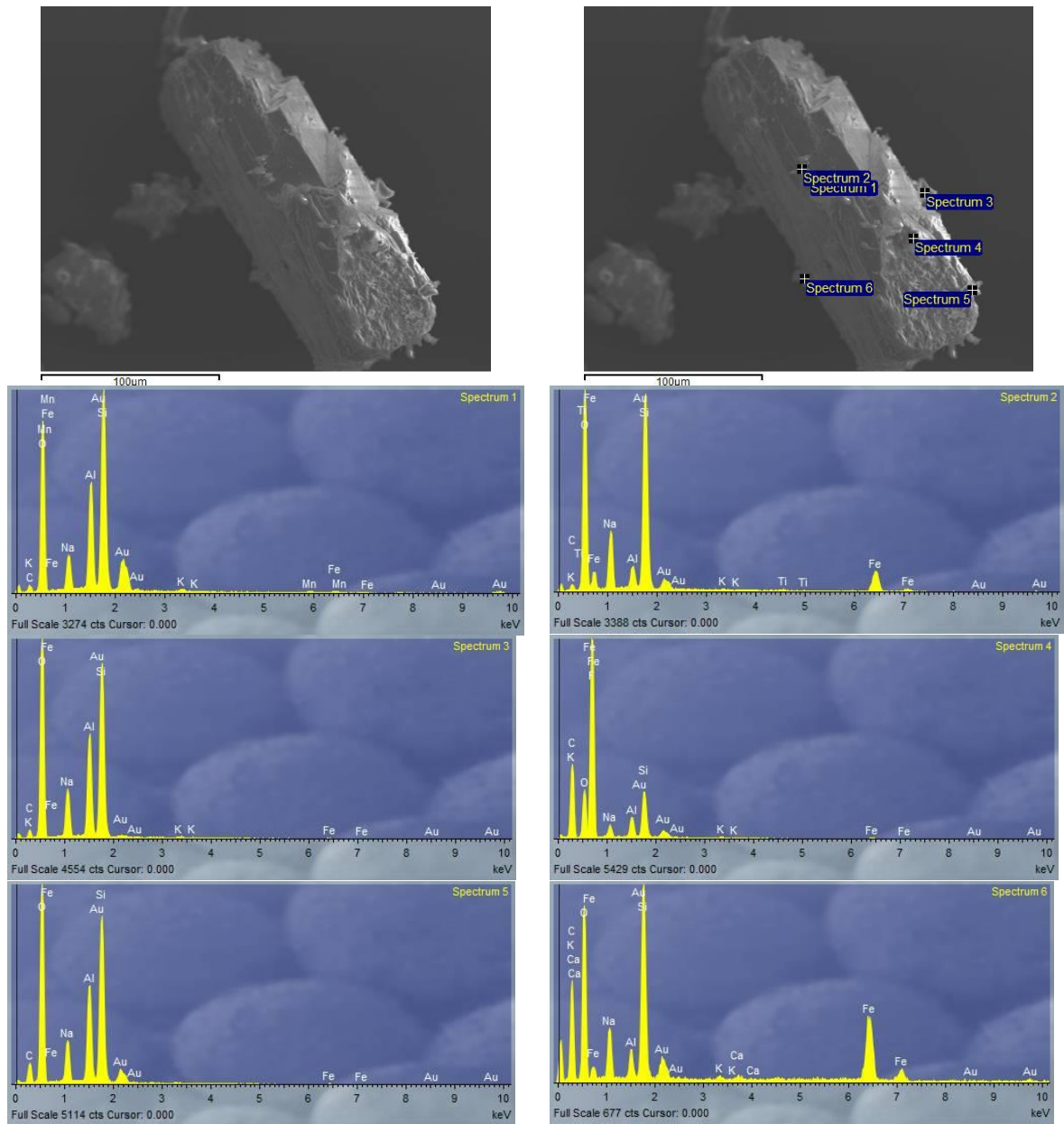
Figure C20. Photomicrograph and spectral analysis of a grain in Na-treated syenite dissolved at 50°C.
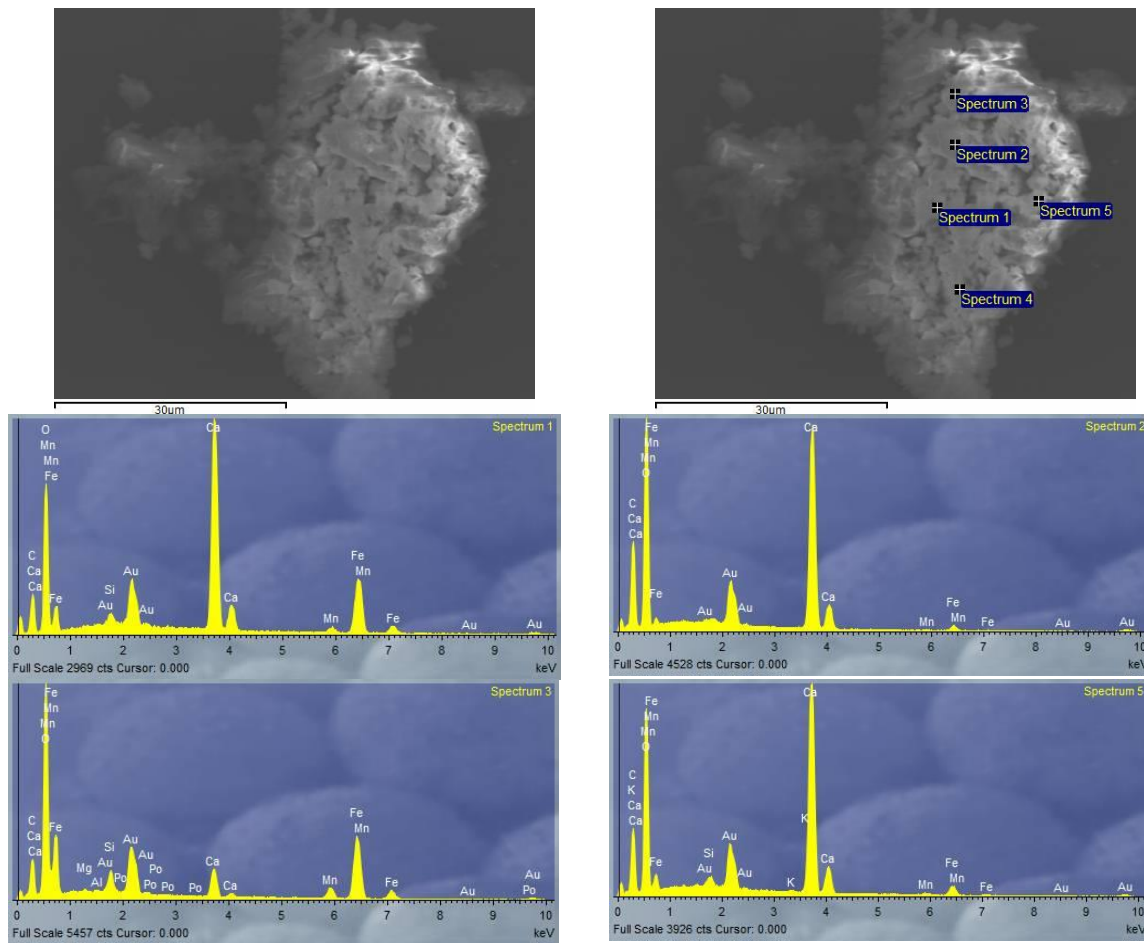
Carbonatite
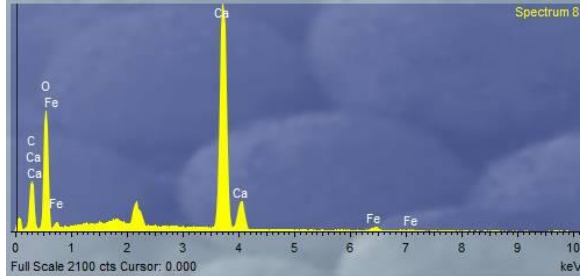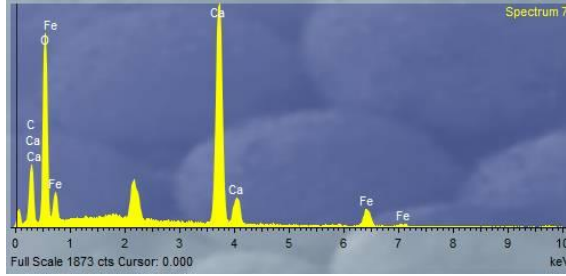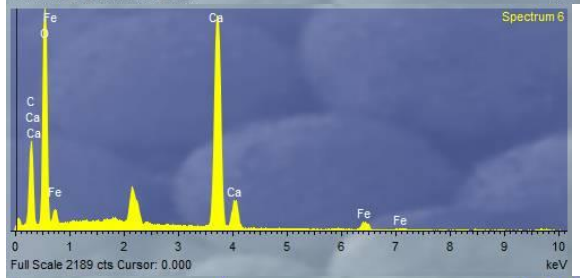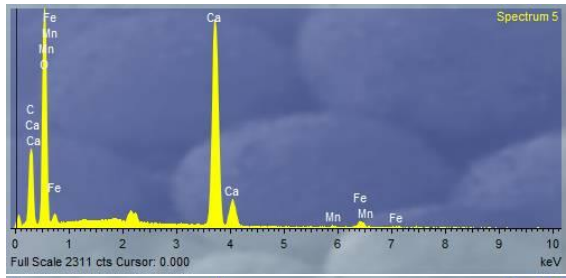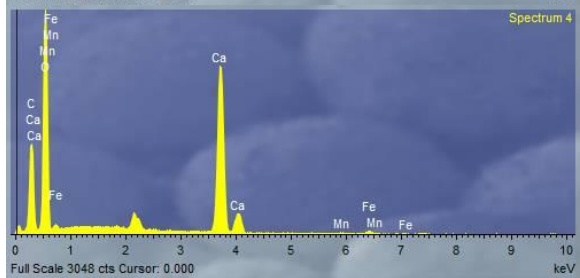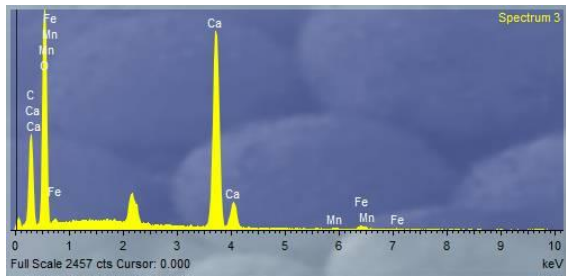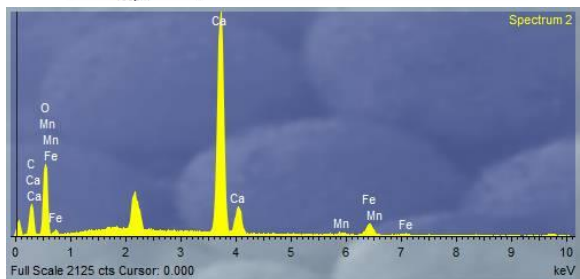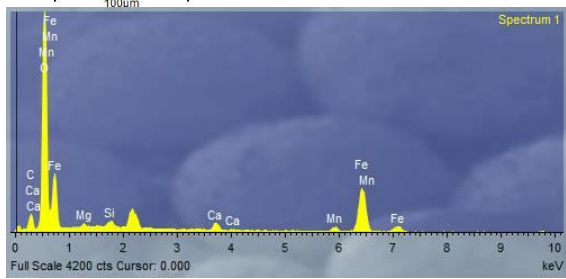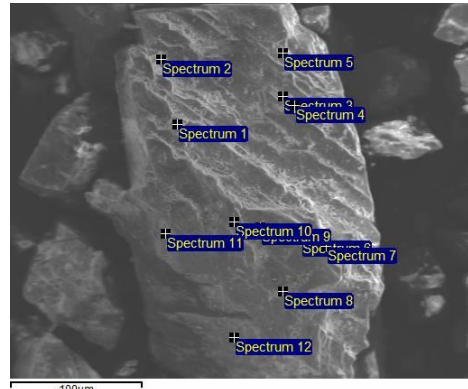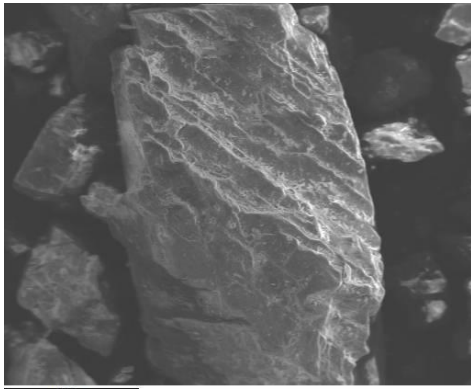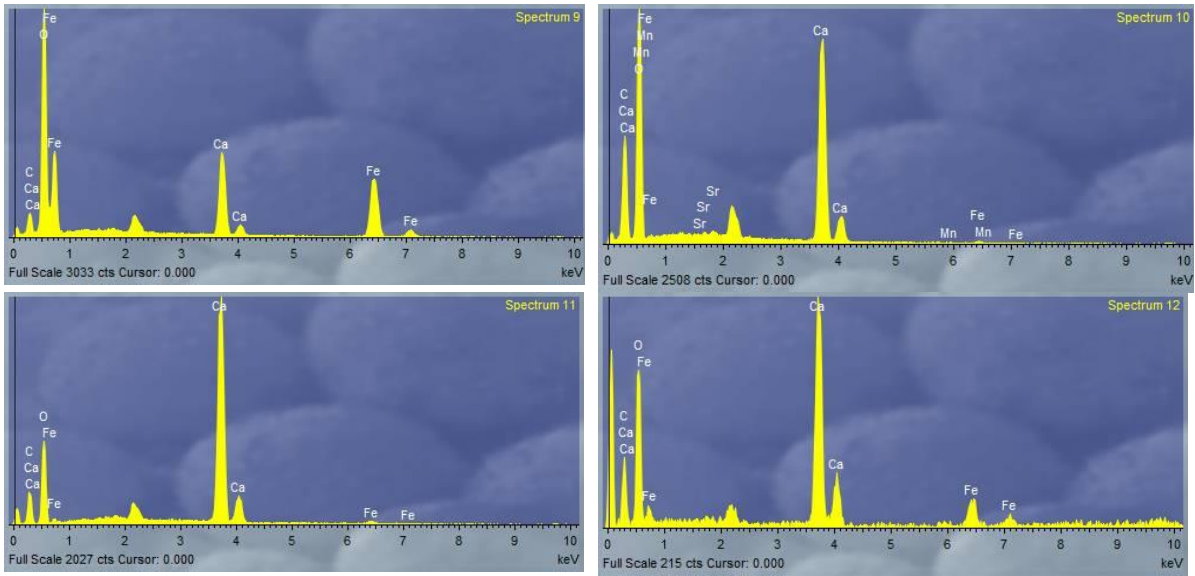
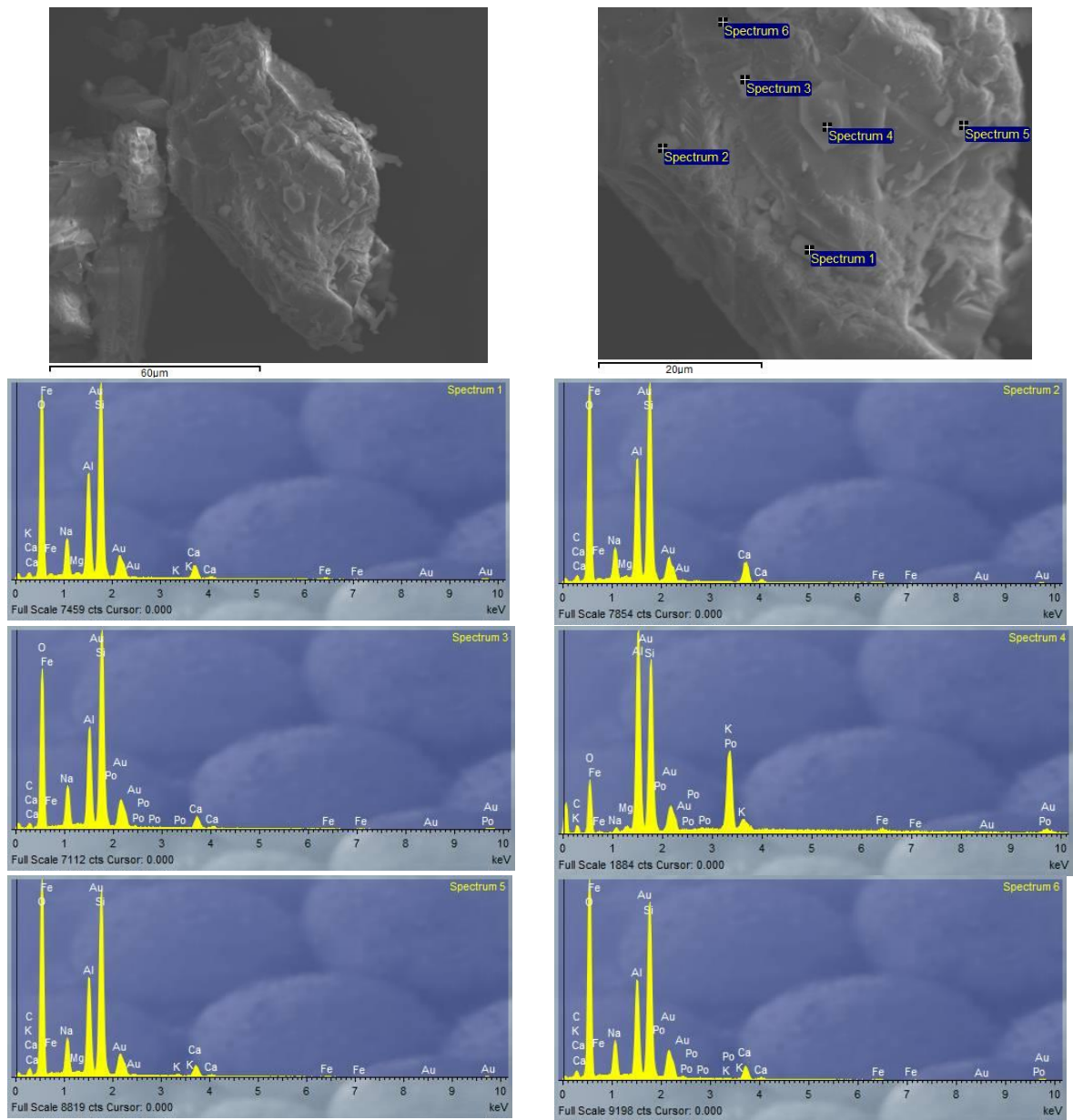Figure C21. Photomicrograph and spectral analysis of a grain in carbonatite dissolved at 50°C.
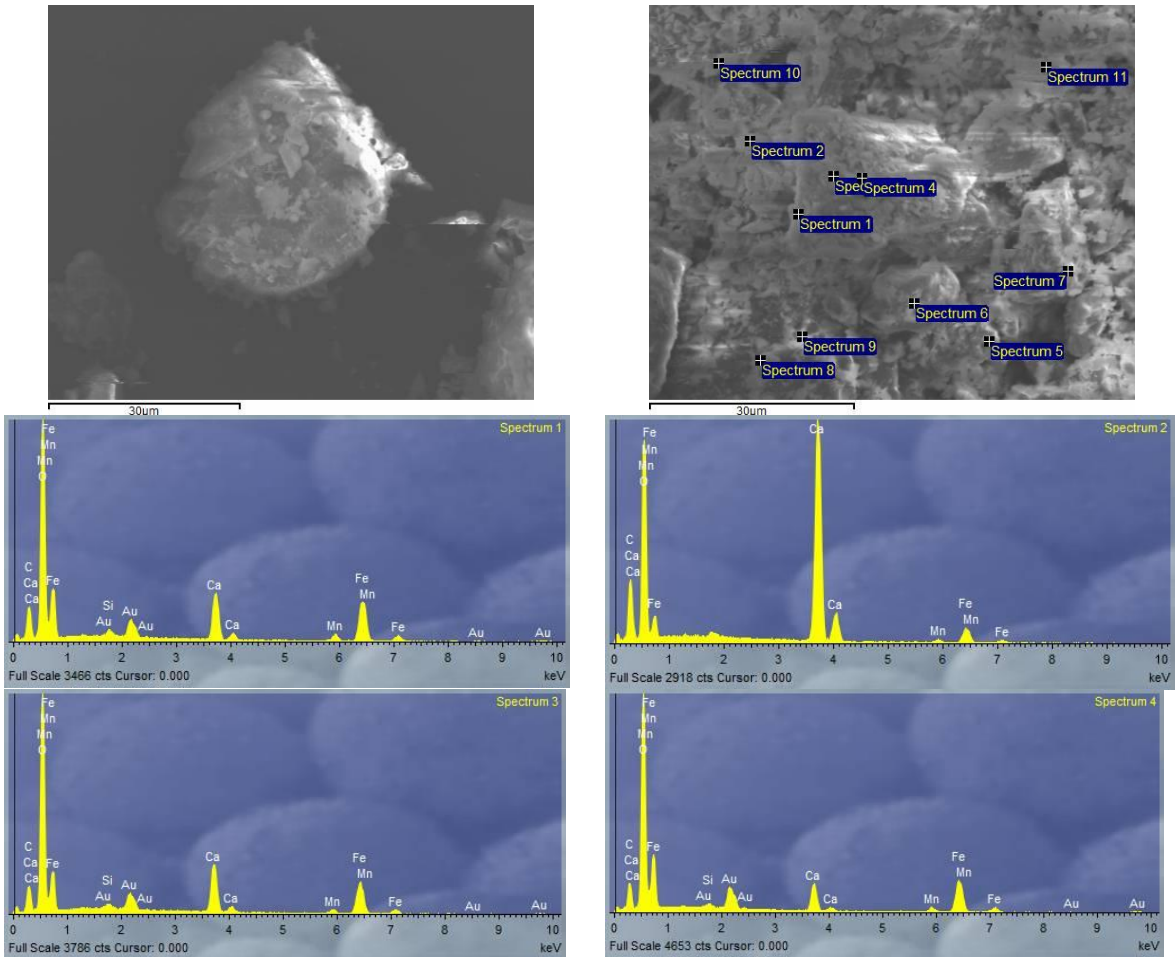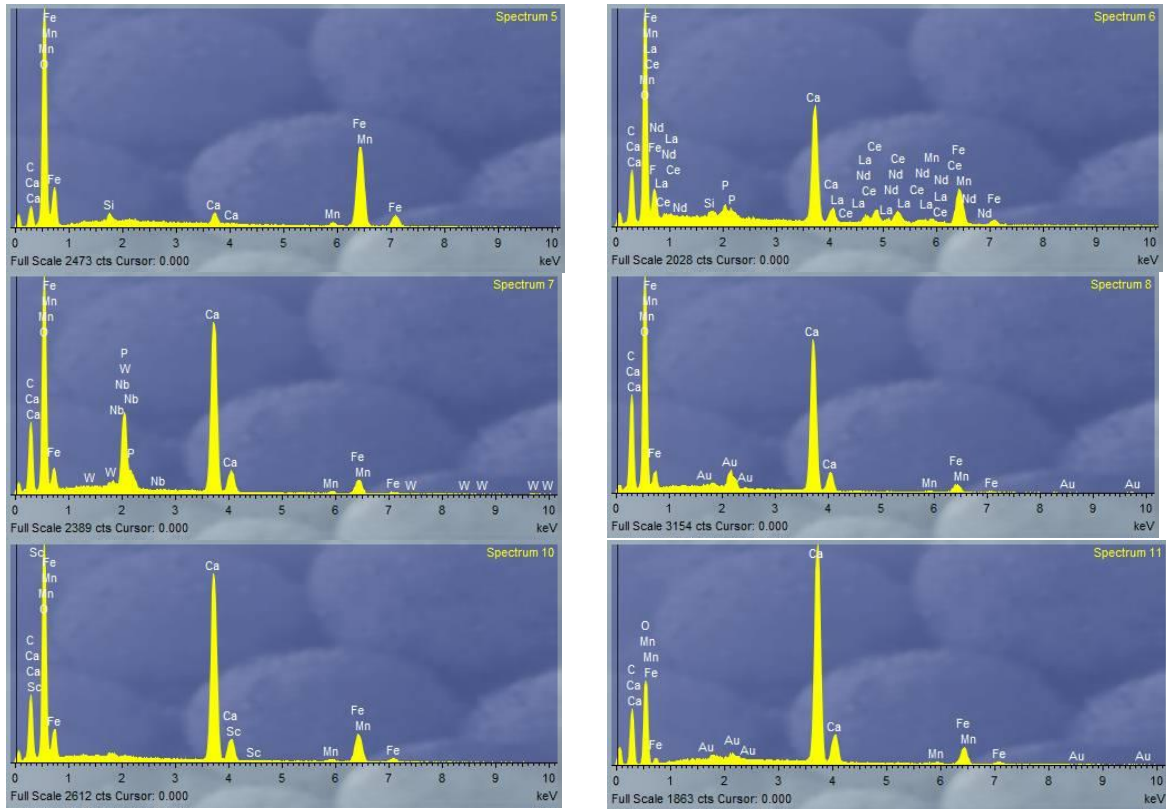
Figure C22. Photomicrograph and spectral analysis of a grain in Na-treated carbonatite dissolved at 50°C. Upper right image is a zoom-in of the left photomicrograph.

Gabbro
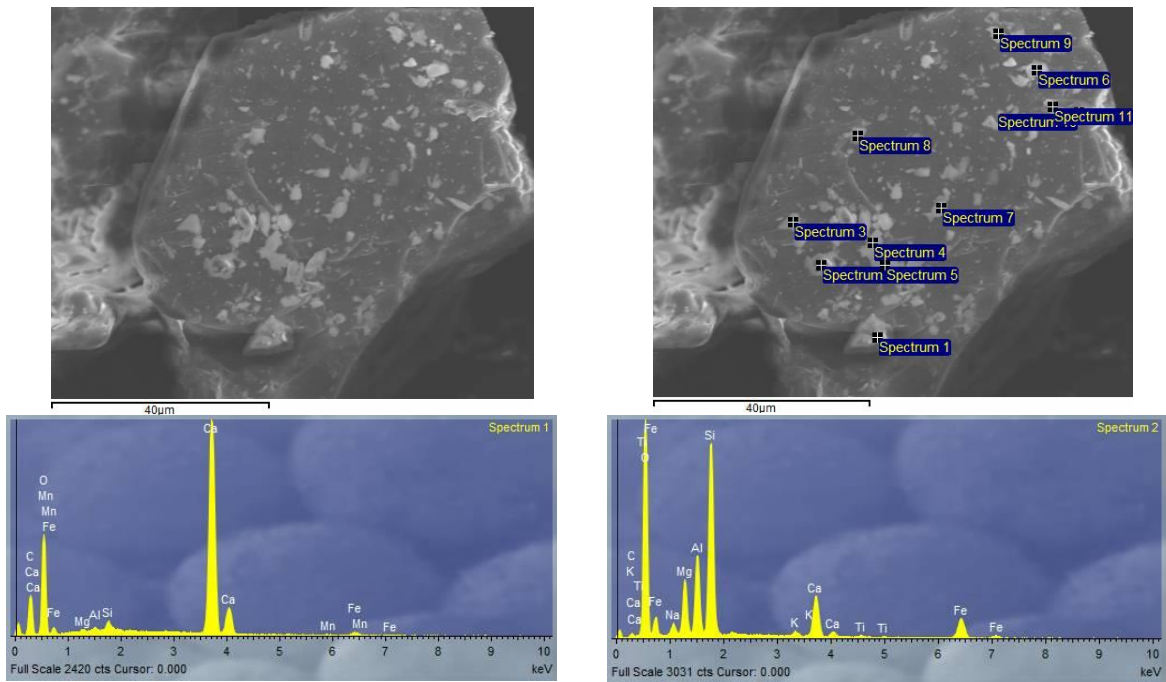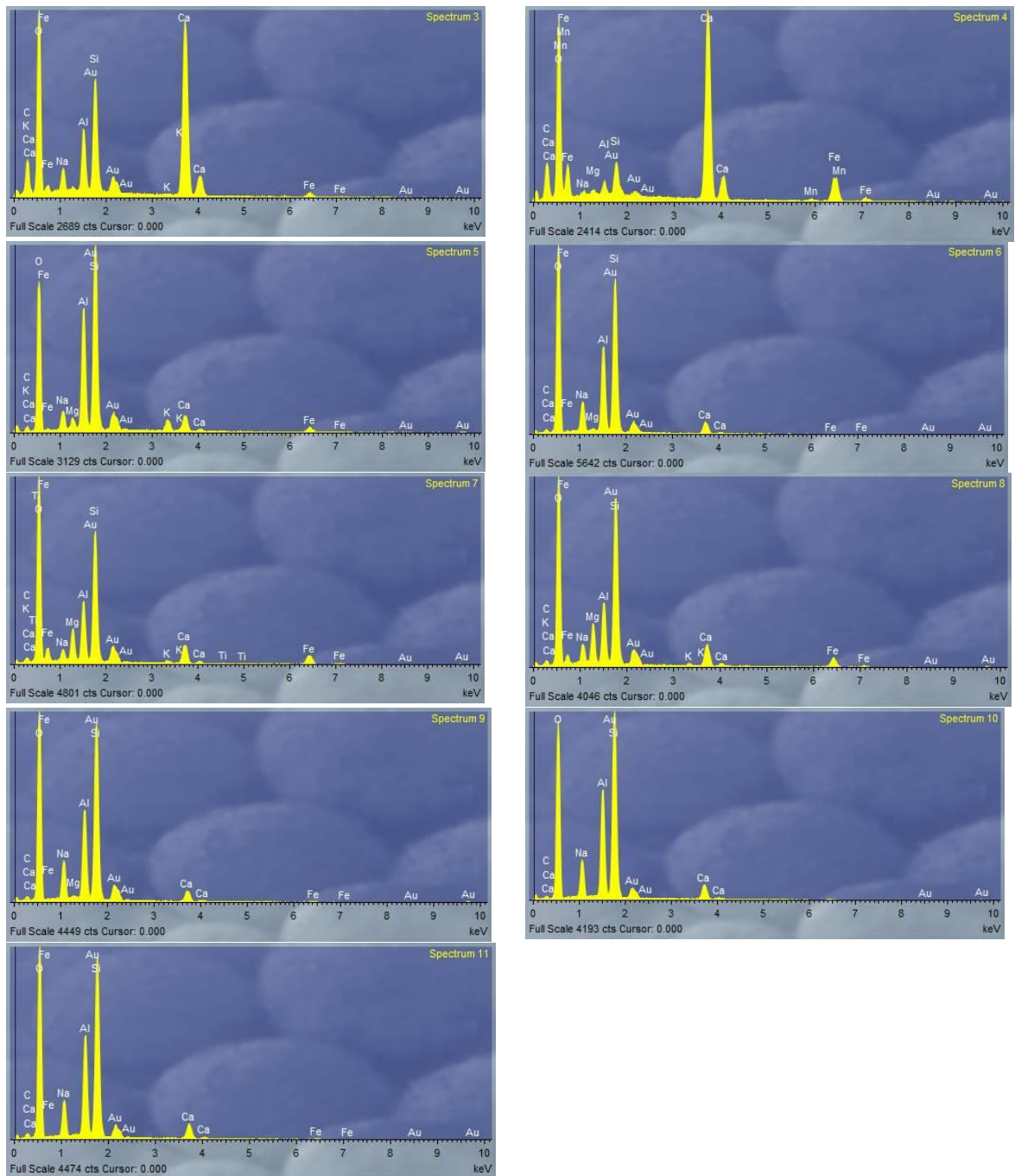
Figure C23. Photomicrograph and spectral analysis of a grain in gabbro dissolved at 50°C.
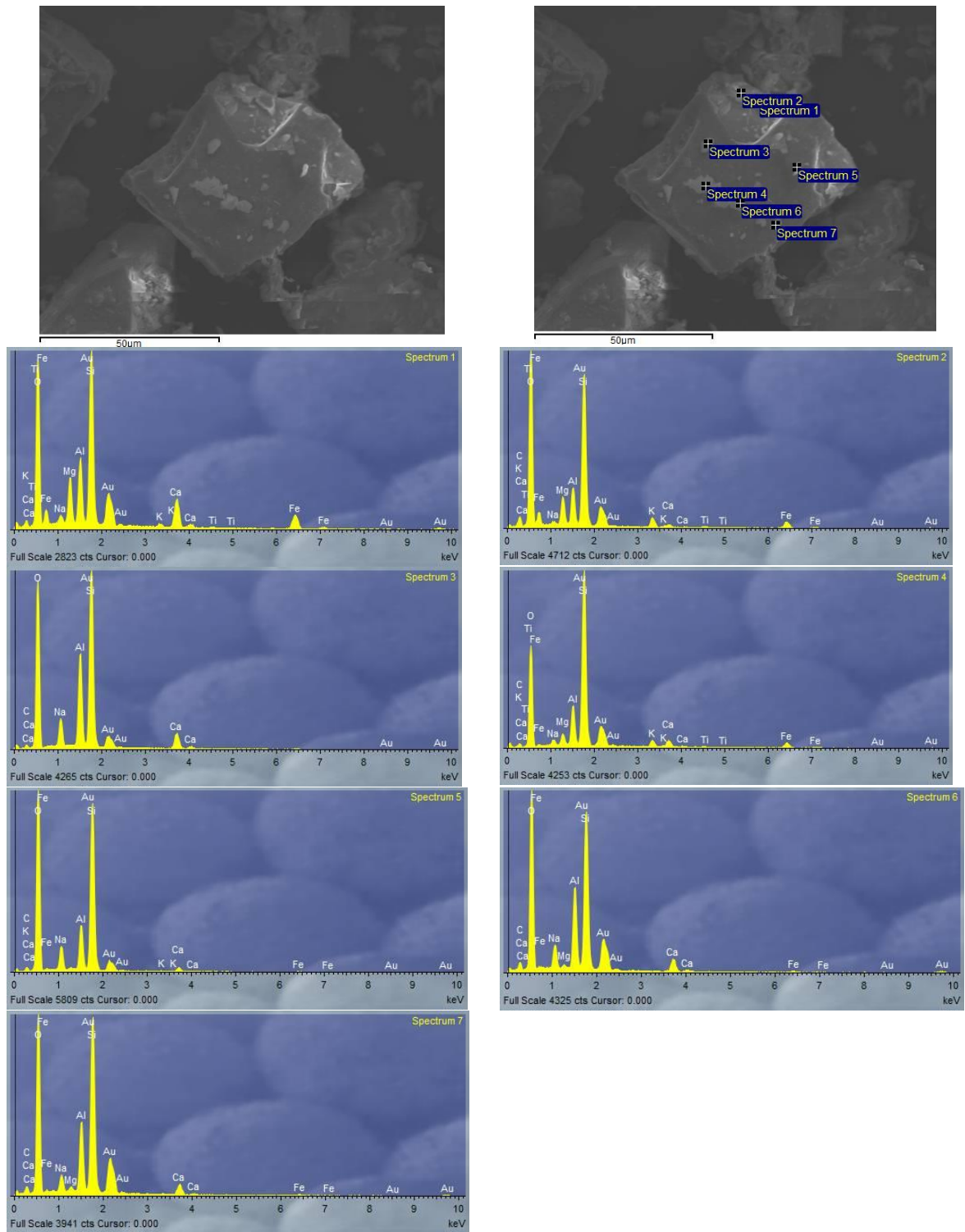
Figure C24. Photomicrograph and spectral analysis of a grain in Na-treated gabbro dissolved at 50°C.

Granite
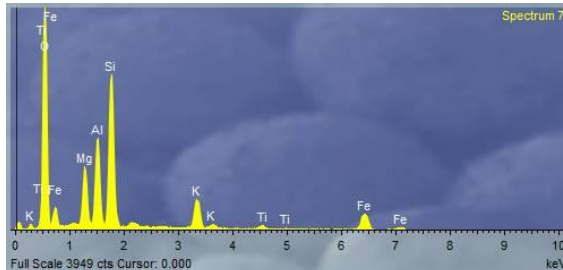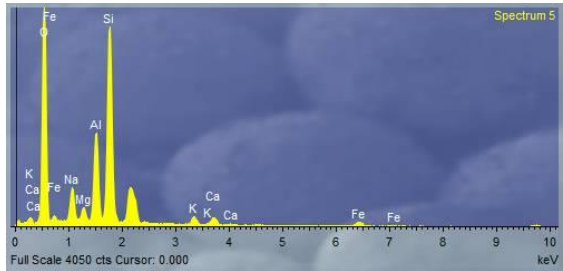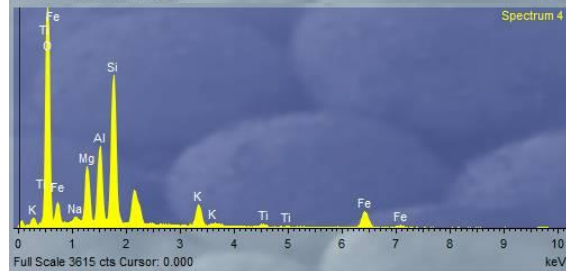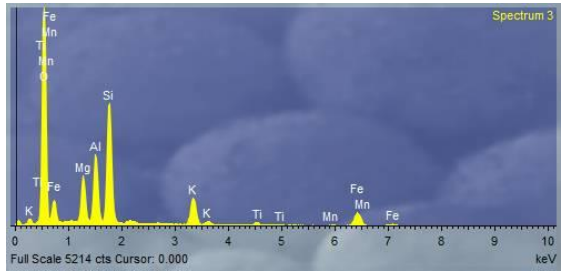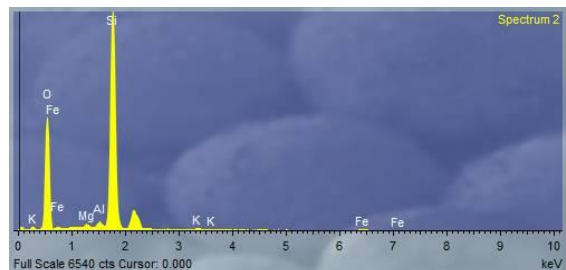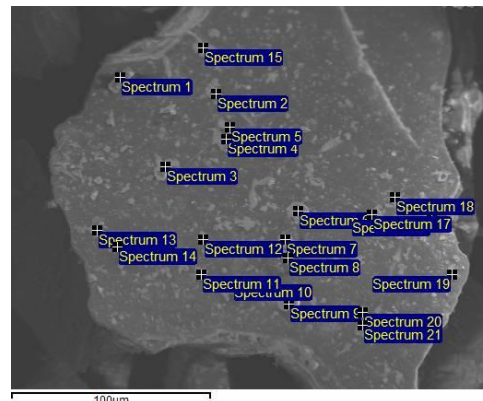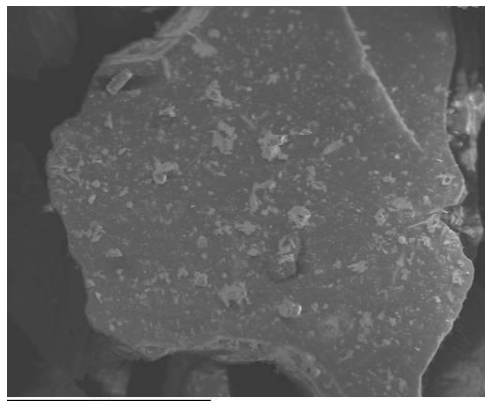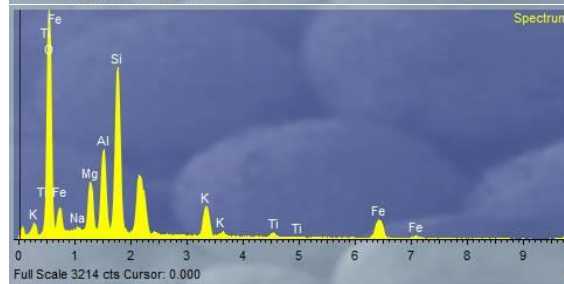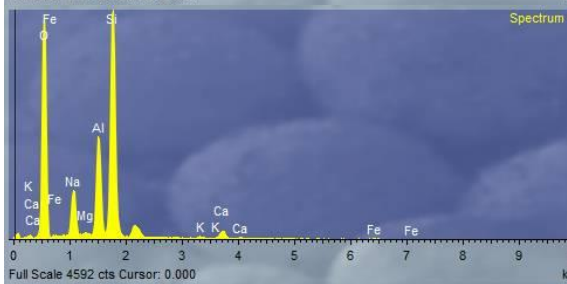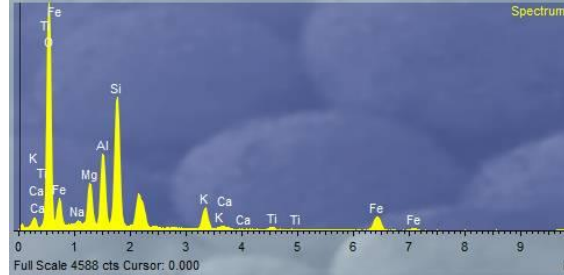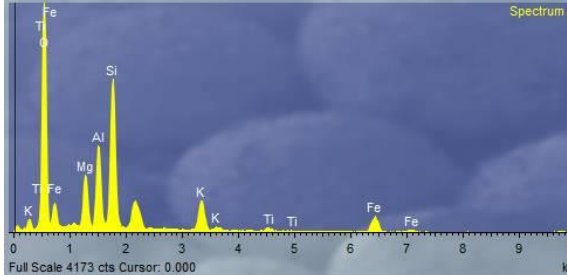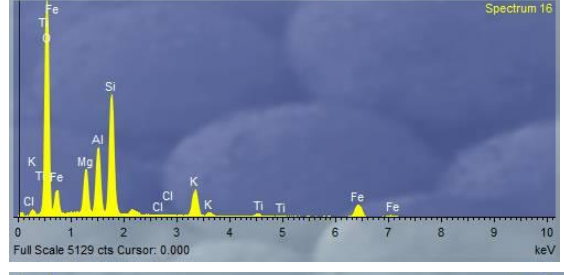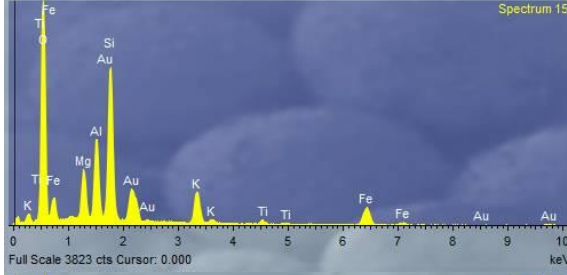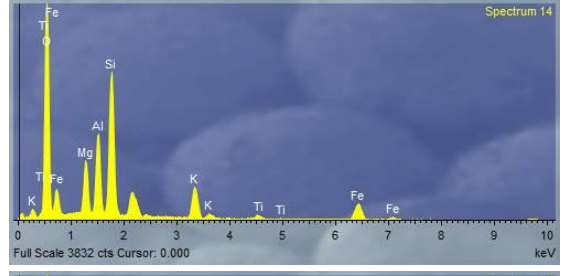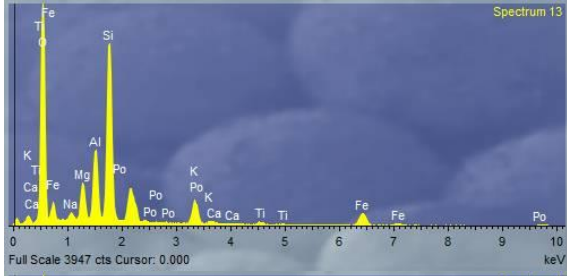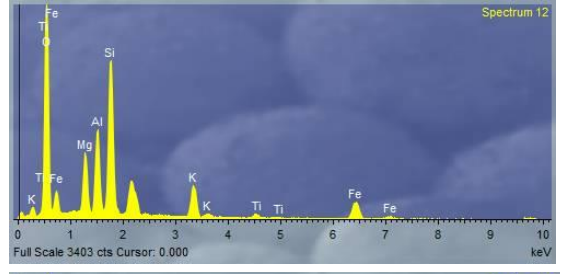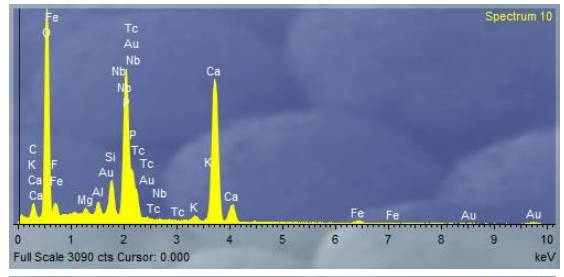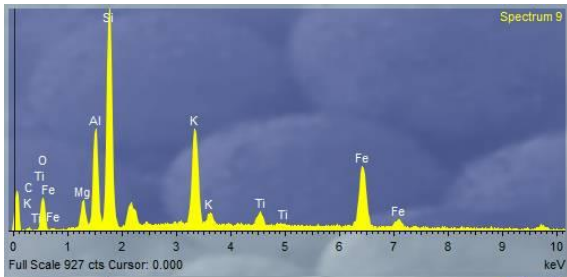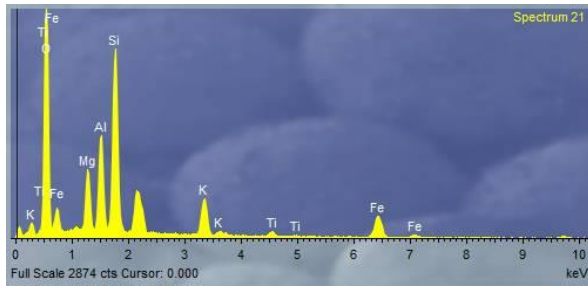
Figure C25. Photomicrograph and spectral analysis of a grain in granite dissolved at 50°C.
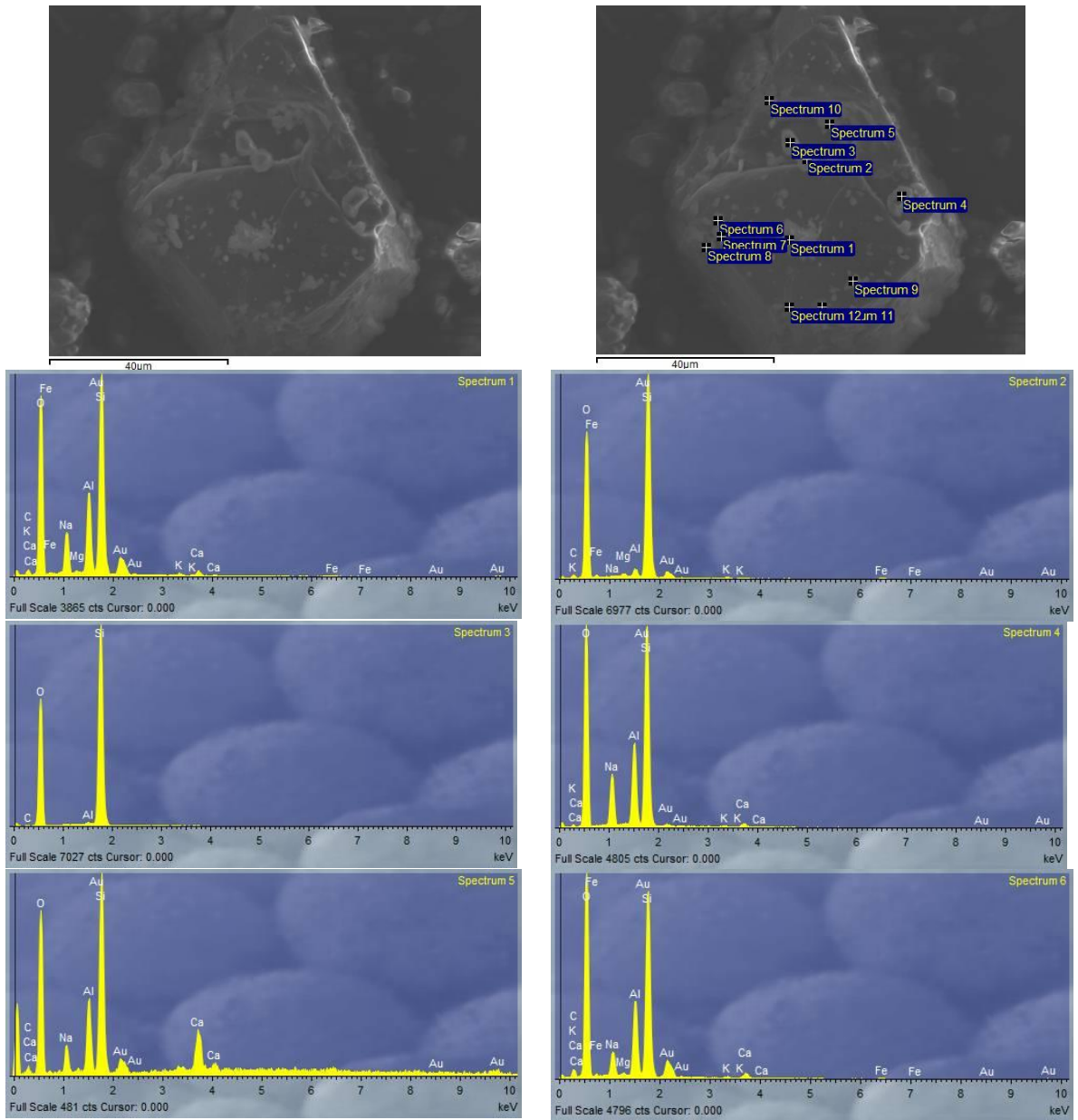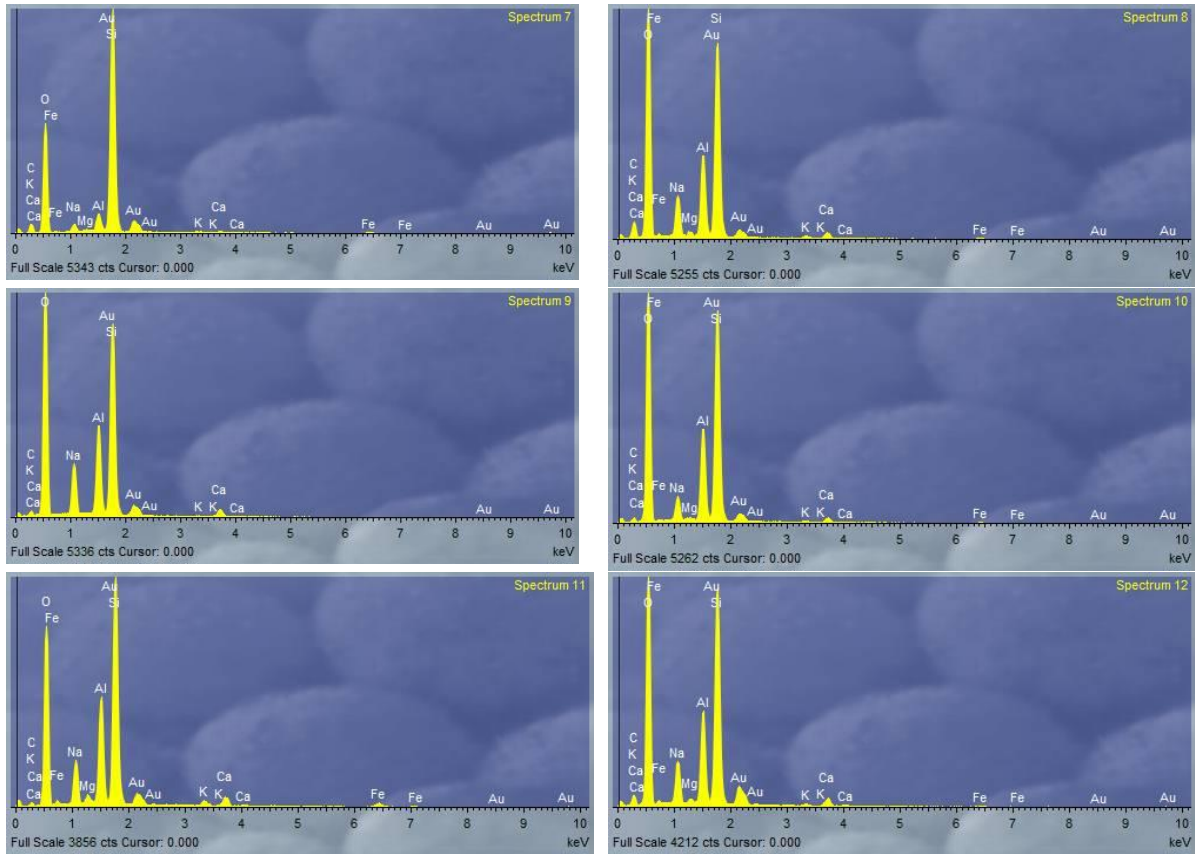
Figure C26. Photomicrograph and spectral analysis of a grain in Na-treated granite dissolved at 50°C.

Dolerite
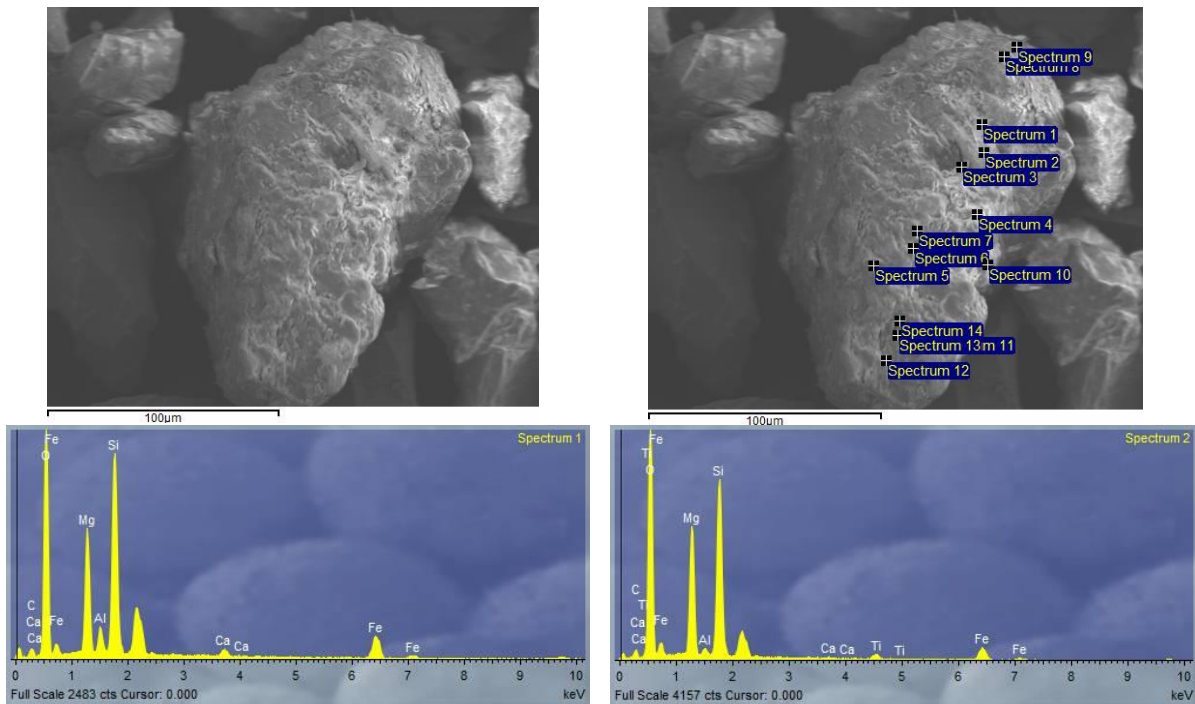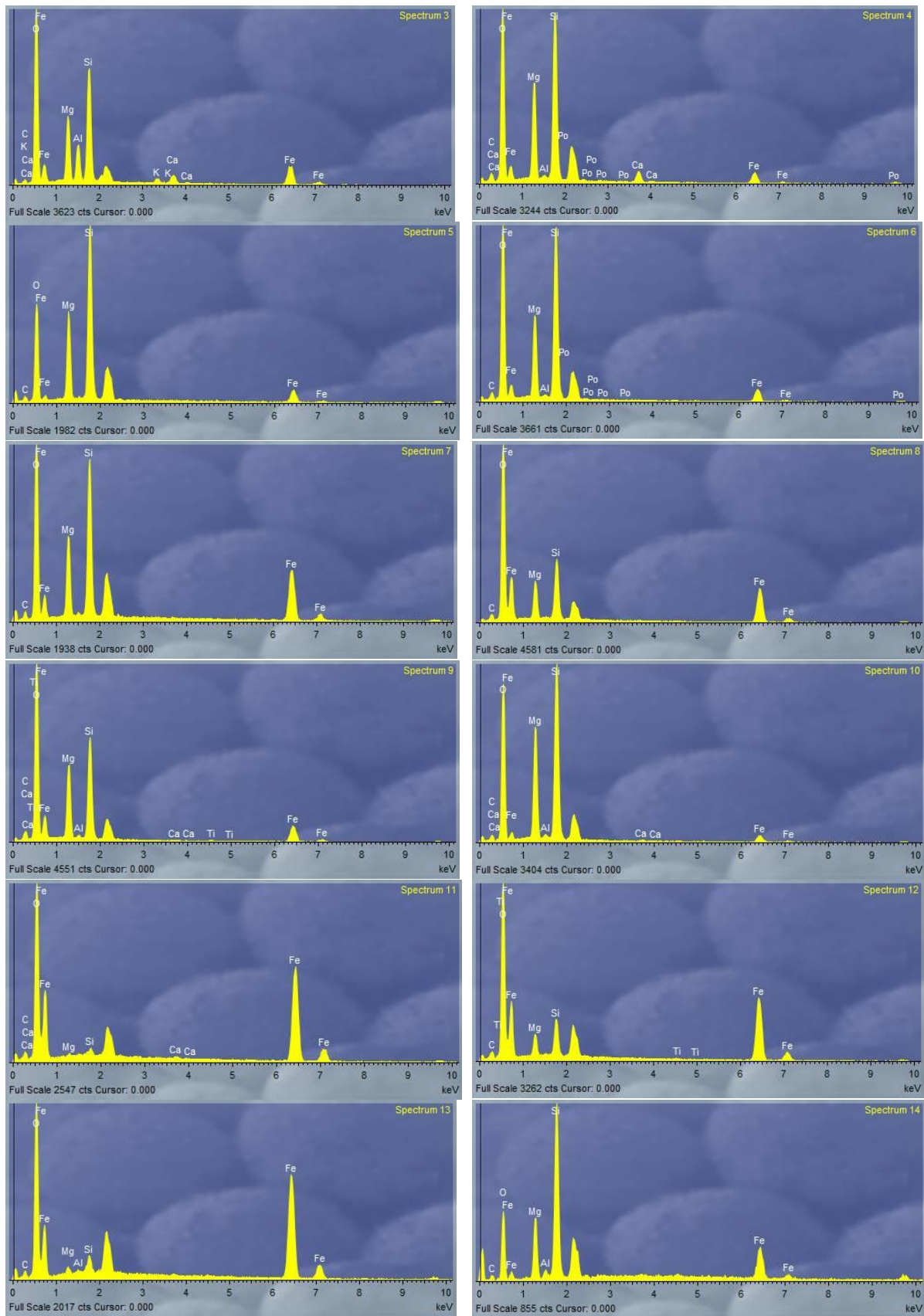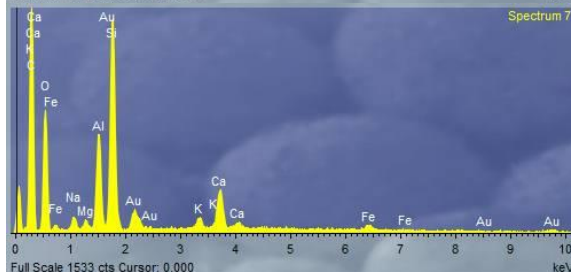
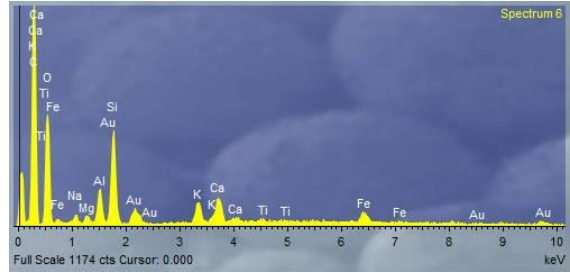*Figure C27. Photomicrograph and spectral analysis of a grain in dolerite dissolved at 50°C.*
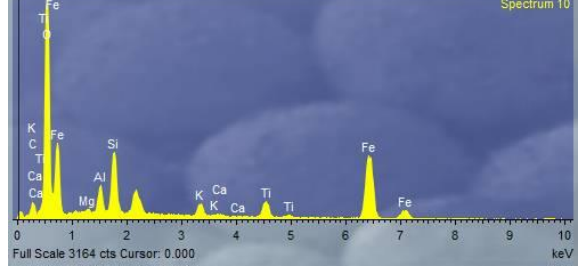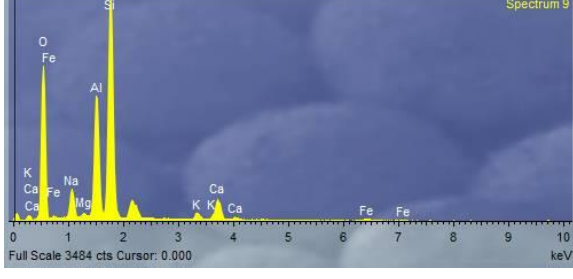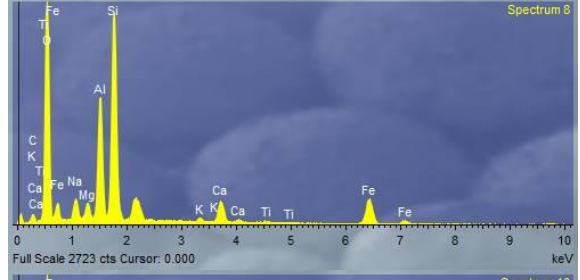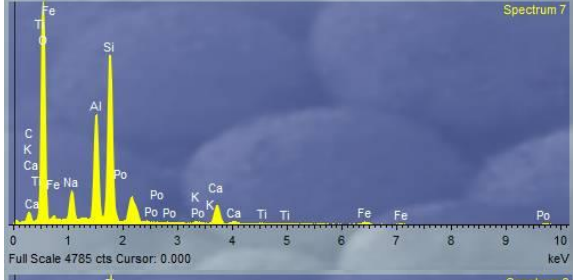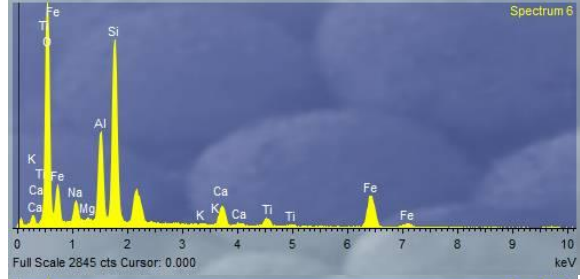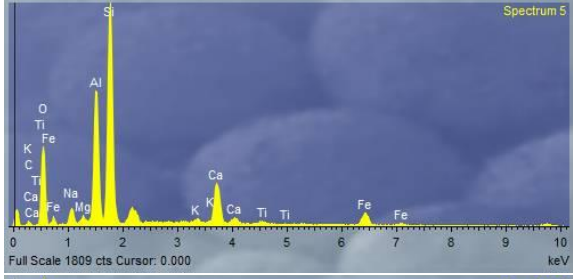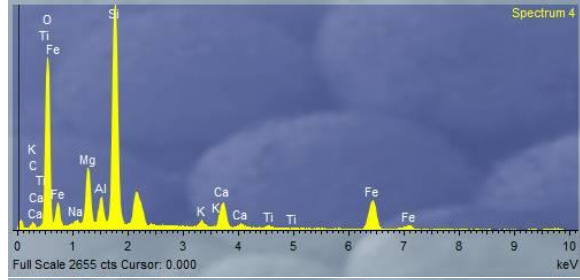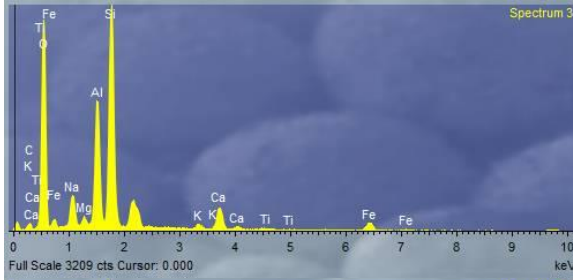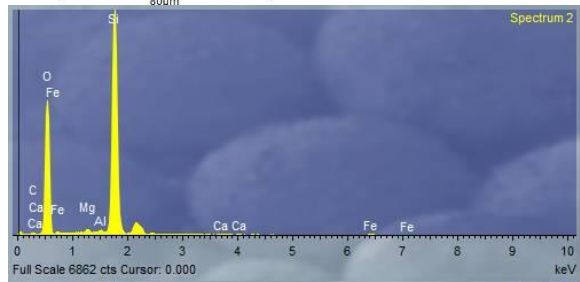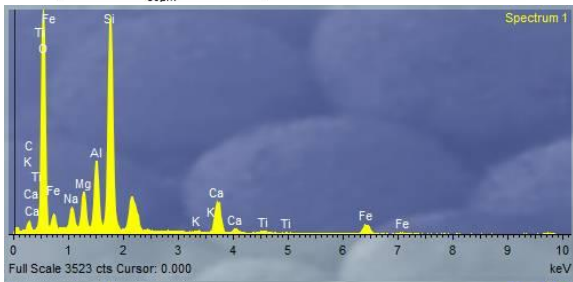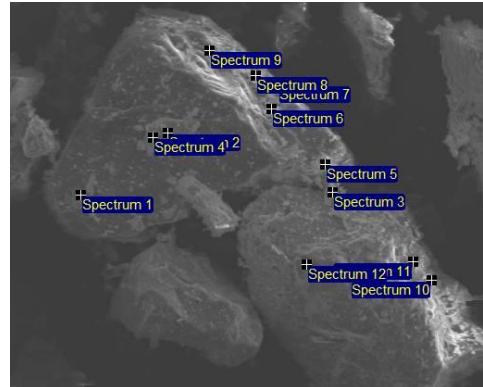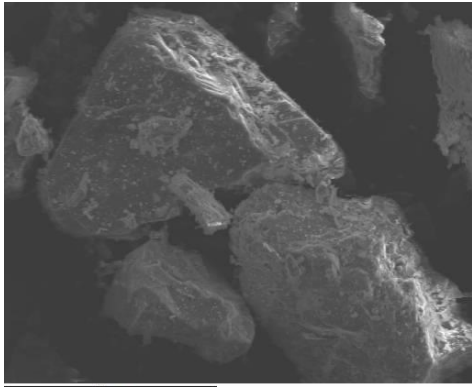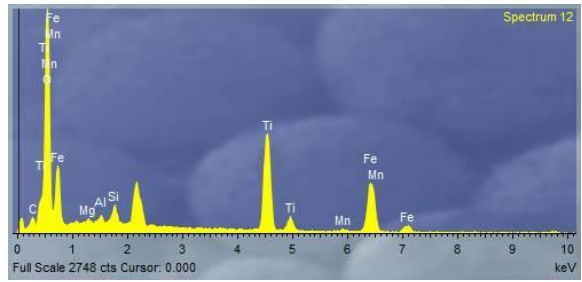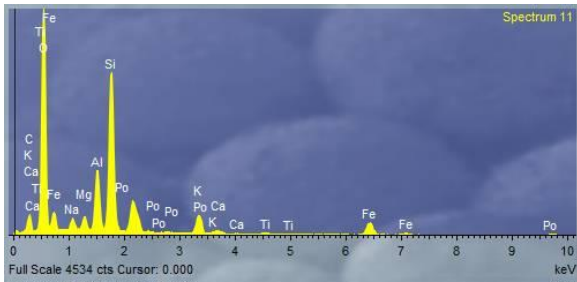
Figure C28. Photomicrograph and spectral analysis of a grain in Na-treated dolerite dissolved at 50°C.

Basalt
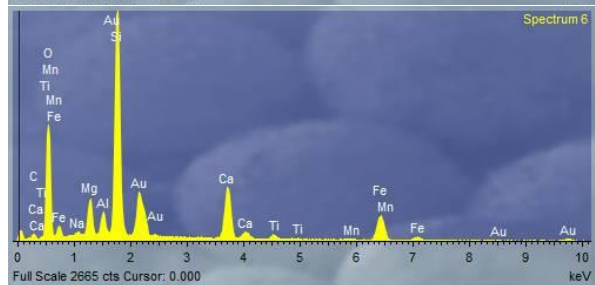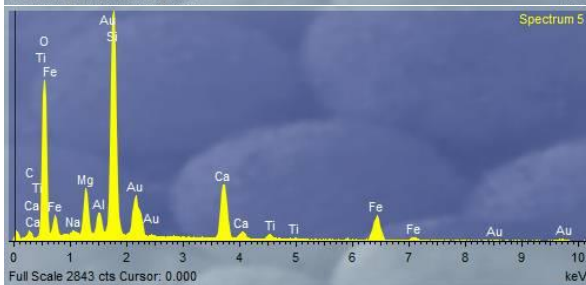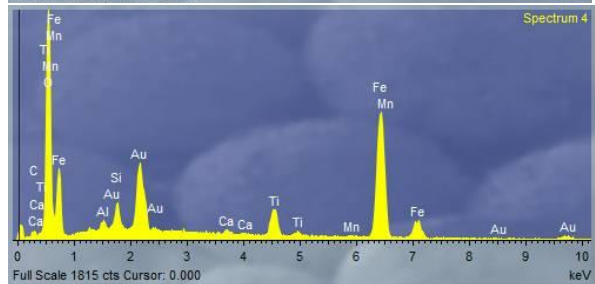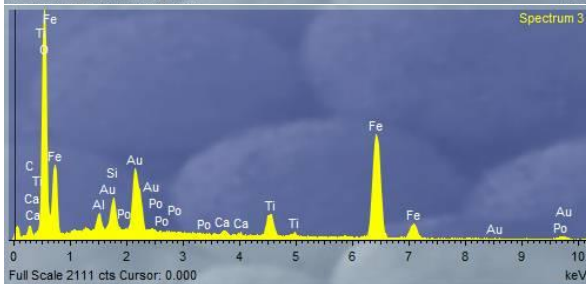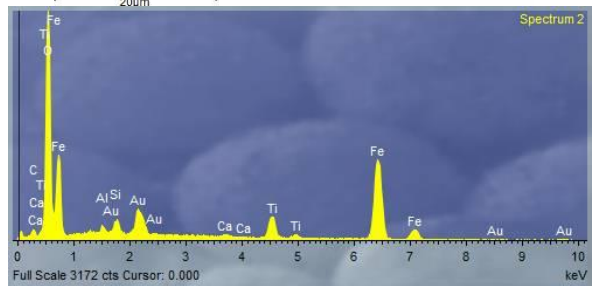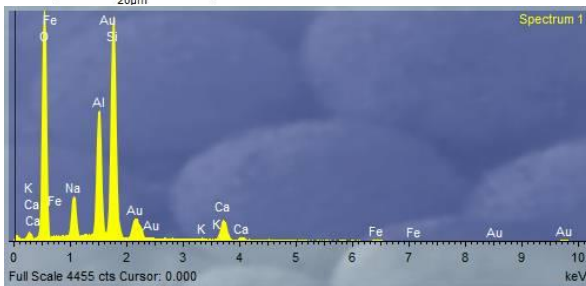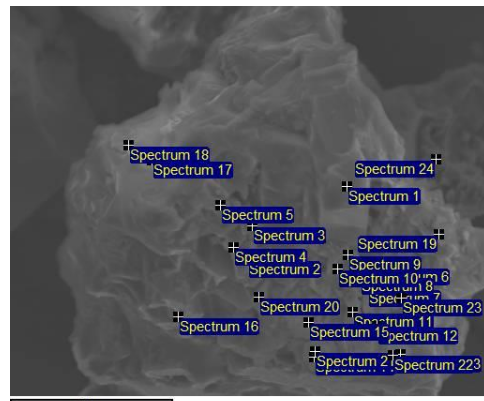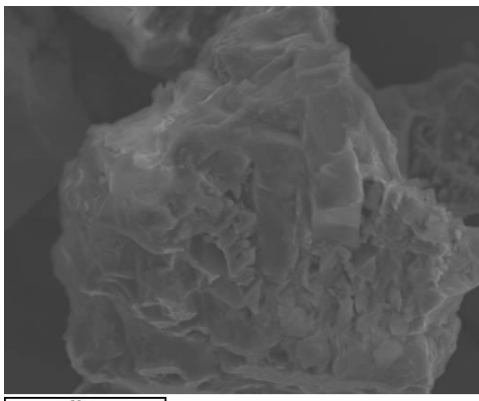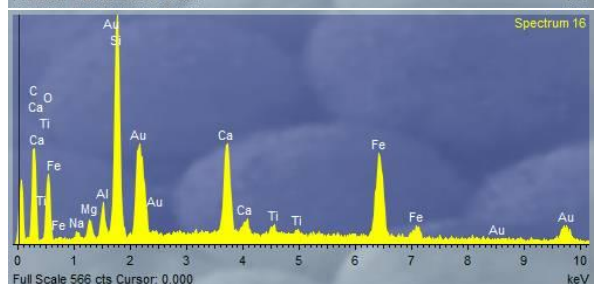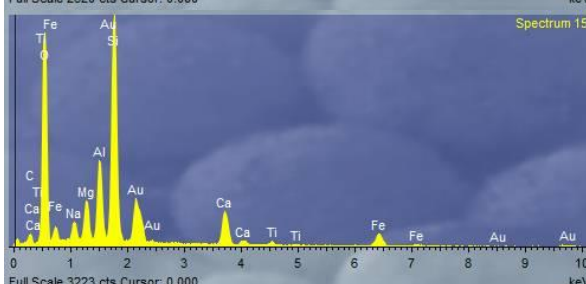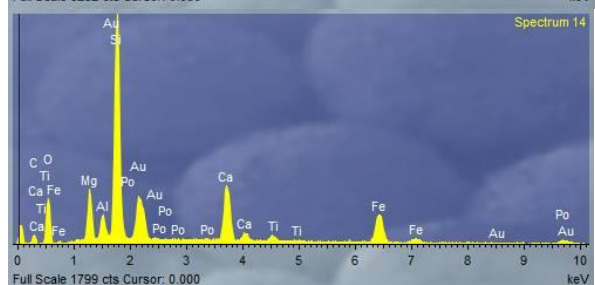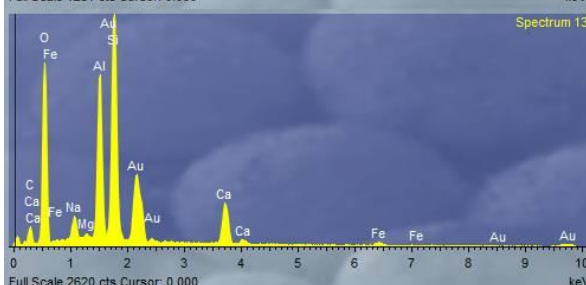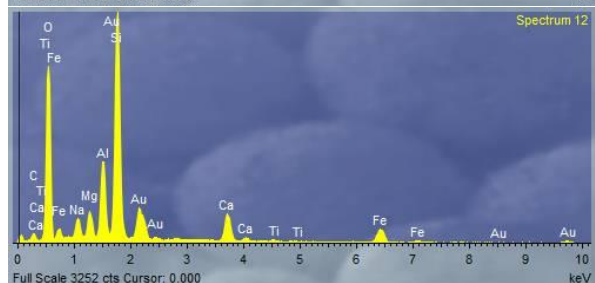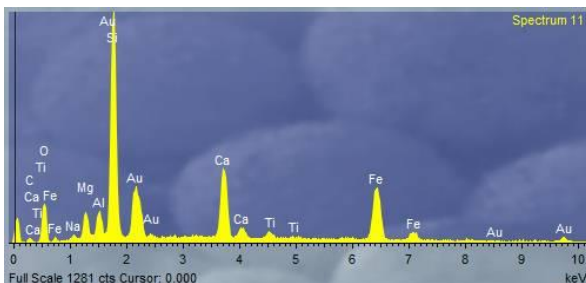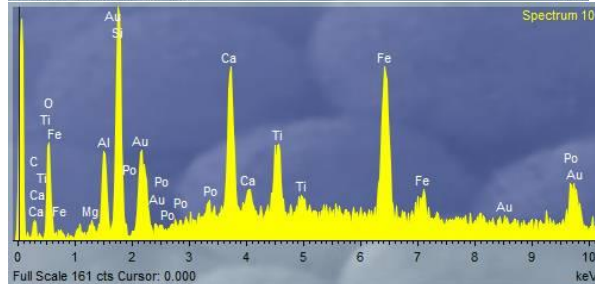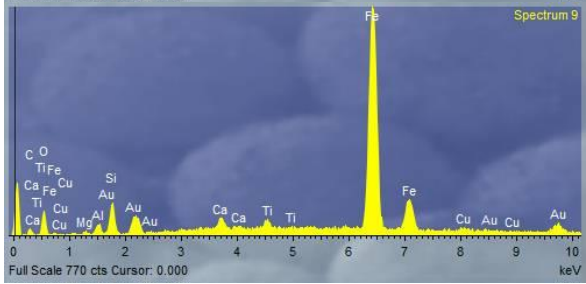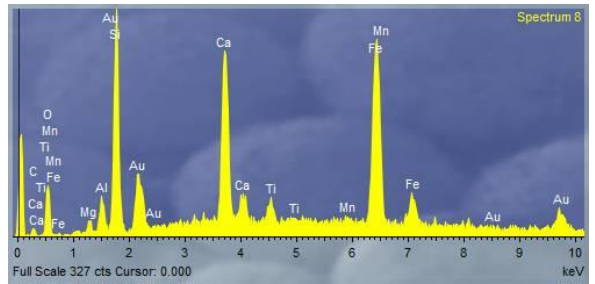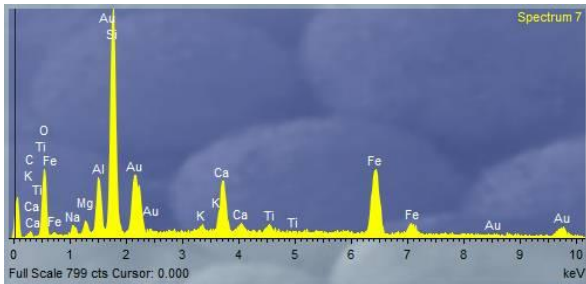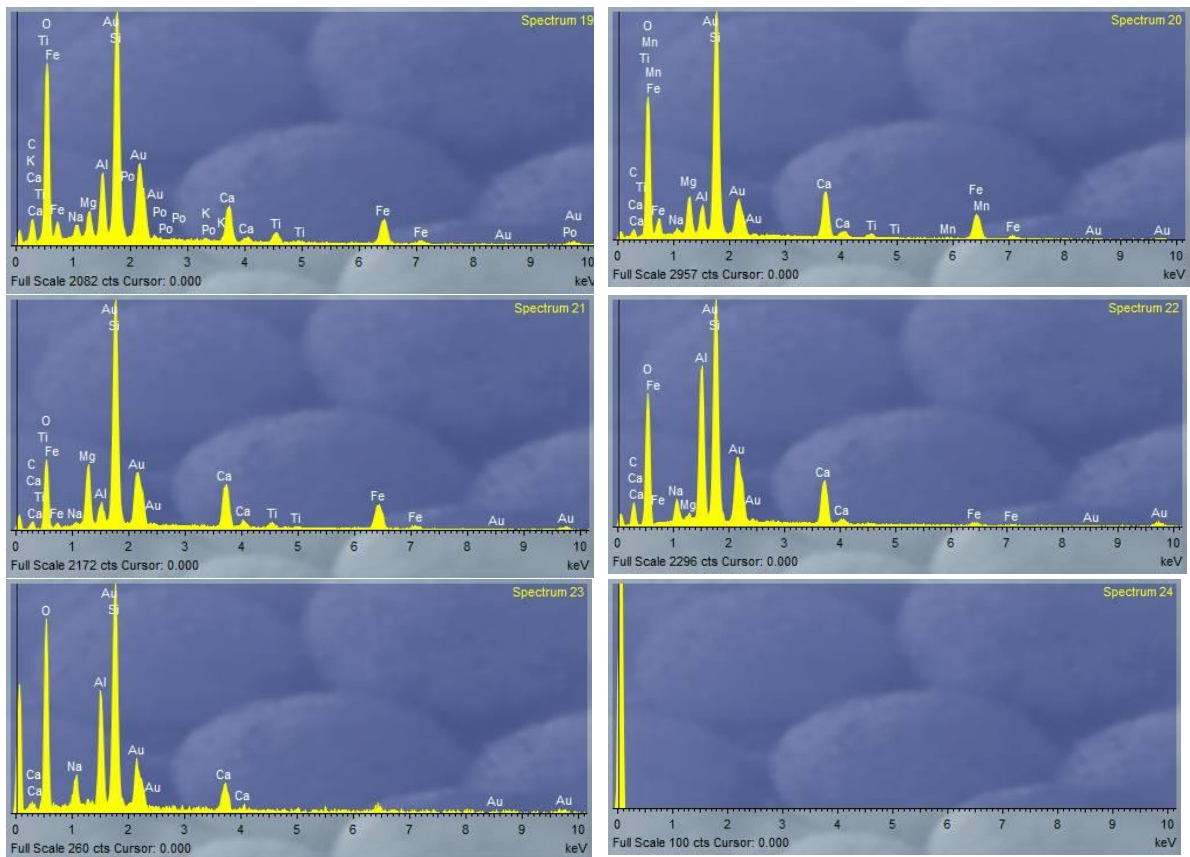
Figure C29. Photomicrograph and spectral analysis of a grain in basalt dissolved at 50°C.

118
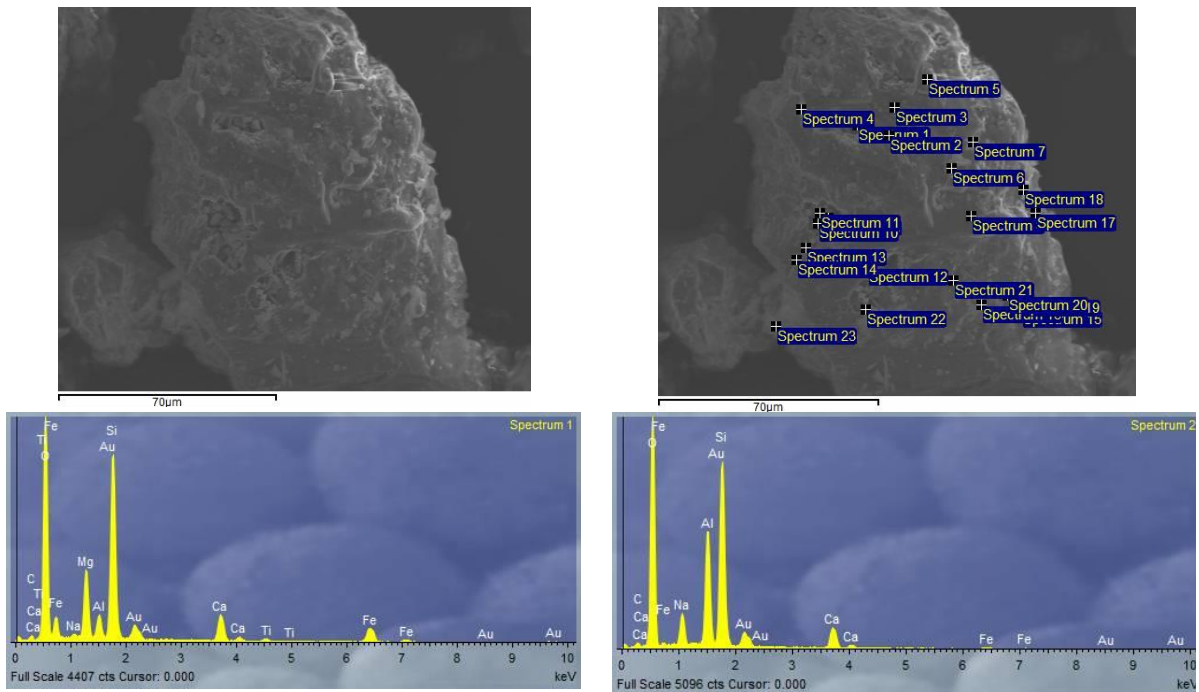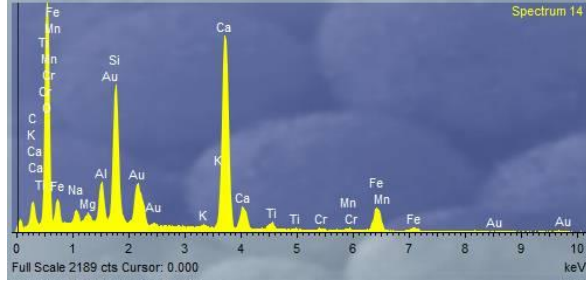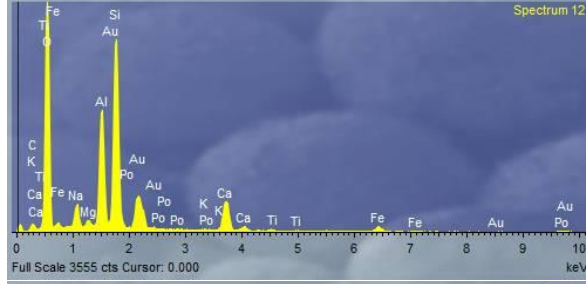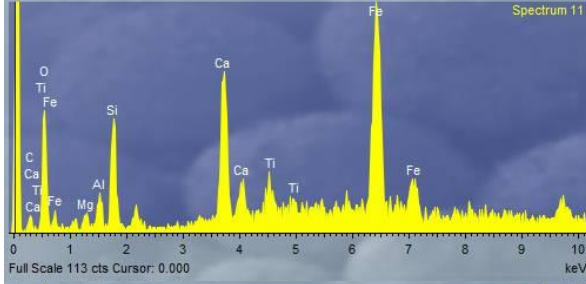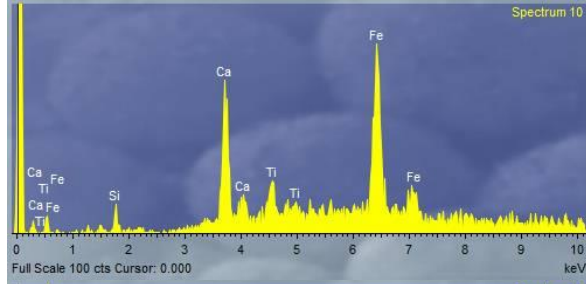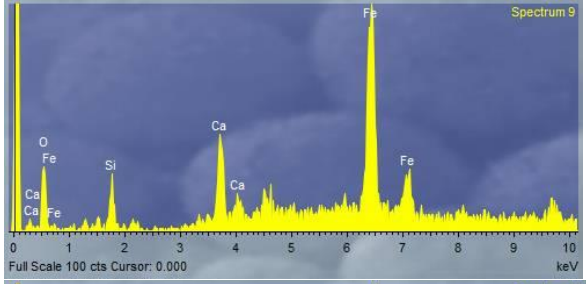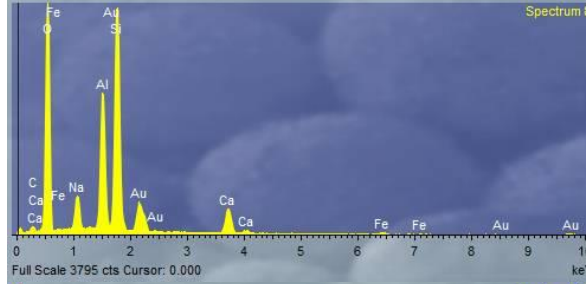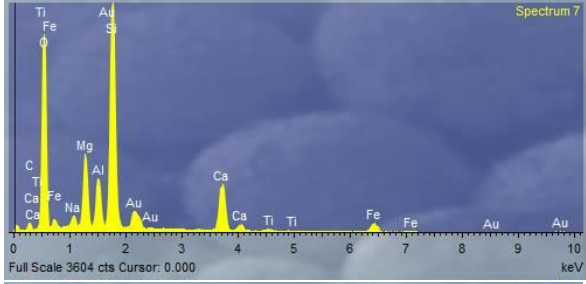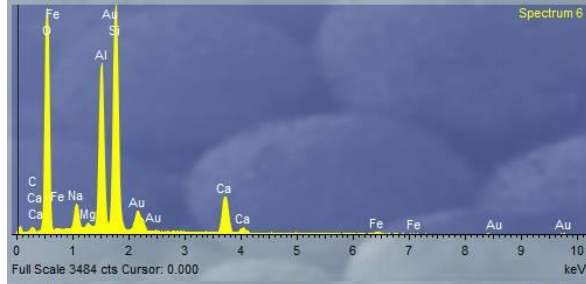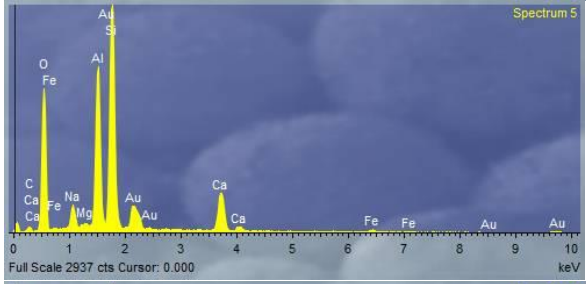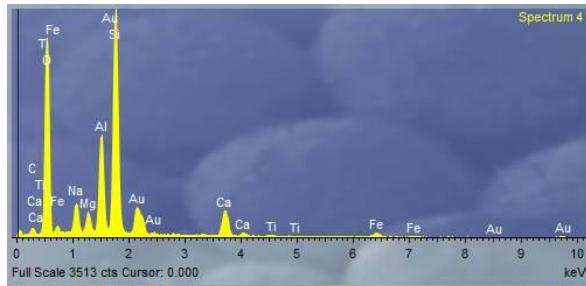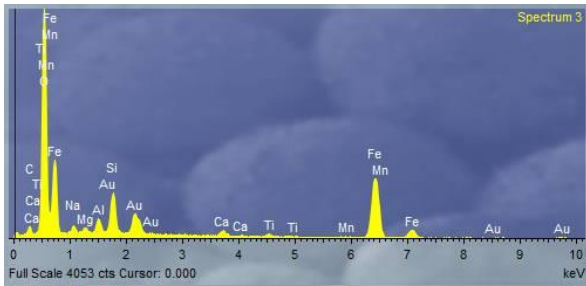
Figure C30. Photomicrograph and spectral analysis of a grain in Na-treated basalt dissolved at 50°C.

C4. Experiments at 100°C

Syenite

Figure C31. Photomicrograph and spectral analysis of a grain in syenite dissolved at 100°C.

Carbonatite

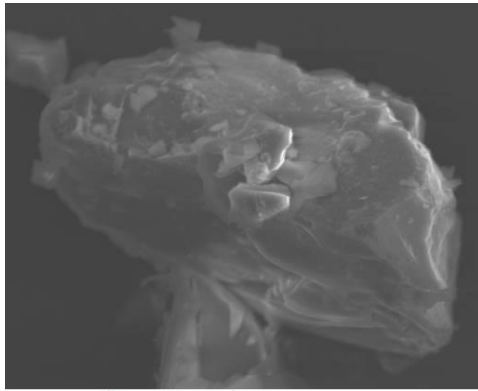Figure C32. Photomicrograph and spectral analysis of a grain in carbonatite dissolved at 100°C.

Gabbro

Figure C33. Photomicrograph and spectral analysis of a grain in gabbro dissolved at 100°C. Upper right image is a zoom-in of the upper left photomicrograph.
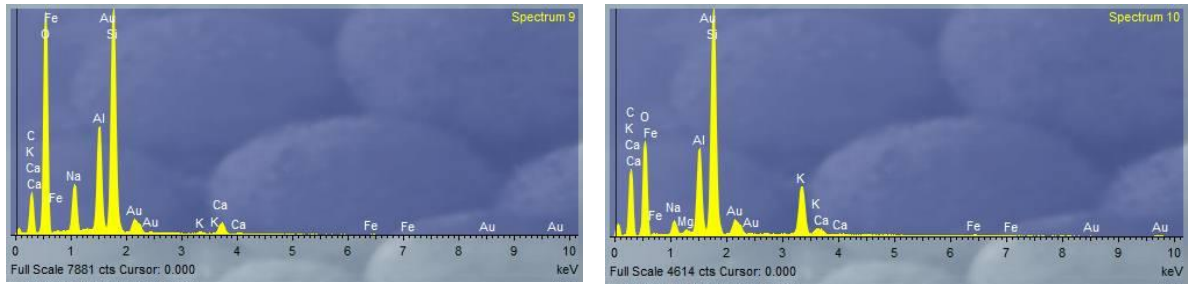
Granite
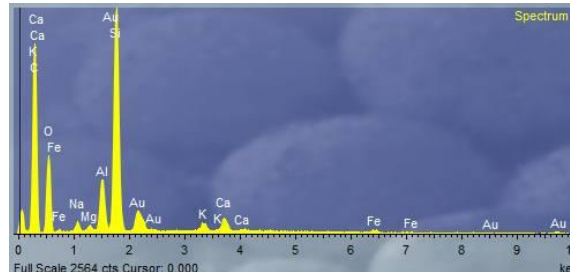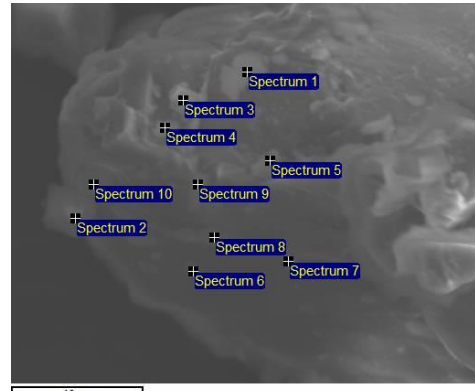
Figure C34. Photomicrograph and spectral analysis of a grain in granite dissolved at 100°C. Upper right image is a zoom-in of the upper left photomicrograph.
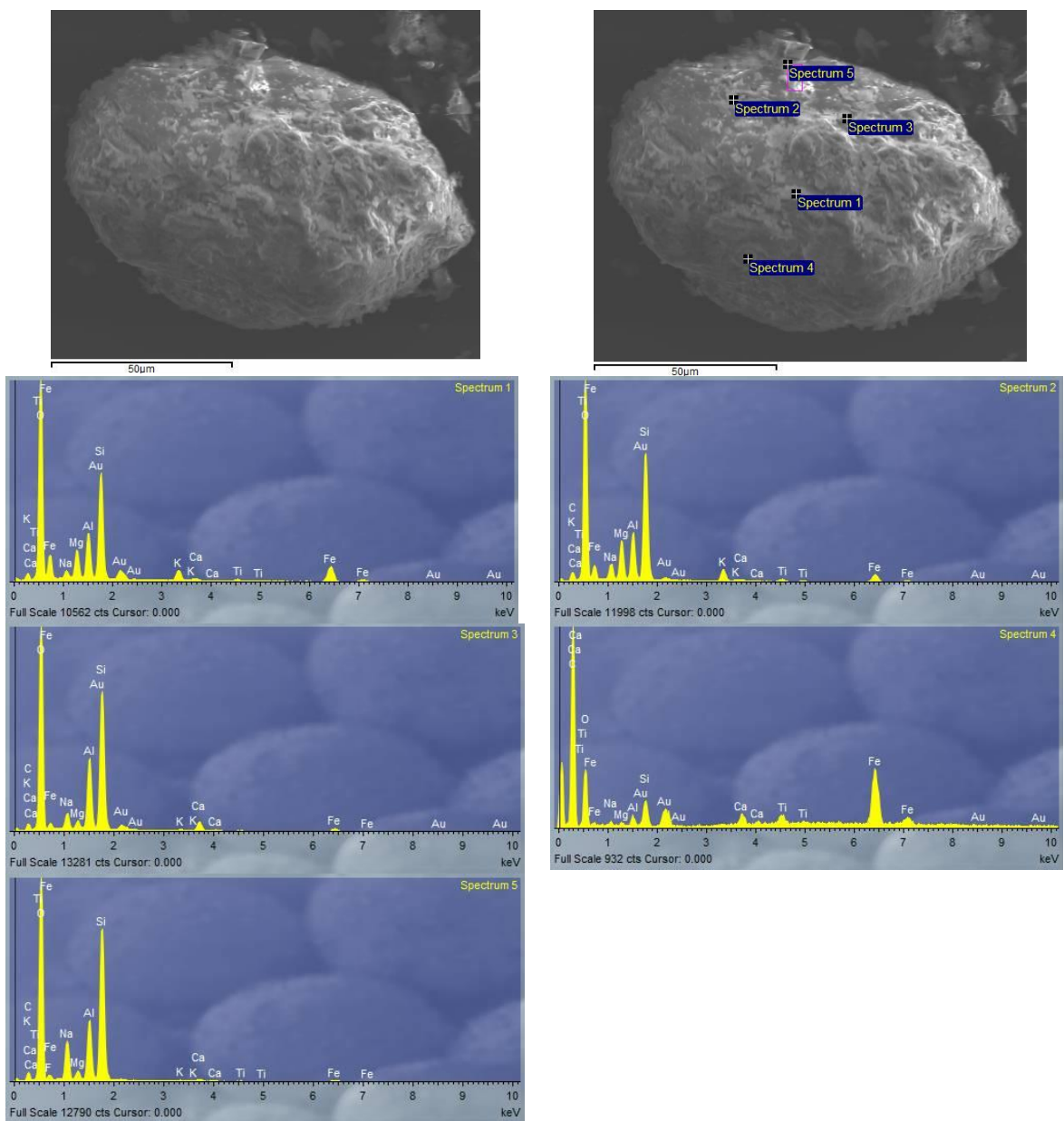
Dolerite

Figure C35. Photomicrograph and spectral analysis of a grain in dolerite dissolved at 100°C.
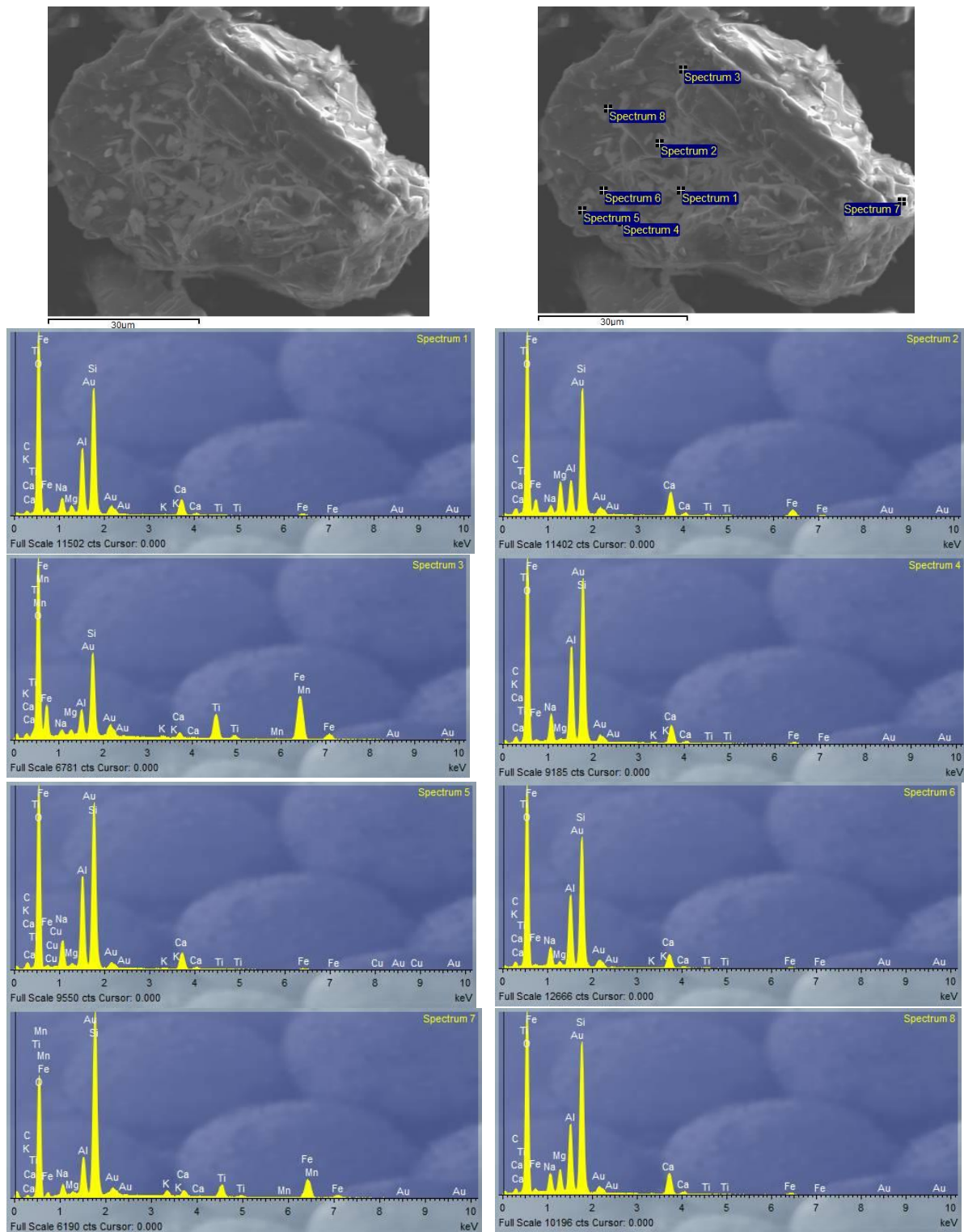
Basalt

Figure C36. Photomicrograph and spectral analysis of a grain in basalt dissolved at 100°C.